Universidad Autónoma de Madrid

Plasmonics for lasing action at the nanoscale.

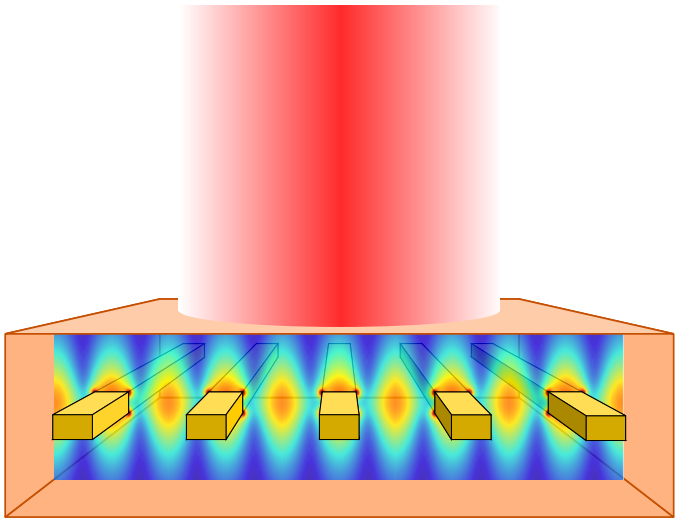

Javier Cuerda Rodríguez

Universidad Autónoma de Madrid

Departamento de Física Teórica de la Materia Condensada

Condensed Matter Physics Center (IFIMAC)

Tesis doctoral dirigida por:

Jorge Bravo Abad y Francisco José García Vidal

Madrid, agosto de 2017

If you can force your heart and nerve and sinew
To serve your turn long after they are gone,
And so hold on when there is nothing in you
Except the Will which says to them: 'Hold on!'

Rudyard Kipling, *If.*

Agradecimientos

En primer lugar, quiero dar gracias a mis directores, Jorge y FJ, por la oportunidad que ha representado realizar esta tesis. Considero que me propusieron un proyecto ambicioso y coherente, y que me han dotado de todas las herramientas para desarrollarlo. Aparte de las nociones de Física, me han inculcado el rigor y la honestidad claves para una investigación de calidad. Quiero dar gracias especialmente por la educación recibida en el aspecto de la comunicación científica, así como los consejos para convertirme en un investigador independiente. No quiero olvidar tampoco cómo, con su apoyo, he podido presentar mi trabajo en diferentes congresos.

Junto a ellos, Felix ha sido una pieza esencial en el desarrollo de mi tesis, permitiéndome acceder a gran parte de su sabiduría numérica. El período en que coincidimos en el departamento fue de intenso aprendizaje; gracias por el tiempo invertido en satisfacer mis tempranas dudas de Comsol, Linux, y de toda índole.

El hecho de colaborar con un grupo experimental ha supuesto un reto y un grato estímulo, que me ha obligado muchas veces a repensar y re-expresar mis ideas. Por ello, quiero agradecer a Esteban Bermúdez y Romain Quidant la intensa y fructífera colaboración que hemos mantenido. Aparte de ser un inquieto y excelente investigador, el carácter positivo y amigable de Esteban ha hecho de nuestra interacción un verdadero placer.

Deseo expresar mi agradecimiento a Luisa Bausá, Esteban Moreno, María A. Díaz García, Jaime Gómez Rivas y Alejandro Martínez su participación como Tribunal de Tesis. Asimismo, deseo hacer extensiva mi gratitud a Álvaro Blanco y Sergio Gutiérrez Rodrigo por su disponibilidad como miembros suplentes.

Hace ya 5 años que comencé mi andadura en el Departamento, realizando el trabajo de Fin de Master. Desde entonces hasta ahora, mi grupo ha crecido y se ha diversificado; sin embargo, no puedo dejar de agradecer los buenos ratos, las risas, las conversaciones científicas y no tanto, y en general el apoyo que he recibido de Juan Antonio, Pu, Jo-

hannes, Alex, Diego, Ricardo, Paloma, Rui-Qi, Rocío, Ning... Gracias a Carlos G. y los Javis por ser estupendos y atentos compañeros, de doctorado y de viaje. Gracias a Antonio por sus consejos, en especial aquellos relativos a la última etapa de mi tesis y a los siguientes pasos.

En el Departamento no sólo hay grandes científicos, sino también grandes compañeros y personas. Por ello, quiero agradecer a Rubén S., Víctor, Sergio, Carlos R., María, Álvaro F., etc. el clima de amistad que han creado cada día, y los eventos tan divertidos que hemos compartido.

Gracias a Fernando D., quien me introdujo en el grupo con el que como todos los días y fue un apoyo importante en un momento duro de mi tesis. Gracias a Linda, de una fortaleza enorme. A Ángel. A Stefan, que con su humor no deja de sorprendernos. Lo prometido es deuda: Desde aquí hago un llamamamiento por la iniciativa: 'Un jamón para Stefan', por todo lo que nos ayuda. Gracias a César, con quien comparto humor ácido y de quien he recibido grandes consejos sobre el mundo científico.

Gracias a Fabrice, Elena, (¡y Julia!), Carlos S., Blanca, Camilo, David, y al resto del grupo Polaflow, por incluirme en sus divertidos eventos, comidas y descansos para café, por Polachess, y por darme un excelente ejemplo de que el trabajo y la buena investigación no están reñidas con el cariño y la franca amistad.

El Despacho 513 ha sido una influencia tremendamente positiva en mi entorno laboral. En él he encontrado a personas, y amigos, tremendamente afines, que saben compatibilizar los momentos de concentración con la distensión y los momentos de absurdismo. Quiero agradecer a Diego M., que fue mi primer mentor de Comsol y de otras muchas cosas que un estudiante novato no conoce. A Edwin, que con su risa nos alegró los días durante 3 meses. A William. A David (Je ne suis pas le hussard!), quien del rugby se pasó al ajedrez y descubrió que tenía madera de IM. A Diego S., quien en poco tiempo se ha convertido en un buen amigo que siempre me motiva con conversaciones apasionantes. A Eduardo sólo puedo decirle una cosa: Basta. A Blanca, con quien he compartido las incertidumbres propias de esta etapa. A Miguel, con quien he hecho el doctorado en paralelo, quien aparte de un gran nadador que no dejará de hacerme pagar cenas, ha sido un tremendo apoyo con Gnuplot, los trámites de tesis, y muchas cosas más. Muy especialmente a Ricardo, en lo profesional y en lo personal: Gracias por las frustraciones comsolianas compartidas, por tu absoluta generosidad a la hora de ayudarme con todos mis problemas y estados de ánimo, y por las conversaciones culturetas sobre literatura, política, arte, fotografía, danza o cotilleos varios. Te deseo mucha suerte con tu etapa actual.

Resulta difícil resumir en unas pocas páginas todo el cariño y apoyo que he recibido

de un número muy alto de personas a las que puedo llamar amigos. Pero no he llegado hasta aquí para no intentarlo: A 'papi' Ayar V., ser afín a pesar de las obligaciones, con el que siempre me comunico como si fuera mi hermano. A Elena C., por las amistades renacidas, y por compartir nuestras ansiedades vitales. A Aza, quien me ha aportado tanto, y en tantos sentidos, que sólo puedo resumir: Es mi tesis, John.
Deseo agradecer a Estrella del Pozo su asesoría para afrontar el último tramo de mi tesis. Sin duda, profesionales como ella, pero sobre todo personas, hacen grande la palabra vocación.
Gracias al equipo de ajedrez Santa María del Pilar, en especial a Tamayo, Dani, Aitor, Ricardo, Rubén y Yago, por entender que el desarrollo de un doctorado a veces está reñido con jugar bien los domingos... y, sobre todo, por la diversión y alegría que los rodea.
Gracias a mis biolocos: Sandra, por intentar comprender más allá de la obsesión, por el intenso cariño e infinito apoyo de los inicios. A los Bastilleros o Sonorámicos: Ana Olivas (por esa afinidad sempiterna y callarnos siempre a la vez para dejar hablar al otro), Laura Melgar (¡echando el ancla estoy!) y Litos, tan lejos con sus invasiones pero tan cerca y pendientes. A Antonio Talavera, reputado sabio, biólogo, músico y humorista sin par. A Sara y a Mar, que se estarán bailando unas sevillanas (qué duro es ser biólogo de b@ta).
Gracias a la *Secta*. A Jorge, que es la mejor persona que he conocido. A Belén, porque la guerra de pulsos chinos no terminará nunca. A Álvaro por spamearnos hasta el delirio, y enseñarnos a no dejar de ser niños. A Berta, porque siempre adoraré su humor ácido. A Mari Campo. A Javi Juanes. A David, que lleva la vocación de servicio a la práctica, llegando a niveles farmacéuticos, demostrando un corazón que no le cabe en el pecho; y a Ruth (mi vecinilla), que siempre me cuida en el sentido más terapéutico de la palabra, no por ello menos cercano, ni leal. Suena *Free bird* en la calle mientras escribo esto, ¿casualidad? Gracias por el Coche 1 y los debates encendidos a través de la noche. Gracias a Far y a Rubén, amigos desde el colegio, por los LeBar y por la sensación de volver siempre a algún sitio que puedo llamar hogar.
A Elena, que ha demostrado ser una compañera ejemplar, llevándome a encontrar el punto justo entre la comprensión y la exigencia hacia mi trabajo y hacia mí mismo. Estos últimos meses han sido especialmente duros y pese a todo ella siempre ha estado ahí; no puedo expresar con palabras (ni en números) la magnitud de su cariño y su generosidad. Por los veintes, los merequetengues, las promesas de bailes, la prueba del garrote y la ternura del dodecaedro. Y sobre todo por el presente y el futuro: Muchas gracias.

Gracias a los amigos de la carrera, que todavía siguen ahí desde que comíamos frente a Teórica. Gracias a La morada de la liche. A nuestra patrona, la Lute. A Sergio, de quien tanto he aprendido, y con quien más he charlado (¡con diferencia!) a nivel virtual. A Aday, que he visto resugir cual ave fénix. A Julia, por visitarme de vez en cuando en la UAM para constatar mi salud mental. A Juanma, la persona que más me ha sufrido este último año, por las conversaciones interminables, por abrir mis perspectivas, por enseñarme a disfrutar de la vida y querer compartir techo y experiencias conmigo. A Víctor, por haber sido mi primer compañero de piso, demostrar una empatía más allá de lo humano, y con su sonrisa imborrable inspirarnos a ser mejores. Por Every y las conversaciones eruditas de 200 mensajes por las mañanas. Finalmente y no por ello menos importante a Santi, quien ha sido un apoyo telemático constante, me ha ayudado a levantarme las mil veces que me he caído, y me ha demostrado que un buen libro y un poco de *hate* liberado a tiempo son suficientes para afrontar cualquier situación. Por las infinitas conversaciones que hacen de este mundo un lugar menos gris.

Gracias a toda mi familia. A mi abuela Nieves, que me cuidaba y me enseñó a jugar a las damas; a mi tío Javier, que decidió que aquello no era suficiente y me hizo un obseso del ajedrez. Algo de esa obsesión se ha trasladado, de algún modo, a la Física. Gracias mis hermanos Tomás y David, a mis cuñadas Concha y Yolanda, y a mis sobrinas Nieves y Nuria, por los eventos de cumpleaños y por preocuparse siempre por mí. Sobre todo, a mis padres, Nieves y Tomás, por trascender a sí mismos para comprender mi realidad y abrirme todas las puertas a aquello que anhelo conseguir. Por su apoyo constante, siempre, pase lo que pase. Porque ellos saben lo que han representado todas las horas invertidas en esta Tesis. A ellos les dedico todo mi trabajo.

Contents

Abstract

English

This thesis is devoted to the study of lasing action in plasmonic nanostructures. In order to treat the non-linear interaction of plasmonic resonances and active laser medium, we have developed a theoretical formalism based on a time-domain generalization of the finite element method. Within this framework, we analyze recent proposals of experimental designs of nanolasers in terms of the plasmonic modes that enable lasing action. This approach provides access to the full spatio-temporal dynamics of the electromagnetic fields and the population densities of the active medium.

We start by analyzing recent proposals based on propagating surface modes in plasmonic waveguides. We show that, under coherent pumping, plasmonic waveguides can be used, together with a feedback mechanism, to enable loss-compensation and laser self-sustained oscillations in this class of systems.

Our theoretical formalism also enables us to analyze the lasing properties of periodic metallic nanostructures, so-called plasmonic crystals. Considering recent experiments, we show the role of non-radiative modes in the near-field laser emission, finding that there exists an optimal lasing regime that enables accessing enhanced light-emission properties. Moreover, our results allow us to discuss the existence of an optimal set of geometrical parameters for this class of periodic nanostructured lasers.

Finally, we analyze lasing action in core-shell metallic nanoparticles, focusing on how the laser properties evolve when going from an spherical geometry towards an elongated nanorod configuration. Discussion of these results in view of the current experimental paradigm, as well as physical insight based on a semianalytical approach, is finally provided.

Castellano

Esta tesis está dedicada al estudio de la acción láser en nanoestructuras plasmónicas. A efectos de tratar la interacción no lineal de los modos electromagnéticos plasmónicos con el medio láser, se ha desarrollado un formalismo teórico basado en una generalización en dominio de tiempos del método de elementos finitos. Esta herramienta nos permite analizar propuestas recientes de diseños experimentales de nanoláseres, en términos de los modos plasmónicos que habilitan la acción láser. Este enfoque permite acceder a la totalidad de la dinámica espacial y temporal de los campos electromagnéticos que rigen dichos sistemas, así como la distribución de ganancia en el medio activo.

Comenzamos analizando propuestas recientes de nanoláseres basadas en el uso de modos de superficie propagantes en guías de onda plasmónicas. Los resultados muestran que el bombeo coherente de dichos sistemas, unido a la implementación de un sistema de retroalimentación, otorga acceso a regímenes de compensación de las pérdidas, y permite iniciar oscilaciones láser auto-sostenidas.

Asimismo, mediante nuestro formalismo teórico, analizamos las propiedades láser de nanoestructuras metálicas con perforaciones periódicas, denominadas cristales plasmónicos. En base a experimentos recientes, mostramos el papel que juegan los modos no radiativos en la emisión láser de campo cercano, encontrando que existe un régimen que permite acceder a propiedades de emisión óptimas. Adicionalmente, nuestros resultados nos permiten argumentar la existencia de un conjunto de parámetros geométricos óptimo a efectos de crear láseres con dichas nanoestructuras periódicas.

Finalmente, se analiza la acción láser en nanopartículas metálicas con recubrimiento dieléctrico, poniendo especial atención en la evolución de las propiedades láser a medida que se realiza la elongación desde una geometría esférica a una estructura tipo nanovarilla. Estos resultados se sitúan en contexto de los últimos resultados experimentales que conforman el paradigma actual en este tipo de láseres. Por último, se realiza un estudio semianalítico que permite obtener información cualitativa de la física de dichos sistemas.

List of acronyms

This is a list of the acronyms used in the text (in alphabetical order).

1D	One dimension
2D	Two dimensions
3D	Three dimensions
ACS	Absorption cross section
ASE	Amplified spontaneous emission
BC	Boundary condition
CMT	Coupled mode theory
CPP	Channel plasmon polariton
CW	Continuous wave
ECS	Extinction cross section
EM	Electromagnetic
FDTD	Finite-difference time-domain method
FEM	Finite element method
FRET	Förster resonant energy transfer
LRSPP	Long range surface plasmon polariton
LSP	Localized surface plasmon
NW	Nanowire
PML	Perfect matched layer
RF	Radio-frequency
SCS	Scattering cross section
SPP	Surface plasmon polariton

SRSPP	Short range surface plasmon polariton
TE	Transverse electric
TM	Transverse magnetic
VG	V-Groove

1 | General Introduction

Lasers have represented a huge breakthrough both in the technology of the twentieth century and in the understanding of light-matter interaction. Although their fundamental principles were formulated by Einstein in 1917 [1], their implementation was not realized until Maiman, following an idea by Schawlow and Townes [2], pumped a ruby crystal situated between two silver mirrors. In view of the technological revolution that followed, it is ironic to recall now how the laser was called "a solution looking for a problem" in 1960, due to the apparent lack of practical usefulness at that time. Nowadays, reproducing CD-ROM devices, performing delicate surgery on the human eye, or cutting and welding thick pieces of metal, are only a few samples of the vast variety of applications that lasers exhibit. The first generation of solid-state, organic dye and gas lasers, based on the centimetre scale, has evolved to allow for new unprecedented features, as extreme peak powers on the petawatt scale, increased efficiency, or devices with sizes ranging from the giant pulsed-lasers to lasers operating at the nanoscale.
Following Moore's law, the number of on-chip devices is doubled each eighteen months, a trend which still nowadays has been being followed since the 60's, and has its most clear manifestation in the miniaturization trend followed by transistors and microelectronic components. A similar development was observed in the field of Photonics in an early stage [3], and since the past decade strong efforts are devoted to implement optical amplifiers, lasers, couplers, (de)multiplexers and filters as building blocks of small optical circuits. In this context, nanoscale laser sources would have a huge impact for on-chip optical communications and data processing, with higher bandwidth and faster data transmission rates beyond the realm of electronics [4], new pathways in medical imaging and sensing, opening the door to biocompatible and implantable nanodevices [5], and 3D displays and advanced holography [6], not to say that they would constitute

an enormously insightful platform to analyze strong light-matter interaction at small scales.

Progress in laser miniaturization involves rethinking the essential components of a lasing system. In general, a laser cavity consists in an active medium enclosed within some optical feedback mechanism. When externally pumped (e.g. optically or electrically), the constituents of the active medium (atoms, molecules, ions, or some kind of semiconductor) are excited to higher quantum levels. If a condition of population inversion is created between the levels of a considered optical transition (the lasing transition), the active medium is said to achieve optical gain. On the other hand, the optical feedback elements allow a beam of radiation to propagate back and forth through the cavity and build-up electromagnetic energy with spatial and temporal coherence. The population inversion created in the active medium then acts to deliver energy to the electromagnetic cavity modes by means of a process called stimulated emission, replicating the input signal with a dramatic increase in amplitude. The lasing threshold will be reached if the accumulated optical gain balances the cavity losses at some critical pumping strength, leading to intense, coherent and directional narrowband light emission.

Figure 1.1 sketches a typical Fabry-Perot laser cavity in which the optical feedback is generated by means of two parallel planar mirrors with reflectivity values R_1 and R_2, delimiting the cavity. We say that a beam of radiation completes a round-trip when a single oscillation, while travelling back and forth across this cavity, is completed. At the lasing threshold, the value of the electric field amplitude E_0 should remain unaltered after one round-trip, yielding the condition [7]:

$$E_0\sqrt{R_1R_2}e^{(G_m-\alpha_i)L}e^{i4\pi nL/\lambda_0} = E_0 \tag{1.1}$$

where n is the refractive index inside the cavity, L is the cavity length, G_m is called the modal optical gain, and α_i is the absorption cavity loss coefficient. The equation above imposes constraints either on the cavity length and on the phase of the exponential factors. Namely, in order to reach the lasing threshold, the length L must be equal to a multiple of 2π:

$$L = m\frac{\lambda_0}{2n} \tag{1.2}$$

with m being an integer. Thus, the shortest cavity length for this cavity is given by the diffraction size limit: $L = \lambda_0/2n$. In addition, at the lasing threshold, the absorption

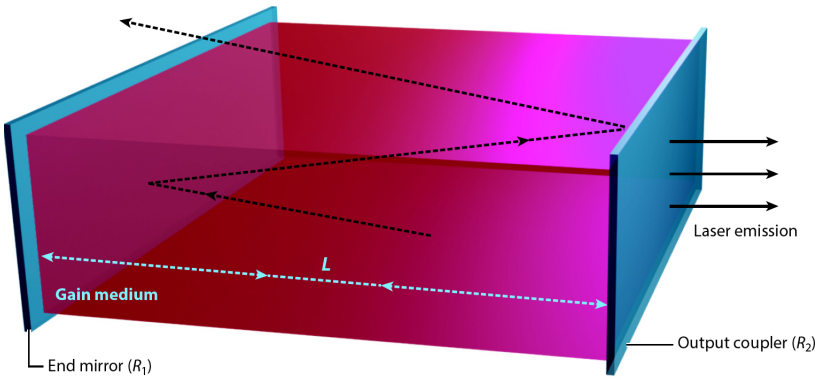

Figure 1.1: Conventional Fabry-Perot cavity used for laser light generation. The mirrors select the direction of laser light emission (blue dashed line), while photons with other direction escape from the cavity (black dashed line) (Figure reprinted from [8]).

losses are balanced with the material gain and the radiative mirror losses at each round trip, yielding:

$$L = \frac{-\ln\left(R_1 R_2\right)}{2\left(G_m - \alpha_i\right)} \tag{1.3}$$

The modal gain G_m is a quantity characteristic of each mode and is closely related to the material gain G_a, through the confinement factor, Γ, that accounts for the field distribution of the considered mode, with the gain material: $G_m = \Gamma G_a$. The internal cavity loss α_i and the radiative mirror losses R_1 and R_2 can be related to the quality or $Q-$factor of the system, by means of the relation:

$$Q = \frac{2\pi}{\lambda_0}\left(\frac{\alpha_i - (1/2L)\ln(R_1 R_2)}{n}\right)^{-1} \tag{1.4}$$

The expressions above allow us to early identify the main participants in lasing action, ruled by the cavity loss, through the $Q-$factor, the confinement of the EM fields inside the cavity, given by the quantity Γ, and the material gain G_a, which is an intrinsic property of the active medium. We will later provide further information on how to recognize lasing action in a given setup.

Very much in the same spirit of the cavity model shown above, the initial proposals for laser miniaturization relied on small dielectric structures, incorporating distributed Bragg reflectors (DBR) for optical feedback. These systems displayed low internal cavity losses, with high $Q-$factors (> 1000) and confined electromagnetic energy at scales

limited by diffraction. As a consequence, low-threshold power operation in these laser devices required not only a high degree of confinement Γ, but also suitable active media displaying high material gain G_a that may compensate for their low cavity volumes, including organic dyes, colloidal quantum dots, and semiconducting nanowires [7].

The first initiative towards a small-sized laser consisted of highly-reflective DBR devices, with $R_{1,2} \simeq 0.99$, sandwiching an active region stacking one or more semiconductor thin layers called quantum wells (QWs). This system was called vertical-cavity surface-emitting laser (VCSEL). Such a device was realized on 1979, and was limited to cryogenic temperatures [9] and optically pumped. It took a decade to attain electrically-pumpled [10] continuous-wave operation in room-temperature conditions [11] for this class of structures, and in the late 1990s, the first available commercial devices appeared [12]. Owing to the thin depth of the QW layers, VCSELs confine electromagnetic energy within small distances (around 10 nm) in the growth direction (see Fig. 1.2(a)). However, their transversal confinement is quite poor (of the order of several wavelengths). An alternative design consists in the use of semiconductor nanowires [13, 14] that feature improved transversal confinement but a reduced reflection coefficient ($R_{1,2} \simeq 0.9$). Upon strong optical pumping each single nanowire act as a cavity and as a gain medium by itself, with the high refractive index of its facets providing optical feedback without an additional device. [15, 16]. Refined experimental techniques have allowed to manufacture such devices in self-assembled sets [17].

The search for more compact lasing systems led to cavity geometries featuring radial symmetry, that achieve a round-trip oscillation by means of modes circulating around their edge. In this manner, the mirror losses at the ends of the linear geometries above are prevented. The first microdisk lasers arised in the 1990s, composed of a thin disk of semiconducting material which supports whispering gallery modes that display high $Q-$factors, up to 10^7 in the most optimized case of SiO_2 toroid structures [18]. The typical size of these systems is 3 μm in the transversal direction (see Fig 1.2(c) for a typical device). The minimum achievable thickness is of the order of hundreds of nanometers, without accounting for the pillars needed to provide electrical pumping [19]. Instead, if an optical pumping mechanism is used, the full device size is in the submicrometer range. Further decreasing the diameter leads to increased radiative losses which raise unadvantageously the laser footprint. Subsequent landmarks on this class of lasers included continuous-wave electrical pumping [20], and in the late 2000s, this class of devices found its implementation in on-chip platforms [21, 22].

Recent advances on crystal growth and fabrication technology have strongly attracted interest in engineering optical microcavities to achieve complete control over light prop-

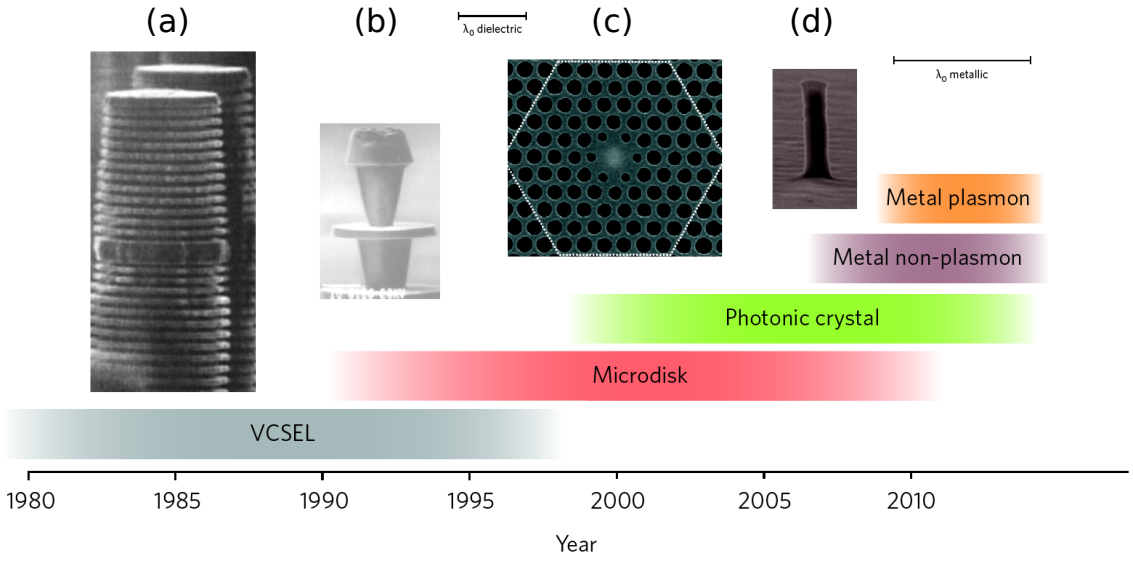

Figure 1.2: Overview of small laser cavities. The timeline of development of the considered device, since their discovery until their mass-scale production, is depicted together with typical examples compared with the operating wavelength λ_0. (a) VCSEL. (b) Microdisk laser. (c) Photonic crystal laser. (d) Non-plasmonic metallic microcavity. (Figure adapted from [7]).

agation. One of the most promising alternatives in this direction consists in creating periodically structured dielectric media of alternating refractive index. If the absorption of its consituents is small enough, they consitute photonic analogues of electronic crystals, with a band structure that includes photonic band gaps, preventing the propagation of light in specific directions and at certain frequency ranges. Such systems are known as *photonic crystals* [23–26]. Creating defects on the perfect lattice that they conform, allows confining light in nanoscale dimensions down to the diffraction limit. This fact led to a new type of microcavity laser at a single defect of a nanofabricated 2-dimensional photonic crystal [27] (see Fig. 1.2(c)). Photonic crystal cavities also make use of Bragg gratings to confine light through total internal reflection. Such systems can reach $Q-$factors up to 3000 and operate at room temperatures incorporating either optical pumping or pulsed electrical pumping [28]. These values, together with the small gain volume featured by these structures, have permitted accessing the lowest lasing thresholds demonstrated so far for a semiconductor laser at room temperature. Furthermore, 3-dimensional photonic crystals have been used, which allow attaining $Q-$factors of 40000 [29].

During a long time, metallic cavities were disregarded to create microlasers, owing to

the high dissipative losses that makes the lasing regime only reachable under extreme pumping conditions, and that introduce heating in the system. However, using a vertical travelling-wave core-shell structure enclosed between Bragg gratings, efficient heat removal is attained [30] and contacts for electrical pumping can be easily implemented. Substantially small transversal sizes with respect to the laser models above can be obtained by means of a cavity formed by a metallic cladding enclosing a high-gain semiconductor material. This configuration completely encapsulates the active volume, forcedly reducing the transverse mode size. The smallest device of this type was attained by Hill et al. [31] (see Fig. 1.2(d)), with a corresponding transverse size of ~ 260 nm.

The size of the cavity modes featuring lasing in the designs above presents the fundamental restriction given by the diffraction limit, and subsequent attempts for miniaturization have met increased associated losses that lead to practically unreachable high values of the lasing threshold. In this context, plasmonic nanostructures emerge as optimal candidates to enable lasing action at the nanoscale. Surface plasmon polaritons (SPPs) [32] are collective oscillations of the EM fields arising at the interface of a metal (or highly doped semiconductor) and a dielectric medium. These mixed light-matter bound modes strongly couple light below the diffraction limit, due to their evanescent character, with lifetimes ranging from femtoseconds to picoseconds in the optical and near-infrared EM spectrum, opening the door to ultrafast time-dynamical operational lasers. In addition, plasmonic nanostructures allow for on-chip integration of the nanolaser proposals, together with other photonic passive devices, as other plasmonic elements [33, 34], biosensors [35, 36], or circuitry.

From a fundamental perspective, the idea of a nanolaser device supporting plasmonic modes that can work analogously as photons in conventional laser cavities, is appealing. Such a system is conceivable because, alike photons, surface plasmonic modes are electrically neutral, elementary bosonic excitations of spin 1. In addition, the surface plasmon modes weakly interact with each other. Hence, when the gain medium is inverted, radiative decay can be produced into plasmonic modes of the cavity, being massively produced with the same phase and thus follow a process totally analogous to stimulated emission in conventional lasers. This idea led to the theoretical conception of a device undergoing surface plasmon amplification by stimulated emission of radiation (*spaser*) [37]. Note, however, that since photons are not emitted in the cavity, the system is an emitter of SPPs which enhances near EM-field intensity but do not couple to far-field radiation. In other words, the spaser is a *dark* coherent emitter of plasmons, which can be exploited by means of a near-field probe or disrupting the symmetry of the considered system [38].

On 2009, intense efforts for developing lasers below the diffraction limit gave birth to

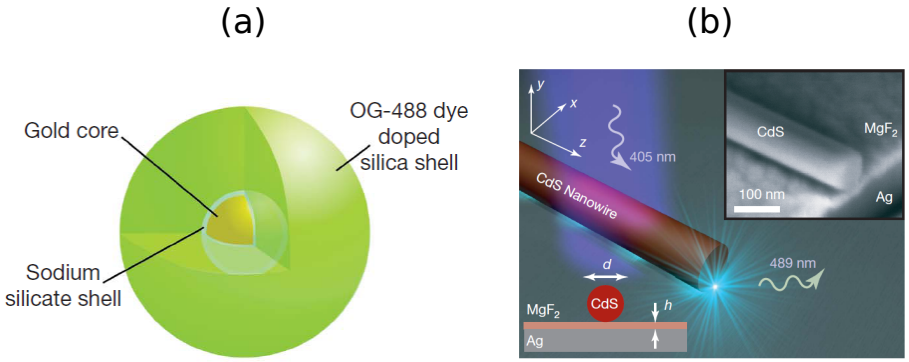

Figure 1.3: First architectures of nanolasers based on plasmonic modes. (a) Plasmonic nanolaser based on localized surface plasmonic modes [39]. (b) Plasmonic laser consisting of a CdS semiconductor nanowire on top of a silver substrate, separated by a nanometre-scale MgF_2 layer of thickness $h = 5$ nm [40].

the first laser architectures exploiting plasmonic modes. Since the physical size of a plasmonic laser is related to the smallest attainable plasmonic cavity, there was initially a strong interest in achieving lasing action in deep-subwavelength metallic particles supporting localized surface plasmons. These elementary excitations emerge when a single nanoparticle is illuminated at certain discrete values of the wavelength, and lead to a resonant phenomenon that dramatically enhances its optical spectral response, behaving as a radiating dipole. As a consequence, the field intensity squeezes down and confines to the metallic surface. In these conditions, the single nanoparticle conforms a cavity without the need of an additional feedback mechanism. The quest for the smallest plasmonic laser culminated with a claim of lasing action occurring in an ensemble of 44 nm diameter spherical nanoparticles, with a gold core of radius 7 nm, coated with a dielectric shell doped with OG-488 organic dye molecules [39] (see Fig. 1.3(a)). The authors claimed that, when optically pumped, each of such core-shell nanoparticles were able to act as a single plasmonic laser, reaching the smallest-sized laser to date. Moreover, since the outcoupling of surface plasmon oscillations to far-field photonic modes is found at 531 nm, this system was claimed to be the first operating nanolaser in at visible wavelengths.

Plasmonic structures often feature high losses due to energy dissipation in the metal, that fundamentally limits the maximum attainable $Q-$factor. For instance, the plasmonic laser above displays $Q = 16.4$ [39], which is certainly lower than for non-plasmonic microlasers above. In order to exploit the subwavelength character of surface plasmon modes while reducing the dissipation inside the metal, a possible path is to design a

system in which the field intensity associated to the plasmon mode resides in a dielectric medium with no dissipation. This idea led to a second demonstration of plasmonic lasing in a device that hybridizes dielectric waveguiding with plasmonics, consisting of a high-gain semiconductor nanowire lying on a flat metallic surface, from which is separated by a 5 nm insulating gap [40] (see Fig. 1.3(b)). This configuration creates hybrid photonic-plasmonic cavity mode with relevant dimension (the size of the experimentally detected laser spot at the ends of the structure) of $\lambda/20$. Moreover, this system enables controlling the size of the spot by varying the width of the insulating gap and the diameter of the nanowire, featuring ultrasmall mode volumes while the gap size is decreased.

The interest of having a fully operating nanolaser based on plasmonic waveguides is indeed evident. Even without a feedback mechanism that encloses the cavity, the performance of subwavelength metallic waveguides would benefit from the integration with gain materials that enable amplification of the SPP modes that they support, since the decay of the electromagnetic energy with propagation seriously limit their ability to guide light through photonic circuits. This issue stimulated early studies of the interaction of SPPs with gain [41], and the first suggestion of the possibility of a laser based on SPPs was made [42]. Lasing action at far-infrared wavelengths was even demonstrated [43, 44], due to the low absorption of metals in that regime. The first research work demonstrating amplification of surface plasmons at optical wavelengths was, however, carried by Seidel *et al.*, for a an organic laser dye embedded in a liquid medium, and deposited on a planar silver surface [45]. At the moment, this experimental study could not manage the effective gain to overcome the high losses of the SPP modes. Further works with similar structures featuring a polymer doped with rhodamine 6G (R6G) as a gain medium, claimed a SPP loss reduction up to 35% [46]. The observation of out-coupled SPP light by means of a prism configuration was there interpreted as 'laser-like' emission, suggesting that compensation of SPP loss by gain was indeed possible [47].

A large material gain is needed to amplify surface plasmons propagating along a single metallic interface between a metal surface and the gain medium. As an alternative, thin metallic films supporting long range surface plasmons (LRSPPs) have received attention recently [48]. These propagating modes arise from the coupling of SPPs at each surface of the used films, resulting in lower confinement and higher propagation length than obtained for a single interface. In this way, propagation losses due to plasmon propagation are reduced and thus less optical gain is needed for loss-compensation, which enables accessing the lasing regime at moderate pump powers. Besides, it has been found that the rate of spontaneous emission of a dipolar emitter into LRSPP modes is very low [52], leading to low-noise optical amplification. Finally, and owing to the already available nan-

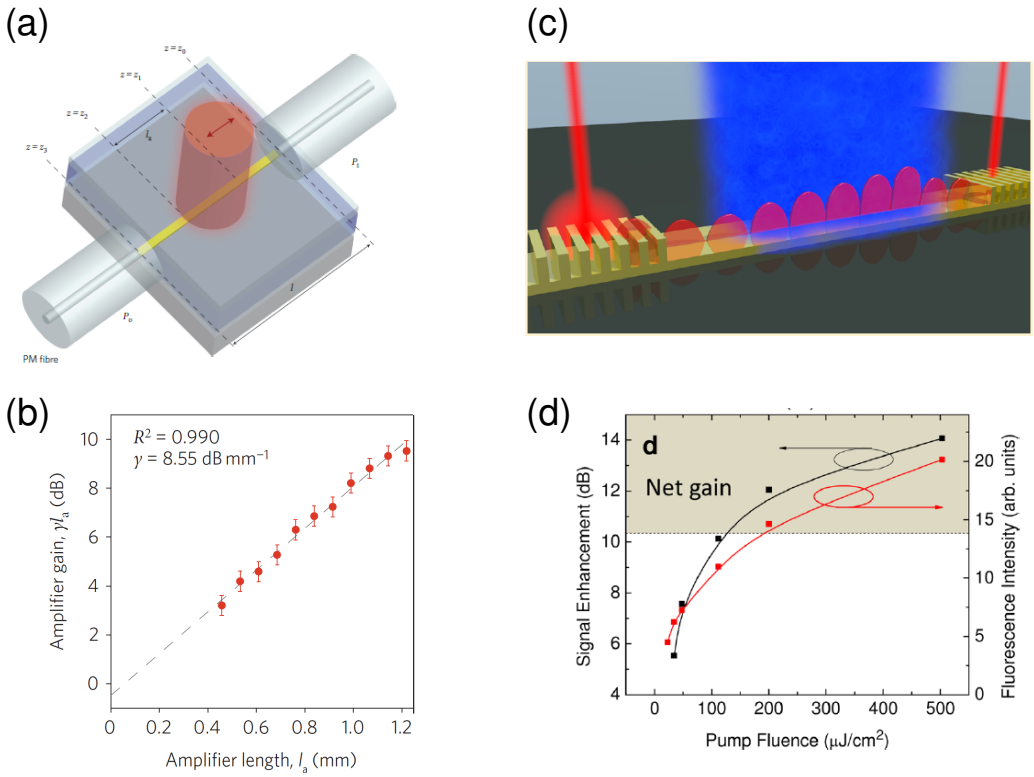

Figure 1.4: (a) Schematic representation of a LRSPP amplifier from [52], comprising a gold stripe on SiO_2 (on silicon) covered by a dye gain medium (IR-140). The pump is polarized along the stripe length, and applied to the top of the structure. End-fire coupled input/output polarization-maintaining (PM) fibres are also shown. (b) Increasing linear amplifying gain as a function of the amplifier length, accounting for optical amplification (adapted from [52]). (c) Sketch of the LRSPP waveguide based coherent amplifier from [53], consisting of a thin gold stripe embedded in Alq_3:DCM gain medium. The corresponding in- and out-coupling grating mechanism is also shown. (d) Signal enhancement and fluorescence intensity as a function of the pump fluence, showing that there exists loss-compensation (reprinted from [53]).

photonic technology, LRSPP-based amplifiers and lasers would be easily implementable within optical circuits, together with the already existing passive elements as four-port couplers, $y-$junctions, bandgap structures or Mach-Zender interferometers [49, 50].
The stimulated emission of LRSPPs was first observed at telecom wavelengths for thin gold strips, surrounded by erbium-doped phosphate glass and a pump-probe configuration [51]. However, the first *direct* observation of optical amplification of LRSPPs was realized by De Leon et al. [52], using a 20-nm thick gold stripe on a dielectric substrate,

covered by 100 μm of the organic laser dye IR-140 (see Fig. 1.4(a)). The structures were pumped from above and probed by means of a grating coupling at the wavelength $\lambda = 882$ nm. The increase of the measured amplifier gain with length yields a linear increase whose slope reveals an LRSPP mode power gain of 20 cm^{-1} (see Fig. 1.4 (b)). Importantly, in a similar configuration, direct observation of optical amplification has been recently achieved [53]. Figure 1.4(c) shows a schematic representation of this active waveguide, which incorporates an organic laser dye 4 - dicyanomethylene - 2 - methyl - 6 - (p-dimethylaminostyryl) - 4H - pyran (DCM) dispersed in a tris(8 - hydroxy - quinolinato) aluminum (Alq_3) matrix. This guest-host medium allows high absorption while keeping the ground state optical losses negligible, allowing full-loss compensation. The black line from Fig. 1.4(d) renders the signal enhancement as a function of the pump fluence for a 40 μm−long waveguide, showing that net gain can be achieved for this system.

In contrast to conventional lasers, the plasmonic lasers described so far lack of directionality in light emission. This fundamental limitation comes from the large mismatch of the wavevector characterizing SPP modes with that of free-space light. For that reason, scattering of surface plasmon modes results in light emission in all directions. As a step towards directional laser emission in the form of a coherent and collimated beam, it was theoretically proposed to arrange single plasmonic nanocavities into 2-dimensional periodically arrays [38], integrated with a suitable gain material. This idea has been experimentally realized in periodic arrays of bowties [54], metallic nanoparticles [55, 56] or nanoholes perforated on a thin metallic film [57, 58]. Each single nanocavity radiates as an oscillating dipole, coupling its emission to the far-field light modes. However, when put together in the array, the dipolar interaction between neighboring nanocavities builds up constructive interference between the individual EM modes in the plane of the array, resulting in enhanced local fields around the metallic nanostructures. The resulting extended plasmonic modes also display reduced radiative losses, leading to a higher Q−factor than for the individual constituents. The formation of these resonances enables a distributed feedback mechanism through which laser light is emitted to the external world in the form of a directional beam with small divergence, rather than in all directions by each single nanocavity.

Fig. 1.5(a) shows a schematic representation of one of the key configurations of this class of devices, consisting of a periodic array of gold nanoparticles, embedded in a IR-140 organic laser dye medium [55]. Under femtosecond-pulsed optical pumping at the wavelength 800 nm, the emission spectra collected at a detection angle of $\alpha = 0°$ (see Fig. 1.5(b)) shows a clear dependence on the pump energy, developing a narrow lasing

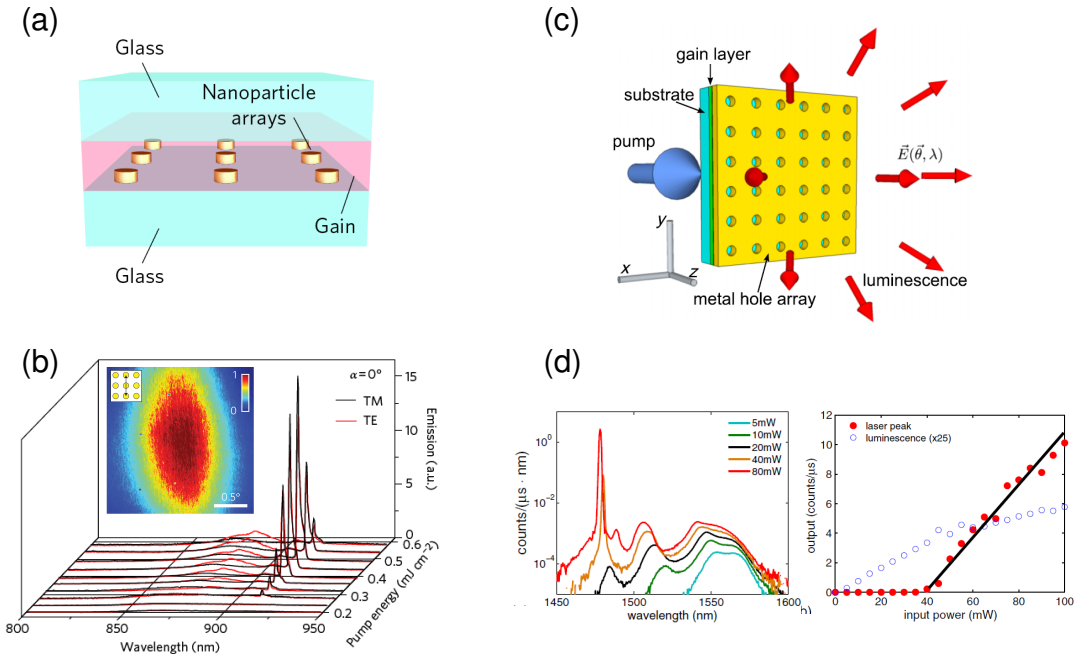

Figure 1.5: (a) Plasmonic nanoparticle array laser. Schematic representation of the system, depicting a square lattice of metallic nanorods embedded in a IR-140 organic laser dye. (b) Emission spectra collected at normal detection angle ($\alpha = 0°$) for increasing input pump pulse energies, either for transverse electric (TE) and for transverse magnetic (TM) polarization. Inset shows the far-field lasing emission beam for pump polarization parallel to the lattice direction of nanoparticle arrays. (Figure adapted from [55]). (c) Plasmonic nanohole array laser. Schematic representation of the structure. A semiconductor layer, adjacent to a metal hole array, is pumped optically. (d) Left panel: Luminescence spectra as a function of pump power, plotted on a semilog scale. A narrow lasing peak emerges as the pump power is increased. Right panel: Power dependence of the laser peak as a function of the input pump power. A lasing threshold behavior is clearly observed. (Adapted from [57]).

emission peak that emerges at $\lambda = 913$ nm, above a threshold pump energy value. Importantly, a coherent beam builds up in the lasing regime (see inset from Fig. 1.5(b)). Another relevant structure in this context is sketched in Fig. 1.5(c), showing a metallic nanohole array placed in proximity of a semiconductor gain layer. Left panel from Fig. 1.5(d) renders the linewidth narrowing of the laser in an analogous way as for the previous structure, and the right panel shows the output-to-input power ratio, with the clear presence of a lasing threshold.

The search for new nanolasers making use of plasmonic structures is a rapidly growing

and yet a flourishing field, and neverstopping claims of experimental advances towards room-temperature operation, injection of continuous-wave electrical currents for pumping, or improved ultrafast operational devices are being frequently made nowadays. Recently, concerns on the robustness of some of these proposals have been raised. In fact, the journal *Nature Photonics* published very recently an Editorial bringing attention to this issue [59], and launched a mandatory reporting checklist for manuscripts claiming lasing devices, in order to unify the standards of laser operation, as well as increase the level of transparency and reproducibility.

The lasing characteristics of a plasmonic laser should be interpreted in an analogous way as photonic and conventional lasers, and can be reviewed in four phenomena [60–64]: (*i*) The output-to-input power ratio of a laser is defined by a linear increase with high slope efficiency, above a threshold pump value. (*ii*) At the lasing threshold, narrowing of the spectral linewidth of the emission occurs, leading to a well defined peak that emerges over the noisy signal background. (*iii*) Spatial coherence, resulting in a coherent emitted beam, also builds-up in the lasing regime. (*iv*) Temporal coherence, meaning that the strong output beam must display a well defined polarization, selected by the feedback mechanism. In order to validate the claims of lasing in upcoming devices, researchers must provide enough evidence of the accomplishment of the conditions above. Some coherent processes not directly related to lasing action may, however, cause confusion and mislead the interpretation of the results. For instance, plasmonic cavities feature ultrasmall cavity volumes that, in turn, modify the spontaneous emission of the gain medium, which leads to spectral narrowing that can be misinterpreted as lasing. In addition, spontaneously emitted photons may be amplified through the gain medium itself, without being affected by the cavity. This process, known as amplified spontaneous emission (ASE), has some common properties with laser light, as narrow linewith, polarization, and directionality, and thus care must be taken in unveiling the role played by the cavity in light amplification. Usually, the linewidth associated to ASE is one order of magnitude or more than the laser linewidth [65]. Finally, a 'laser-like' spot can be created by means of outcoupling spontaneously emitted light in waveguide geometries. Moreover, these systems can feature leaky waves resonating due to the presence of a substrate, which result in narrow emission linewidth [66, 67]. These linear processes should be discarded due to the absence of a threshold behavior. The lasing characteristics can also deviate from the classical standard performance specified above, if more than one mode participate in lasing emission, which usually leads to mode competition phenomena.

Nanofabrication of the plasmonic structures and synthesis of the involved materials must be performed thoughtfully to offer a clean interpretation of their lasing properties, oth-

erwise blurring the main features of lasing action assisted by plasmons. In fact, the use of metallic nanostructures does not ensure subwavelength confinement, and careful studies should examinate the intrinsic plasmonic nature of the cavity modes assisting lasing action. Namely, the feedback mechanisms can create the conditions for lasing of a non-plasmonic mode even in this type of resonators, as for example, by back-reflections on the sample surface [68]. This problem can be avoided by confining the gain medium to the metal surfaces. Moreover, measuring the lasing characteristics of individual spasers (see, for example, systems from refs. [39] and [69]) can be challenging, since small differences in the composition or the geometry of the samples may complicate identifying the threshold behavior and broaden the lasing emission linewidth. Interaction of individual nanolasers can lead to resonance effects like random lasing, causing misinterpretation of the observation as lasing assisted by a single plasmonic resonator. Careful emission wavelength and linewidth tuning of the gain medium are also important in order to achieve optimal lasing efficiency based on the use of plasmonic modes.

The above phenomena highlight the need of theoretical modeling of active plasmonic systems, in order to support interpretations of lasing action as well as guide future developments. One of the key tests is the comparison of the accumulated loss of the plasmonic cavity, by calculating the $Q-$factor, with the available optical gain that the active medium can provide. In this context, optimization of the device geometry is useful to minimize the cavity loss and enhance the spontaneous emission decay into the lasing mode, which can considerably reduce the lasing threshold [52]. Moreover, modeling of the modes supported by the cavity and subsequent comparison against the experimental lasing spectrum is a way to substantiate the claims of plasmonic lasing. Quantifying the mode volume relatively to the diffraction limit, would further support the statement that a subwavelength optical resonance is indeed lasing.

Although the principles of laser theory are mainly established [61, 62], the rise of Plasmonics has renewed the fundamental interest in coherent phenomena occurring at the nanoscale. In addition, as stated above, quantitative theoretical support is essential to perform a rigorous analysis of the claims of new operative nanolaser architectures. In this regard, implementing a systematic numerical framework within the same computational platform, that is able to describe the wide variety of underlying effects involved in the laser performance, would be of great interest. However, the computational modeling of plasmonic systems faces some difficulties when aiming to achieve such a task. First, the dramatic enhancement of the near-field optical response in the lasing regime has an impact on the population dynamics of the considered active medium, by locally destroying the available population inversion, which is accompanied with a reduction of the avail-

able local gain. This, in turn, leads to a reduction of the field intensity, which enables an increase of the population inversion. Thus, overall, a complete theory of the laser will be inherently non-linear. In addition, the plasmonic modes sustained by nanophotonic cavities display a non-homogeneous spatial electromagnetic field distribution that dictates the amount of gain that the active medium can provide, and a detailed description of lasing systems should also include a generic dependence of spatial variables. This raises the additional difficulty of accounting for the relevant length scales in these systems, which range from the few-nanometer squeezing of the electric field in plasmonic resonances, to hundreds of nanometers for the operating wavelengths, or even microns, to calculate its response in the far-field. Ultrafast dynamical features are also expected to arise in plasmonic lasers, which make them excellent candidates to perform very precise operations at the nanoscale. The interest to explore these effects make the treatment necessarily time-dependent, and the response induced by the action of the pump is conditioned by the timescales inside the active medium, which can range from femtoseconds to nanoseconds, making the problem non-local with time. A number of further aspects must be covered, as the spectral dispersion of the gain medium, or the emergence of lasing from noise.

As a result of the above issues, the quantitative analysis of lasers is a challenging numerical problem, involving the full spatio-temporal modeling of the involved materials within the very different characteristic space and time scales. This complexity gives rise to a wide range of interesting phenomena, as dynamical mode competition of lasing modes for gain [70, 71], spatial hole-burning [72], or filamentation [73], that continuously motivates the development of sophisticate numerical frameworks for nanolaser devices. One of the most promising formalisms to achieve this goal is based on a finite difference time-domain approach [74, 75]. However, the use of structured grids of these schemes to discretize the real space seriously limits their ability to accurately discretize some deep subwavelength, geometrically complex plasmonic cavities. Therefore, prior to this thesis, an ab-initio full time-domain numerical framework that is able to describe the intrincate physics of plasmonic nanolasers while suitably discretizing the corresponding geometry, was − to our knowledge − still lacking.

Up to now, we have provided an overview of the current state-of-the-art in nonlinear amplification and lasing in active plasmonic systems. We end our summary discussing prospects and landmarks to be assessed in the near future. Some applications already benefit from the high-intensity and extremely localized fields featured by plasmonic lasers. In particular, digital optical information processing may be readily implemented with bandwidths greater than 1 THz [76, 77], requiring a moderate input power and

offering the advantages of their high-speed dynamics over electronic systems. However, future laser models should face difficulties as directional flow of information or robustness against the current manufacturing paradigm. Of course, plasmonic lasers and amplifiers have the immediate application to complex plasmonic circuits, since the high absorption losses of the metal are overcome by the inclusion of the gain medium. In addition, plasmonic lasers may also be and efficient platforms for sensing with low power demands, offering a broad bandwitdth with strong Purcell enhancements due to small cavity volume that they feature. The most promising system to address this issue are localized plasmon lasers, or spasers, due to their ultrasmall device size. Linewidth narrowing of a single plasmonic resonator, either via near-field microscopy or by isolating the system, prevail to be demonstrated. Very recently, spasers have been demonstrated as biological probes for cancer treatment [78], which could stimulate further research in this line.
Prospects of application of plasmonic lasers to communications or computing may be also achievable. However, some work must still be done in three different lines: first, low-threshold electrically pumped lasers at room-temperatures must be obtained. Electrical injection currents are currently of the order of miliamperes but could be lower in theory [79, 80]. In addition, improvements on the device lifetime and on the efficient out-coupling of plasmonic lasing modes into free-space radiation or into other plasmonic or photonic structures should be made [7]. The incorporation of unprecedented classes of active components in the context of plasmonic lasers, such as solid-state laser ions [81], or strained quantum wells [82], anticipates the implementation of a new generation of gain materials. Further advances of the trade-off of small cavity volumes and dissipation losses, also remain to be addressed [7].

1.1. Motivation and structure of this thesis.

As outlined above, the current paradigm of plasmonic lasers makes it necessary the development of an ab-initio self-consistent numerical framework that is able to deal with the non-linear interaction of the active medium with the spatially non-uniform plasmonic resonances displayed by plasmonic nanostructures.
Motivated by this fact, we introduce in Chapter 2 the core of our theoretical tools, consisting in a time-domain generalization of the finite element method, able to systematically treat the novel architectures of plasmonic lasers, by properly discretizing both real space and time. The use of adaptive meshing for non-linear optical problems while combining with a full time-domain description represents, in this context, a substantial

advance from FDTD algorithms described above. Moreover, in order to unveil the microscopical origin of lasing action, we present different semianalytical methods, consisting of a coupled-mode theory, and a laser rate-equation approach.
Having introduced our theoretical methods, we shall present the results obtained during the course of this thesis, devoted to the theoretical study of optical amplification and lasing action in plasmonic systems. Our starting point is the analysis of some of the experimental milestones reviewed above, focusing on three representative classes of systems: plasmonic waveguides, periodic metallic nanostructures and single metallic nanoparticles. In what follows, we offer an overview of the research performed along each of these lines, structured in three Chapters.
Chapter 3 presents our results of the theoretical modeling of plasmonic waveguides and of their use for loss-compensation and lasing action. We focus on two main structures. The first system consists of a thin metallic film, on which a layer of dye molecules is deposited. We demonstrate optical amplification, reaching the loss compensation regime. Moreover, by enclosing this system between parallel mirrors, we show that lasing action is attainable in this class of systems. Additionally, a V-Groove waveguide carved on a metallic surface, incorporating a semiconductor nanowire at its bottom, is studied. We demonstrate that the nanowire is able to couple its emission to the V-Groove, as well as provide the necessary feedback to create a plasmonic laser.
In Chapter 4, we analyze lasing action in 2-dimensional periodic metallic nanostructures, here termed *plasmonic crystals*, embedded in optically-pumped four-level quantum gain media. In particular, we study two limiting cases of this class of structures: a nanoslit array and a nanowire array. We study the nonlinear optical response of these systems when tuning the laser emission to the respective resonant features that these systems exhibit. Finally, we perform a fair comparison of their corresponding lasing characteristics.
We conclude the results of this thesis by presenting a rigorous study of the spatio-temporal dynamics and long-term lasing characteristics of single core-shell metallic nanoparticles optically pumped with continuous-wave radiation. The corresponding results are presented in Chapter 5. We explore how the lasing characteristics are modified when the shape of the considered nanoparticle is varied from a spherical configuration towards a nanorod structure. We further provide insight into our numerical results in terms of the spatial and temporal confinement.
Finally, in Chapter 6, we offer an overview of our results and the general conclusions of this thesis.

2 | Theoretical methods.

2.1. Introduction

This chapter covers the mathematical tools developed in this thesis for the modeling of plasmonic amplifiers and lasers. As described in Chapter 1, the anatomy of a laser consists of an optical cavity that sustains one or more electromagnetic modes, due to some feedback mechanism. Optical amplification of the associated electromagnetic field is possible by introducing an active material inside this cavity, which can be a chemical solution containing dye molecules [39, 45, 47, 52, 55, 57, 83], or some kind of defect introduced in a semiconducting material [31, 40, 84–87]. By means of a pumping mechanism, the quantum energy levels of these materials can be populated by electrons, which in turn can decay to lower energy levels through stimulated-emission, thus creating coherent light at the frequency of the considered transition. If the intensity of the pump surpasses some threshold value, the gain accumulated by the active medium will overcome the losses associated to the cavity, dramatically enhancing the optical response at the emission frequency, and entering in the lasing regime.

In the quest to achieve a complete theory that enables to systematically treat optical amplification and lasing action in a wide range of plasmonic systems, some difficulties arise. First, the huge field-enhancement associated to lasing action, and its interplay with the local population inversion of the active medium, makes the problem of lasing inherently non-linear. Second, the spatial non-homogeinity of the electromagnetic field of plasmonic resonances makes necessary a generic dependence on the spatial variables. However, the relevant length scales involved in the description of plasmonic systems range from few nanometers to microns, and a suitable numerical framework should pro-

vide accurate discretization of the real space, by means of adaptive meshing of the geometry of the corresponding components of the laser cavity. Finally, the very different time-scales involved in the dynamics, ranging from the fast plasmon lifetime and non-radiative relaxation processes ocurring in the gain medium, to long-lived molecular states, should be accounted for in a time-domain description. In this thesis, we develop an ab-initio self-consistent framework that is able to deal with the non-linear interaction of the gain medium with the spatially non-homogeneous EM fields displayed by plasmonic nanostructures. Moreover, we introduce semianalytical linear approaches to evaluate the principal features contributing to build up lasing action.
This chapter is organized as follows: First (section 2.2) we introduce the main equations describing locally the constituents of our laser designs, including Maxwell equations accounting for the classical electromagnetic field, and its coupling to the optical non-linear response of a collection of dye molecules acting as a gain medium. Next (section 2.3), we introduce our 'home-made' time-domain generalization of the finite element method (FEM), which has been implemented within the commercial package Comsol Multiphysics [129], and represents the core of the theoretical tools developed to obtain the results of this thesis (in particular, we use the FEM mesh generator and differential equation solver of Comsol Mutiphysics to implement our numerical time-dependent method). We discuss the resolution of the generic non-linear time-dependent problem of lasing action in plasmonic structures as a coupled set of partial differential equations within this framework, through space and time discretization, that lead to a resulting algebraic problem that must be solved by computational means. In section 2.4, we introduce the frequency-domain implementation of the finite-element method, with interesting additional techniques suited for analyses in the optical linear regime. Finally, semianalytical formalisms based on a coupled-mode theory approach and on laser rate equation analysis are addressed in the section 2.5, which will enable us to gain insight into the results obtained by the numerical simulations.

2.2. Maxwell-Bloch semiclassical formalism.

In this section, we present the mathematical expressions that account for the spatio-temporal dynamics of lasing action in the plasmonic systems analyzed in this thesis. Namely, we introduce a self-consistent formalism that governs the non-linear interaction

of the classical electromagnetic fields with the active medium, described as a collection of quantum systems with discrete energy levels.
To that purpose, we define a macroscopic description of the electromagnetic fields that relies on the resolution of the Maxwell equations. Moreover, we introduce a inherently non-linear, time-dependent formulation of the active medium that allows to model the stimulated absorption and emission processes that drive the coherent features studied at the considered structures. Such approach defines a macroscopic local response of the gain medium by means of the Bloch equations. In addition, a time-domain description of the metallic components, necessary to accurately account for the cavity losses, is addressed through the time-domain Drude-Lorentz model. This enables to implement a systematic approach to model a laser independently of its particular geometry. These ideas have been implemented previuously within FDTD schemes [74, 75].
It is worth discussing whether a more microscopical theory of lasing action to model plasmonic nanosystems should be introduced. The description of the high number of emitters inside the active medium encourages to use the density matrix operator to account for the quantum statistics while coupling to the macroscopic electromagnetic field [88]. However, this approach needs to introduce phenomenological, non-hermitian Lindblad terms in the governing Hamiltonian to account for the inherent losses of the cavity. Alternatively, a macroscopic QED formalism in absorbing and dispersive media can be used for the modeling of a high number of quantum emitters inside a cavity [89, 90], but the formalism is hardly applicable beyond the low-excitation regime, making it not suitable to describe the system upon high pumping needed to reach the lasing threshold. Microscopical approaches like these are therefore out of the scope of this thesis, at the expense of incorporating features like spontaneous emission and Purcell effect in a more qualitative manner. Nevertheless, note that the semiclassical description performed by the Bloch equations is equivalent to describing the stimulated absorption and emission processes by applying the Liouville operator to a 2-Level system treated with the density matrix formalism.

2.2.1. Maxwell equations.

The macroscopic electromagnetic field can be considered as the result microscopic contributions averaged out over distances for which the atomistic nature of matter ceases to be relevant [91]. We can generally assume that this averaging is valid because, despite the few-nanometer size displayed by some of the structures presented here, the high-density of free carriers in metals is such that the energy difference between their quantum levels

is very low compared to the thermal excitations at room temperature [32]: $\Delta E \ll k_B T$. In these circumstances, we can formulate the macroscopic Maxwell equations for the electric field $\mathbf{E}(\mathbf{r}, t)$ and the magnetic field $\mathbf{H}(\mathbf{r}, t)$, given by:

$$\nabla \times \mathbf{E} = -\frac{\partial \mathbf{H}}{\partial t}, \tag{2.1}$$

$$\nabla \times \mathbf{H} = \mathbf{J}_{ext} + \frac{\partial \mathbf{D}}{\partial t}. \tag{2.2}$$

$$\nabla \cdot \mathbf{D} = \rho_{ext}, \tag{2.3}$$

$$\nabla \cdot \mathbf{B} = 0, \tag{2.4}$$

where we separate the contribution of the external charge or current densities from the internal or induced sources: $\mathbf{J}_{tot} = \mathbf{J}_{ext} + \mathbf{J}$, and $\rho_{tot} = \rho_{ext} + \rho$. From now on, we will assume that there are no free charges and currents and hence: $\rho_{ext} = |\mathbf{J}_{ext}| = 0$. Note that the fact that the charge and current densities are continuous functions in space is resulting from the macroscopic averaging over singular charges and their associated currents [92].

The displacement field $\mathbf{D}$ and the magnetic induction field $\mathbf{B}$ in Maxwell equations dictate the response of the elecromagnetic field inside a material and can be related to them by means of a macroscopic polarization and magnetization fields:

$$\mathbf{D}(\mathbf{r}, t) = \epsilon_0 \mathbf{E}(\mathbf{r}, t) + \mathbf{P}(\mathbf{r}, t) \tag{2.5}$$

$$\mathbf{B}(\mathbf{r}, t) = \mu_0^{-1} \mathbf{H}(\mathbf{r}, t) + \mathbf{M}(\mathbf{r}, t) \tag{2.6}$$

The whole electric and magnetic response of the material can be enclosed in a relative permittivity $\epsilon(\mathbf{r}, t)$ and a relative permeability $\mu(\mathbf{r}, t)$, introduced through the constitutive relations:

$$\mathbf{D} = \epsilon_0 \epsilon \mathbf{E}; \qquad \mathbf{B} = \mu_0 \mu \mathbf{H} \tag{2.7}$$

with:

$$\mathbf{P} = \epsilon_0 (\epsilon - 1) \mathbf{E}; \qquad \mathbf{M} = \mu_0 (\mu - 1) \mathbf{H} \tag{2.8}$$

We will generally deal with non-magnetic materials, so from now on we will consider $\mu = 1$. Moreover, we perform a separation between the time-dependent and the overall response of the polarization into a time-independent part, through a static permittivity $\epsilon(\mathbf{r})$, and a time-dependent response, manifested through the induced polarization $\mathbf{P} = \mathbf{P}(\mathbf{r}, t)$. The equation (2.5) therefore reads:

$$\mathbf{D}(\mathbf{r}, t) = \epsilon_0 \epsilon(\mathbf{r}) \mathbf{E}(\mathbf{r}, t) + \mathbf{P}(\mathbf{r}, t) \tag{2.9}$$

Now we operate in the Maxwell equations to obtain an expression that can account for the whole dynamical response of the electromagnetic field inside an arbitrary material. We introduce here the magnetic vector potential, which can be related with both the electric and the magnetic field vectors. Using the gauge condition $\partial \mathrm{A}_0 / \partial t = 0$, together with $\mathrm{A}_0(t = 0, \mathbf{r}) = 0$, the electric and magnetic field are defined by:

$$\mathbf{E} = -\frac{\partial \mathbf{A}}{\partial t} \quad ; \quad \mathbf{H} = \frac{1}{\mu_0} \nabla \times \mathbf{A} \tag{2.10}$$

By using these expressions inside Ampère-Maxwell law (2.2), and using the consitutive relation with the separation performed in (2.9), we find:

$$\nabla \times \left(\frac{1}{\mu_0} \nabla \times \mathbf{A} \right) + \epsilon \epsilon_0 \partial_t^2 \mathbf{A} = \partial_t \mathbf{P} \tag{2.11}$$

Thus, we obtain a field equation for that accounts for all the macroscopic response of the electromagnetic field, through the vector potential $\mathbf{A}(\mathbf{r}, t)$. The induced polarization $\mathbf{P}(\mathbf{r}, t)$ in this expression depends on the local material response, through a functional form $\mathbf{P} = \mathbf{P}[\mathbf{A}]$, that makes the problem self-consistent. We couple a microscopic description of the active medium to the classical electromagnetic field through this time-dependent polarization, introducing a non-linear response that enables to model lasing action. Moreover, we define another polarization field to account for the metallic compounds that support the surface plasmons that play the role of amplified cavity modes in our systems. The description of these polarization fields is performed in the following subsections.

2.2.2. Optical response of metals: The Drude-Lorentz model.

A metal is an optically asborbing material composed by ions in a lattice, with weakly bound electrons occupying conduction bands, conforming a system of quasi-free electrons, also called the Fermi sea [93]. The degree to which the light is able to couple to these electrons is dictated by how fast they are able to react to the incoming electric field, through a relaxation time τ_d characteristic of each metal: if the wavelength is very short, the electrons will not be able to react at the proper time to screen the radiation and will weakly bound to it, and the radiation will be able to penetrate inside it. For very long wavelengths, the electrons will screen the incoming light efficiently, thus reflecting the most part of it, and will penetrate just a few nanometers. In the intermediate regime, we know that the incoming radiation is able to excite coherent oscillations in the Fermi sea, so-called surface plasmons, thus confining to the metal interface, with a certain penetration depth. In noble metals, these SPs are generally excited in the visible and near-infrared range of the electromagnetic spectrum. A first approach for the response in the time domain can be modelled by the Drude model, in which a free-electron approach is assumed, and the metal is characterized as an oscillator whose natural frequency is the plasma frequency ω_p, and the relaxation rate is $\gamma_d = \tau_d^{-1}$, by the following differential equation:

$$\frac{\partial \mathbf{P}_d}{\partial t} + \gamma_d \mathbf{P}_d = -\epsilon_0 \omega_p^2 \mathbf{A} \tag{2.12}$$

The preferred metal used for the purposes of this thesis is gold (Au). For this case, the parameters above are chosen as $\omega_p = 8.729$ eV, $\gamma_d = 0.065$ eV, taken from Ref. [94].
This is free-electron model has proven its applicability in the visible range of the electromagnetic spectrum. However, for the nobel metals that are most used in plasmonic structures (Ag, Cu, Au), it is found that when $\omega > \omega_p$, the filled $d-$band is close to the Fermi energy and thus add an extra polarization term on the free-electron model [32]. This can be modelled by adding the following term to the total polarization:

$$\mathbf{P}_\infty(\mathbf{r}, t) = \epsilon_0 (\epsilon_\infty - 1) \mathbf{E}(\mathbf{r}, t) \tag{2.13}$$

with $\epsilon_\infty = 5.967$.
Another serious limitation on the free-electron model is the excitation electrons between bands without changing its k-vector in Brillouin's first zone. In the case of Au, this

effect becomes important in the region between the visible and the near-infrared. These interband transitions [93] can be accounted for in terms of an extra Lorentzian-type polarization added to the response given by (2.12) and (2.13). Depending on the considered metal, one or more terms of this class must be added [95]. For the case of gold, only one term is needed:

$$\frac{\partial^2 \mathbf{P}_l}{\partial t^2} + 2\gamma_l \frac{\partial \mathbf{P}_l}{\partial t} + \omega_l^2 \mathbf{P}_l = \epsilon_0 \Delta\epsilon_l \omega_l^2 \mathbf{E} \tag{2.14}$$

with $\Delta\epsilon_l = 1.09$, $\omega_l = 2.684$ eV, $\gamma_l = 0.433$ eV.
We conclude that the overall optical response of the metal in the optical and near-infrared, which is the operational regime of surface plasmons, can be accurately described by three contributions:

$$\mathbf{P}_m(\mathbf{r}, t) = \mathbf{P}_\infty(\mathbf{r}, t) + \mathbf{P}_d(\mathbf{r}, t) + \mathbf{P}_l(\mathbf{r}, t) \tag{2.15}$$

where $\mathbf{P}_d(\mathbf{r}, t)$ and $\mathbf{P}_l(\mathbf{r}, t)$ are solved directly in the time-domain. The sum of these contributions conform the *Drude-Lorentz model* for the optical response of metals. Assuming a harmonic time-dependence for the polarization, we can obtain a complex relative permittitvity associated to the metal response:

$$\epsilon_m = \epsilon_\infty - \frac{\omega_p^2}{\omega(\omega + i\gamma_d)} - \frac{\Delta\epsilon_l \omega_l^2}{\omega^2 - \omega_l^2 + i\omega\gamma_l} \tag{2.16}$$

We note that the result of this model fits to the experimental data from Johnson and Christy [96] in the considered range of the electromagnetic spectrum.

2.2.3. Coupling to the active medium. Bloch equations.

Although Maxwell equations can explain a wide range of the electromagnetic phenomena, they fail when describing very essential processes occuring in light-matter interaction: the absorption and emission of light [97]. Therefore, we treat the quantum-mechanical nature of the active medium explicitly, although taking some approximations to complete our semiclassical approach.
It is a well-known fact that atoms and molecules display quantized energy levels which are filled with electrons with increasing energy by respecting the Pauli exclusion principle. If the electrons get promoted to a higher level, they will tend to relax by losing

a quantum of energy $E = h\nu$ to a lower energy level, being ν the frecuency associated to the difference between two levels. This downward transition must be allowed by the selection rules, and there are different decay channels by which the energy is released. We speak of fluorescence or *spontaneous emission* when the mechanism is radiative, released in the form of photons. Complementarily, the decay mechanism can be non-radiative, by transferring thermal or acoustic energy to the medium in which the active components are embedded. It is found that, between the two levels considered, the decay rate is governed by an exponential law [62]:

$$\frac{dN}{dt} = -\frac{N}{\tau} \tag{2.17}$$

where $\tau^{-1} = \tau_{sp}^{-1} + \tau_{nr}^{-1}$, accounting for the spontaneous and non-radiative decay times, and N is the population of the upper level. As we can see, both mechanisms can be present in a considered decay, and its value is dictated by the structure of energy levels of the active medium. However, it is usual that one dominates over the other.
The most important processes involved in lasing action occur when a pumping mechanism is forced at the frecuency associated to the difference between two energy levels. If the electrons populate mostly the lower level, the incoming radiation interacts resonantly with the transition, thus causing the electrons to gain energy and massively populate the upper level. Importantly, an inverse process takes place when the upper level is more populated than the lower level: The quantum emitters then behave as resonant dipolar antennas oscillating in phase (*coherently*) with the incoming signal, amplifying the input radiation while replicating its original profile. These two mechanisms are called stimulated absorption and stimulated emission, respectively.
Under the presence of an electric field close to the respective transition frequency $\omega_{a,e}$, the stimulated absorption/emission may be envisioned classically as an oscillating dipole moment induced by the external field into the charge distribution of each emitter. The contribution of each dipole builds up a macroscopic polarization given by [61]:

$$\mathbf{P}_{a,e} = \sum_{i}^{M} e\mathbf{d}_i^{a,e} \tag{2.18}$$

where M is the number of emitters. The coupling of the active medium to the electric field may thus be written as:

$$\frac{\partial^2 \mathbf{P}_{a,e}(\mathbf{r},t)}{\partial t^2} + 2\Gamma_{a,e}\frac{\partial \mathbf{P}_{a,e}(\mathbf{r},t)}{\partial t} + \omega_{a,e}^2 \mathbf{P}_{a,e}(\mathbf{r},t) = -K_{a,e}\Delta N_{a,e}\mathbf{E}_{loc}(\mathbf{r},t) \tag{2.19}$$

Where the local electric field $\mathbf{E}_{loc}$ is the macroscopically averaged electric field, accounting for the corrected polarizability inside a dielectric host with refractive index n_h [98]: $\mathbf{E}_{loc} = (n_h^2 + 2)\mathbf{E}/3$. The half-linewidth of the transition $\Gamma_{a,e}$ accounts for the radiative damping, and $\Delta N_{a,e}$ is the population inversion boosting the absorption or the emission transition. The coupling strength to the population inversion and to the electric field is given by [99]:

$$K_{a,e} = 2\epsilon_0 n_h c \Gamma_{a,e} \sigma_{a,e} \tag{2.20}$$

where $\sigma_{a,e}$ is the cross section of the corresponding transition and c is the velocity of light in vacuum.
We note that the population of the energy levels involved in the stimulated transition also depend on the applied electric field $\mathbf{E}(\mathbf{r}, t)$ at the considered frequency. The power per unit volume supplied by an arbitrary current $\mathbf{J}(\mathbf{r}, t)$ is:

$$\frac{du}{dt} = \mathbf{E}(\mathbf{r}, t) \cdot \mathbf{J}(\mathbf{r}, t) \tag{2.21}$$

But the current relates to the polarization by: $\mathbf{J} = \partial_t \mathbf{P}$, so if the energy relates to the population N of an energy level by: $u = \hbar\omega N$, where ω is the frequency associated to the transition, we can write the decay rate due to stimulated/emission or absorption as:

$$\frac{dN}{dt} = \pm \frac{1}{\hbar\omega} \left\{ \mathbf{E}\left(\mathbf{r}, t\right) \cdot \frac{\partial \mathbf{P}\left(\mathbf{r}, t\right)}{dt} \right\} \tag{2.22}$$

where plus/minus sign applies to the population of the upper/lower level of the considered stimulated transition.
Let us locate the main processes we just described occuring in a typical active medium. Figure 2.1(a) shows the whole family of quantum energy levels displayed by Nd:YAG, a solid-state laser medium, among which radiative and non-radiative transitions are both involved. Remarkably, above the ${}^4F_{3/2}$ level, there is a set of levels that may be populated by the pump, but they decay rapidly to this metastable level. We can consider that effectively, the ${}^4F_{5/2}$ is populated by means of stimulated-absorption at $\lambda_{03} = 808$ nm, decaying only non-radiatively to the ${}^4F_{3/2}$ level with the phenomenological decay time τ_{32}. Similarly, by taking into account the typical decay times of each transition and ruling out the fastest, we can build up a simpler picture of the active medium, in which

four quantum levels survive (see Fig. 2.1(b)). If we label these levels with increasing numbers, we can notice fast non-radiative transitions $3 \rightarrow 2$ and $1 \rightarrow 0$, compared to the non-radiative transition at $\lambda_{21} = 1064$ nm: $\tau_{21} \gg \tau_{32}, \tau_{10}$. At the relevant time-scales of this medium, the transition accumulates enough population inversion at the level 2 to produce a stimulated-emission transition to level 1 if a high field intensity is present at the associated frequency $\omega_{21} = 2\pi c/\lambda_{21}$. Note that in this picture, we have disregarded spontaneous emission. We will discuss this topic later.

Although presented for a particular material, this 4-Level system representation of the

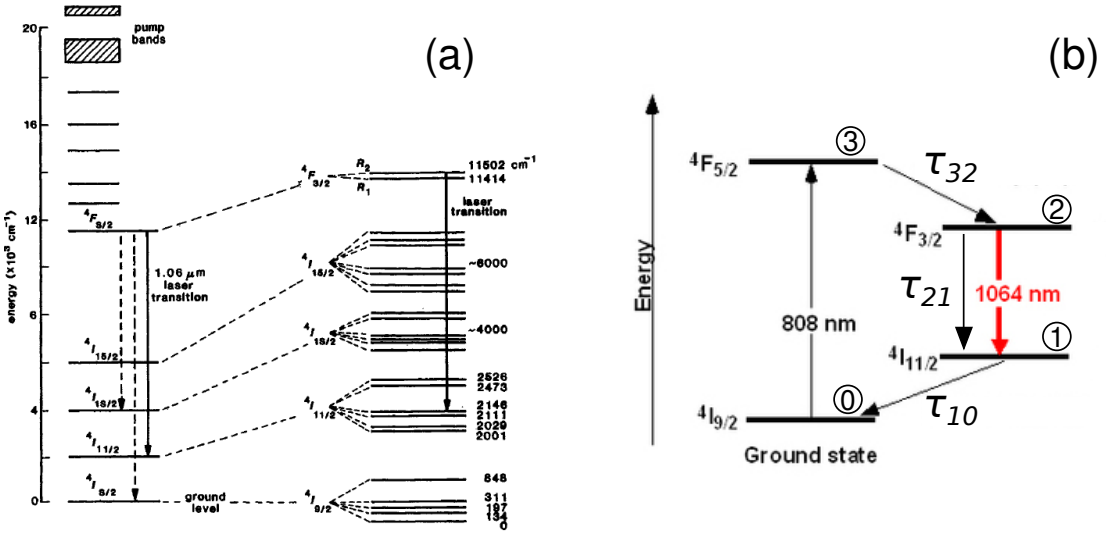

Figure 2.1: (a) Energy levels and transitions for a non-simplified Nd:YAG laser medium (reprinted from [61]). (b) Simplified four level system, with two fast non-radiative transitions $3 \rightarrow 2$ and $1 \rightarrow 0$, a slow non-radiative transition $2 \rightarrow 1$, a stimulated absorption transition $0 \rightarrow 3$, and a stimulated emission transition $2 \rightarrow 1$.

gain medium is quite general for the most part of lasers. The active media used for experimental designs of plasmonic lasers is typically some kind of organic dye-molecule solution or semiconductor. In this thesis, we will mainly focus on dye laser media [100], which, by a similar reasoning, can be accurately represented by three or four level systems. The modeling of semiconductors is left for subection 2.5.2. By using the corresponding expressions for non-radiative transitions (2.17) and stimulated absorption and emission (2.22), one can write a system of equations that governs the population densities $N_3 - N_0$ of a 4-level system like in Fig. 2.1(b) in the following form:

$$\frac{\partial N_3(\mathbf{r},t)}{\partial t} = \frac{1}{\hbar\omega_a}\frac{\partial \mathbf{P}_a(\mathbf{r},t)}{\partial t}\cdot\mathbf{E}_{loc}(\mathbf{r},t) - \frac{N_3(\mathbf{r},t)}{\tau_{32}} \tag{2.23}$$

$$\frac{\partial N_2(\mathbf{r},t)}{\partial t} = \frac{N_3(\mathbf{r},t)}{\tau_{32}} + \frac{1}{\hbar\omega_e}\frac{\partial \mathbf{P}_e(\mathbf{r},t)}{\partial t}\cdot\mathbf{E}_{loc}(\mathbf{r},t) - \frac{N_2(\mathbf{r},t)}{\tau_{21}} \tag{2.24}$$

$$\frac{\partial N_1(\mathbf{r},t)}{\partial t} = \frac{N_2(\mathbf{r},t)}{\tau_{21}} - \frac{1}{\hbar\omega_e}\frac{\partial \mathbf{P}_e(\mathbf{r},t)}{\partial t}\cdot\mathbf{E}_{loc}(\mathbf{r},t) - \frac{N_1(\mathbf{r},t)}{\tau_{10}} \tag{2.25}$$

$$\frac{\partial N_0(\mathbf{r},t)}{\partial t} = \frac{N_1(\mathbf{r},t)}{\tau_{10}} - \frac{1}{\hbar\omega_a}\frac{\partial \mathbf{P}_a(\mathbf{r},t)}{\partial t}\cdot\mathbf{E}_{loc}(\mathbf{r},t) \tag{2.26}$$

This a set of semiclassical *rate equations* that accounts for the discrete nature of the quantum levels of the molecules while coupling to the classical electromagnetic field. Due to their equivalence with the equations for nuclear magnetization, they are also called Bloch equations [101]. Although its derivation was performed in a classical fashion, we note that the exact form of the stimulated-absorption and emission terms can be derived from a microscopic quantum formalism based on the density matrix, by applying the Liouville operator on the density operator [102].

The spontaneous emission.

The spontaneous emission is a purely quantum effect, with no possible derivation from a macroscopic perspective. In the semiclassical picture, the spontaneous emission can be viewed as a collection of randomly oscillating dipoles at the transition frequency, which translates in a noise-like overall response from the gain medium. This incoherent radiation, coming from spontaneous emission, is in contrast with the coherent radiation produced by stimulated-emission, and the combination of both mechanisms in the lasing regime adds a characteristic noise to the dominating features of the stimulated-emission. In other words, the spontaneous emission creates a decoherence mechanism (or dephasing) that adds to the signal in the form of noise. Prior to the lasing regime, the inherent amplification of this radiation due to the excitation of the electrons to quantum levels leads to a regime of amplified spontaneous emission (ASE) [103]. The noise in this regime, however, has two different contributions [104]. One of them is due to collisional dephasing. The other is a pure quantum noise related to the fact that the radiation couples to the statistical environment outside the cavity, as dictated by the fluctuation-dissipation theorem [105].

There are different approaches to introduce these effects within a semiclassical formalism, which influence both the population dynamics from (2.23)-(2.26) and the induced

polarization (2.19). Some authors have performed a rigorous derivation of the Bloch equations for a 2-level system [106] and a 4-level system [107] accounting for stimulated absorption and emission, by applying the Liouville operator on the density matrix. By introducing phenomenological dissipation terms, through relaxation and dephasing rates, interaction with the thermal environment (or reservoir) can be included, which adds stochastic forces to the system. In the Markovian approximation, these effects enter as Langevin noise operators that account for the extra decay channels for spontaneous emission. Non-radiative relaxation rates are also affected by these terms. From a more macroscopic perspective, another approach consists in introducing homogeneously distributed sources inside the active medium to simulate the spontaneous emission [108], each of them generating waves with Lorentzian distribution around the emission frequency ω_e. For the purposes of this thesis, within a *semiclassical approximation*, we do not account for the stochastic noise accompanying spontaneous emission [102], and assume an initial seed excitation (of much smaller amplitude than the pump) of the classical electromagnetic field at the lasing frequency accounting for spontaneous emission at that frequency. We will discuss its implementation in subsection 2.3.5.

The Purcell factor and the $\beta-$factor.

The value of the spontaneous emission decay time discussed above is found to be modified inside an optical cavity. It was Purcell [109] who first discovered the decay time shortening in nuclear magnetic moment transitions, when adding small metallic particles to a nuclear-magnetic medium. The modification of the spontaneous decay rate in vacuum $\gamma_0 = \tau_{sp}^{-1}$ can be described either at the microscopic level according the Fermi golden rule, or by a Lorentz oscillator dipole model. In both cases, the change of the decay rate in terms of the position $\mathbf{r}$ inside the cavity is related to the local density of states ρ, by the relation:

$$\frac{\gamma(\mathbf{r})}{\gamma_0} = \frac{\rho_i(\mathbf{r}, \omega_e)}{\rho^0(\omega_e)} \tag{2.27}$$

where the subscript i stands for the dipole orientation, and the free-space density of states is given by: $\rho^0(\omega_e) = \omega_e^2/(\pi^2 c^3)$. The density of states inside a lossy cavity has a Lorentzian dispersion, and can be written as follows:

$$\rho_i(\mathbf{r}, \omega) = \sum_n \left| E_n^i(\mathbf{r}, \omega) \right|^2 L(\omega) \tag{2.28}$$

with:

$$L(\omega) = \frac{1}{\pi} \frac{\Gamma_n/2}{(\omega - \omega_n)^2 + \Gamma_n^2/4} \tag{2.29}$$

Here, Γ_n is the lifetime of the $n-$th mode, which can be related to the $Q-$factor by: $Q_n = \omega_n \tau_n$.
By normalizing the electric field, one can obtain a value for the maximum decay shortening, which is obtained at the maxium of the electric field inside the cavity. This value is given by the *Purcell factor*, defined by the following expression:

$$P_F = \frac{\gamma}{n\gamma_0} = \frac{3}{4\pi^2} \left(\frac{\lambda}{n}\right)^3 \frac{Q_n}{V_n} \tag{2.30}$$

where n is the refractive index inside the cavity. This shows that the change in the spontaneous decay time is ruled by the $Q-$factor of the considered cavity mode and the modal volume V_n, defined as follows:

$$V_n = \frac{\int_V d^3\mathbf{r} \, |E_n(\mathbf{r}_n)|^2}{\max\left\{|E_n(\mathbf{r}_n)|^2\right\}} \tag{2.31}$$

where V is the volume of the cavity.
The Purcell factor (2.30) points out that the light-matter interactions can be enhanced inside nanophotonic cavities [110]. In the context of nanolasers, the spontaneous emission decay time shortening involves a reduction of the available optical gain, since the population inversion is destroyed easily in the areas where the field enhancement of the associated electromagnetic mode is highest. Such effect is known as the *quenching* of the molecules. The discussion of the Purcell effect and its consequences on the lasing action of the plasmonic structures studied will be continued in the following chapters.
Another interesting quantity, that measures the coupling to the considered mode n, compared to the other possible decay channels, is the $\beta-$factor, defined as follows:

$$\beta = \frac{\gamma_n}{\gamma} \tag{2.32}$$

where γ_n is the decay rate only into the considered mode. Thus, for a considered laser, the $\beta-$factor is able to measure the coupling efficiency of the spontaneous emission to

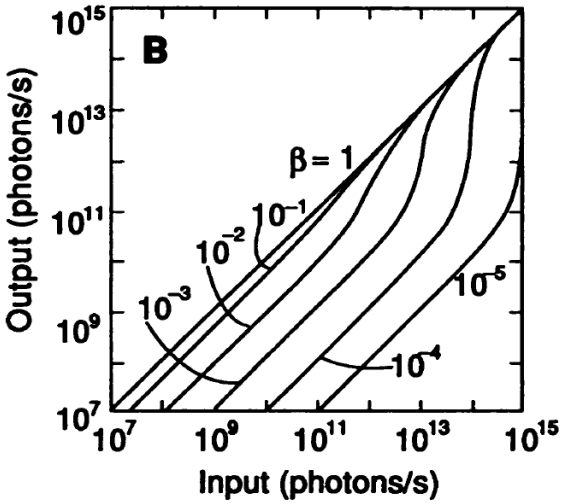

Figure 2.2: Calculated output power vs. input power for a laser microcavity in logarithmic scale (reprinted from [111]).

the mode of interest.

Importantly, the $\beta-$factor has a profound effect on the lasing threshold, since it is intimately related to how the cavity evolves upon pumping from the optical linear regime to the lasing regime. An illustrative example is shown in Fig. 2.2, resulting from calculations by Yokohama et al. [112], relating the output electromagnetic power obtained from a laser microcavity to the input pump power, with varying $\beta-$factor. It can be noticed that for a low value of the $\beta-$factor, three operational regimes are present. A linear regime is obtained for low pump power, in which the system behaves as an optical amplifier, not yet entering in the nonlinear regime. For a certain pump value, an increase in the output response is noticed. This is the is the amplified spontaneous emission regime (ASE), in which the laser transition is being populated enough for the spontaneous emission to be significant, and it is accompanied with a characteristic noise in the dynamical response. Finally, there comes a point in which the pumping is strong enough to compensate the inherent losses of the cavity, thus reaching the lasing threshold and entering in a new linear regime dominated by stimulated-emission. The 'S-shape' in the diagram conformed by the three regimes is a characteristic signature of many types of laser systems. An interesting situation is the limit $\beta = 1$. In this ideal situation, all the photons emitted spontaneously are decaying into the operating mode. For this to be possible, the cavity must be lossless, since no single photon must be able to leak or dissipate, and the limit of a thresholdless laser is reached. Conversely for $\beta = 0$, we reach the semiclassical approximation in which the only coupling to the lasing mode is by means of stimulated-emission.

In the forthcoming chapters, we will discuss the relevance of the $\beta-$factor within our simulations.

2.3. The time-dependent finite element method.

The purpose of the finite element method within the topic of this thesis is to solve the Maxwell equations numerically, by coupling to a macroscopical description of the nonlinear active medium. This approach allows to define the geometry of our laser designs in the real space, by specifying the different physical domains and the equations that account for the local response inside each of them, and to solve the corresponding expressions iteratively in the time-domain. More precisely, the field equation (2.11) is solved numerically at every point of space, by coupling to the Drude-Lorentz polarization defined inside the metal (2.15), and to the polarization accounting for the stimulated absorption and emission (2.19), together with the rate equations (2.23)-(2.26) governing the dynamics inside the active medium. This conforms a system of coupled partial differential equations (PDE), which is treated in an ab-initio manner, without making assumptions in the spatial profile of the modes nor in the time evolution of the governing equations.

A satisfactory numerical resolution of this self-consistent problem is performed through the discretization of the independent spatio-temporal variables. Its resolution will provide vectorial fields that solve for the vector potential $\mathbf{A}(\mathbf{r}^e, t_n)$, such that $\mathbf{r}^e$ is the position inside the subdivision e of the geometry, and t_n is the temporal variable after n time-steps have been performed. Same applies for the polarizations $\mathbf{P}_m(\mathbf{r}^e, t_n)$, $\mathbf{P}_{a,e}(\mathbf{r}^e, t_n)$ and the scalar number densities $N_i(\mathbf{r}^e, t_n)$, $i = 0, \ldots, 3$. Thus, the time-domain description enables to treat the intrinsically nonlinear nature of lasing action, by solving the mentioned equations iteratively. These fields constitute the solution to the boundary-valued physical problem, and they are solved in an exact manner. In this section, we will discuss the exact procedures that allow to discretize both space and time, and how this discretization is the key to transform the original continuous differential problem, with an ideal infinite number of degrees of freedom, in an algebraic problem of N degrees of freedom, that can be solved by computational techniques.

2.3.1. Motivation

The numerical resolution of Maxwell equations has been a subject of research before the 60's, opening the field of computational electrodynamics [113]. The initial interest was motivated by the development of military defense, for which the modeling of radars, circuits, antennas or waveguides were of great interest. At that time, the resolution methods were based on analytical calculations of the steady-state form of the Maxwell's equations, by means of mechanical calculators. After the 60's, the rising of digital computers and random-access memory which allowed the storage of large arrays of numbers, together with programming languages as FORTRAN, opened the door to more refined numerical techniques as high-frequency asympthotic methods [114] and integral equations [115]. However, these methods were limited to treat a variety of structures in complexity, size and composition. During the 70's and the 80's, the subsequent efforts concentrated into frequency-domain integral-equation methods, resulting in large and computationally demanding sets of equations.

The first time-domain algorithm was first established by Yee in 1966 [116], to build up the method of finite differences in the time domain (FDTD). This method solved for the first time Maxwell Equations by discretization both in space dimensions, by means of a structured grid, and in time. Later, Taflove [117] completed the method by introducing a stability criterion and applied it for the first time to a metallic cavity. FDTD method demonstrated to be an interesting alternative over frequency-domain integral-equation methods, since the amount of linear algebra involved in these methods is not needed, and thus its resolution is restricted to a lower number of unknowns. Furthermore, time-domain algorithms are inherently designed to incorporate broadband pulses, including many frequencies in the problem in a natural manner. Moreover, FDTD is a very general and systematic approach, reducing the problem to generate the mesh for the geometry of interest, without additional reformulation of the proper framework. Since Maxwell equations are solved in each of these elements, it is also possible to depict the solution with contour plots that give insight to the time dynamics.

Since the 80's, a number of landmarks have contributed to increase the capabilities of FDTD method, which include incorporating absorbing conditions [118], extending it to other geometries as waveguides, thin wires or microstrips [119–121], and extending it to dispersive materials [122, 123]. Although the time-domain description enabled rapidly to describe the propagation of optical pulses in nonlinear dispersive media [124], it was not until the 2000's that self-consistent approaches for a laser medium coupled to a photonic cavity, incorporating a coherent pump and a probe pulse, appeared [125, 126]. Since then,

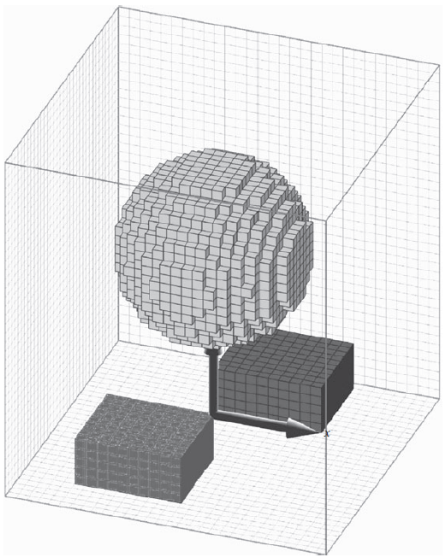

Figure 2.3: Discretization performed by an FDTD algorithm inside a simulation cell. The objects under study are approximated by cubic or rectangular cells. (Reprinted from [128]).

the field of active nanophotonics has experimented a huge increase, with FDTD-schemes able to either predict unexpected phenomena or provide insight into experiments [127]. Usually, the type of discretization involved in FDTD-type algorithms consists in structured grids, like rectangular elements in 2-dimensional analysis, or cubic grids in the case of 3-dimensional geometries (see Fig. 2.3). These elements find problems to fit the shape of complicated or irregular geometries. Moreover, in nanostructures supporting plasmonic resonances, electromagnetic field is known to squeeze down to few-nanometer scale, with huge local variations of the field intensity. This extremely low confinement makes it interesting to reduce the mesh size so we can account for the physics occuring at the nanoscale. Therefore, it is of interest to explore other meshing procedures. Within FDTD, it has been implemented the use of surface-fitted grids as well as completely unstructured grids. Unfortunately, these strategies lead sometimes to a high computational cost or to numerical inaccuracies or instabilities. Therefore, other similar time-domain methods that allow for adaptative meshing as described have received attention.

A natural alternative to FDTD in the family of time-domain methods is the Finite-element method (FEM). In this method, the spatial discretization in simple, non-regular subdomains, is combined with a mathematical approach based only on the description of the nodes or edges at which the subdomains interconnect. The solution inside each of them can be formulated in terms of a set of, in principle, arbitrary interpolation func-

tions, independently of their size or shape. This nodal or edge-based description offers a higher flexibility in terms of spatial discretization, leading to adaptative meshing which is crucial for the strong non spatially homogeneous electromagnetic problems.
Although introduced first by Courant in 1943 and and rapidly extended in the context of structural mechanics, the use of time-dependent FEM in electromagnetics was not introduced until the 80's, due to the problem of spurious solutions at high frequencies that the nodal-based description poses. However, with the introduction of time-stepping algorithms that introduce penalties to these solutions, and the development of vector (curl)-type elements, the method has come to be highly reliable. Also, it has been studied the usage of finite element hybrid techniques within the framework of FDTD, taking advantage of the combined benefits of adaptative meshing and finite difference algorithms. FEM is conventionally used in the field of nanophotonics in its frequency-domain version. However, its application has been traditionally restricted to the linear optical regime. Although the finite-element method in the time domain have been well established for a long time [130], it has only been used recently in the context of loss-compensation and lasing in plasmonic systems [131, 132], due to the advantages of adaptive meshing procedures. The main results of this thesis have been obtained with the finite-element method in the time domain, implemented with the commerical package Comsol Multiphysics [129]. We next describe the formalism followed in close detail.

2.3.2. The basics of the finite element method.

We start providing the mathematical background on which the finite-element method is constructed. Let us assume an arbitrary boundary-value differential problem that must be solved inside a domain Ω, given by:

$$\mathcal{L}u = f \tag{2.33}$$

where we define a differential operator $\mathcal{L}$ that acts on the variable u we want to solve, called solution variable or dependent variable. f is called the forcing vector. For the solution of to be determined, the problem (2.33) must be complemented with boundary conditions on the limiting boundary $\partial\Omega$. Such a problem, in general, cannot be solved analytically. Therefore, approximation methods must be used. One can think of finding an approximated solution $u \simeq U_N$ that can be written as an expansion in terms of N arbitrary basis functions ϕ_j, such that:

$$U_N = \sum_{j=1}^{N} c_j \phi_j \tag{2.34}$$

Upon the substitution of Eq. (2.34) into (2.33), we can obtain a system of equations for the coefficients c_j that *discretizes* the original differential problem into a problem with N degrees of freedom. However, linear independence of the N resulting equations is not guaranteed but in a few number of cases, and the solution is not uniquely determined. To fully determine the approximated solution, an additional constraint must be imposed. Namely, we require minimization of the error of this solution with respect to the exact solution of the differential problem, by imposing a variational principle on the residual $R = \mathcal{L}u - f$. Such condition relies on the selection of N additional functions that multiply the residual, and set to zero the integral of this expression over the whole domain of the problem:

$$\int_{\Omega} d^3\mathbf{r} w \left[\mathcal{L}u - f\right] = 0 \tag{2.35}$$

The function w chosen is called the *test* function or weight function, and the integral in (2.57) is called a weighted integral statement or *weak form* of the original problem (2.33). The requirement is that this expression should hold for every function w, as long as it belongs to the same functional space as the approximated function, $\{\phi_j\}$. This expression provides enough conditions to obtain a linear independent system of equations that solves for the coefficients c_j. In this way, we transform the differential problem in an algebraic problem.

The variational principle based on transforming the original problem (2.33) into its weak form is the basis of the finite-element method. However, we still need to define the basis functions ϕ_j in Eq. (2.34), which enter into the weak form to obtain an accurate approximated solution U_N. One can anticipate that, in general, this can be complicated, since the domain Ω can be highly irregular, and the procedure of finding a proper set of functions for each particular form of $\mathcal{L}$ would make the method not systematic. Therefore, before imposing the statement (2.35), we perform a discretization of the domain Ω, into small simple subdomains Ω^e, $e = 1, \ldots, M$; and define an individual set of basis functions for each of them. Inside of each of these subdomains, or *elements*, the approximated function U_N can be written as:

$$U^e = \sum_{j=1}^{N'} c_j^e \phi_j^e, \tag{2.36}$$

Where now N' is the number of equations taken in the expansion inside the element. We will see that this number is intimately related to the geometry of the subdomains. The approximation function U_N is then defined as a piecewise function which, at each element e, takes the form of U^e:

$$U_N = \sum_{e=1}^{M} U^e \tag{2.37}$$

where continuity between the $e-$th element and its neighboring elements is assumed. The continuity and smoothness of the solution across the elements will be discussed later.

The discretization of the geometry, selection of the interpolation functions ϕ_j^e and formulation of the weighted-integral statement (2.35) underlie the procedure that leads from the original problem (2.33) to a system of equations that solves for the whole set of unknown coefficients c_j^e. In the following subsections, we explain in detail the main stages in which the problem is divided:

- Discretization of the geometry (subsection 2.3.3, page 36).
- Selection of the interpolation functions (subsection 2.3.4, page 39).
- Formulation of the system of equations (subsection 2.3.5, page 45).
- Resolution of the system of equations (subsection 2.3.6, page 61).

2.3.3. Discretization of the geometry

As discussed, the approach that FEM follows to describe the approximated solution in terms of simple interpolation functions involves discretizing the geometry in neighboring simple geometrical domains, or elements. The subdivision of the geometry into small elements gives rise to some vertices and segments where the elements interconnect. These vertices are called *nodes*, segments will be called *edges*, and the whole collection of connected subdomains will be often referred as *mesh*. The FEM involves describing each element by labelling its nodes or edges and identifying their coordinates, which enable to use them as the referent *degrees of freedom* to expand the corresponding interpolation

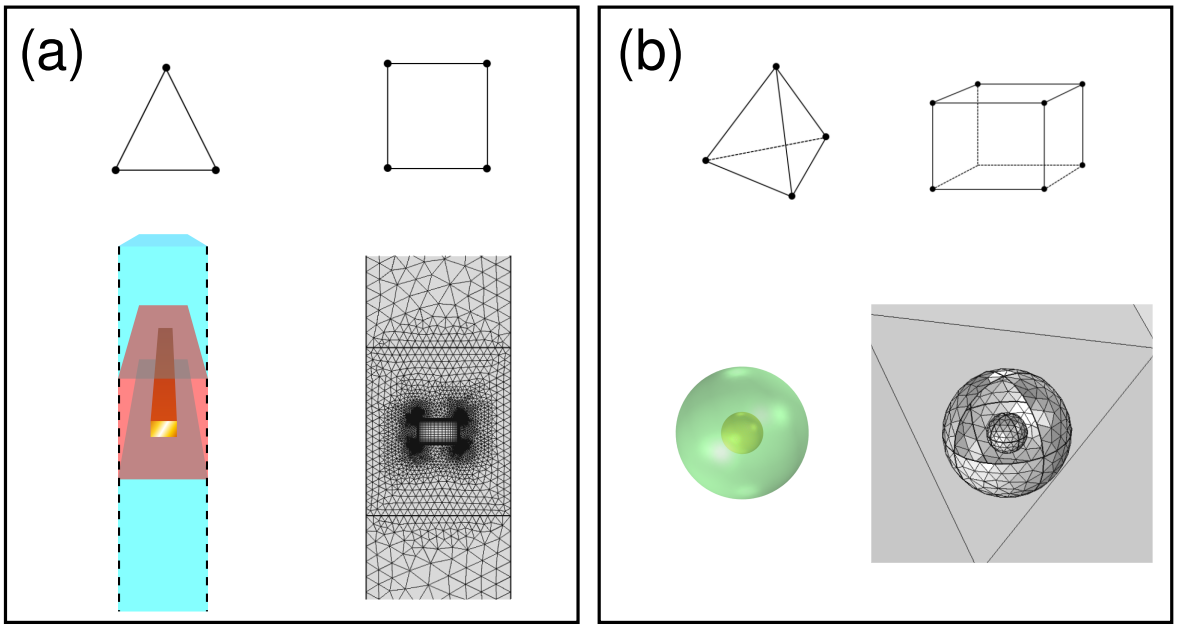

Figure 2.4: Shape of the mesh elements used to discretize the considered geometries with FEM. Examples of used mesh patterns are shown in the lower part of the panels. (a) For 2D geometries, triangles and rectangles are used. (b) For 3D geometries, tetrahedra are preferentially used, together with hexahedra.

functions.

Since one set of interpolation functions is spanned over each element separately, the elements are not meant to intersect or overlap, and they should be as simple as possible, such that a simple class of interpolation functions already provides an accurate solution to the problem. Choosing the type and size of discretization is essential for the convergence of the solution, and it depends on the problem treated, the shape of the geometry of interest, and the physics occuring behind. The meshing algorithms must account for these issues either in 1-dimensional, 2-dimensional (2D), or 3-dimensional problems (3D). The procedure to do this is to fill the geometry by inserting piecewise elements with common nodes and edges. For 1D geometries, this is attained by linking straight lines that will fit a general, maybe curved, geometry. For 2D or 3D, an elementary shape must be chosen that fits the geometry without generating an excessive number of nodes or edges. For rectangular geometries, rectangular or cubic elements are best suited. For irregular geometries, irregular triangles and tetrahedra are better options to fit the considered geometry. For their flexibility, triangular and tetrahedral elements are used in the most part of the cases analyzed in this manuscript. Figure 2.4 shows these elementary shapes

both in 2D (panel a) and 3D (panel b), and real examples of meshed geometries.
In the process of mesh generation, usually an important number of nodes and edges arise from the discretization, which must be ordered to build up the matrices that will solve for the whole set of unknown coefficients c_j^e in (2.36) that constitute the solution. In this thesis, the algorithm of Comsol Multiphysics [129] for mesh generation has been used. The accurate discretization in the areas with high physical interest must be combined with a low number of elements to manage on the computational resources. The capability of adaptive meshing, combining the flexibility of irregular element shape with varying element size is one of the most appealing features of this numerical framework.
Although discretizing a geometry for FEM calculations depends on the problem treated, some general rules apply:

- The areas meshed for the simulation of non-absorbing materials must be discretized such the maximum mesh element is (at least) one quarter of the operating wavelength.

- Absorbing materials, such as metals, should be discretized carefully at the interface with other non-absorbing media, in order to account for the characteristic penetration depth of the radiation. Typically, at least 5 elements are taken to fit this distance. The rest of the metal should display coarse discretization, as the remaining field inside is negligible.

- In general, the meshing must be coherent with the physics being analyzed. Since we are dealing with plasmonic lasing, the meshing should take care of the plasmon modes supported by the system, i.e. insert enough elements to suitably discretize the modal size.

- In systems where periodic boundary conditions are imposed, the mesh corresponding to the edges of the unit cell must be copied in order to accomplish the divergence condition (2.3) and prevent the generation of numerically induced charges into the system.

In every case, it is mandatory to realize a convergence test on the solution, by refining the mesh, i.e. increasing the element number while reducing their size, specially in the areas where the physical interest is highest. A similar test must be carried by increasing the complexity of the interpolation functions introduced next.

2.3.4. Selection of the interpolation functions.

One of the key points of the finite element method is that the resolution of the physical problem is based on a mathematical description of the solution that is performed independently for each mesh element, in terms of the nodes or edges that belong to it, and this description can be made despite the non-regular geometry of the mesh element or the different size or shape of its neighbors. Thus, an independent set of relatively simple functions can be chosen within each element e, and the solution of the problem is a piecewise function conformed by imposing continuity on the respective sets by means of the nodal or edge initial values, respecting the corresponding boundary conditions.
Very generally, we assume that an identical set is chosen on each mesh element belonging to the same physical domain, and the solution is expanded in terms of N unknown coefficients, c_j, with $j = 1, \ldots, N$, and N is the number of nodes or edges. For an arbitrary mesh element in the considered domain, we expand the solution variable as:

$$U^e(\mathbf{r}, t) = \sum_{j=1}^{N} c_j^e(t)\phi_j^e(\mathbf{r}), \tag{2.38}$$

In this expansion, we have considered that the time-dependence of the problem is enclosed inside the coefficients, and the spatial dependence is restricted in some set of set of suitably chosen basis functions or *interpolation functions* ϕ_j^e. This is a good approximation if the time step taken for the numerical resolution is small enough. For this subsection, we will assume the time dependence of c_j implicit.
The convergence and accuracy of the solution is closely related to the selection of the interpolation functions ϕ_j^e. A crucial point is whether we perform a description in terms of the nodes or the edges: As we will see in detail, the first option demands less computational resources, while the latter is needed to overcome certain numerical problems in the description of electromagnetic fields. In general, the interpolation functions can be characterized by two main features: *shape function type*, and *element order*. Usually, the function chosen is some kind of polynomial, since they allow the systematic implementation of numerical interpolation techniques to the order which is required. In addition, the evaluation of integrals of these polynomial is numerically attainable.
The shape function type may be classified depending on their continuity properties: When dealing with a nodal representation, if only continuity on the dependent variables is imposed, they belong to the *Lagrange* family of interpolation functions. Also, if both the dependent variable and its derivatives are used to determine the interpolation functions, they are part of the *Hermite* family of interpolation functions. Moreover, a

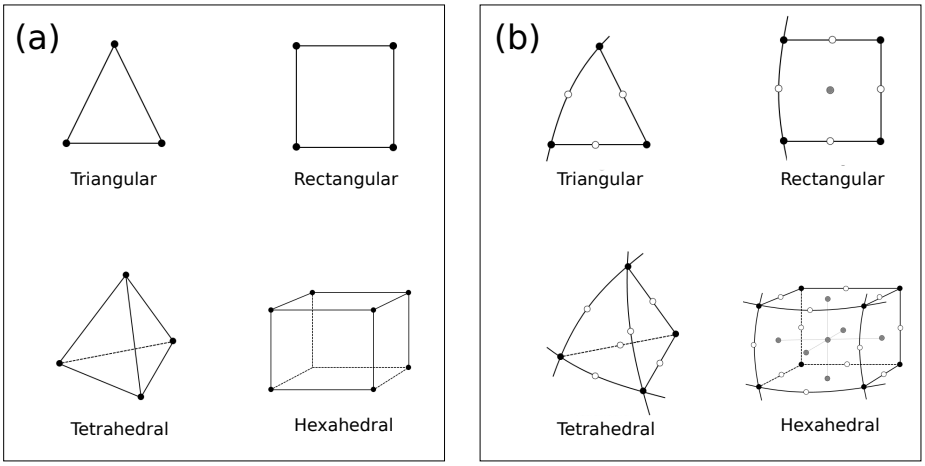

Figure 2.5: (a) Schematic representation of the nodes used for first-order nodal-based description of the 2D and 3D available types of mesh elements. (b) Nodes used for a second-order nodal-based description with the same shape function type (adapted from [129]).

vectorial edge-based representation of the interpolation functions that guarantees the continuity of its tangential component is called *Nédélec* or *curl* elements. The element order refers to the degree of the polynomial used. This creates restrictions on the number or nodes or edges that the description uses, since additional nodes must be described than those imposed by the geometry itself (see examples for nodal-based descriptions in Fig. 2.5). Increasing the element order will, in general, improve the accuracy of the solution.

When dealing with interpolation functions based on the nodal representation, it will be enough, for the purposes of this thesis, to use Lagrange interpolation functions. Moreover, we will use an edge-representation of the interpolation functions, called *Nédélec* or *curl* elements. Both types of interpolation functions are described next in detail.

Lagrange elements.

The Lagrange basis functions are a set of polynomia well suited for interpolation based exclusively in the nodal initial values. An individual set of these functions can be implemented with generality within each mesh element e, thus fully determining the solution inside it. They are characterized by the so-called interpolation properties [133]:

$$L_i^e(\mathbf{r}_j^e) = \delta_{ij} \tag{2.39}$$

$$\sum_{i=1}^{n} L_i^e(\mathbf{r}) = 1, \qquad \text{hence} \quad \sum_{i=1}^{n} \frac{dL_i^e}{dq} = 0 \tag{2.40}$$

where $n-1$ is the element order, $\mathbf{r}_j^e$ is the coordinate of the node j in the element Ω^e, and q stands for the independent spatial variables: for 2-dimensional functions; $q = x, y$. These properties ensure that the interpolation function associated to each node will be zero for the rest of the nodes in the element. Also, the value of the interpolation function at the interface between two elements depends only of its value at the two nodes it is connected. This guarantees the continuity of the solution over the simulation domain.
To exemplify how interpolation functions are introduced, let us introduce an arbitrary example in which a planar surface is meshed with triangular elements. Let us focus on the single mesh element depicted in Fig. 2.6(a). To characterize the corresponding nodes, we number them in counterclockwise order. We name the approximated solution variable inside the element e as $U^e(x, y)$, and denote its fixed values at the nodes as: $U^e(x_i^e, y_i^e) \equiv U_i^e$, with $i = 1, 2, 3$ corresponding to the number assigned.
We suppose now that the interpolation function chosen is a linear polynomial spanning at the coordinates of interest:

$$U^e(x, y) = a_e + b_e x + c_e y \tag{2.41}$$

where a_e, b_e and c_e are constants that can be determined by satisfying the fixed values at the nodes:

$$U_1^e = a_e + b_e x_1 + c_e y_1 \tag{2.42}$$

$$U_2^e = a_e + b_e x_2 + c_e y_2 \tag{2.43}$$

$$U_3^e = a_e + b_e x_3 + c_e y_3 \tag{2.44}$$

By solving this system of equations we obtain the following expressions for the solution variable:

$$U^e(x, y) = \sum_{i=1}^{3} c_i^e L_i^e(x, y) \tag{2.45}$$

and the interpolation functions are given by:

$$L_i^e(x,y) = \frac{a_i^e + b_i^e x + c_i^e y}{2\Delta^e} \qquad i = 1,2,3. \tag{2.46}$$

where:

$$a_1^e = x_2^e y_3^e - x_3^e y_2^e, \qquad b_1^e = y_2^e - y_3^e, \qquad c_1^e = x_3^e - x_2^e, \tag{2.47}$$

$$a_2^e = x_3^e y_1^e - x_1^e y_3^e, \qquad b_2^e = y_3^e - y_1^e, \qquad c_2^e = x_1^e - x_3^e \tag{2.48}$$

$$a_3^e = x_1^e y_2^e - x_2^e y_1^e, \qquad b_3^e = y_1^e - y_2^e, \qquad c_3^e = x_2^e - x_1^e \tag{2.49}$$

and $\Delta^e = (1/2)(b_1^e c_2^e - b_2^e c_1^e)$. Notice that this is the area of the $e-$th element. For visualization purposes, the derived interpolation functions are depicted in Fig. 2.6(b).
A natural extension of this class of interpolation functions can be introduced for 3D discretized geometries. Assuming that the element shape is tetrahedral, and numbering the nodes in the order indicated in Fig. 2.6(c), the counterpart for the linear Lagrange elements (2.46) above is written as follows:

$$L_i^e(x,y,z) = \frac{1}{6V^e}\left(a_j^e + b_j^e x + c_j^e y + d_j^e z\right) \tag{2.50}$$

where, by using the known nodal values $U_i^e = U^e(x_i^e, y_i^e, z_i^e)$, the constants can be determined by solving the following determinants:

$$a_1^e = \begin{vmatrix} x_2^e & x_3^e & x_4^e \\ y_2^e & y_3^e & y_4^e \\ z_2^e & z_3^e & z_4^e \end{vmatrix}; \quad b_1^e = \begin{vmatrix} 1 & 1 & 1 \\ y_2^e & y_3^e & y_4^e \\ z_2^e & z_3^e & z_4^e \end{vmatrix}; \quad c_1^e = \begin{vmatrix} x_2^e & x_3^e & x_4^e \\ 1 & 1 & 1 \\ z_2^e & z_3^e & z_4^e \end{vmatrix}; \quad d_1^e = \begin{vmatrix} x_2^e & x_3^e & x_4^e \\ y_2^e & y_3^e & y_4^e \\ 1 & 1 & 1 \end{vmatrix}$$

being the remaining constants determined by cyclic permutation $1 \to 2 \to 3 \to 4 \to 1$ in the expressions above, and V^e is the volume of the $e-$th tetrahedra, given by:

$$V^e = \frac{1}{6}\begin{vmatrix} 1 & 1 & 1 & 1 \\ x_1^e & x_2^e & x_3^e & x_4^e \\ y_1^e & y_2^e & y_3^e & y_4^e \\ z_1^e & z_2^e & z_3^e & z_4^e \end{vmatrix} \tag{2.51}$$

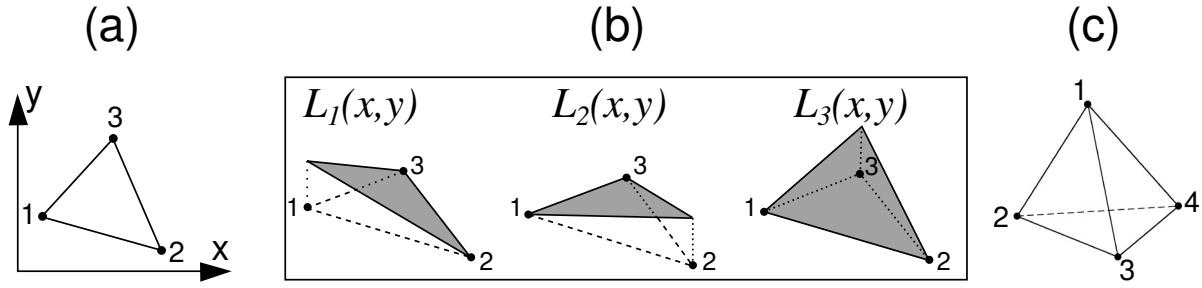

Figure 2.6: (a) Representation of a triangular element used for mesh generation on surfaces. (b) Linear Lagrange interpolation functions for the triangular element depicted in panel (a). (c) Representation of a tetrahedral element used for mesh generation in arbitrary volumes.

Vector finite elements: Curl elements.

The nodal-based representation is in general not valid to represent the electromagnetic field in 3-dimensional geometries, due to the emergence of nonphysical spurious solutions which violate the divergence conditions (2.3) and (2.4). We notice also that the Lagrange elements impose continuity of the fields across the mesh elements. Therefore, this description fails to describe the discontinuities of the tangential and normal components of the electromagnetic fields between different media.

Because of these numerical problems, it is necessary to introduce an alternative description in which the degrees of freedom are not the nodes but the edges of the considered mesh element. This enables to impose continuity in the tangential component at the element boundaries, but not in the normal component, making the curl of the vector field an integrable function. The edge-based finite elements are called vector finite elements, and its associated interpolation functions are named curl-conforming basis functions, or Nédélec elements.

We introduce here the linear curl interpolation functions for a triangular mesh element dividing an arbitrary surface:

$$\mathbf{N}_1^e(x,y) = (L_1^e \nabla L_2^e - L_2^e \nabla L_1^e)\, l_1^e \tag{2.52}$$

$$\mathbf{N}_2^e(x,y) = (L_2^e \nabla L_3^e - L_3^e \nabla L_2^e)\, l_2^e \tag{2.53}$$

$$\mathbf{N}_3^e(x,y) = (L_3^e \nabla L_1^e - L_1^e \nabla L_3^e)\, l_3^e \tag{2.54}$$

Here, the factor l_i^e is the length of the corresponding edge "i" (see Fig. 2.7(a)) and it is placed to make the vector element adimensional. L_i^e are the Lagrange interpolation functions (2.46) for the nodal-based description. Therefore, a vector solution field $\mathbf{U}^e$ in

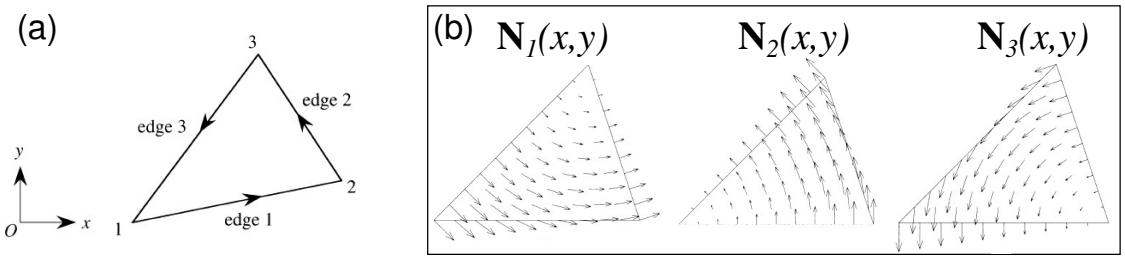

Figure 2.7: (a) Numbering of edges respect to the nodes for curl element functions derivation. (b) Schematic representation of the curl interpolation functions for a single triangular mesh element (Adapted from [130]).

the considered element can be written as:

$$\mathbf{U}^e(x,y) = \sum_{i=1}^{3} c_i^e \mathbf{N}_i^e(x,y) \tag{2.55}$$

These elements have a number of important properties that make them useful to avoid the aforementioned numerical problems that may arise when solving the vector potential:

- First of all, it can be demonstrated that each of them satisfies the divergence condition: $\nabla \cdot \mathbf{N}_i(x,y) = 0$, eliminating the problem of spurious solutions.
- Second, if we define the unit vector $\mathbf{e}_1$ parallel to the edge 1, pointing from the node 1 to the node 2, it can be demonstrated that: $\mathbf{e}_1 \cdot \mathbf{N}_1(x,y) = (l_1^e)^{-1}$. This implies that the function $\mathbf{N}_1^e$ has a constant tangential component along that edge. This is a general property for the rest of the edges, and has the important consequence that the continuity of the tangential component of the fields is guaranteed at the element boundaries.
- They have nonzero curl. Hence, they are suitable to discretize the Maxwell equations.

The vector interpolation functions (2.52)-(2.54) are depicted in Fig. 2.7(b). One can appreciate easily from these pictures that, for each of these functions, there exists a tangential component only at the corresponding edge to which they are adscribed. This ensures that the set of basis functions can suitably conform an alternative description based on the numbering of the edges, rather than the nodes, eliminating all the possible numerical problems associated to these.
The formulation of the curl elements to 3-dimensional geometries can be made in a

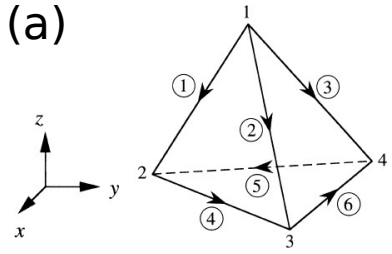

(b)

Edge i	Node i_1	Node i_2
1	1	2
2	1	3
3	1	4
4	2	3
5	4	2
6	3	4

Figure 2.8: (a) Tetrahedral mesh element used as a vector finite element. (b) Table used to refer the numbering used in the assignment of edges i and adjacent nodes i_1, i_2.

straightforward manner. In particular, let us consider the tetrahedral element in Fig. 2.8(a), which is the most suitable shape to fit irregular geometries. The curl interpolation functions for this element with the indicated numbering are the following:

$$\mathbf{N}_i^e(x,y,z) = (L_{i_1}^e \nabla L_{i_2}^e - L_{i_2}^e \nabla L_{i_1}^e) l_i^e \tag{2.56}$$

where the subscript i corresponds to the $i-$th edge and the i_1, i_2 correspond to the nodes to which it is connected, following the order depicted in Fig. 2.8(b). Now L_j^e are the linear 3-dimensional polynomials given by (2.50). The properties found for the 2-dimensional case hold in the 3-dimensional set of 6 functions. Therefore, these elements can (and must) be used for 3-dimensional problems involving the weak-form integration of the Ampere-Maxwell law (2.2).

2.3.5. Formulation of the system of equations. The weak form.

In this subsection, we introduce the mathematical framework that links the formulation of the solution in terms of interpolation functions with the construction of an algebraic system of equations that solves the problem.

We next formulate the variational problem that provides linear independence to the system of equations and determines the degrees of freedom of the discretized problem, translated into N unknown algebraic coefficients, with N the total number of nodes and edges in terms of which the solution was expanded. This formalism is called the weak formulation of the differential problem, and relies on the theory of functional analysis and variational calculus [129–131, 133–135]. We summarize this formulation in three steps that must be followed for the implementation within our finite-element framework:

Step 1. Write the weighted integral statement and select a variational principle.

We put all the terms on the differential problem (2.33) on one side. Then, we multiply by a test function w and integrate this expression over the whole domain of the problem. This is called the weighted-integral form of the equation:

$$\int_\Omega d^3\mathbf{r} w \left[\mathcal{L}u - f\right] = 0 \tag{2.57}$$

By substituting expansion (2.38) in terms of the N degrees of freedom into (2.57), one finds:

$$\int_\Omega d^3\mathbf{r} w \left[\mathcal{L}\left\{\sum_{j=1}^{N} c_j^e(t)\phi_j^e\right\} - f\right] = 0 \tag{2.58}$$

We require that this expression should hold for every form of the test-function w, such its generality is mantained. However, we can see that in this form, we have relaxed the conditions of the original problem, by demanding that the coefficients and solutions remain smooth enough so the expression (2.58) remains integrable.
One must then find the N conditions to make the system linearly independent, through a proper selection of the test functions w. This is where the variational method enters. In this context, a variational method is nothing more that a way of accomplishing the weighted-integral statement above. Mathematically, we can see this by considering the test function as a variation on the exact function u: $u' = u + w$, where u' is a solution coming from the variational method, and u the exact solution from (2.33). In other words, we can formulate w as the variation of u: $w = \delta u$, from a variational principle point of view, and rewrite Eq. (2.58) as:

$$0 = B(\delta u, u) - l(\delta u) \tag{2.59}$$

where we have assumed that for the specific form of $\mathcal{L}$ we can write: $B(\delta u, u) = \delta u(\mathcal{L}u)$, as a bilinear symmetric functional, and $l(u) = (\delta u)f$. These expressions can be further regrouped in: $0 = \delta I(u)$, with: $I(u) = B(u, u) - l(u)$. Hence, the weighted integral statement (2.57) can be rewritten as a variational problem in which the functional $I(u)$ has an extremum value.
There is not an universal choice for the test functions w, and it usually depends on the problem treated. A widely used and well-behaved method is the *Galerkin's method* [134], in which the chosen functions are the same interpolation functions as used to expand the solution variable: $w = \phi_i^e$, with $i = 1, \ldots, N$. Thus, we can write the problem (2.58)

as:

$$\int_{\Omega} d^3\mathbf{r}\phi_i^e \left[\mathcal{L}\left\{ \sum_{j=1}^{N} c_j^e(t)\phi_j^e \right\} - f \right] = 0, \tag{2.60}$$

for $i = 1, \ldots, N$. This a set of N equations that solves for the c_j^e, $j = 1, \ldots, N$ coefficients within the element e. Linear independence is guaranteed for the system above and its solution can be determined, upon the corresponding boundary conditions.

Step 2. Integrate by parts and impose boundary conditions.

The weighted-integral formulation above enables not only to relax the continuity demands on the original equation but also to obtain a boundary term that is used to naturally incorporate some boundary conditions of the problem. This is achieved by following two substeps:

- We integrate by parts on the weighted-integral statement (2.60), and distribute the differentiation of the original problem between the solution variable u and the test function w. If the spatial derivatives in the differential equation are of even order, this gives rise naturally to a boundary term.
- We identify the so-called *secondary variables*, which multiply the test function at the boundary term after differentiation. Specification of these secondary variables can be used to enforce the boundary conditions of the problem.

Note that, by trading the differentiability between the solution variable and the test function, less degree of differentiability is required now on the functions ϕ_j^e that interpolate the approximated solution U^e. For this reason, the expression (2.57), after performing the steps above, is termed *weak form* of the problem, since less strict conditions are demanded than in the original, 'strong' form (2.33).

Step 3. Assembly.

We have illustrated how the discretized problem is formulated inside a single mesh element for the generic differential problem (2.33), by using the interpolation functions (2.38) and the weak formulation. In order to solve the problem for the whole geometry, the respective systems of equations for the coefficients that result from this process must

be related by imposing continuity across the mesh elements, respecting the initial values of the nodes or edges. For the sake of an example, let us assume a time-independent problem and nodal-based interpolation functions. In this case, one can write the system (2.60) for $i = 1, \ldots, n$ in matrix form:

$$[K^e]\{c^e\} = \{b^e\} \tag{2.61}$$

in which the matrix $[K^e]$ relates the coefficient column vector $\{c^e\}$ with the forcing vector $\{b^e\}$ inside the mesh element e, with the following components:

$$K_{ij}^e = \int_{\Omega_e} d^3\mathbf{r}\phi_i^e \mathcal{L}\phi_j^e; \qquad b_j^e = f\phi_j^e \tag{2.62}$$

The M matrices resulting from the systems (2.61) corresponding to each mesh element, $e = 1, \ldots, M$, merge into an unique global matrix which is used to solve the problem. If the problem is time-dependent, the number of global matrices constructed will correspond to the order of the differential equation. This process is called *assembly*.
The procedure involves labelling the nodes of each single mesh element with local numbers, and relating them with a proper set of numbers chosen for the whole set of nodes. This is called the global number. One may define a connectivity array that relates the local numbers with the global numbers and use it to relate the components of the individual $n \times n$ matrices, to the components of an augmented $N \times N$ matrix, being N the total node number, by zero-filling the remaining components. In a similar fashion, one may expand the forcing vector from a $n-$component to a $N-$component vector. Therefore, the system can be reformulated as follows:

$$[K]\{c\} = \{b\} \tag{2.63}$$

where $[K]$ is the augmented matrix and and $\{b\}$ is the augmented forcing vector, which can be defined as follows:

$$[K] = \sum_{e=1}^{M} [\overline{\overline{K^e}}]; \qquad [b] = \sum_{e=1}^{M} [\overline{b^e}] \tag{2.64}$$

where the overlines represent the expansion to the $N \times N$ and $N \times 1$ dimensions, respectively.

Implementing the weak formulation. Approximations.

We now focus on the problem of the space and time-dependent field equation (2.11) that solves for the macroscopic electromagnetic field, coupled to the optical response of the metal components and to the nonlinear active medium. Following the steps described above, we make the correspondence $\mathcal{L} = \mu_0^{-1}(\nabla \times \nabla\times) + \epsilon\epsilon_0\partial_t^2$ in Eq. (2.33), where the solution variable is the field variable $\mathbf{A}(\mathbf{r}, t)$ corresponding to the vector potential, and we choose an associated test function $\tilde{\mathbf{A}}(\mathbf{r}, t)$. For simplicity, we assume that the assembly process described is implicit in the following discussion. Thus, the weak form is directly formulated for the assembled field variable $\mathbf{A} = \sum_{e=1}^{M} \overline{\mathbf{A}}^e$ on the domain of the problem Ω, and the boundary conditions arising from partial integration are automatically accomplished elsewhere but at the boundaries $\partial\Omega$ of the simulation cell. With this in mind, the weak form for the vector potential is written as follows:

$$\int_\Omega d^3\mathbf{r}\tilde{\mathbf{A}} \cdot \left[\nabla \times \left(\frac{1}{\mu_0}\nabla \times \mathbf{A}\right) + \epsilon\epsilon_0\partial_t^2\mathbf{A} - \partial_t\mathbf{P}\right] = 0 \tag{2.65}$$

where $\mathbf{A}$ is a vector that is expanded in terms of vector finite elements (see subsection 2.3.4):

$$\mathbf{A}(\mathbf{r}, t) = \sum_{i=1}^{N} c_i(t)\mathbf{N}_i(\mathbf{r}) \tag{2.66}$$

where c_i is a set of time-dependent coefficients, and N is the total number of edges.
The polarization that enters inside this weak-form equation is defined for each domain under consideration. In the gain medium, the polarization is given by the coupling equation to the external field and to the population inversion (2.19). In the metal, it is given by the Drude-Lorentz response (2.15). Therefore, we define a distinct form of the polarization field for each domain:

$$\mathbf{P}(\mathbf{r}, t)\big|_{\Omega_m \subset \Omega} = \mathbf{P}_m(\mathbf{r}, t)$$
$$\mathbf{P}(\mathbf{r}, t)\big|_{\Omega_g \subset \Omega} = \mathbf{P}_g(\mathbf{r}, t)$$

where Ω_g stands for the active medium domain and Ω_m is the metal domain. Thus, we define a local response inside of each domain for which the corresponding weak forms are solved. Inside the gain medium, we write the weak form of the polarization as follows:

$$\int_{\Omega_a} d^3\mathbf{r}\tilde{\mathbf{P}}_a^g \cdot \left[\frac{\partial^2 \mathbf{P}_a^g(\mathbf{r},t)}{\partial t^2} + 2\Gamma_a \frac{\partial \mathbf{P}_a^g(\mathbf{r},t)}{\partial t} + \omega_a^2 \mathbf{P}_a^g(\mathbf{r},t) + K_a \Delta N_a \mathbf{E}_{loc}(\mathbf{r},t)\right] = 0 \quad (2.67)$$

$$\int_{\Omega_g} d^3\mathbf{r}\tilde{\mathbf{P}}_e^g \cdot \left[\frac{\partial^2 \mathbf{P}_e^g(\mathbf{r},t)}{\partial t^2} + 2\Gamma_e \frac{\partial \mathbf{P}_e^g(\mathbf{r},t)}{\partial t} + \omega_e^2 \mathbf{P}_e^g(\mathbf{r},t) + K_e \Delta N_e \mathbf{E}_{loc}(\mathbf{r},t)\right] = 0 \quad (2.68)$$

for the absorption and emission transition in the laser medium, respectively. The optical response of the metal is dictated by the polarization $\mathbf{P}_m$ in (2.15), with the time-dependent Drude and Lorentz contributions $\mathbf{P}_d$ and $\mathbf{P}_l$ from (2.12) and (2.14), solved by:

$$\int_{\Omega_m} d^3\mathbf{r}\tilde{\mathbf{P}}_d \cdot \left[\frac{\partial \mathbf{P}_d}{\partial t} + \gamma_d \mathbf{P}_D + \epsilon_0 \omega_p^2 \mathbf{A}\right] = 0 \quad (2.69)$$

$$\int_{\Omega_m} d^3\mathbf{r}\tilde{\mathbf{P}}_l \cdot \left[\frac{\partial^2 \mathbf{P}_l}{\partial t^2} + 2\gamma_l \frac{\partial \mathbf{P}_l}{\partial t} + \omega_l^2 \mathbf{P}_l + \epsilon_0 \Delta\epsilon_l \omega_l^2 \mathbf{E}\right] = 0 \quad (2.70)$$

and, finally, for the rate equations (2.23)-(2.26), we have:

$$\int_{\Omega_a} d^3\mathbf{r}\tilde{N}_3 \left[\frac{\partial N_3(\mathbf{r},t)}{\partial t} - \frac{1}{\hbar\omega_a}\frac{\partial \mathbf{P}_a(\mathbf{r},t)}{\partial t} \cdot \mathbf{E}_{loc}(\mathbf{r},t) + \frac{N_3(\mathbf{r},t)}{\tau_{32}}\right] = 0 \quad (2.71)$$

$$\int_{\Omega_a} d^3\mathbf{r}\tilde{N}_2 \left[\frac{\partial N_2(\mathbf{r},t)}{\partial t} - \frac{N_3(\mathbf{r},t)}{\tau_{32}} - \frac{1}{\hbar\omega_e}\frac{\partial \mathbf{P}_e(\mathbf{r},t)}{\partial t} \cdot \mathbf{E}_{loc}(\mathbf{r},t) + \frac{N_2(\mathbf{r},t)}{\tau_{21}}\right] = 0 \quad (2.72)$$

$$\int_{\Omega_a} d^3\mathbf{r}\tilde{N}_1 \left[\frac{\partial N_1(\mathbf{r},t)}{\partial t} - \frac{N_2(\mathbf{r},t)}{\tau_{21}} + \frac{1}{\hbar\omega_e}\frac{\partial \mathbf{P}_e(\mathbf{r},t)}{\partial t} \cdot \mathbf{E}_{loc}(\mathbf{r},t) + \frac{N_1(\mathbf{r},t)}{\tau_{10}}\right] = 0 \quad (2.73)$$

$$\int_{\Omega_a} d^3\mathbf{r}\tilde{N}_0 \left[\frac{\partial N_0(\mathbf{r},t)}{\partial t} - \frac{N_1(\mathbf{r},t)}{\tau_{10}} + \frac{1}{\hbar\omega_a}\frac{\partial \mathbf{P}_a(\mathbf{r},t)}{\partial t} \cdot \mathbf{E}_{loc}(\mathbf{r},t)\right] \quad (2.74)$$

For the polarization fields and the rate equations, it suffices to use Lagrange elements. Thus, we expand for each component of the polarization:

$$P^{(k)}(\mathbf{r},t) = \sum_i^{N_p} p_{ki}(t) L_i(\mathbf{r}); \qquad k = 1,2,3. \quad (2.75)$$

where N_p is the number of nodes involved in the description and $\mathbf{P} = P^{(1)}\mathbf{x} + P^{(2)}\mathbf{y} + P^{(3)}\mathbf{z}$ are the components of the generic polarization field. For the population densities the expansion reads:

$$N_j = \sum_i^{N_g} n_i^j(t) L_i(\mathbf{r}) \quad (2.76)$$

with $j = 0, \ldots, 3$, and N_g is the number of nodes inside the discretized gain medium. The use of a variational principle by a suitable selection of the test functions denoted by the superscript "$\sim$" above, ensure that the system of equations (2.65),(2.67)-(2.74) will find a solution, through the determination of the coefficients $\{c\}$, $\{p_k\}$ and $\{n^{(j)}\}$. The last step is incorporating the corresponding boundary conditions of the problem, by distributing the spatial differentiation in the equation (2.65). Integrating by parts on the first term of this expression, we find:

$$\begin{aligned}\int_\Omega d^3r\tilde{\mathbf{A}}\cdot\nabla\times\left(\frac{1}{\mu_0}\nabla\times\mathbf{A}\right) = \\ = \int_\Omega d^3r\left(\nabla\times\tilde{\mathbf{A}}\right)\cdot\left(\frac{1}{\mu_0}\nabla\times\mathbf{A}\right) - \int_{\partial\Omega} d^2r\mathbf{n}\cdot\left[\tilde{\mathbf{A}}\times\left(\frac{1}{\mu_0}\nabla\times\mathbf{A}\right)\right]\end{aligned} \tag{2.77}$$

obtaining a boundary term. Now, by making use of the vectorial identity: $\mathbf{a}\cdot(\mathbf{b}\times\mathbf{c}) = \mathbf{b}\cdot(\mathbf{c}\times\mathbf{a})$ and the fact that: $\mathbf{H} = (1/\mu_0)\nabla\times\mathbf{A}$, we can find that:

$$\begin{aligned}-\int_{\partial\Omega} d^2r\mathbf{n}\cdot\left[\tilde{\mathbf{A}}\times\left(\frac{1}{\mu_0}\nabla\times\mathbf{A}\right)\right] = -\int_{\partial\Omega} d^2r\mathbf{n}\cdot\left[\tilde{\mathbf{A}}\times\left(\frac{1}{\mu_0}\nabla\times\mathbf{A}\right)\right] \\ = -\int_{\partial\Omega} d^2r\tilde{\mathbf{A}}\cdot(\mathbf{H}\times\mathbf{n})\end{aligned} \tag{2.78}$$

In conclusion, the weak form of the field equation reads:

$$\begin{aligned}\int_\Omega d^3r\left(\nabla\times\tilde{\mathbf{A}}\right)\cdot\left(\frac{1}{\mu_0}\nabla\times\mathbf{A}\right) - \int_{\partial\Omega} d^2r\tilde{\mathbf{A}}\cdot(\mathbf{H}\times\mathbf{n}) \\ + \int_\Omega d^3r\tilde{\mathbf{A}}\cdot\left[\epsilon_0\partial_t^2\mathbf{A} - \partial_t\mathbf{P}\right] = 0\end{aligned} \tag{2.79}$$

in which the degree of differentiation has been reduced on the field variable $\mathbf{A}$, and a boundary term has been found. The specification of the variables that multiply the test function in this term allow to impose the boundary conditions of the problem. In other words, the boundary conditions of this problem are introduced by specifying the tangential component of the magnetic field $\mathbf{H}$ inside the term:

$$W \equiv -\int_{\partial\Omega} d^2r\tilde{\mathbf{A}}\cdot(\mathbf{H}\times\mathbf{n}) \tag{2.80}$$

The weak-form equations (2.67)-(2.74) and (2.79) constitute a closed set of coupled PDEs that provides full spatio-temporal resolution of Maxwell equations combined with the population dynamics of the laser medium. Indeed, the fact that numerical resolution is performed directly in the time-domain, ensures that no approximation is taken in the frequency domain, nor it is restricted to a discrete number of frequencies. However, for some gain materials, it can be experimentally demonstrated that the spectral overlap between the gain profile and the absorption is not very high (see an example in Fig. 2.9). Moreover, in solving the general form of (2.65) for the vector magnetic potential, we are taking into account high frequency numerical oscillations that represent the most part of the computational demands [131]. Therefore, we shall consider that we can treat the pump and the lasing fields independently, by solving two independent sets of Maxwell equations, linked uniquely by the rate equations. This motivates us to define the following expansion of the vector potential around the frequencies of interest:

$$\mathbf{A}\left(\mathbf{r},t\right)=\mathbf{A}_{a}\left(\mathbf{r},t\right)\exp(-i\omega_{a}t)+\mathbf{A}_{e}\left(\mathbf{r},t\right)\exp(-i\omega_{e}t), \tag{2.81}$$

And similarly, for the polarization fields:

$$\mathbf{P}\left(\mathbf{r},t\right)=\mathbf{P}_{a}\left(\mathbf{r},t\right)\exp(-i\omega_{a}t)+\mathbf{P}_{e}\left(\mathbf{r},t\right)\exp(-i\omega_{e}t), \tag{2.82}$$

Now we can solve the Maxwell equations only for the pairs of slowly-varying amplitudes $\mathbf{A}_{a,e}$ and $\mathbf{P}_{a,e}$, thus optimizing the speed of a typical calculation.

Furthermore, we perform a time-average over the optical cycle on the stimulated transitions terms inside rate equations (2.23)-(2.26), and they read, under the above considerations, as:

$$\frac{\partial N_3}{\partial t}=\frac{1}{\hbar\omega_a}\left\langle\frac{\partial\mathbf{P}_a}{\partial t}\cdot\mathbf{E}_a^{loc}\right\rangle-\frac{N_3}{\tau_{32}}, \tag{2.83}$$

$$\frac{\partial N_2}{\partial t}=\frac{N_3}{\tau_{32}}+\frac{1}{\hbar\omega_e}\left\langle\frac{\partial\mathbf{P}_e}{\partial t}\cdot\mathbf{E}_e^{loc}\right\rangle-\frac{N_2}{\tau_{21}}, \tag{2.84}$$

$$\frac{\partial N_1}{\partial t}=\frac{N_2}{\tau_{21}}-\frac{1}{\hbar\omega_e}\left\langle\frac{\partial\mathbf{P}_e}{\partial t}\cdot\mathbf{E}_e^{loc}\right\rangle-\frac{N_1}{\tau_{10}}, \tag{2.85}$$

$$\frac{\partial N_0}{\partial t}=\frac{N_1}{\tau_{10}}-\frac{1}{\hbar\omega_a}\left\langle\frac{\partial\mathbf{P}_a}{\partial t}\cdot\mathbf{E}_a^{loc}\right\rangle \tag{2.86}$$

where the time-average is defined as: $\langle\mathbf{A}\cdot\mathbf{B}\rangle=(1/2)\mathrm{Re}\{\mathbf{A}\cdot\mathbf{B}^{*}\}$.

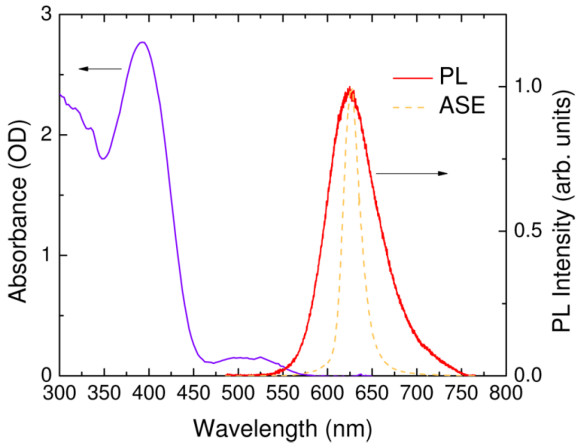

Figure 2.9: Absorbance (purple line), accounting for the spectral distribution of absorption, and photoluminiscence (red line), representative of the spectral gain, for the laser medium Alq_3:DCM. It can be noticed that the overlap between both is very low (Reprinted from [53]).

With these considerations, the problem is reduced to determine the slowly-varying amplitudes $\mathbf{A}_a$, $\mathbf{A}_e$, $\mathbf{P}_a$ and $\mathbf{P}_e$, by solving two identical subsets of equations $\{\mathbf{A}_\alpha, \mathbf{P}_\alpha^{dl}, \mathbf{P}_\alpha^{g}\}$ for the field variables at $\alpha = a, e$; together with the rate equations. We next write the weak form that solves each of these subsets, by using the approximations above. The weak form for the slowly varying field-amplitude $\mathbf{A}_\alpha$ is given by:

$$\int_\Omega d^3\mathbf{r}\left(\nabla\times\tilde{\mathbf{A}}_\alpha\right)\cdot\left(\frac{1}{\mu_0}\nabla\times\mathbf{A}_\alpha\right)-\int_{\partial\Omega}d^2\mathbf{r}\tilde{\mathbf{A}}_\alpha\cdot(\mathbf{H}_\alpha\times\mathbf{n})-$$
$$-\epsilon_0\omega_\alpha^2\int_\Omega d^3\mathbf{r}\tilde{\mathbf{A}}_\alpha\mathbf{A}_\alpha-2i\epsilon_0\omega_a\int_\Omega d^3\mathbf{r}\tilde{\mathbf{A}}_\alpha\partial_t\mathbf{A}_\alpha+\int_\Omega d^3\mathbf{r}\tilde{\mathbf{A}}_\alpha\partial_t^2\mathbf{A}_\alpha-\int_\Omega d^3\mathbf{r}\tilde{\mathbf{A}}_\alpha\partial_t\mathbf{P}_\alpha=0 \tag{2.87}$$

where $\mathbf{H}_\alpha = \nabla\times\mathbf{A}_\alpha$. For the Drude-Lorentz approach inside the metal, we must solve $\mathbf{P}_\alpha^{dl} = \epsilon_0(\epsilon_\infty - 1)\mathbf{E}_\alpha + \mathbf{P}_\alpha^d + \mathbf{P}_\alpha^l$, where the fields: $\mathbf{P}_\alpha^d$ and $\mathbf{P}_\alpha^l$ are solved by integrating their corresponding weak forms:

$$\int_{\Omega_m} d^3\mathbf{r}\tilde{\mathbf{P}}_\alpha^d\cdot\left[\frac{\partial\mathbf{P}_\alpha^d}{\partial t}+\gamma_d\mathbf{P}_\alpha^d+\epsilon_0\omega_p^2\mathbf{A}_\alpha\right]=0 \tag{2.88}$$

$$\int_{\Omega_m} d^3\mathbf{r}\tilde{\mathbf{P}}_\alpha^l\cdot\left[\frac{\partial^2\mathbf{P}_\alpha^l}{\partial t^2}+2\gamma_l\frac{\partial\mathbf{P}_\alpha^l}{\partial t}+\omega_l^2\mathbf{P}_\alpha^l+\epsilon_0\Delta\epsilon_l\omega_l^2\mathbf{E}_\alpha\right]=0 \tag{2.89}$$

and for the gain medium, the polarization field $\mathbf{P}_\alpha^g$ that couples to the population inver-

sion and the electric field is integrated now as follows:

$$\int_{\Omega_a} d^3\mathbf{r}\tilde{\mathbf{P}}_\alpha^g \cdot \left[\frac{\partial^2 \mathbf{P}_\alpha^g(\mathbf{r},t)}{\partial t^2} + 2\Gamma_\alpha \frac{\partial \mathbf{P}_\alpha^g(\mathbf{r},t)}{\partial t} + \omega_\alpha^2 \mathbf{P}_\alpha^g(\mathbf{r},t) + K_\alpha \Delta N_\alpha \mathbf{E}_\alpha(\mathbf{r},t)\right] = 0 \quad (2.90)$$

with $\mathbf{E}_\alpha = -\partial_t \mathbf{A}_\alpha$. Finally, the weak form of the rate equations that link the components at the absorption and the emission frequency is given by:

$$\int_{\Omega_a} d^3\mathbf{r}\tilde{N}_3 \left[\frac{\partial N_3(\mathbf{r},t)}{\partial t} - \frac{1}{\hbar\omega_a}\left\langle \frac{\partial \mathbf{P}_a(\mathbf{r},t)}{\partial t} \cdot \mathbf{E}_a^{loc}(\mathbf{r},t)\right\rangle + \frac{N_3(\mathbf{r},t)}{\tau_{32}}\right] = 0 \quad (2.91)$$

$$\int_{\Omega_a} d^3\mathbf{r}\tilde{N}_2 \left[\frac{\partial N_2(\mathbf{r},t)}{\partial t} - \frac{N_3(\mathbf{r},t)}{\tau_{32}} - \frac{1}{\hbar\omega_e}\left\langle \frac{\partial \mathbf{P}_e(\mathbf{r},t)}{\partial t} \cdot \mathbf{E}_e^{loc}(\mathbf{r},t)\right\rangle + \frac{N_2(\mathbf{r},t)}{\tau_{21}}\right] = 0 \quad (2.92)$$

$$\int_{\Omega_a} d^3\mathbf{r}\tilde{N}_1 \left[\frac{\partial N_1(\mathbf{r},t)}{\partial t} - \frac{N_2(\mathbf{r},t)}{\tau_{21}} + \frac{1}{\hbar\omega_e}\left\langle \frac{\partial \mathbf{P}_e(\mathbf{r},t)}{\partial t} \cdot \mathbf{E}_e^{loc}(\mathbf{r},t)\right\rangle + \frac{N_1(\mathbf{r},t)}{\tau_{10}}\right] = 0 \quad (2.93)$$

$$\int_{\Omega_a} d^3\mathbf{r}\tilde{N}_0 \left[\frac{\partial N_0(\mathbf{r},t)}{\partial t} - \frac{N_1(\mathbf{r},t)}{\tau_{10}} + \frac{1}{\hbar\omega_a}\left\langle \frac{\partial \mathbf{P}_a(\mathbf{r},t)}{\partial t} \cdot \mathbf{E}_a^{loc}(\mathbf{r},t)\right\rangle\right] \quad (2.94)$$

We remark that the described approximations lead to a huge increase of the computational efficiency of this method, that allows simulating plasmonic nanolaser systems that have been untreatable with any other numerical approach.

Enforcing boundary conditions: Creating a pump.

We noted previously that the derivation of the weak-form expression of the field equation gives rise naturally to a boundary term through partial derivation. Within the approximations above, same procedure is followed to obtain one boundary term for each slowly-varying amplitude $\mathbf{A}_{a,e}$ in which we have expanded the vector potential. Namely, from equation (2.87), we find:

$$W_a \equiv -\int_{\partial\Omega} d^2 r \tilde{\mathbf{A}}_a \cdot (\mathbf{H}_a \times \mathbf{n}) \quad (2.95)$$

$$W_e \equiv -\int_{\partial\Omega} d^2 r \tilde{\mathbf{A}}_e \cdot (\mathbf{H}_e \times \mathbf{n}) \quad (2.96)$$

in which the associated slowly-varying magnetic field amplitude $\mathbf{H}_{a,e}$ appears. By properly defining the magnetic field at the boundaries of interest, these terms can create the boundary conditions inside the weak form for which a light pulse is illuminating the simulation domain. This is interesting to define an incoming pump at the frequency ω_a

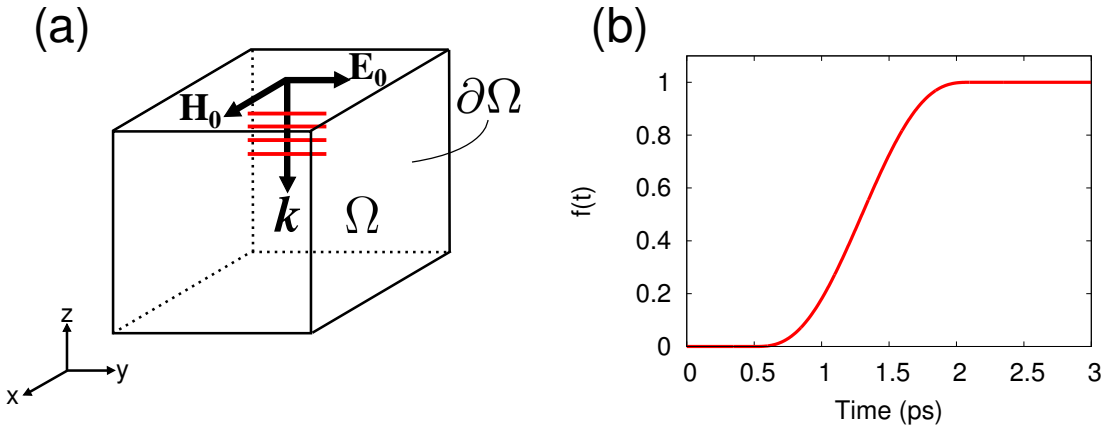

Figure 2.10: (a) Schematic representation of a simulation cell in which a $y-$polarized plane wave propagating downwards is enforced, with amplitude $\mathbf{E}_0$ and wavevector $\mathbf{k}$. (b) Modulation function typically used to introduce a continuous-wave pulse inside the simulation cell.

but also to introduce our approach to model spontaneous emission at the frequency ω_e. Imagine a simulation cell like in Fig. 2.10(a) in which we want to recreate a plane wave polarized in the $y-$direction and propagating downwards with a wavevector $\mathbf{k}_d = -k\mathbf{z}$, without obtaining unphysical reflections, at any of the frequencies of interest: $k = \omega/c$ (we remove the subscript a, e for now). We assume that the electric field is polarized in the $y-$direction, with amplitude: $\mathbf{E_0} = E_0\mathbf{y}$, and hence $\mathbf{H}_0 = H_0\mathbf{x}$ is the incident magnetic field amplitude.

First, boundary conditions should be imposed to enforce the excitation of this plane wave at the upper boundary, and to absorb the radiation due to possible reflections. The reflected magnetic field is written as:

$$\mathbf{H}_r = \frac{1}{\mu_0\omega}\mathbf{k}_u \times \mathbf{E}_r, \tag{2.97}$$

with $\mathbf{k}_u$ is the wave-vector propagating upwards. If $\mathbf{H}_r = \mathbf{H} - \mathbf{H}_0$, $\mathbf{E}_r = \mathbf{E} - \mathbf{E}_0$, and magnetic and electric incident fields are related by: $\mathbf{H}_0 = (1/\mu_0\omega)\mathbf{k}_d \times \mathbf{E}_0$, then:

$$\begin{aligned}\mathbf{H} &= \frac{1}{\mu_0\omega}\left[(\mathbf{k}_d - \mathbf{k}_u) \times \mathbf{E_0} + \mathbf{k}_u \times \mathbf{E}\right] \\ &= \frac{1}{\mu_0\omega}\left[k\left(2E_0 - E_y\right)\mathbf{x} + kE_x\mathbf{y}\right]\end{aligned} \tag{2.98}$$

Therefore, the boundary term at the "top" boundary yields:

$$-\int_{\text{top}} d^2\mathbf{r}\tilde{\mathbf{A}}\cdot\left(\hat{\mathbf{H}}\times\mathbf{n}\right)=-\int_{\text{top}} d^2\mathbf{r}\tilde{A}_x\frac{k}{\mu_0\omega}E_x+\int_{\text{top}} d^2\mathbf{r}\tilde{A}_y\frac{k}{\mu_0\omega}\left(2E_0-E_y\right) \tag{2.99}$$

Next, we impose boundary conditions for the lower boundary to be transparent to the plane wave crossing through it. At this "bottom" boundary, there is only transmitted field, and the contribution is simply:

$$\mathbf{H}=\frac{1}{\mu_0\omega}\mathbf{k}_d\times\mathbf{E} \tag{2.100}$$

And we find:

$$-\int_{\text{bottom}} d^2\mathbf{r}\tilde{\mathbf{A}}\cdot\left(\hat{\mathbf{H}}\times\mathbf{n}\right)=-\int_{\text{bottom}} d^2r\tilde{A}_x\frac{k}{\mu_0\omega}E_x-\int_{\text{bottom}} d^2r\tilde{A}_y\frac{k}{\mu_0\omega}E_y \tag{2.101}$$

To accomplish with the fact that a plane wave needs an empty space in the transversal direction to its propagation, we use periodic boundary conditions in the four remaining limiting boundaries. Thus, the boundary terms are written in the following form:

$$\begin{aligned}W_{a,e}=&-\int_{\text{top}} d^2\mathbf{r}\tilde{A}^x_{a,e}\frac{k_{a,e}}{\mu_0\omega_{a,e}}E^x_{a,e}+\int_{\text{top}} d^2\mathbf{r}\tilde{A}^y_{a,e}\frac{k_{a,e}}{\mu_0\omega_{a,e}}\left(2E^{a,e}_0-E^y_{a,e}\right)\\&-\int_{\text{bottom}} d^2\mathbf{r}\tilde{A}^x_{a,e}\frac{k_{a,e}}{\mu_0\omega_{a,e}}E^x_{a,e}-\int_{\text{bottom}} d^2\mathbf{r}\tilde{A}^y_{a,e}\frac{k_{a,e}}{\mu_0\omega_{a,e}}E^y_{a,e}\\&-[\text{Periodic boundary conditions}]\end{aligned} \tag{2.102}$$

Let us remark that the imposition of the boundary conditions is not restricted to the excitation of a plane wave. In fact, the terms (2.95), (2.96) allows for plenty of input conditions. Absorbing boundary conditions can be enforced naturally in this way. As explained in Appendix A, it is also possible to recreate a cavity between two partially reflecting mirrors. Here, we bring attention to the fact that a time-dependent modulation can be added to the input electric field amplitude: $E^{a,e}_0(t)=E^{a,e}_0 f(t)$, which allows not only to simulate continuous-wave operation but also an incoming optical pulse. This is essential when initializing the system: Typically the active molecules will be prepared in their ground state at time $t=0$, and the pump pulse must be smoothly turned on to accurately track off the transition to the upper level, via stimulated absorption, without introducing numerical effects. Figure 2.10(b) shows an illustrative example of how the pump and lasing fields are enforced with time. Importantly, such a pulse at the emission frequency is also necessary, since in the semiclassical approximation, spontaneous

emission is not modelled and the stimulated-emission term inside (2.92), (2.93) must numerically be forced to be distinct than zero to initiallize the lasing field. The excitation generated to that purpose is of amplitude much less than the pump. As we will show, the results presented in this manuscript do not depend on the duration of that seed excitation.

Construction of the system of equations.

After imposing the boundary conditions, it is left to formulate the system of algebraic equations that must be solved for the nonlinear system in the time-domain. We use the same expansion as in the general full time-domain description, describing the slowly-varying vector potential amplitudes $\mathbf{A}_a(\mathbf{r},t)$ and $\mathbf{A}_e(\mathbf{r},t)$ from equations (2.87) at the respective absorption and emission frequencies in terms of curl interpolation functions or vector finite elements:

$$\mathbf{A}_{a,e}\left(\mathbf{r},t\right)=\sum_{i=1}^{N}c_i^{a,e}(t)\mathbf{N}_i\left(\mathbf{r}\right) \tag{2.103}$$

where N is the total number of edges.
Since continuity is demanded for the polarization amplitudes $\mathbf{P}_{a,e}(\mathbf{r},t)$ and the population densities $N_0(\mathbf{r},t)-N_3(\mathbf{r},t)$ inside their respective physical domains, numerical issues are not expected when using the nodal-based interpolation functions. Therefore, we use Lagrange elements for their expansion. For each component of the polarization, we obtain:

$$P_{a,e}^{(k)}\left(\mathbf{r},t\right)=\sum_{i=1}^{N_p}p_{i;k}^{a,e}(t)L_i\left(\mathbf{r}\right);\qquad k=1,2,3. \tag{2.104}$$

where N_p is the number of nodes involved in the description and $\mathbf{P}_{a,e}=P_{a,e}^{(1)}\mathbf{x}+P_{a,e}^{(2)}\mathbf{y}+P_{a,e}^{(3)}\mathbf{z}$. For the scalar population densities the expansion reads:

$$N_j=\sum_{i}^{N_g}n_i^{(j)}(t)L_i\left(\mathbf{r}\right) \tag{2.105}$$

with $j=0,\ldots,3$; and N_g is the number of nodes inside the discretized gain medium.
As discussed, the interpolation of the continuous field variables does not suffice to provide a linearly independent algebraic system of equations. One must further formulate

a variational principle to choose the test functions that, within the weak formulation, provide the necessary constraints to formulate the algebraic system. In this text, we use the Galerkin's method, by which the selected test functions are chosen the same basis functions as used to interpolate the field variables. In this manner, the N test-functions that multiply the field equation for the vector potential are $\tilde{\mathbf{A}}_{a,e} = \{\mathbf{N}_i\}$, with $i = 1, \ldots, N$. Similarly, for the gain polarization and for the population inversion we will use: $\tilde{P}^{(k)}_{a,e} = \{L_i\}$, $i = 1, \ldots, N_p$; for each of the components of the test function $\tilde{\mathbf{P}}_{a,e}$, and $\tilde{N}_i = \{L_i\}$, $i = 1, \ldots, N_g$; for the population density of each quantum energy level.
We now formulate the algebraic system of equations. We anticipate that subsystems of field equations (2.87) will be solved separately, with an input coming from the polarization fields. Therefore, we focus on the single weak-form equation:

$$\int_\Omega d^3\mathbf{r}\left(\nabla\times\tilde{\mathbf{A}}_\alpha\right)\cdot\left(\frac{1}{\mu_0}\nabla\times\mathbf{A}_\alpha\right) - \int_{\partial\Omega} d^2\mathbf{r}\tilde{\mathbf{A}}_\alpha\cdot(\mathbf{H}_\alpha\times\mathbf{n}) - \\ - \epsilon_0\omega_\alpha^2\int_\Omega d^3\mathbf{r}\tilde{\mathbf{A}}_\alpha\mathbf{A}_\alpha - 2i\epsilon_0\omega_\alpha\int_\Omega d^3r\tilde{\mathbf{A}}_\alpha\partial_t\mathbf{A}_\alpha + \int_\Omega d^3r\tilde{\mathbf{A}}_\alpha\partial_t^2\mathbf{A}_\alpha - \int_\Omega d^3r\tilde{\mathbf{A}}_\alpha\partial_t\mathbf{P}_\alpha = 0. \tag{2.106}$$

with $\alpha = a, e$ accounting for both the pump field and the lasing field. In what follows, we remove this subscript, since the discussion will be completely analogous for both subsets of equations $\{\mathbf{A}_\alpha, \mathbf{P}_\alpha\}$.
As discussed, the boundary term inside expression (2.106) is used to enforce boundary conditions. For the sake of an example, we incorporate the boundary condition used to excite a continuous-wave pulse gradually turned on from $t = 0$, given by (2.102). By inserting the expansion (2.103) into this boundary condition and using the test-functions chosen following Galerkin's method, we obtain:

$$-\int_{\partial\Omega} d^2\mathbf{r}\tilde{\mathbf{A}}\cdot(\mathbf{H}\times\mathbf{n}) = -\{q\} - [U]\frac{d\{c\}}{dt} \tag{2.107}$$

where two terms arise: one of them takes the form of a $1\times N$ column vector: $\{q\} = [q_1, \ldots, q_N]^T$ proportional to the test function vector $y-$component $\tilde{A}_y = N_i^y$ integrated at the top boundary, which contains the excitation term that drives the system:

$$q_i = \frac{1}{\mu_0 c}\int_{\text{top}} d^2r N_i^y\,(2E_0(t)) \tag{2.108}$$

The remaining term is the product of a $N\times N$ square matrix $[U]$ with the rest of contributions inside (2.102), and the column vector consituted by the time-derivatives of each coefficient used in the expansion: $\{c\} = [c_1, c_2, \ldots, c_N]^T$. The elements of this matrix are

given by:

$$U_{ij} = \frac{1}{\mu_0 c}\Bigg(\int_{\text{top}} d^2 r N_i^x N_j^x + \int_{\text{top}} d^2 r \tilde{N}_y N_y - \int_{\text{bottom}} d^2 r N_i^x N_j^x - \int_{\text{bottom}} d^2 r N_i^y N_j^y \Bigg) + [\text{Periodic boundary conditions}] \tag{2.109}$$

where a similar expansion has been performed in the periodic boundary conditions, which we will not discuss here.
Remarkably, the expansion of the field variables in the corresponding interpolation functions, together with the Galerkin's method, are the necessary conditions that provide a solution of the field equation, by means of a system of coupled ordinary differential equations in time. Namely, by using (2.103) and incorporating the boundary condition (2.107) above into the weak form (2.106), it is found:

$$[M]\frac{d^2\{c\}}{dt^2} + [C]\frac{d\{c\}}{dt} + [K]\{c\} - \{f\} = 0, \tag{2.110}$$

which constitute the N conditions to solve for the $c_i(t)$ coefficients of the expansion. $[M]$, $[C]$, $[K]$ are $N \times N$ square matrices given by:

$$M_{ij} = \int_\Omega d^3 r \mathbf{N}_i \cdot \mathbf{N}_j \tag{2.111}$$

$$C_{ij} = -2i\epsilon_0 \omega T_{ij} - U_{ij} \tag{2.112}$$

$$K_{ij} = \int_\Omega d^3 r \left(\nabla \times \mathbf{N}_i\right) \cdot \left(\nabla \times \mathbf{N}_j\right) - \epsilon_0 \omega^2 T_{ij} \tag{2.113}$$

called *mass* matrix, *damping* matrix, and *stiffness* matrix, respectively, due to the resemblance of equation (2.110) to expressions arising in the field of structural mechanics. $\{f\}$ is a column vector:

$$f_i = \int_\Omega d^3 r \mathbf{N}_i \partial_t \mathbf{P} + q_i \tag{2.114}$$

If we analyze carefully the structure of Eq. (2.110) inside the active medium, it is evident that the electromagnetic field, represented by the vector potential amplitude $\mathbf{A}_{a,e}(\mathbf{r}, t)$

through the set of coefficients $\{c\}$, is boosted by the driving term $\{f\}$, that contains both the polarization of the gain medium, and the field time-dependent amplitude $E_0(t)$, which at the absorbing frecuency, is nothing but the pump strength delivered to the system.

The gain-induced polarization (2.90) is integrated by means of its own weak formulation. By using the expansion (2.104) in Lagrange-type interpolation functions and inserting the corresponding test function, we obtain:

$$[S]\left(\frac{d^2\{p_k\}}{dt^2}+2\Gamma\frac{d\{p_k\}}{dt}+\omega\{p_k\}\right)-\{b_k\}=0; \qquad k=1,2,3. \tag{2.115}$$

where $[S]$ is a $N_g \times N_g$ square matrix whose elements are given by:

$$S_{ij}=\int_\Omega d^3\mathbf{r}L_i\cdot L_j \tag{2.116}$$

where $L_i(\mathbf{r})$ are Lagrange elements, and $\{p_k\}$ and $\{b_k\}$ are $1\times N_g$ column vectors given by:

$$\{p_k\}=[p_{1;k},\ldots,p_{N_p;k}] \tag{2.117}$$

$$\{b_k^i\}=\int_\Omega d^3\mathbf{r}L_i\Delta N E_k \tag{2.118}$$

where the $p_{i;k}$ are the time-dependent coefficients used for the expansion in (2.104), and E_k, $k=1,2,3$ correspond to the x, y and $z-$components of the input electric field slowly-varying amplitude, respectively, and ΔN is the population inversion.

An analogous procedure is performed to obtain ordinary differential equations in time for the coefficients $n_i^j(t)$ at (2.105), in terms of which we expand the population densities, finding:

$$[S]\left(\frac{d\{n^{(3)}\}}{dt}+\frac{\{n^{(3)}\}}{\tau_{32}}\right)-\{p_i^a\}=0 \tag{2.119}$$

$$[S]\left(\frac{d\{n^{(2)}\}}{\partial t}+\frac{\{n^{(2)}\}}{\tau_{21}}\right)-\frac{\{N_i^{(3)}\}}{\tau_{32}}-\{p_i^e\}=0 \tag{2.120}$$

$$[S]\left(\frac{d\{n^{(1)}\}}{dt}+\frac{\{n^{(1)}\}}{\tau_{10}}\right)-\frac{\{N_i^{(2)}\}}{\tau_{21}}+\{p_i^e\}=0 \tag{2.121}$$

$$[S]\left(\frac{d\{n^{(0)}\}}{dt}\right)-\frac{\{N_i^{(1)}\}}{\tau_{10}}+\{p_i^a\}=0 \tag{2.122}$$

Where the definition of $[S]$ corresponds to (2.116) above, and the forcing $1 \times N_g$ column vectors $\{p_i^{a,e}\}$ and $\{N_i^{(j)}\}$ are given by:

$$\{p_i^{a,e}\} = \frac{1}{2\hbar\omega_{a,e}} \int_{\Omega_a} d^3\mathbf{r} L_i \mathrm{Re}\left\{ \frac{\partial \mathbf{P}_{a,e}}{\partial t} \cdot \mathbf{E}_{a,e}^{loc*} \right\} \tag{2.123}$$

$$\{N_i^{(j)}\} = \int_{\Omega_a} d^3\mathbf{r} L_i N_j; \qquad j = 0, \ldots, 3 \tag{2.124}$$

with a $1 \times N_g$ column vector with the coefficients of the expansion:

$$\{n^{(j)}\} = \left[n_1^{(j)}, \ldots, n_{N_g}^{(j)} \right]^T; \qquad j = 0, \ldots, 3 \tag{2.125}$$

We next proceed with the resolution of the coupled set of time-dependent coefficients $\{c\}$, $\{p_k\}$ and $\{n^{(0)}\} - \{n^{(3)}\}$.

2.3.6. Resolution of the system of equations.

The expressions (2.110), (2.115) and (2.119)-(2.122) consitute a set of ordinary differential-algebraic equations that solve for the time-dependent coefficients in which the electromagnetic field, the polarization fields, and the population densities are expanded. The complete numerical resolution of the problem involves discretizing the time-derivative in these equations. Here, we introduce a systematic algorithm which provides a solution for the expressions above by time-stepping, while solving implicitly the non-linearity introduced by the field variables involved in the active medium description. As a side note, we mention that the resolution inside the metal domains is completely analogous. We have concluded that the field equation, together with its boundary conditions, has been transformed into two subsets of second-order differential equations:

$$[M]\frac{d^2\{c^a\}}{dt^2} + [C^a]\frac{d\{c^a\}}{dt} + [K^a]\{c^a\} = \{f^a\} \tag{2.126}$$

$$[M]\frac{d^2\{c^e\}}{dt^2} + [C^e]\frac{d\{c_e\}}{dt} + [K^e]\{c^e\} = \{f^e\} \tag{2.127}$$

where the sets of coefficients $\{c^{a,e}\}$ stand for the expansion coefficients of the slow-varying vector potential amplitudes $\mathbf{A}_{a,e}$ In the gain medium, the forcing vectors $\{f^a\}$ and $\{f^e\}$ are not independent, since they are ruled by the induced polarization at the absorption

and the emission frequency, respectively:

$$f^{a,e} = \int_{\Omega} d^3 r \mathbf{N}_i \partial_t \mathbf{P}^{a,e} + q_i^{a,e} \tag{2.128}$$

coupled by means of rate equations, since the polarization amplitudes $\mathbf{P}_{a,e}$ are boosted by the population inversions ΔN_a and ΔN_e. These forcing vectors are updated with time by solving the corresponding coefficients at the equation (2.115). In the same fashion, differential equations (2.119)-(2.122) are solved to find the population densities $N_0 - N_3$ with the marching time. Since the population densities also require the vector potential and the gain medium polarization amplitudes as an input, it is clear that the aforementioned system of equations is a self-consistent problem whose numerical resolution is provided by time-discretization, implicitly solving its non-linearity by alternatively updating the corresponding sets of coefficients $\{c^{\alpha}\}$, $\{p_k^{\alpha}\}$, with $k = 1, 2, 3$ and $\alpha = a, e$; and $\{n^{(0)}\} - \{n^{(3)}\}$.

The numerical resolution of such a set of algebraic coefficients in the time domain is carried by means of the Generalized$-\alpha$ algorithm. Although its main features are introduced for equations with a structure like (2.110), the formalism is completely general to solve also (2.115) and (2.119)-(2.122). This algorithm was developed due to arising high-frequency spurious solutions that, for a long time, made time-domain methods non-reliable, specially when treating first order differential equations [136]. As we will see, numerical dissipation is introduced for these high frequencies.

Generalized$-\alpha$ is a one-step time-integration method, since the solution at the time t_{n+1} depends only of that at the time t_n. Moreover, it is a three-stage method, since the solution vectors are being updated: $\{a\}_n$, $\{v\}_n$, named by analogy with the velocity and the acceleration vectors, are solved together with $\{c\}_n$, as numerical approximations found for the values of: $\{d_t^2 c|_{t=t_n}\}$, $\{d_t c|_{t=t_n}\}$, and $\{c(t = t_n)\}$, respectively.

The basic form of the Generalized$-\alpha$ algorithm can be written as follows:

$$\{c\}_{n+1} = \{c\}_n + \Delta t \{v\}_n + \Delta t^2 \left(\left(\frac{1}{2} - \beta \right) \{a\}_n + \beta \{a\}_{n+1} \right) \tag{2.129}$$

$$\{v\}_{n+1} = \{v\}_n + \Delta t \left((1 - \gamma) \{a\}_n + \gamma \{a\}_{n+1} \right) \tag{2.130}$$

$$[M]\{a\}_{n+1-\alpha_m} + [C]\{v\}_{n+1-\alpha_f} + [K]\{c\}_{n+1-\alpha_f} = \{f\left(t_{n+1-\alpha_f}\right)\} \tag{2.131}$$

where initial values are defined as:

$$\{c\}_0 = \{c\} \tag{2.132}$$
$$\{v\}_0 = \{v\} \tag{2.133}$$
$$\{a\}_0 = [M]^{-1}\left(\{f(t_0)\} - [C]\{v\} - [K]\{c\}\right) \tag{2.134}$$

and:

$$\{c\}_{n+1-\alpha_f} = (1-\alpha_f)\,\{c\}_{n+1} + \alpha_f\{c\}_n \tag{2.135}$$
$$\{v\}_{n+1-\alpha_f} = (1-\alpha_f)\,\{v\}_{n+1} + \alpha_f\{v\}_n \tag{2.136}$$
$$\{a\}_{n+1-\alpha_f} = (1-\alpha_f)\,\{a\}_{n+1} + \alpha_f\{a\}_n \tag{2.137}$$
$$t_{n+1-\alpha_f} = (1-\alpha_f)\,t_{n+1} + \alpha_f t_n \tag{2.138}$$

where $n = 0, \ldots, N-1$, N is the number of time steps, and Δt is the time steps.
Now, some relations must be provided between the parameters α_f, α_m, β and γ. It has been demonstrated [137] that the method can be made unconditionally stable, and accurate even for first-order differential equations, with the following selection of parameters:

$$\gamma = \frac{1}{2} - \alpha_m + \alpha_f \tag{2.139}$$
$$\beta = \frac{1}{4}\left(1 - \alpha_m + \alpha_f\right)^2 \tag{2.140}$$
$$\alpha_m = \frac{2\rho_\infty - 1}{\rho_\infty + 1} \tag{2.141}$$
$$\alpha_f = \frac{\rho_\infty}{\rho_\infty + 1} \tag{2.142}$$

Here, ρ_∞ is a parameter that ranges between 0 and 1, and it controls the high-frequency numerical damping. $\rho_\infty = 1$ means no numerical damping at all, which is certainly the case for linear problems. $\rho_\infty = 0$ means the maximum numerical damping allowed by the method, and should be used only for highly nonlinear problems. In all the calculations performed in this thesis, the numerical damping has been fixed to $\rho_\infty = 0.75$, in order to provide stability without changing the physical results.

Figure 2.11 shows the three main stages resulting from iteratively solving the time dynamics of the non-linear coupled set of differential equations in our implementation. Let us consider that initially, the molecules are preparated in their ground state: $N_0(0) = N_{tot}$, and: $N_1(0) = N_2(0) = N_3(0) = 0$, with a total molecule density N_{tot}. By

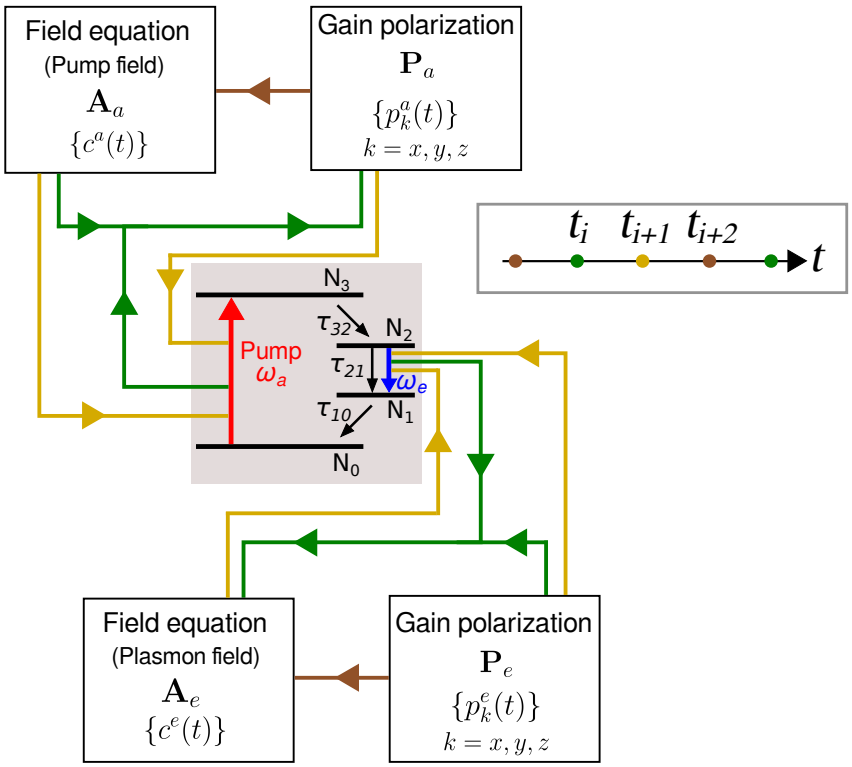

Figure 2.11: Stages resulting from the numerical resolution of the vector potential amplitudes $\mathbf{A}_{a,e}$, the polarization amplitudes induced in the gain medium $\mathbf{P}_{a,e}$, and the population densities $N_0 - N_3$, through the determination of their associated time-dependent coefficients. The coloured lines illustrate the steps followed to iteratively update these quantities with time-stepping.

enforcing a boundary condition as described in (2.102), an incoming pulse is smoothly turned on and pump field distribution $\mathbf{A}_a$ is created around the system of interest. The induced polarization ruled by equation (2.90) is created at this point (time t_i, green arrows), boosted by the population inversion ΔN_a and the pump field. If the polarization is significant, a certain fraction of the electrons in the ground state N_0 will be promoted to the higher level N_3, and the population inversion ΔN_a is updated (time t_{i+1}, yellow arrows), through the stimulated-absorption term: $\langle \partial \mathbf{P}_a \cdot \mathbf{E}_a^{loc} \rangle$. Finally, the vector potential in the gain medium is itself modified (time t_{i+2}, brown arrows), driven by the recently created polarization inside the medium, closing the cycle at the absorption frequency ω_a, and these steps are followed all over again.

Similar guidelines are followed by the time dynamics at the lasing frequency: a pulse with amplitude much less than the pump is initialized with time at the emission frequency

ω_e, allowing the building-up of the vector potential amplitude distribution $\mathbf{A}_e$ at this frequency, thus accounting for spontaneous emission. The spatial profile of the field corresponds to the inhomogeneous distribution associated to the plasmonic mode amplified for the specific design of laser. As discussed, if population inversion $\Delta N_a > 0$ is created at the absorption frequency, it rapidly decays non-radiatively into the metastable level 2, causing the accumulation of a population inversion $\Delta N_e > 0$ at the emission frequency. The steps followed above are replicated, now leading to the creation of the induced polarization field $\mathbf{P}_e$ inside the gain medium and updating the population densities N_1 and N_2. When relevant, the stimulated-emission term $\langle \partial \mathbf{P}_e \cdot \mathbf{E}_e^{loc} \rangle$ now locally *destroys* the available population inversion, which in turn decreases the available gain by reducing the induced polarization that enters into the field equation. The creation and destruction of population inversion due to stimulated absorption and emission, fueled by the pump and lasing fields, conduces to a complex nonlinear behavior in the time dynamics that will be analyzed for each system of interest in the next Chapters.

Choosing the time step

The time step used must take some considerations in mind. When dealing with multimode operating systems, one of the constraints is not to induce a non-physical mode-switching. This is translated into that the maximum time-step allowed is dictated by the separation in frecuencies $\Delta\omega_s$ of the examined mode and the closest one, by the relation:

$$\Delta t_s \leq \frac{2\pi}{\Delta\omega_s} \tag{2.143}$$

Moreover, in our formalism, we ruled out fast oscillations by splitting harmonic dependences around the frequencies of interest $\omega_{a,e}$. However, the resulting slowly-varying vector potential amplitudes $\mathbf{A}_{a,e}$ are still time-dependent, and it is important to suitably discretize in time the variations that these amplitudes display. For the lasing field, this can be accounted for by considering that the main time-dependence inside this amplitude is harmonic:

$$\mathbf{A}\left(t;\omega_e\right) = \underbrace{\mathbf{A}'(t)\exp(-i\Delta\omega_f t)}_{=\mathbf{A}_e(t)\ \text{(Overall slowly-vaying amplitude)}} \times\ \exp(-i\omega_e t),$$

where now $\mathbf{A}'(t)$ is very slowly varying. The magnitude of the corresponding frequency $\Delta\omega_f$ can be numerically calculated as follows:

$$\Delta\omega_f = -\mathrm{Im}\left\{\frac{\partial_t \mathbf{A}(t)}{\mathbf{A}(t)}\right\}.$$

Now, in order to accurately simulate these oscillations, 10 times should at least be fitted in each period. This establishes a criteria for the maximum time-step Δt_f in lasing simulations:

$$\Delta t_f \leq 0,1 \times \frac{2\pi}{\Delta\omega_f}$$

In conclusion, the maximum time-step allowed from numerical considerations is given by:

$$\Delta t_{max} = \min\left\{\Delta t_s, \Delta t_f\right\} \tag{2.144}$$

with the definitions of Δt_s and Δt_f above.

2.4. The finite element method in the frequency domain.

So far we have presented a time-domain generalization of the finite-element method that solves the Maxwell equations in an exact manner, coupled to a non-linear active medium. Although very general, this method is inherently time demanding, since the very different timescales involved need for a time-discretization of the order of femtoseconds, and the typical dynamical processes can take hundreds of picoseconds or even nanoseconds to settle down to a steady-state. Throughout this manuscript, there is a number of numerical results that need to be solved in the linear optical regime. In these cases, we will be interested in the steady state result for $t \to \infty$ for a single frequency ω, and the pump time-dependence can be considered as a continuous-wave sinusoidal signal. For these cases, we implement the finite element method in the frequency domain. This approach is much less time consuming, and can be readily implemented within the radiofrequency (RF) module of Comsol Multiphysics, with predefined governing equations that are integrated by means of the weak form. The frequency-domain analysis also brings a number of interesting computational techniques, being the use of perfect matched layers (PMLs) the most significant one. This section is devoted to further explain these concepts.
In the finite-element implementation of the resolution of the Maxwell equations in the frequency domain, we use the consitutive relations $\mathbf{D} = \epsilon_0\epsilon\mathbf{E}$ and $\mathbf{B} = \mu_0\mu\mathbf{H}$ inside

and the Faraday law (2.1) and the Ampère-Maxwell law (2.2) from Maxwell equations, leading to the following coupled equations:

$$\nabla \times \mathbf{H} = \epsilon_0 \frac{\partial(\epsilon \mathbf{E})}{\partial t} \tag{2.145}$$

$$\nabla \times \mathbf{E} = -\mu_0 \frac{\partial(\mu \mathbf{H})}{\partial t} \tag{2.146}$$

Furthermore, we assume that the time-dependence is harmonic with a single oscillating frequency ω:

$$\mathbf{E}(\mathbf{r}, t) = \mathbf{E}_0(\mathbf{r}) e^{-i\omega t}; \qquad \mathbf{H}(\mathbf{r}, t) = \mathbf{H}_0(\mathbf{r}) e^{-i\omega t} \tag{2.147}$$

By introducing these expressions into Eqs. (2.145) and (2.146), we can reduce them into a single expression for the electric field:

$$\nabla \times (\nabla \times \mathbf{E}_0) - k_0^2 \epsilon \mathbf{E}_0 = 0 \tag{2.148}$$

with $k_0 = \omega / c_0$, and c_0 is the light speed of vaccum. Now, for the numerical resolution of the Maxwell equations in frequency domain finite element based approaches, the variable to solve can be chosen as the static electric field $\mathbf{E}_0(\mathbf{r})$ or the static magnetic field $\mathbf{H}_0(\mathbf{r})$, with identical results. From now on, we will choose $\mathbf{E}_0$ as the dependent variable.
In the frequency-domain FEM, the steps that lead from the formulation of the physical problem to its resolution in terms of an algebraic system of equations are common to those followed for its time-dependent counterpart. However, some appreciations should be made:

- Selection of the interpolation functions:
  The solution variable expanded in terms of suitably chosen interpolation functions is now time-independent. Thus, in general, the solution U^e inside the mesh element e can be written as:

$$U^e(\mathbf{r}) = \sum_{i=1}^{N} c_i^e \phi_i^e(\mathbf{r}) \tag{2.149}$$

  where N is the number of degrees of freedom, and the c_i^e coefficients are now time-independent. The features concering the interpolation functions are identical as

explained in subsection 2.3.4, including the use of Lagrange nodal-based interpolation functions $\phi_i^e = L_i^e(\mathbf{r})$, or vector edge-based interpolation functions $\phi_i^e = \mathbf{N}_i^e(\mathbf{r})$.

- Variational principle and the weak form:
  The expansion of the solution variable in terms of interpolation functions enable the construction of an algebraic system of equations whose unknowns are the c_i^e coefficients. As we saw, however, this does not provide linear independence to the resulting system, and thus the solution will not be uniquely determined. Therefore, we must impose an additional constraint through a variational principle, that creates the remaining conditions to solve the problem. The weak form, in this case, is formulated in terms of the electric field $\mathbf{E}_0$ and its corresponding test function $\tilde{\mathbf{E}}_0$, accomplishing (2.57), with $\mathcal{L} = (\nabla \times \nabla \times) - k_0^2 \epsilon$. The forced term, if distinct from zero, is generated by the imposition boundary conditions. The variational method chosen to complete the N conditions needed to guarantee linear independence of the system of N unknown coefficients, is again the Galerkin's method: $w = \phi_i^e$.

- Formulation of the system of equations:
  With the conditions above, and combining the expansion of the interpolation functions with the Galerkin's method, one can obtain an algebraic system of equations in the same fashion as in subsection 2.3.5. Since the coefficients do not depend on time, the derivatives in equation (2.110) are zero now. Therefore, the mass and damping matrices are null matrices, and we are left with an equation involving only the stiffness matrix:

$$[K]\{c\} = \{f\} \tag{2.150}$$

In conclusion, to solve the problem in the frequency domain, one must calculate the unknown coefficient vector $\{c\} = [c_1, \ldots, c_N]^T$, where N is the number of degrees of freedom. Since the problem is linear, the resolution can be performed in a direct way, without the need of a time-stepping algorithm. In what follows, we examine different cases of Eq. (2.150) which apply to the physical situations analyzed in this manuscript, depending on whether the forcing vector $\{f\}$ is zero or not. As we noted with time-dependent FEM, this term represents excitations that drive the optical response of the system, like an external source, or some boundary condition that creates a flux of energy into the domain of the problem.

2.4.1. Scattering problems.

Let us first suppose the physical problem in which the forcing term $\{f\}$ is distinct from zero, in any of its forms. This means that there exists some external source or boundary condition that is driving the system. Such a situation, in the context of linear FEM simulations in radio-frequency modeling, resembles a scatterer subject to either a charge density or density current, or illuminated by an incident light pulse.
Scattering simulations are performed in this thesis for scatterers that are the counterparts of the plasmonic lasers in the optical linear regime, when the density of dye molecules is set to zero. These *passive* structures sustain electromagnetic modes that act as the cold-cavity modes amplified in the laser, and frequency-domain calculations allow to retrieve the field-distribution associated to them. An example of a 3D simulation is shown in Figure 2.12. A plane wave can be forced to impinge on a core-shell metallic nanosphere, and obtain its response in the steady-state at some frequency. In the picture, a dipolar resonance is excited inside the particle, and the on-resonant Fourier component ω_{res} is captured. Interestingly, this formulation enable us to separate the input field $E_x^{in}(\mathbf{r}, \omega_{res})$ at the panel (a), from the scattered field E_{scat} (Total field is depicted in the panel (b), with: $E_x^{tot}(\mathbf{r}, \omega_{res}) = E_x^{in}(\mathbf{r}, \omega_{res}) + E_x^{scat}(\mathbf{r}, \omega_{res})$). For the purposes of characterizing light generation, we can calculate relevant quantitites as the $Q-$factor, the confinement factor, and the absorption, scattering and extinction cross sections. Some of these values are also the input for the semianalytical approaches introduced in section 2.5.

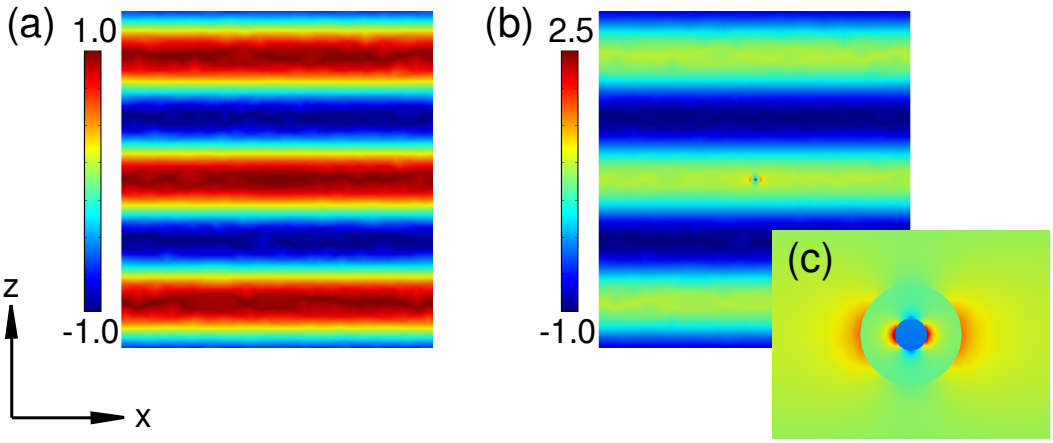

Figure 2.12: Frequency-domain scattering simulation for a core-shell metallic nanosphere from Chapter 5. (a) $x-$component of the electric field (E_x, in V/m) for an impinging $x-$polarized plane wave propagating in the $+z$ direction. (b) $x-$component of the total electric field (E_x) obtained for the simulation. (c) Close-up of the total E_x-field represented in the panel (b).

2.4.2. Eigenvalue problems.

If the forcing term is $\{f\} = 0$ in equation (2.150), the system is source-free, not driven by any external excitation, and the problem can be reformulated as:

$$[A]\{c\} = \lambda[B]\{c\} \tag{2.151}$$

where the stiffness matrix $[K]$ has been rewritten as: $[K] = [A] - \lambda[B]$, and λ is an eigenvalue to be determined. In a frequency-domain equation, the absence of sources means that the solution will be trivial but for a discrete number of complex eigenvalues. The corresponding solutions are called eigenmodes, and they are associated to resonances in cavities or to propagating modes inside a waveguide. Since the solutions are degenerated by a multiplicative factor, only the shape of the solution is meaningful, but not its magnitude.

The procedure to find a particular eigenmode in an arbitrary structure is the following: one defines a linearization point λ, which is a seed value with a shift $\sigma = |\lambda - \lambda_0|$ with respect to the closest eigenvalue λ_0. This eigenvalue is computed by means of the implicitly restarted Arnoldi method (IRAM) [138] which computes the largest eigenvalues of the matrix $C = (A - \sigma B)^{-1}B$. By updating the linearization point, the shift is reduced to zero and convergence is reached, enabling access to the whole physical information of the eigenmode.

Figure 2.13 presents two examples of results obtained in this thesis by using this methodology. Panel (a) shows a periodic array of metallic nanoparticles, that sustains a resonant mode of plasmonic nature. Panel (b) shows the cross section of a V-groove waveguide, with a channel plasmon polariton propagating out-plane. In practice, the interest in eigenvalue frequency-domain FEM simulations come from the possibility of accessing solutions of the problem without the need of an external excitation. For example, the mode shown plasmonic crystal from Fig. 2.13(a) cannot be excited by a normal incident plane wave (at least, in the linear regime) for symmetry reasons. In addition, the channel plasmon shown in Fig. 2.13(b) can be excited with a TM plane wave, but generating reflections at the planar metal surface that add to the scattered field and hinders the main features of the waveguide mode.

2.4.3. Boundary conditions.

The physical problem formulated by expression (2.148) can be fully determined within the frequency-domain FEM framework after imposing proper boundary conditions. Here

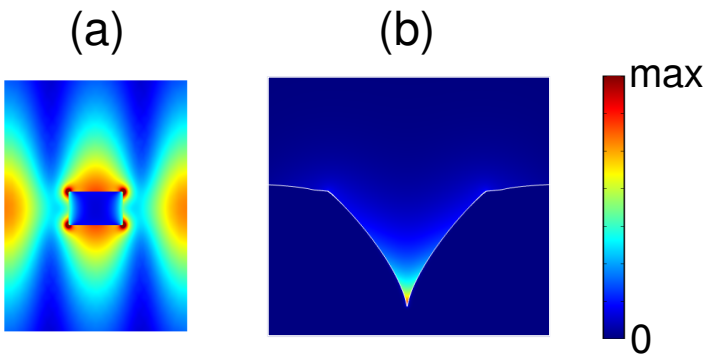

Figure 2.13: Examples of eigenmode calculations presented in this thesis. Electric field amplitude $|\mathbf{E}(\mathbf{r},\omega_0)|$ is presented for the eigenfrequency $f_0 = \omega_0/2\pi$. (a) Surface lattice resonance shown for a unit cell of a periodic array of metallic nanowires, presented in Chapter 4. (b) Channel plasmon polariton (CPP) propagating through an infinite V-Groove waveguide, with translational symmetry, presented in Chapter 3.

we provide the boundary conditions used to enforce electromagnetic modes inside the domain of the problem, absorbing boundary conditions suitable for a wide variety of mode profiles and wavefronts, as well as continuity conditions to connect neighboring cells in infinite periodic lattices.

Periodic boundary conditions.

These conditions enable us to provide periodicity between the limits of some considered unit cell (see Fig. 2.14). The electric field at some source boundary $\mathbf{E}_{src}$ can then be related to that at a destination boundary, through the relation:

$$\mathbf{E}_{dst} = \mathbf{E}_{src} e^{-i\mathbf{k}_F \cdot (\mathbf{r}_{dst} - \mathbf{r}_{src})} \tag{2.152}$$

where $\mathbf{E}_{dst}$ is the electric field at the destination boundary, $\mathbf{k}_F$ is the wavevector that can be chosen to be propagated through the periodic geometry and $\mathbf{r}_{src}$, $\mathbf{r}_{dst}$ are the relative positions of the considered source and destination boundaries.

Port boundary conditions.

In many of the scattering problems treated in this thesis, it is of interest to enforce the excitation or absorption of one or many electromagnetic modes whose shape and propa-

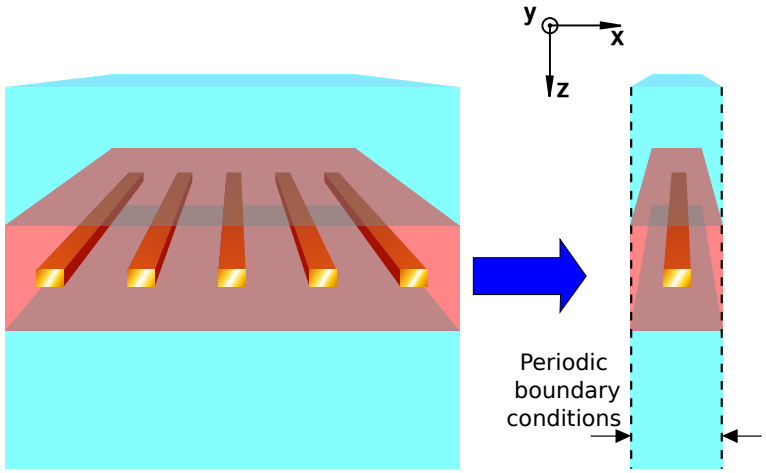

Figure 2.14: Periodic boundary conditions are imposed to recreate perfect periodicity in plasmonic crystals from Chapter 4.

gation constant are known and well defined. The computational implementation of these boundary conditions can be mathematically described by an expansion into mutually orthogonal modes, represented by individual port boundary conditions distributed over the involved surfaces. In this way, the propagation of a waveguide mode or the absorption of several modes of diffraction from a plasmonic grating can be described.
Every port is restricted to excite or absorb one single electromagnetic mode. At each corresponding boundary, the port condition is formulated by enforcing the power flow of the mode:

$$\mathbf{n} \cdot \mathbf{S}_{av} = \mathbf{n} \cdot \frac{1}{2} \mathrm{Re} \left(\mathbf{E} \times \mathbf{H}^* \right) \tag{2.153}$$

where $\mathbf{S}_{av}$ is the time-averaged Poynting vector. The mode shape can be introduced either in terms of the electric field or of the associated magnetic field. In addition, a propagation constant is defined, which allows to specify the incoming or outgoing wave direction.
The port formulation is based on the transmission line theory, which involves the use of the scattering matrix, with $n \times n$ dimension, where n is the total number of ports. The terms S_{ij} inside this matrix, called $S-$parameters, are defined in terms of transmitted and reflected voltage waves. For example, let us assume that we want to excite an arbitrary mode with electric field profile $\mathbf{E}_c$ at a flat boundary B1 and let it propagate until it reaches another flat boundary B2, which must be transparent to the mode outflow.

The corresponding $S-$parameters created by the port-conditions are defined as follows:

$$S_{11} = \frac{\int_{\mathrm{B1}} \left((\mathbf{E}_c - \mathbf{E}_1) \cdot \mathbf{E}_1^* \right) dA_1}{\int_{\mathrm{B1}} \left(\mathbf{E}_1 \cdot \mathbf{E}_1^* \right) dA_1} \tag{2.154}$$

$$S_{21} = \frac{\int_{\mathrm{B2}} \left(\mathbf{E}_c \cdot \mathbf{E}_2^* \right) dA_2}{\int_{\mathrm{B2}} \left(\mathbf{E}_2 \cdot \mathbf{E}_2^* \right) dA_2} \tag{2.155}$$

where $\mathbf{E}_1$ and $\mathbf{E}_2$ are the fundamental eigenmodes at the considered boundaries, assuming we know its electric field profile. By definition, the $S-$parameters correspond to the square root of the power flow crossing the boundary B2, divided by that coming from boundary B1. Therefore, transmission (T) and reflection (R) corresponding to the isolated eigenmodes can be obtained as the squared port-contribution: $R = |S_{11}|^2$ and $T = |S_{21}|^2$.

Besides, it is possible that the wave excites an additional propagating mode $\mathbf{E}_3$ at the structures that must be absorbed as well. Hence, we must define at the corresponding boundaries B1 and B2 new ports to avoid unphysical reflections at them:

$$S_{31} = \frac{\int_{\mathrm{B2}} \left(\mathbf{E}_c \cdot \mathbf{E}_3^* \right) dA_1}{\int_{\mathrm{B1}} \left(\mathbf{E}_1 \cdot \mathbf{E}_1^* \right) dA_1}; \qquad S_{32} = \frac{\int_{\mathrm{B2}} \left(\mathbf{E}_c \cdot \mathbf{E}_3^* \right) dA_2}{\int_{\mathrm{B2}} \left(\mathbf{E}_2 \cdot \mathbf{E}_2^* \right) dA_2} \tag{2.156}$$

This procedure can be made as general as required to include more eigenmodes or even additional boundaries.

Ports represent an essential tool in the modeling of plasmonic gratings. It is known that by illuminating this class of structures with radiation of wavelengths shorter than the period, one or more diffraction orders may be excited, by the relation:

$$m\lambda_0 = p(\sin\beta_m - \sin\alpha) \tag{2.157}$$

for a particle-array embedded in air, see Figure 2.15. Thus, the diffraction angle β_m for the order m can be obtained in terms of the wavelegth λ_0, the period p, and the angle of the incident radiation α. Assuming that $\lambda_0 > (p/2)(|\sin\alpha| + 1)$, there exists only one order of diffraction, and we must be able to excite the impinging radiation at the boundary B1, absorbing not only the zeroth order reflected component, but also that associated to $m = \pm 1$ diffraction orders. Similarly, boundary B2 must be transparent for the transmitted radiation associated to $m = 0, \pm 1$ diffraction orders. To achieve this goal, we define three ports per boundary, exciting a plane wave at the boundary B1. Each

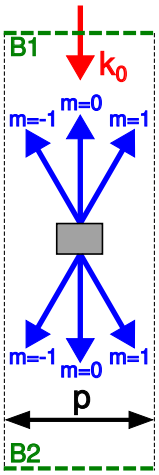

Figure 2.15: Representation of the diffraction orders arising when illuminating a plasmonic nanowire grating (a unit cell is depicted). Individual port boundary conditions are needed either to excite a normal-incident plane-wave, and to absorb each corresponding diffracted wave, for the orders: $m = 0, \pm 1$, both at the upper boundary B1 and at the lower boundary B2.

port allows to define the vectorial components of the electric or magnetic field and its propagation constant. Therefore, for an impinging TM plane wave, which for simplicity is considered normal incident ($\alpha = 0$), we impose as the input field: $H = exp(ik_0 y)\mathbf{z}$ at the B1, and demand to absorb $H = exp(i\mathbf{k}_m \cdot \mathbf{r})\mathbf{z}$, where $\mathbf{k}_m = k_0(\cos\beta_m \mathbf{x} + \sin\beta_m \mathbf{y})$, with $m = \pm 1$ at both boundaries, and $m = 0$ at boundary B2.

Perfectly matched layers.

The simulation of open boundaries is a challenging topic in electromagnetism simulations, since the dispersed radiation must be able to exit the domain of the problem without reflecting back numerical reflections to the physical area of interest. In some scattering problems, this radiation cannot be described with a well-defined direction of propagation nor in terms of an expansion in orthogonal modes, and the use of ports should be avoided. To overcome this issue, we truncate the external physical boundary with a volume in which a complex transformation of the spatial variables is performed (see Fig. 2.16(a)). This class of boundary layer is known as perfect matched layer (PML) [139]. For a general coordinate variable t, the PML uses the following transformation:

$$t' = \left(\frac{t}{\Delta_w}\right)^n (1 - i)\lambda F \tag{2.158}$$

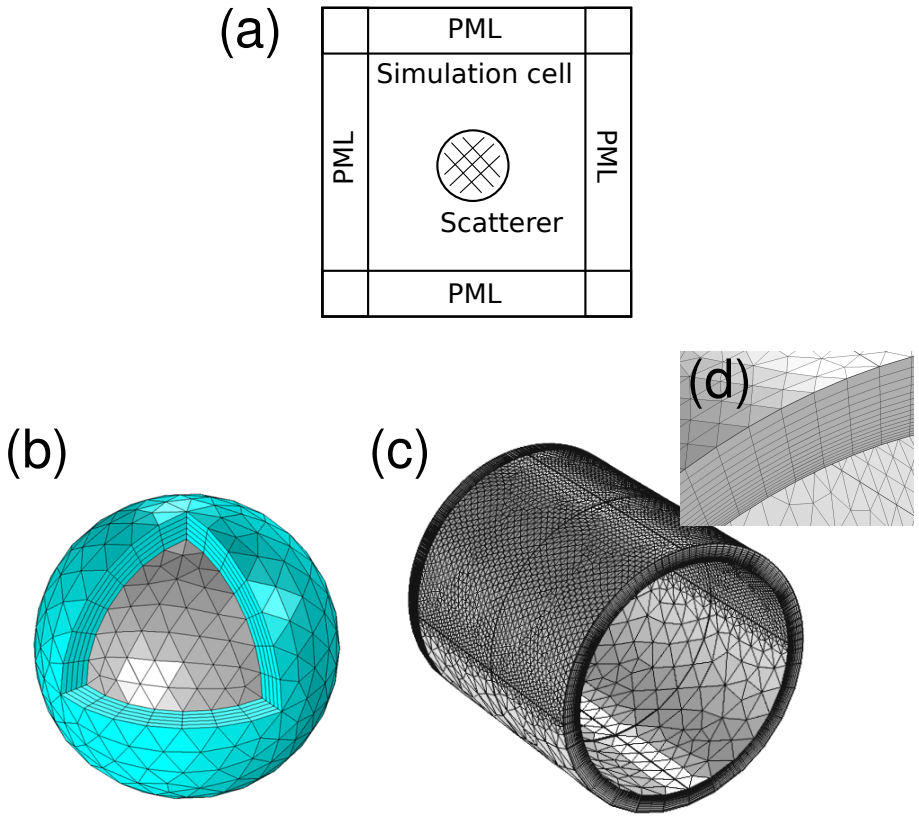

Figure 2.16: (a) Schematic representation of PML domains surrounding a simulation cell to absorb generic free-space radiation in a scattering problem. (b) Example of a meshed PML domain (in blue) for a spherical geometry. (c) Meshed PML domain for a cylindrical geometry. (d) Close-up on the discretization performed close to the interface with the simulation domain to optimize the PML performance.

where t is the considered coordinate, Δ_w is the width of the PML region, λ is the operating wavelength. The scaling factor F and the PML order n are parameters designed to improve the PML features for each situation of interest. Such a formulation can be deduced direcly from the Maxwell equations, by performing a conformal mapping from the complex-valued coordinates to the real coordinates. It is possible to demonstrate that the PML domains resemble an absorbing uniaxial material, with constitutive relations that yield an anisotropic complex-valued permittivity $\tilde{\epsilon}$ and permeability $\tilde{\mu}$ tensors [130] for the optical response. Importantly, under the condition that the wave impedance remains unaffected at the interface with the PML domain, this transformation ensures that all the outgoing radiation will be absorbed with no back-reflections, independently

of the incident angle or the shape of the wave front.
The PML domains can be cartesian, cylindrical or spherical, depending on the symmetry of the treated problem. Since they are not physical domains, they should be placed at the outer boundaries of the simulation cell, and ideally in the far field. An efficient discretization of the PML is needed to accomplish the mathematical formulation above. Figures. 2.16(b) and (c) show examples of properly meshed PMLs, for spherical and cylindrical simulation cells. The maximum width of the layer must be equal to the operating wavelength, at least with five elements fitted within. The optimal performance is obtained by dividing the domain in parallel sub-layers with decreasing size with the distance towards the interface with the simulation domain. Close-up in Fig. 2.16(d) shows an example of this procedure. Since PMLs add extra degrees of freedom to the FEM resolution, it is recommendable to increase the element size as the radiation is expected to vanish across the layer.

2.5. Semianalytical methods.

2.5.1. Coupled mode theory.

In this section, we complement the finite element approaches explained so far with semi-analytical methods that provides insight into the results obtained by pure numerical procedures, much in the same way that has occured traditionally in macroscopic laser systems [140]. We introduce here a framework that belongs to a family of very general methods called temporal coupled-mode theories [142–145], that mathematically correspond to time-dependent first-order perturbation theory, much in the same way that is performed, for example, in the scattering theory of quantum mechanics [146]. The application of the ideas here presented is widely extended in photonic crystals, both in the linear [147, 148] and in the non-linear regime [149–154]. Coupled-mode theory relies on the following assumptions [23]:

- Conservation of energy.
- Weak coupling to the perturbed system.
- Time-invariance of materials/geometry.

In coupled-mode theory, we suppose that there exists some isolated system whose solution is known, and couple it weakly to some environment, thus perturbing the system.

We next calculate this response, by assuming an isolated optical nanocavity sustaining a single electromagnetic mode. In this case, it is known that the electromagnetic energy density stored will decay in an exponential fashion with a decay rate τ_{cav} characteristic of the cavity:

$$\frac{\partial u\left(\mathbf{r},t\right)}{\partial t}=-\frac{u\left(\mathbf{r},t\right)}{\tau_{cav}} \tag{2.159}$$

Now, we calculate the effect of a small perturbation in this system, by introducing a small electric current $\delta\mathbf{J}$ inside the Maxwell equations (2.1)-(2.4). In this case, we can use the Poynting theorem to show the change in the energy density produced by this perturbation. By assuming that the change produced in the electromagnetic field is, to first order, such that: $\mathbf{E}\rightarrow\mathbf{E}+\delta\mathbf{E}$ and $\mathbf{H}\rightarrow\mathbf{H}+\delta\mathbf{H}$, the power per unit volume supplied by the current is found to be [141]:

$$P_{in}=-\frac{1}{2}\mathrm{Re}\left\{\mathbf{E}^{*}\left(\mathbf{r},\mathbf{t}\right)\cdot\delta\mathbf{J}\left(\mathbf{r},\mathbf{t}\right)\right\} \tag{2.160}$$

Therefore, if we assume that the perturbing current is related to some induced polarization: $\delta\mathbf{J}=\partial_{t}\mathbf{P}$, we conclude that, to first order, the rate of change of the electromagnetic energy density of the perturbed system is given by:

$$\frac{du\left(\mathbf{r},t\right)}{dt}=-\frac{u\left(\mathbf{r},t\right)}{\tau_{cav}}-\frac{1}{2}\mathrm{Re}\left\{\mathbf{E}^{*}\left(\mathbf{r},\mathbf{t}\right)\cdot\frac{\partial\mathbf{P}\left(\mathbf{r},\mathbf{t}\right)}{\partial\mathbf{t}}\right\} \tag{2.161}$$

This is a very general, first order-perturbation theory expression that depends on both space and time. We next make some assumptions to implement a spatially-averaged formulation that enables to obtain analytical expressions to model plasmonic lasing systems in the optical linear regime. First of all, we normalize the single-mode profile sustained by the cavity. We separate the space and time dependences by defining the electric field distribution $\mathbf{E}_{0}(\mathbf{r})$ and the slowly-varying complex amplitude $a(t)$ as follows:

$$\mathbf{E}(\mathbf{r},t)=\frac{\mathbf{E}_{0}(\mathbf{r})}{\sqrt{\int_{V}d^{3}\mathbf{r}\epsilon_{0}\epsilon(\mathbf{r})|\mathbf{E}_{0}(\mathbf{r})|^{2}}}a(t)e^{-i\omega_{e}t} \tag{2.162}$$

where $\mathbf{E}(\mathbf{r},t)$ is the electric field of the cavity-mode, $\epsilon(\mathbf{r})$ is the relative permittivity, ω_{e} is the resonant frequency, and V is the volume of the cavity. Moreover, we normalize the electric field distribution such that:

$$\int_V d^3\mathbf{r}\epsilon_0\epsilon(\mathbf{r})|\mathbf{E}_0(\mathbf{r})|^2 = 1 \tag{2.163}$$

We also note that for dielectric materials in the optical linear regime, the total electromagnetic energy density is related to the electric energy density by: $u(\mathbf{r},t) = 2u_E(\mathbf{r},t) = \epsilon_0\epsilon(\mathbf{r})|\mathbf{E}(\mathbf{r},t)|^2$. Therefore, the total energy stored inside the resonant mode is given by:

$$\int_V d^3\mathbf{r}u(\mathbf{r},t) = |a(t)|^2 \tag{2.164}$$

Furthermore, we will assume that the perturbing polarization $\mathbf{P}(\mathbf{r},t)$ is given by the local response of the active medium, acting on the single cavity mode sustained by the passive cavity. In a similar fashion, we introduce the following expansion for the polarization:

$$\mathbf{P}\left(\mathbf{r},t\right) = \mathbf{E}_0\left(\mathbf{r}\right)P(t)\exp\left(-i\omega_e t\right) \tag{2.165}$$

Hence, integrating the equation (2.161) over the whole simulation domain and introducing the definitions (2.162) and (2.165), with the considerations (2.163) and (2.164), we find a spatially-averaged formulation of the first-order of perturbation theory equation above:

$$\frac{da(t)}{dt} = -\left(\frac{1}{\tau_{rad}} + \frac{1}{\tau_{nr}}\right)a(t) + \xi_1\left[i\omega_e P(t) - \frac{dP(t)}{dt}\right], \tag{2.166}$$

where we have separated the losses of the cavity into radiative and dissipative contributions: $\tau_{cav} = \tau_{rad}^{-1} + \tau_{nr}^{-1}$. Here, the factor $\xi_1 = (1/2)\int_A d^3\mathbf{r}|\mathbf{E}_0\left(\mathbf{r}\right)|^2$ comes from the fact that the integration of the second term of (2.161) is performed only over the active medium, where the polarization $\mathbf{P}(\mathbf{r},t)$ is nonzero, accounting for the fraction of the cavity mode field distribution that overlaps with the gain medium and contributes to lasing. Therefore, we call this quantity the *confinement factor*.

Next, within our first-order of perturbation theory approach, we show that the expression for the coupling of the induced polarization in the gain medium to the external field (2.19) can be reduced to a first-order differential equation. By substituting (2.165) inside this equation, we find:

$$\mathbf{E}_0\left(\mathbf{r}\right)\left[\frac{d^2P}{dt^2} - \left(2i\omega + \Gamma_e\right)\frac{dP}{dt} - i\omega\Gamma_e P\right]e^{-i\omega_e t} = -\Delta N_e\left(\mathbf{r},t\right)K_e\mathbf{E}_0\left(\mathbf{r}\right)a(t)e^{-i\omega_e t} \tag{2.167}$$

And, by integrating over the whole volume of the system, we readily obtain:

$$\frac{d^2P}{dt^2} - (2i\omega + \Gamma_e)\frac{dP}{dt} - i\omega\Gamma_e P = -\langle \Delta N_e(t)\rangle K_e a(t) \tag{2.168}$$

where the spatial average performed over the population inversion is defined by projecting its profile onto the eigenmode field profile:

$$\langle \Delta N_e(t)\rangle = \frac{\int_A d^3\mathbf{r}|\mathbf{E}_0(\mathbf{r})|^2 \Delta N_e(\mathbf{r},t)}{\int_A d^3\mathbf{r}|\mathbf{E}_0(\mathbf{r})|^2} \tag{2.169}$$

We apply now two further approximations [61], namely:

- That the gain linewidth will be much smaller than its resonant wavelength, $\Gamma_e \ll \omega_e$, which in general is true, see [100] for some examples of dye molecules. Thus, the second term in (2.168) can be approximated as:

$$(2i\omega_e + \Gamma_e)\frac{dP}{dt} \simeq 2i\omega_e \frac{dP}{dt} \tag{2.170}$$

- We apply the so-called *Slowly-Varying Envelope Approximation*, which assumes that assume that the amplitude $P(t)$ varies signicantly in a time scale comparable to Γ_e^{-1}, but not for shorter times:

$$\frac{d^2P}{dt^2} \sim \Gamma_e^{-2} P \ll \omega_e \Gamma_e^{-1} P \sim \omega_e \frac{dP}{dt} \tag{2.171}$$

  The second derivative can then be dropped relative to the term which contains the first derivative.

With these approximations, equation (2.168) is rewritten in the following form:

$$\frac{dP}{dt} + \frac{\Gamma_e}{2}P = -i\frac{K_e}{2\omega_e}\langle \Delta N_e(t)\rangle a(t) \tag{2.172}$$

Finally, we adapt the set of expressions that govern the population densities of the quantum levels of the molecules to the coupled-mode theory formulation. We perform spatial averages over the population densities from the rate equations (2.23)-(2.26) in the form dictated by (2.169), finding:

$$\frac{d\langle N_3(t)\rangle}{dt} = R_p\langle N_0(t)\rangle - \frac{\langle N_3(t)\rangle}{\tau_{32}}, \tag{2.173}$$

$$\frac{d\langle N_2(t)\rangle}{dt} = \frac{\langle N_3(t)\rangle}{\tau_{32}} - \frac{\langle N_2(t)\rangle}{\tau_{21}} + \frac{\xi_2}{2\hbar}\mathrm{Re}\left\{a(t)\left[iP^*(t) + \frac{1}{\omega_e}\frac{dP^*(t)}{dt}\right]\right\}, \tag{2.174}$$

$$\frac{d\langle N_1(t)\rangle}{dt} = R_p\langle N_0(t)\rangle - \frac{\langle N_3(t)\rangle}{\tau_{32}} - \frac{\xi_2}{2\hbar}\mathrm{Re}\left\{a(t)\left[iP^*(t) + \frac{1}{\omega_e}\frac{dP^*(t)}{dt}\right]\right\}, \tag{2.175}$$

$$\frac{d\langle N_0(t)\rangle}{dt} = -R_p\langle N_0(t)\rangle + \frac{\langle N_1(t)\rangle}{\tau_{10}}, \tag{2.176}$$

where we define:

$$R_p = \frac{K_a}{2\hbar\omega_a\Gamma_a}\frac{\int_A d^3\mathbf{r}|\mathbf{E}_0(\mathbf{r})|^2|\mathbf{E}_a(\mathbf{r})|^2}{\int_A d^3\mathbf{r}|\mathbf{E}_0(\mathbf{r})|^2} \tag{2.177}$$

corresponding to the pump rate, calculated assuming $N_0 \gg N_3$ and a harmonic time-dependence of the polarization at the pump frequency: $\mathbf{P}_a(\mathbf{r},t) = \mathbf{P}_a(\mathbf{r})\exp(-i\omega_a t)$, and using equation (2.19) to relate it to $\mathbf{E}_a(\mathbf{r},t)$. The pump field distribution is calculated by frequency-domain FEM simulations in the optical linear regime.
The factor ξ_2 in the equations (2.174) and (2.175):

$$\xi_2 = \frac{\int_A d^3\mathbf{r}|\mathbf{E}_0(\mathbf{r})|^4}{\int_A d^3\mathbf{r}|\mathbf{E}_0(\mathbf{r})|^2} \tag{2.178}$$

comes from averaging on the stimulated-emission terms, and account for the spatial inhomogeneity dictated by the population inversion distribution. Hence, we name it the *spatial hole-burning factor*.
We next illustrate how to use the set of semianalytical equations (2.166),(2.172) and (2.173)-(2.176) to obtain a derivation of the slope-efficiency and the lasing threshold. If we assume that the system has reached equilibrium in a steady-state for $t \to \infty$, the time-derivative can be set to zero in the equation (2.172), and polarization amplitude gets reduced to:

$$P_{sdst} = \frac{-iK_e}{\omega_e\Gamma_e}a_{sdst}\langle\Delta N\rangle_{sdst} \tag{2.179}$$

where the subscript *sdst* will be used to account for the steady state variables from now on. Equivalently, by setting the time-derivative to zero in the equation (2.166) that

drives the electric field amplitude $a(t)$ and using (2.179), we obtain:

$$\left(-\frac{1}{\tau_{tot}}+\xi_1\frac{K_e}{\Gamma_e}\langle\Delta N\rangle_{sdst}\right)a_{sdst}=0 \tag{2.180}$$

This expression has two possible solutions. One of them is the trivial case $a_{sdst}=0$, which corresponds with the behaviour below threshold, within this simplified model. The other enforces the bracket to be zero. If we look carefully, we see that the terms inside this bracket balance the losses, enclosed in the cavity decay time τ_{tot}, with the gain provided by the population inversion, when the lasing threshold has been reached. We obtain for the steady-state population inversion:

$$\langle\Delta N\rangle_{sdst}=\frac{\Gamma_e}{\xi_1 K_e\tau_{tot}} \tag{2.181}$$

Next, we set the derivatives from the rate equations can be set to zero. By substracting Eq. (2.175) from (2.174), we find:

$$\frac{\xi_2}{\hbar}\left[\mathrm{Re}\left\{ia_{sdst}P^*_{sdst}\right\}\right]+\frac{\langle N_3\rangle_{sdst}}{\tau_{32}}-\frac{2\langle N_2\rangle_{sdst}}{\tau_{21}}+\frac{\langle N_1\rangle_{sdst}}{\tau_{10}}=0 \tag{2.182}$$

where the subscript a_{sdst}, P_{sdst}, and $\langle N_i\rangle$, $i=0,\ldots,3$; account for the time-dependent amplitudes and the population densities in the steady state. By adding and substracting the term $2\langle N_1\rangle_{sdst}/\tau_{21}$, the population inversion ΔN enters in this expression:

$$\frac{\xi_2}{\hbar}\left[\mathrm{Re}\left\{ia_{sdst}P^*_{sdst}\right\}\right]+\frac{\langle N_3\rangle_{sdst}}{\tau_{32}}-\frac{2\langle\Delta N\rangle_{sdst}}{\tau_{21}}+\langle N_1\rangle_{sdst}\left(\frac{1}{\tau_{10}}-\frac{2}{\tau_{21}}\right)=0 \tag{2.183}$$

It is straightforward to find that $\langle N_3\rangle_{sdst}=\tau_{32}R_pN_0$ from Eq. (2.173) and $\langle N_1\rangle_{sdst}=\tau_{10}R_pN_0$ from (2.176). Moreover, from setting the steady-state in Eq. (2.172), we obtain:

$$\mathrm{Re}\left\{ia_{sdst}P^*_{sdst}\right\}=-\frac{K_e}{\omega_e\Gamma_e}|a_{sdst}|^2\langle\Delta N\rangle_{sdst} \tag{2.184}$$

Using all this information and inserting (2.184) inside (2.183) yields:

$$\frac{1}{\hbar}\xi_2\frac{K_e}{\omega_e\Gamma_e}|a_{sdst}|^2\langle\Delta N\rangle_{sdst}-\frac{2\langle\Delta N\rangle_{sdst}}{\tau_{21}}+2R_pN_0\left(1-\frac{\tau_{10}}{\tau_{21}}\right)=0 \tag{2.185}$$

Finally, using (2.181) and doing some algebra yields:

$$|a_{sdst}|^2 = \hbar\omega_e \left\{ 2N_0\tau_{tot} \left(\frac{\xi_1}{\xi_2}\right) \left(1 - \frac{\tau_{10}}{\tau_{21}}\right) R_p - \frac{2\Gamma_e}{\tau_{21}\xi_2 K_e} \right\} \tag{2.186}$$

which is an expression that accounts for the linear trend followed by the electric field intensity beyond some threshold value R_p^{th}, obtained by setting $\left|a_{sdst}(R_p^{th})\right|^2 = 0$:

$$R_p^{th} = \frac{\Gamma_e}{\tau_{21}\xi_2 K_e N_0 \tau_{tot}} \left(\frac{\xi_2}{\xi_1}\right) \left(1 - \frac{\tau_{10}}{\tau_{21}}\right)^{-1} \tag{2.187}$$

and the slope efficiency can be easily identified as:

$$S.E. = 2\hbar\omega_e N_0 \tau_{tot} \left(\frac{\xi_1}{\xi_2}\right) \left(1 - \frac{\tau_{10}}{\tau_{21}}\right) \tag{2.188}$$

Note that this description rely on three parameters obtained from frequency-domain FEM simulations in the linear optical regime. Namely, we can identify the confinement factor ξ_1, the spatial hole-burning factor ξ_2 and the $Q-$factor, accounting for the losses through the relation: $\tau_{tot} = Q/\omega_e$. The interplay of these quantities provides insight into the physical origin of lasing action, as a complement with the full-numerical time-domain simulations performed in previous sections. Indeed, we will combine both approaches to fully characterize laser light generation by the active devices proposed in Chapter 5.

2.5.2. Laser rate equation analysis.

As an alternative approach to the coupled-mode theory, we present a spatially averaged formulation of the rate equations that allow to obtain analytical expressions for the slope-efficiency and lasing threshold. Such description is often referred in the literature as laser rate equation analysis [16, 40, 155], not to confuse with the spatio-temporal dependent rate equations (2.23)-(2.26).

The Poynting theorem, accounting for the conservation of the electromagnetic energy density $U(\mathbf{r}, t)$ inside an optical cavity, can be written as a rate equation, so that the dissipative (or amplificative) contributions can be renormalized as effective rates which depend on the population inversion N, to measure the efficiency of the energy transfer to each decay channel [156]:

$$\frac{dS}{dt} = -\frac{S}{\tau_p} + \beta_{sp}\hat{R}_{sp}(N) + \hat{R}_{st}(N)S \tag{2.189}$$

where $S = (\hbar\omega_e)^{-1}\int_V d^3\mathbf{r}U(\mathbf{r},t)$ accounts for the photon number, β_{sp} is the $\beta-$factor modifying the spontaneous vacuum decay rate $\hat{R}_{sp}(N)$ inside the cavity, $\hat{R}_{st}(N)$ is the stimulated emission rate. The cavity lifetime τ_p can be related to the $Q-$factor of the cavity by the relation: $\tau_p = Q/\omega_e$, where $Q^{-1} = Q_{rad}^{-1} + Q_{nr}^{-1}$ accounts for both the radiative and dissipative losses.
Similarly, a conventionally used rate equation for the spatially-averaged population inversion is [140]:

$$\frac{dN}{dt} = \hat{R}_{pump} - \hat{R}_{nr}(N) - \hat{R}_{sp}(N) - \hat{R}_{st}(N)S \tag{2.190}$$

where $\hat{R}_{pump}$ is the pump rate and $\hat{R}_{nr}$ accounts for the population decay rate by non-radiative processes.
If the expressions (2.189) and (2.190) are divided by the volume of the cavity V, one can obtain their counterparts for the photon density s and the population inversion density dividing by the volume of the active medium V_a:

$$\frac{dn}{dt} = R_{pump} - R_{nr}(n) - R_{sp}(n) - R_{st}(n)s \tag{2.191}$$

$$\frac{ds}{dt} = -\frac{s}{\tau_p} + \Gamma\beta_{sp}R_{sp}(n) + \Gamma R_{st}(n)s \tag{2.192}$$

where $\Gamma = V_a/V_{eff}$ is a confinement factor and V_{eff} is the modal volume. Following [157], the Γ can be calculating in terms of energy confinement:

$$\Gamma = \frac{\int_{V_a} d^3\mathbf{r}\left[\epsilon_g(\mathbf{r},\omega) + \epsilon_R(\mathbf{r},\omega)\right]\left|\tilde{\mathbf{E}}(\mathbf{r})\right|^2}{\int_V d^3\mathbf{r}\left[\epsilon_g(\mathbf{r},\omega) + \epsilon_R(\mathbf{r},\omega)\right]\left|\tilde{\mathbf{E}}(\mathbf{r})\right|^2} \tag{2.193}$$

where ϵ_R is the real part of the relative permittivity and ϵ_g is the relative part of the group permittivity, given by: $\epsilon_g = \partial[\omega\epsilon_R]/\partial\omega$. The field amplitude $\tilde{\mathbf{E}}(\mathbf{r})$ is defined such: $\mathbf{E}(\mathbf{r},t) = \mathrm{Re}\{\tilde{\mathbf{E}}(\mathbf{r})e^{-i\omega t}\}$, normalized as a single photon field.
Equations (2.191) and (2.192) constitute a set of commonly used rate equations [157] that we now adapt for the different situations examined in this manuscript.

Slope-efficiency and lasing threshold in dye lasers.

We next use the derived rate equations to obtain a slope-efficiency and a lasing threshold that can be used to compare to the exact time-dependent FEM simulations. This approach is alternative to that followed by the coupled-mode theory.
For laser media based in dye molecules solutions, we neglect the coupling of spontaneous emission to the cavity mode ($\beta_{sp} = 0$), and set the non-radiative decay rate from expressions (2.189) and (2.190) as: $\hat{R}_{nr} = N/\tau_{21}^{nr}$. Moreover, we follow the approach from [158] and define the stimulated-emission rate as $\hat{R}_{stim} = \Gamma v_g \zeta g$, with $g = \sigma_e N/V_a$, where v_g is the material group velocity: $v_g = c/n_g$ with $n_g = \partial(\omega n_a')/\partial\omega$, where n_a' is the refractive index of the active medium. ζ is called the *spatial hole burning factor*:

$$\zeta = \frac{\int_{V_a} d^3\mathbf{r}\Delta N\left(\mathbf{r},t\right)\left|\mathbf{E}\left(\mathbf{r},t\right)\right|^2}{\left[V_a^{-1}\int_{V_a} d^3\mathbf{r}\Delta N\left(\mathbf{r},t\right)\right]\times\left[\int_{V_a} d^3\mathbf{r}|\mathbf{E}\left(\mathbf{r},t\right)|^2\right]} \tag{2.194}$$

By setting $dN/dt = 0$, N can be obtained as a function of S from (2.190):

$$N = \frac{R_{pump}}{(\tau_{21}^{nr})^{-1} + \left(\dfrac{\Gamma v_g \zeta \sigma_e}{V_a}\right) S},$$

Similarly, considering $dS/dt = 0$ and substituting N in eq. (2.189), we find:

$$\frac{\omega_e}{Q} = \frac{\Gamma v_g \zeta \sigma_e}{V_a} \frac{\hat{R}_{pump}}{(\tau_{21}^{nr})^{-1} + \left(\dfrac{\Gamma v_g \zeta \sigma_e}{V_a}\right) S}. \tag{2.195}$$

and rewritting this expression as a function $S = S(\hat{R}_{pump})$:

$$S\left(\hat{R}_{pump}\right) = \left(\frac{Q}{\omega_e}\right)\hat{R}_{pump} - \left(\frac{V_a}{\Gamma v_g \zeta \sigma_e \tau_{21}^{nr}}\right), \tag{2.196}$$

where a linear dependence is found. Slope efficiency (SE) and lasing threshold can then be readily obtained by fixing $S(\hat{R}_{pump}^{th}) = 0$:

$$\mathrm{SE} = \frac{Q}{\omega_e} \quad ; \quad \hat{R}_{pump}^{th} = \frac{\omega_e V_a}{Q\Gamma v_g \zeta \sigma_e \tau_{21}^{nr}}. \tag{2.197}$$

The pump rate introduced in this relation is calculated directly from the FEM time-

domain simulations, by the relation: $R_p = (\hbar\omega_a)^{-1}\int_{V_{gain}}\langle\partial_t\mathbf{P}_a\cdot\mathbf{E}_a\rangle$.
We will apply these expressions in Chapter 4 to compare with our numerical results.

Rate equation approach for semiconductors

We have restricted our modeling to lasing action with dye molecules acting as a gain medium. However, it is also possible to model lasing action linearly in semiconducting materials [16, 140]. We extend the above formalism to the case $\beta_{sp} > 0$ accounting for coupling of the spontaneous emission to a single cavity mode. Moreover, we use the following expressions for the pump, non-radiative, stimulated and spontaneous decay rates that appear in the governing equations (2.191) and (2.192):

$$R_{pump} = \eta_p\frac{P}{\hbar\omega_a V_a};\quad R_{nr}(n) = \frac{n}{\tau_{nr}} + Cn^3;\quad R_{sp}(n) = \frac{n}{\tau_{sp}};\quad R_{st}(n) = v_g g(n)$$

where η_p is the pumping efficiency and P is the pump power. The parameters C and τ_{nr} are the non-radiative recombination lifetime and the Auger recombination coefficient, respectively, of the gain medium. $g(n)$ is a logarithmic gain function, given by:

$$g(n) = g_0\ln\left(\frac{N+N_s}{N_{tr}+N_s}\right) \tag{2.198}$$

where g_0 N_s and N_{tr} are material-dependent parameters of the gain medium.
For the purposes of this thesis, we will model a semiconducting nanowire whose facets provide the neccesary feedback to reach the lasing threshold. The photon lifetime inside this cavity is given by the round-trip oscillation condition of Fabry-Perot lasers:

$$\frac{1}{\tau_p} = v_g\left[\alpha_i + \frac{1}{2L_{NW}}\ln\left(\frac{1}{R^2}\right)\right] \tag{2.199}$$

where α_i is the propagation losses of the sustained mode, L_{NW} is the nanowire length and R is the reflection coefficient of the nanowire facets, obtained by frequency-domain FEM simulations.
By using these definitions and setting the derivatives to zero in equations (2.191) and (2.192), we can obtain again expressions to determine the ratio of the output laser power to the input pump power. Importantly, the obtained expressions allow to create a single-mode approach to model semiconductor lasers, including spontaneous emission. Moreover, this simple theory will allow to perform a fitting of parameters with data from an experimental setup, thus revealing the nature of lasing action in that system.

3 | Lasing action enabled by plasmonic waveguides.

3.1. Introduction.

Propagating plasmonic modes are collective oscillations of the electromagnetic field at a metal surface, that naturally guide light in the nanoscale. However, due to their evanescent nature, the confinement in subwavelength volumes also results in the decay of the electromagnetic energy in the direction of propagation. In other words, the dissipation losses associated to nanoscale confinement lead to a reduced propagation length, and possible applications face their greatest limitations in the visible and near-infrared regions of the electromagnetic spectrum, where the lifetimes of surface plasmon modes are remarkably low. This issue has stimulated a great deal of research in order to overcome the inherent absorption losses of metallic nanostructures supporting plasmonic modes, and thus improve their performance for emerging nanotechnologies.

Although the first experimental study of surface plasmon polariton (SPP) involving gain was reported more than 30 years ago [41], it has only recently been demonstrated that optical amplification in plasmonic waveguides, supporting long-range surface plasmons [52, 159, 160], is possible. Further studies have claimed partial loss-compensation under continuous wave pump excitation [161], but a direct measurement of the loss-compensation in a plasmonic waveguide has only been demonstrated in Ref. [53] so far. From the theory side, there is a strong interest in unveiling the fundamental processes that are involved in plasmon-polariton amplification in planar structures, and studies on the quenching of the used organic dye molecules close to metal surfaces, the effect of spontaneous emission, or noise, have been performed [163–165].

On a different note, some works have demonstrated hybrid systems combining nanowire lasers with plasmonic waveguides. These systems, commonly known as NW plasmon lasers [40, 86, 162], exhibit hybrid plasmonic modes that feature ultralow mode volumes.

The ever increasing demands for miniaturization of plasmonic devices yield the necessity of controlling the laser emission by means of new experimental, room-temperature configurations, as well as the ability of integrating these schemes in on-chip devices. Here, we present our theoretical contributions along these two breaking trends of nanolasers based on plasmonic waveguides. This Chapter is organized as follows: In Section 3.2, we review the main properties of the plasmonic waveguides supporting propagating subwavelength modes, which are of interest for amplification within an active scheme. Next, we study both the loss-compensation and lasing for thin metallic films based waveguides supporting long-range surface plasmons (Section 3.3). Finally, in Section 3.4 we will study laser light generation in a experimentally realistic configuration, consisting of a semiconducting nanowire able to couple its laser emission to the channel plasmon polaritons propagating in a V-Groove waveguide.

3.2. Optical properties of passive plasmonic waveguides.

As discussed in Chapter 1, a plasmonic laser cavity can be created by enclosing a plasmonic waveguide within an optical feedback mechanism, and incorporating a suitably chosen gain medium. It is thus convenient to introduce the optical properties of the passive plasmonic waveguides used to study lasing action, prior to the analysis of their amplification properties and lasing characteristics. In this section, we analyze the plasmonic modes sustained by such waveguides. In order to introduce the main concepts and terminology, we first describe surface plasmon polaritons (SPPs) propagating along single metallic surfaces. Next, we extend our analysis to the plasmonic modes (short-range, and long-range surface plasmons − SRSPPs and LRSPPs) arising at thin metallic films. Finally, we focus on channel plasmon polaritons (CPPs) propagating along the bottom of a V-Groove waveguide.

3.2.1. Surface plasmon-polariton on a flat metallic surface.

We begin by characterizing surface plasmon propagating modes in one of the simplest devices that can be imagined for guiding light at the nanoscale. A sketch of the system is depicted in the inset from Fig. 3.1, consisting of a single flat interface between a dielectric, lossless half space ($z > 0$) whose optical response is described by a real positive dielectric constant ϵ_2 and an adjacent metallic half space ($z < 0$) described with

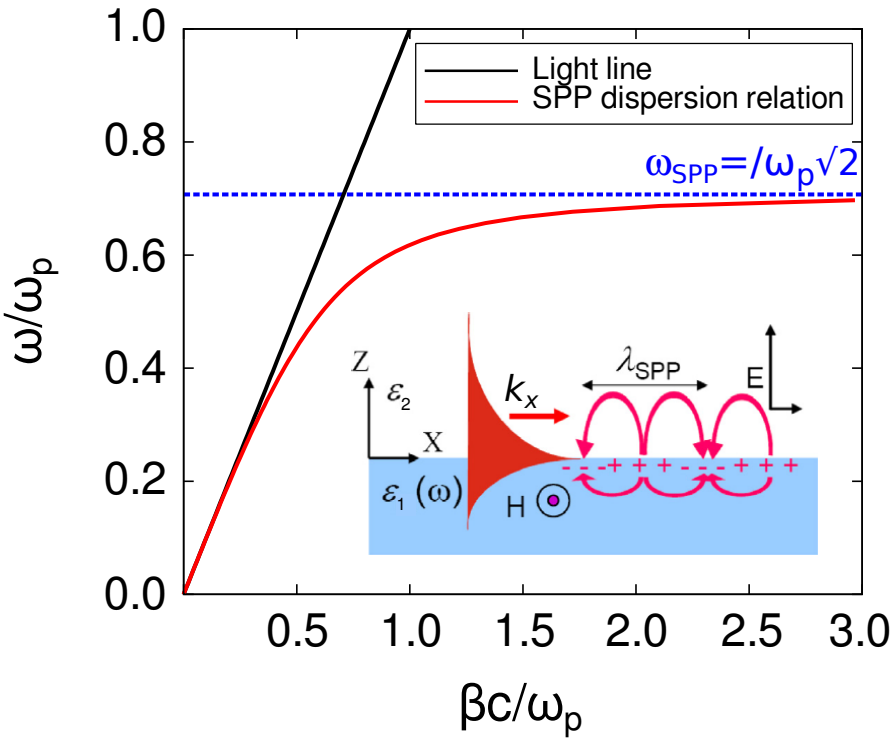

Figure 3.1: Dispersion relation of the SPP mode (red line), calculated for a silver/vacuum planar interface. Inset (adapted from [166]) sketches a schematic representation of a SPP propagating along a planar metallic waveguide.

a dielectric function $\epsilon_1(\omega)$.

Bound modes in this geometry can be obtained as solutions of the source-free homogeneous wave equation, which can be derived directly from Maxwell's equations:

$$\nabla \times \nabla \times \mathbf{E}(\mathbf{r},\omega) - \frac{\omega^2}{c^2}\epsilon(\mathbf{r},\omega) = 0 \tag{3.1}$$

The one-dimensional symmetry of this geometry already simplifies the problem such the spatial dependence of the permittivities is restricted to the $z-$direction: $\epsilon(\mathbf{r}) = \epsilon(z)$. Moreover, if the solutions are propagating waves in the $x-$direction, with an harmonic time-dependence, the electric field is reduced to: $\mathbf{E}(\mathbf{r},\omega) = \mathbf{E}(z)e^{-i\beta x}e^{-i\omega t}$, where β is a complex parameter called the *propagation constant*. With these considerations, equation (3.1) becomes:

$$\frac{\partial^2 \mathbf{E}(z)}{\partial z^2} + \left(k_0^2\epsilon - \beta^2\right)\mathbf{E} = 0 \tag{3.2}$$

Since we are interested in confined bound modes, we demand that the normal components of the wavevector are purely imaginary in both media, giving rise to exponentially decaying solutions away from the interface: $\mathbf{E}(z) = \mathbf{E}e^{-ik_i z}$, with $i = 1, 2$ denoting the different media and $\mathbf{E}$ is a constant vector. We arrive to the conclusion that for the desired solutions, all the EM field components have the same space and frequency dependence.

The symmetry of the problem allows for two sets of solutions to this equation, in terms of the different polarization properties of the propagating waves. The first set are the transverse magnetic (TM or p) modes, with the magnetic field pointing outside the plane of the page. Hence, only the field components E_x, E_z and H_y are nonzero. The second set is given by transverse electric (TE or s) modes, with nonzero H_x, H_z and E_y field components. We anticipate that only TM polarization yields bound solutions to the surface [32]. Henceforth, we will focus on TM solutions of the wave equation above.

In order to solve the expressions of the corresponding components of the EM field, some conditions must be met: first, boundary conditions must be imposed at the interface of the problem. Namely, continuity of both the H_z field and of the quantity $\epsilon_i E_z$ is demanded. Second, it can be shown that for the existence of a surface bound mode, the permittivities of the involved media must be related as follows [92]:

$$\epsilon_1(\omega) \cdot \epsilon_2 < 0 \tag{3.3}$$

$$\epsilon_1(\omega) + \epsilon_2 < 0 \tag{3.4}$$

Finally, the EM fields must accomplish the wave equation (3.2), leading to the following expressions:

$$k_i^2 = \beta^2 - k_0^2 \epsilon_i; \quad i = 1, 2 \tag{3.5}$$

If these criteria are fulfilled, we obtain the following expression for the component of the wavevector propagating along the interface:

$$\beta = k_0 \sqrt{\frac{\epsilon_1 \epsilon_2}{\epsilon_1 + \epsilon_2}} \tag{3.6}$$

Main panel from Fig. 3.1 (red line) depicts the modal frequency as a function of the

parallel wavevector given by (3.6): this is known as the *dispersion relation* of the surface plasmon polariton (SPP). For comparison, the dispersion relation of free-space radiation: $\omega = c\beta$ (the light line, black line) is addressed.
The functional dependence of the dispersion relation clearly shows two distinct regimes, depending on the value of β: For low values of the propagation constant, the dispersion relation of the SPP approaches the light line, which reveals the unlocalized nature of the plasmon in this limit. These plasmons are loosely confined to the metal surface, and are better known as Sommerfeld-Zenneck waves [167]. On the other hand, with increasing value of β, the dispersion relation bends apart from the light line, due to the departure from the pure light-like character of SPPs. At this point, the increase of the wavevector with respect to the light line, Δk_x, is caused by the fact that the mode is acquiring a light-matter mixed nature, and the additional wavevector is attributed to electrons being dragged by light as the SPP oscillations occur. This leads to a lowering of the group velocity of the mode: $v_g = \partial\omega/\partial k$. An important consequence of this behavior is that SPP modes cannot be excited by conventional $p-$polarized light, but by means of gratings or mirrors able to provide the matching with the same wavevector [168, 169]. For very high ω, a new regime is reached, characterized by the asymptotic limit at $\omega \to \omega_{SPP}$, with: $\omega_{SPP} = \omega_p/\sqrt{1+\epsilon_2}$, where ω_p is the plasma frequency of the metal. In this case, the wavevector tends to infinity as the frequency approaches ω_{SPP}, and the group velocity tends to zero: $v_g \to 0$.
In general, the propagating plasmonic modes can be characterized in terms of two key characteristics: the spatial field-confinement and the propagation length. An analysis on how these features evolve with increasing β is thus convenient. One of the main consequences of the evanescent inherent nature of the SPP modes is the fact that they confine light at the nanoscale, with maximum intensity at the interface between the media, and exponentially decaying away from it at a different rate depending on the dielectric response ϵ_i of each medium. A simple way to quantify the confinement is thus given by the penetration depth, defined as the distance at which the value of the maximum intensity falls to $1/e$:

$$\hat{z}_i = \frac{1}{|k_z^i|}; \qquad i = 1, 2. \tag{3.7}$$

In a similar fashion, we define the propagation length as follows:

$$L_p = (2\mathrm{Im}\{\beta\})^{-1} \tag{3.8}$$

Remarkably, the propagation length is directly connected to the confinement. From relation (3.5), it is apparent that an increase in the perpendicular wavevector (which in turn, results in improved confinement), leads to a higher value of the parallel wavevector (which decreases the propagation length L_p). Therefore, a tradeoff takes place between both quantities, since increased confinement leads to higher dissipative losses inside the metal and hence the SPP decays faster in the direction of propagation. In the context of the dispersion relation analysis above, the SPP modes show very poor confinement (of several wavelengths) for moderate values of the propagation constant β, but with a high propagation length, whereas they attain subwavelength confinement as the frequency converges to ω_{SPP}, with a limited propagation length. For instance, for a silver/air surface, we find $\hat{z}_2 = 180$ nm and $L_p = 16$ μm for free-space wavelength $\lambda_0 = 450$ nm, while for $\lambda_0 = 1.5$ μm, it is obtained $L_p = 1080$ μm and $\hat{z}_2 = 2.6$ μm [32].

3.2.2. Long-range SPP-based waveguides.

The semi-infinite flat metallic surface above displays propagation properties based uniquely on the optical properties inherent to the composition of the metal, and of the surrounding dielectric medium. Single surface SPPs may be excited and studied by means of different experimental configurations [42, 45], but their implementation and control for plasmonic circuitry remain elusive, partly due to their high inherent losses. In view of the current nanofabrication techniques, there is a natural interest in attaining plasmonic waveguiding structures whose confinement and propagation properties may be configured by tailoring the geometry instead of changing the composition for the same geometry. Therefore, as a natural step, we examine the subwavelength modes that arise when going from a single metallic interface to a thin metallic slab.

We next derive the conditions for the existence of surface modes confined at a metallic thin film which is considered infinite in the horizontal direction (see inset of 3.2(a)). In this case, the SPP modes supported at each interface of the slab couple with each other, altering the properties of bound modes from the single interface case. Namely, by imposing the boundary conditions as above, it is found the following trascendental equation that relates the propagating wavevector β with the free space frequency ω [32]:

$$e^{-k_m L} = \frac{k_m/\epsilon_m + k_h/\epsilon_h}{k_m/\epsilon_m - k_h/\epsilon_h} \tag{3.9}$$

where L is the thickness of the metallic film, k_m is the wavevector perpendicular to the

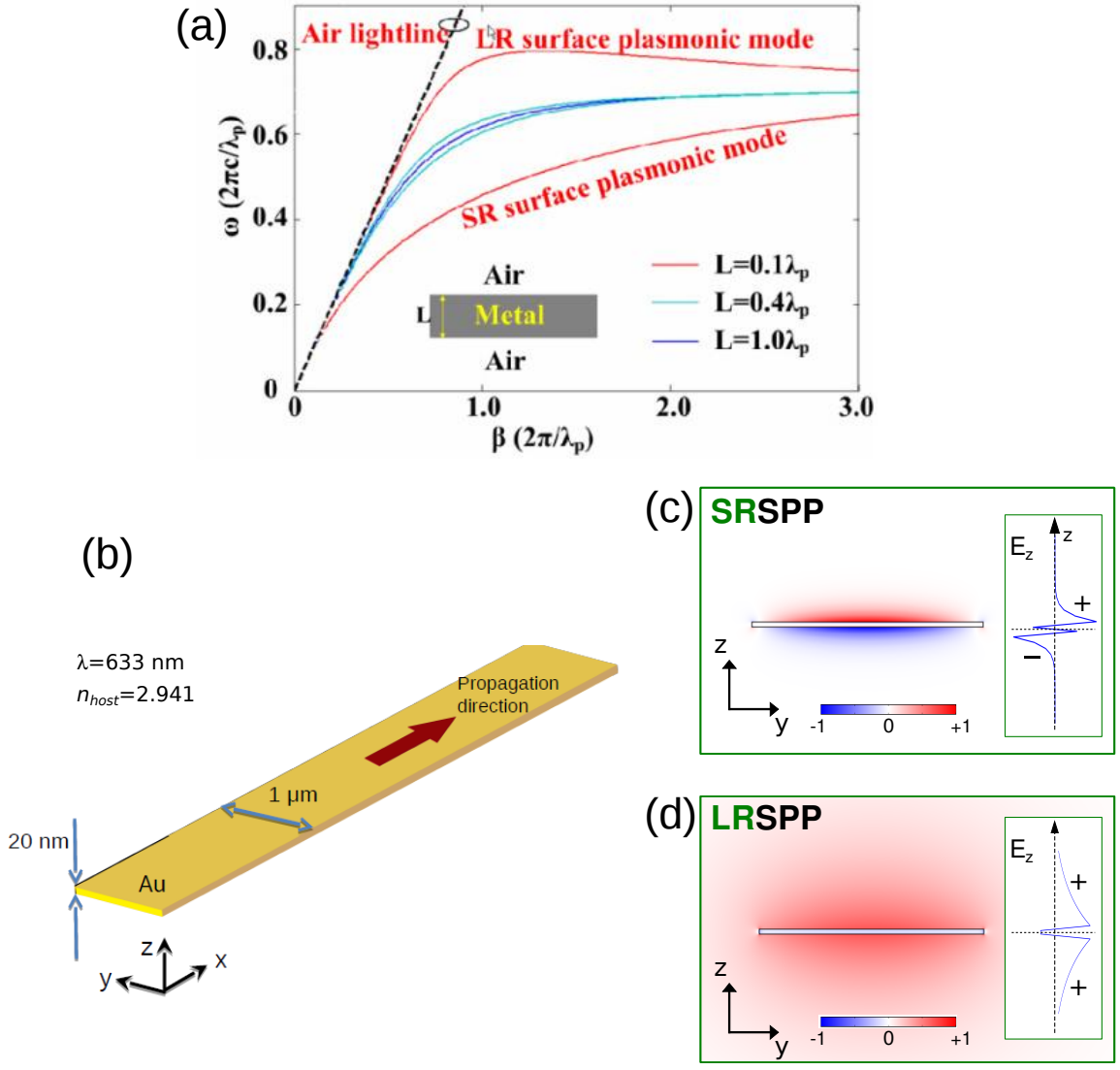

Figure 3.2: Characteristics of plasmonic waveguides based on thin metallic films. (a) Dispersion relation of long-range and short-range SPPs supported by infinitely wide metallic films embedded in air ($n_h = 1$), with increasing thickness $L = 0.1\lambda_p$ (red line), $L = 0.4\lambda_p$ (light blue line) and $L = 1.0\lambda_p$ (dark blue line), with $\lambda_p = 138$ nm (reprinted from Ref. [170]). (b) Geometry of the LRSPP based waveguide discussed in this text, consisting of a 21 nm-thick and 1 μm-wide gold slab, embedded in a dielectric medium with $n_h = 1.71$. Panels (c) and (d): Field distribution of the E_z-field component, of both the short-range surface plasmon polariton (SRSPP, panel (c)) and the long-range surface plasmon polariton (LRSPP, panel (d)), obtained from eigenmode calculations for the wavelength $\lambda = 633$ nm. Insets of these panels depict the real part of the E_z-field component cut vertically across the midpoint of the metallic slab.

surface in the metal domain, ϵ_m the permittivity of the metal, and k_h and ϵ_h are their counterparts for the non-absorbing dielectric host, respectively. This new dispersion relation can be splitted into the following pair of equations:

$$\tanh(k_m L/2) = -\frac{k_h \epsilon_m}{k_m \epsilon_h}; \qquad \tanh(k_m L/2) = -\frac{k_m \epsilon_h}{k_h \epsilon_m} \tag{3.10}$$

These two expressions reveal the existence of two bound modes with different propagation and confinement properties. The corresponding solutions are displayed in Fig. 3.2(a), for a waveguide embedded in air ($\epsilon_h = 1$). When compared with the single SPP-case, dispersion relation of one of the new bound modes lies closer to the light line. This points out to the fact that this mode is less confined than the SPP, leading to increased propagation length. For this reason, this mode is called *long range surface plasmon polariton* (LRSPP). Conversely, the remaining mode displays large wavevectors compared with the SPP. This means that the mode is tightly confined and also its propagation length is lower, due to increased dissipation losses within the metal. Thus, this mode is termed short-range surface plasmon polariton (SRSPP). It is shown that, for increasing length (ranging from $L = 0.1\lambda_p$ (red line) to $L = 1.0\lambda_p$ (dark blue line), with $\lambda_p = 138$ nm), the SPPs at each metallic surface decouple, converging again to the conventional dispersion relation for a single surface.

As a further step towards attaining active devices based on LRSPP, we focus on the waveguide depicted in Fig. 3.2(b), along with the reference system used. Such configuration has been recently used in experimental implementations to attain optical amplification [52, 53]. This system consists of a 21 nm-thick and 1 μm-wide metallic slab, embedded in a uniform dielectric host with refractive index $n_h = 1.71$, which sustains long-range and short-range SPPs propagating in the $x-$direction. As will be discussed later, the finite width of the waveguide is not expected to play a significant role, since the characteristic wavelength of the plasmon oscillation λ_{SPP} is expected to be lower than this width. Therefore, dispersion relations of the LRSPP and SRSPP modes in this new system conserve the main features presented in Fig. 3.2(a).

Figures 3.2(c) and (d) show the vertical E_z electric-field component associated to the SRSPP and the LRSPP mode, giving access to their respective symmetry properties. Namely, the LRSPP mode is characterized by a symmetric combination of the single-SPPs, with symmetry in the E_z and the H_y components and antisymmetric E_x component, describing a mode of even parity. On the other hand, the SRSPP mode is a mode of odd parity, with antisymmetric E_z and H_y components and symmetric E_x-component.

By means of eigenmode FEM calculations, we found for the waveguide from Fig. 3.2(b), that the LRSPP displays a propagation length of $L_p \simeq 40$ μm and modal area of $A_m \simeq \lambda^2/2$, while for the SRSPP it was found $L_p \simeq 0.3$ μm and $A_m \simeq \lambda^2/32$.

3.2.3. V-Groove waveguides.

The waveguides analyzed so far display confinement in the vertical direction, due to the evanescent nature of plasmonic modes. As a response to the ever increasing demands of miniaturization, there is interest in attaining confinement also in the transversal plane of polarization. V-Groove waveguides represent ideal candidates for the propagation of light at deep subwavelength scales, featuring low damping and robustness of the mode properties against channel bending [171]. V-Grooves support a special type of plasmonic propagating modes termed channel plasmon polaritons (CPPs) [172]. These modes, tightly confined at the bottom of the V-Groove structures, show very low mode volumes and have found implementation in multiple devices as Y-splitters, Mach–Zehnder interferometers and waveguide–ring resonators, [173] mainly at telecommunication wavelengths [174].

Here we review the main properties of the CPP modes, arising in an experimentally feasible [175] V-Groove shaped waveguide carved on a flat gold (Au) surface. A schematic sketch of the cross-section is depicted in Fig. 3.3(a). Main panel from Figure 3.3 shows the dispersion relation calculated by means of eigenmode FEM calculations for such a structure embedded in air. As it is characteristic for a plasmonic mode, for high values of the parallel wavevector k_x, the mode departs from the light line, attaining subwavelength confinement. This is clearly demonstrated in Fig. 3.3(c) for $\lambda = 700$ nm, showing a cross section of the waveguide, for which the field intensity is concentrated at the V-Groove bottom with a very low mode-volume. The CPP is polarized (primarily) parallel to the sample surface (electric field lines at the inset of Figure 3.3(c)), and combines strong EM field confinements (modal lateral size and area of 538 nm and 0.067 μm^2, respectively) with good propagation characteristics (19.96 μm at 870 nm).

For low values of the parallel wavevector k_x, the mode lies close to the light line, and the EM fields get delocalized. This is shown in Fig. 3.3(b)) for the wavelength $\lambda = 950$ nm, at which the mode is also hybridizing with modes emerging at the sharp corners of the metallic surface. These modes, termed wedge plasmon polaritons (WPPs), have their own interest for waveguiding [176], with very high propagation lengths as well as confinement properties due to the hot spots present at these corners, but will not be further discussed in this manuscript.

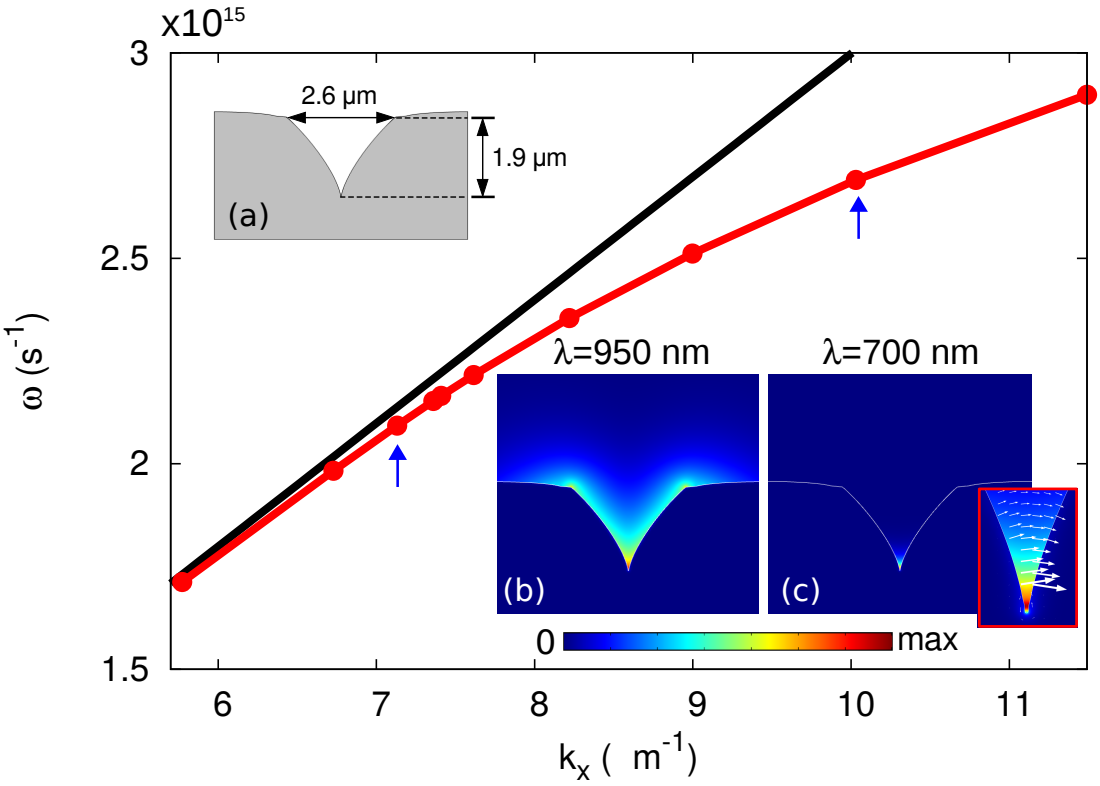

Figure 3.3: Dispersion relation of V-groove waveguides (red points) departing from the light line (black line). (a) Schematic representation of the V-Groove cross-section, with its characteristic geometrical parameters. Panels (b),(c) show the field amplitude norm $|E|$ obtained from eigenmode calculations, for wavelength values of (b) $\lambda = 950$ nm and (c) $\lambda = 700$ nm (the position of the corresponding wavelengths is pinpointed in the dispersion line with blue arrows). Inset from panel (c) shows a close-up of the $E-$field amplitude norm at the VG-bottom, with white arrows depicting the magnitude and direction of the transversal $E-$field.

3.3. Loss compensation and lasing in LRSPP waveguides.

The unique properties displayed by LRSPP waveguides above has motivated much research work in their implementation for active plasmonic devices. As already was indicated, the LRSPP modes display very low propagation losses, as compared with other plasmonic modes. In addition, the decay rate of these modes to spontaneous emission (the $\beta-$factor) of a generic dipolar gain medium is extremely low [164]. Finally, the current nanofabrication techniques are refined enough to produce LRSPP-based on-chip

devices for their integration in nanophotonic circuits. All these features, together with the inherent ability of plasmonic modes to confine light at the nanoscale make these devices suitable for implementing amplifiers and low-threshold nanolasers based on LR-SPP propagating modes. Applications of these ideas would lead to refined biosensors [177], as well as allow for practical combination with the rest of the existing passive optical components, as can be four-port couplers, Y-junctions, bandgap structures or Mach-Zender interferometers [49, 50].

The interest on this class of active waveguiding schemes has been manifested through a number of experiments, displaying optical amplification of the LRSPP modes by incorporating an optically pumped dipolar gain medium [52]. More recently, complete loss-compensation has been directly observed in thin gold stripes covered with a layer of organic gain medium [53]. In this section, we present an extensive study of this class of active subwavelength systems, within the experimental conditions of this reference, showing that lasing action can be obtained in this class of devices.

Figure 3.4(a) presents a possible realization of the LRSPP-based active waveguide. A 21-nm thick gold (Au) and 1 μm-wide slab is simulated, covered by a layer of gain material of thickness t inside a homogeneous dielectric environment with refractive index $n_h = 1.71$. The selected gain medium is the organic laser dye molecules DCM (4-dicyanomethylene-2-methyl-6-(p-dimethylaminostyryl)-4H-pyran), dispersed in a Alq_3 (tris (8 - hydroxy - quinolinato) aluminum) matrix (see Fig. 3.4(b)). This active medium is based on Förster energy transfer from a wide optical host to a narrow gap guest, which find numerous advantages from the single-component organic dyes [178–181]. Namely, the emission band is substantially redshifted from the host absorption spectrum in materials with Förster transfer (see Fig. 3.4(c)), causing absorption loss at the emission wavelengths to be minimized. Also as a consequence, the absorbance of the host is very high.

3.3.1. Semiclassical formalism.

In order to treat the active configuration of the LRSPP waveguides introduced above with non-linear time-dependent numerical framework from Chapter 2, it is necessary to introduce some modifications in the rate equations describing the population dynamics, to account for more general type of laser media. Moreover, in order to introduce the necessary feedback to create a laser cavity, a partially-reflecting boundary condition must be properly formulated at the ends of the waveguide. We next provide details on the first issue, and leave the latter for the Appendix A.

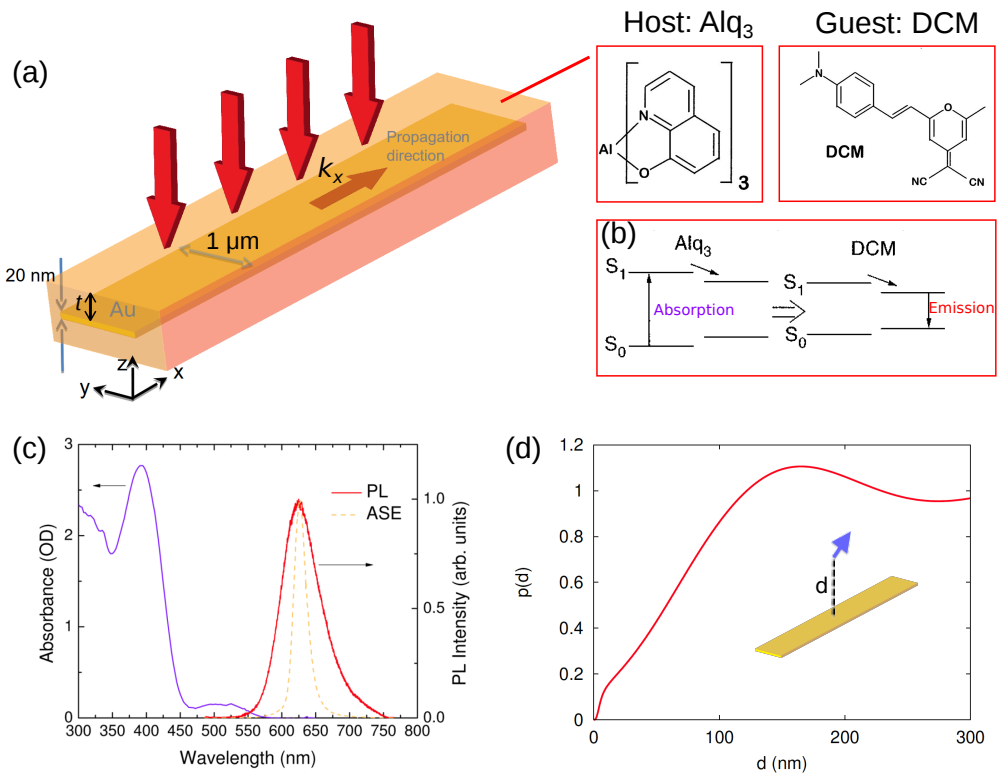

Figure 3.4: (a) Active plasmonic waveguide supporting LRSPP modes, consisting of a gold metal stripe embedded in Alq_3:DCM laser medium. The geometrical parameters have been selected according reference [53]. (b) Schematic representation of the energy levels of the host-guest gain medium connected by FRET. (c) Absorbance (purple line), accounting for the spectral distribution of absorption, and photoluminiscence (red line), representative of the spectral gain, for the organic dye laser medium Alq_3:DCM. (Reprinted from [53]). (d) Spatial dependence of the radiative lifetime on the vertical distance d above the metallic surface, calculated for a 2D thin film.

Rate equations

Organic molecules (DCM) embedded in an host (Alq_3) are used as gain medium. The system is pumped at a wavelength $\lambda_{pump} = 355$ nm, which lies within the optical gap of the host system (see purple line in Fig 3.4(c)), and the guest molecules are subsequently excited via Förster energy transfer. The experimental results [53] show that gain saturation in this system is mainly caused a bimolecular annihilation mechanism. A simple set of rate equations, that enables to accurately describe the dynamics of the gain medium, is given by:

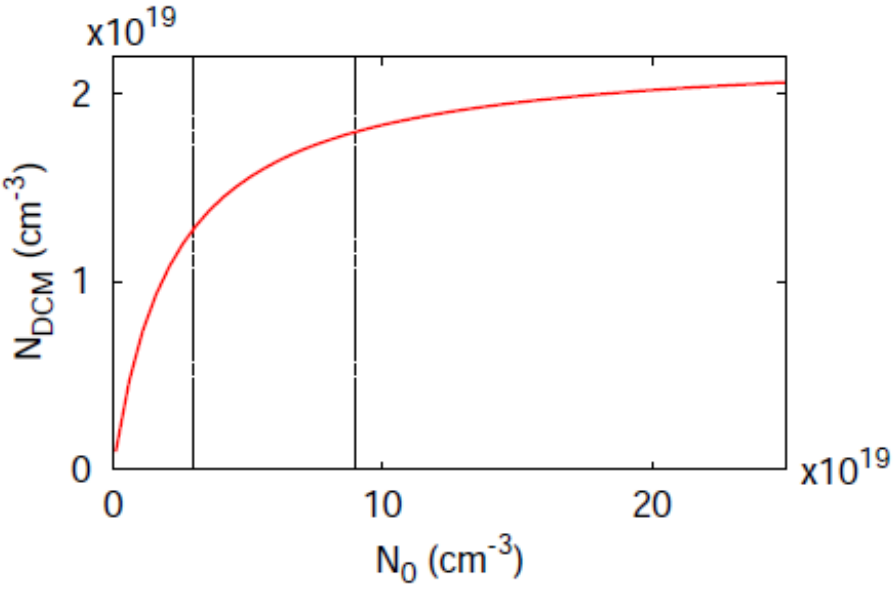

Figure 3.5: Density of excited organic molecules as function of the total molecule density, obtained by calculating the steady state of the rate equations for a pump strength well above the saturation level. The dashed lines mark the two densities used in the simulations. For high densities, the number of active molecules saturates owing to quenching.

$$\partial_t N_{Alq} = G - \frac{N_{Alq}}{\tau_{Alq}} - k_t N_{Alq} \tag{3.11}$$

$$\partial_t N_{DCM} = k_t N_{Alq} - \frac{N_{DCM}}{\tau_{DCM}} - k_{an} N_{Alq} N_{DCM} + \frac{1}{2\hbar\omega}\mathrm{Re}\left(\partial_t \mathbf{P} \cdot \mathbf{E}^*\right) \tag{3.12}$$

where N_{Alq} and N_{DCM} are the densities of excited Alq and DCM-molecules, respectively. The lifetimes of the host-guest system are $\tau_{Alq} = 16$ ns and $\tau_{DCM} = p(z)$ ns [53]. The Purcell effect is included through an explicit dependence of τ_{DCM} on the distance to the waveguide, by considering the waveguide as an infinitely wide thin metallic film. In this approximation, small modifications of the radiative lifetime owing to the waveguide edges are neglected. Close to the metallic surfaces, this lifetime is calculated using a method presented in Ref. [182]. For illustration, the resulting Purcell-factor calculated for a 21 nm-thick silver film is shown in Figure 3.4(d).

The additional parameters in Eqs. (3.11) and (3.12) are the annihilation rate $k_{an} = 8 \times 10^{-14}$ m^3·s^{-1} and the Förster transfer rate $k_t = 1.8 \times 10^{12}$ s$^{-1}\frac{N_0 - N_{DCM}}{N_0}$, conveniently fitted to the experimental values. In particular, the value of k_t is calculated for a value of the density of DCM-molecules $N_0 = 3 \times 10^{25}$ m^{-3}.

The pump rate G depends on the pump field (i.e., the space and time dependent electric

field distribution $\mathbf{E}_{pump}(\mathbf{r},t)$ created at the pump frequency $\omega_p = \omega_a = 2\pi c/\lambda_p$), and is written as follows:

$$G(\mathbf{r},t) = \frac{1}{2\hbar\omega_{pump}} c\epsilon_0 \alpha n_h \left|\mathbf{E}_{pump}(\mathbf{r},t)\right|^2 \tag{3.13}$$

where the absorption coefficient is $\alpha = 3.11 \times 10^6$ m^{-1} and the refractive index of the host is $n_h = 1.71$.
The polarization density $\mathbf{P}$ is driven by the plasmonic electric field, in an analogous form to Eq. (2.19):

$$\frac{\partial^2 \mathbf{P}}{\partial t^2} + 2\gamma \frac{\partial \mathbf{P}}{\partial t} + \omega_e^2 \mathbf{P} = -K_e N_{DCM} \mathbf{E} \tag{3.14}$$

where K_e is the coupling strength, given by:

$$K_e = 2\sigma\epsilon_0 c n_h \gamma \tag{3.15}$$

with $\sigma = 2.76 \times 10^{-20}$ m^{-2}, and $\gamma = 5 \times 10^{13}$ s^{-1}.
Finally, the last term in Eq. (3.12), which describes depopulation of the excited DCM-state due to stimulated emission is averaged over one period of the emission frequency ω_e of the DCM molecules.
This model of the gain dynamics can reproduce the quenching responsible for the reduction of available gain with increasing DCM molecules density. This fact is evidenced by fixing the time-derivatives to zero in the rate equations (3.11) and (3.12), and calculating the resulting steady-state density of excited organic molecules with the total density, for a pump rate well above the saturation level, and in absence of stimulated emission. Figure 3.5 shows the resulting dependence of the density of excited organic molecules as a function of the total density (solid red line), and black dashed lines pinpoint the values of the density used in this section. It is found that the density of excited molecules saturates as a function of the total density, and so does the gain. Hence, an increment of the density of organic molecules above the concentration used in our simulations, would not result in a significant further increase of the effective gain.
The set of rate equations described above does not account for the excitation of long-lifetime triplet states, which may prevent continuous-wave gain. Although some strategies of how to achieve continuous-gain gain in the used gain medium have been demonstrated [183, 184], we have restricted our simulation time to less than 5 ns, when the

effects of the triplet states are not still present.

3.3.2. Loss compensation in LRSPP-based waveguides.

In order to create a laser cavity based on a plasmonic waveguide, two elements must be combined: loss-compensation enabled by the gain medium, and an optical feedback mechanism enclosing the resonator. Here, as a step towards lasing action, we study loss-compensation in a feasible active LRSPP-waveguide.

We simulate a waveguide as shown in Fig. 3.4(a), with a single layer of gain medium of thickness $t = 130$ nm deposited on the metallic film, and pump this structure with normal incident E_y-polarized light impinging downwards, of amplitude E_{pump}. The geometrical parameters for this case are the same as for the experimental configuration in Ref. [53]. In order to find the amount of effective gain that this structure can achieve, we discuss the propagation properties of LRSPP modes. For that purpose, we introduce a first approach based on eigenmode frequency-domain FEM calculations of the 2D cross-section of a infinite waveguide, based on the following approximations: For a waveguide without feedback, the intensity of the LRSPP is much smaller than the pump field. Therefore, the depopulation of the excited DCM state due to stimulated emission is negigible and the term from equation (3.12) can be neglected. Moreover, we assume that the pump rate is time-independent, which is true for a continuous-wave pump. The field intensity distribution $|\mathbf{E}(\mathbf{r};\omega_a)|^2$ at the pump frequency that enters into $G(\mathbf{r})$ is obtained by means of a frequency-domain scattering simulation for a downward impinging plane wave. In this case, an analytical expression is found for the steady-state populations N_{Alq} and N_{DCM}, by making zero the time-derivatives in the rate equations (3.11) and (3.12). For the host population density, we find:

$$N_{Alq} = \Delta^{-1}\left(\alpha - \sqrt{\alpha^2 - 2\Delta G}\right) \tag{3.16}$$

with the constants above grouped in the following definitions:

$$\Delta = \left(2\tau_{DCM}\left(\frac{k_F}{N_0}\right)\left[k_F - \left(\frac{k_{an}N_0}{k_F}+1\right)\left(\frac{1}{\tau_{Alq}}+k_F\right)\right]\right)^{-1} \tag{3.17}$$

and:

$$\alpha = \left(\frac{1}{\tau_{Alq}}+k_F\right) - \left(\frac{k_F}{N_0}\right)\left(\frac{k_{an}N_0}{k_F}+1\right)\tau_{DCM}G \tag{3.18}$$

The value of the guest population density is given as a function of the expression of N_{Alq}

above:

$$N_{DCM}(N_{Alq}) = \tau_{DCM}\left[k_F - \left(\frac{k_{an}N_0}{k_F}+1\right)\left(\frac{1}{\tau_{Alq}}+k_F\right)\right]N_{Alq} + \left(\frac{k_{an}N_0}{k_F}\right)\tau_{DCM}G \tag{3.19}$$

in which the Purcell effect enters as a spatial modulation of the decay time τ_{DCM}. The spatially non-uniform dielectric permittivity associated to the response of the DCM dye molecules is connected to the population density (3.19), through the emission polarization field defined as in (3.14). From the fact that $\mathbf{P} = \epsilon_0(\epsilon_{DCM} - 1)\mathbf{E}$, we end up with:

$$\epsilon_{DCM}(\mathbf{r}) = 1 - i\frac{K_e N_{DCM}(\mathbf{r})}{2\gamma\epsilon_0\omega_e} \tag{3.20}$$

We performed eigenmode FEM calculations of the considered LRSPP mode with the above optical and geometrical parameters, and making use of the spatial dependent permittivity ϵ_{DCM} to account for the non-homogeneous gain medium response. The resulting values of the imaginary part of the propagation constant for the simulated active LRSPP waveguides as a function of the applied pump strength $|E_{pump}|^2$ are shown in Fig. 3.6(a) (black line). As it is clearly observed, full-loss compensation and amplification ($\mathrm{Im}(k_x) < 0$) can be reached, and for the highest pump intensities $\mathrm{Im}(k_x)$ saturates at values in the order of -2×10^4 m^{-1}.

We also examine the Purcell effect by simulating both the results with the spatial modulation from Ref. [182]. For comparison, blue line from Fig. 3.6(a) shows the imaginary part of the propagation constant without including the spatial modulation of the radiative time τ_{DCM} accounting for Purcell effect. This comparison illustrates the influence of the Purcell effect on the effective gain. For the smaller intensities of the pump field ($|E_{pump}|^2 < 5 \times 10^{12}$ V^2/m^2), the reduced lifetime of the excited DCM state results in a significantly reduced gain coefficient when the Purcell effect is included. This effect is less pronounced for larger values of E_{pump}, mainly due to the fact that the bimolecular annihilation becomes significant at higher density of excited molecules. In addition, we present cross-sectional cuts displaying the spatial distribution of the $N_{DCM}(\mathbf{r})$ inverted molecules when including Purcell effect (Fig. 3.6(b)) or without it (Fig. 3.6(c)). Comparison of both figures reveals that the decrease of the available effective gain is spatially localized in a layer of quenched molecules close to the metal surfaces, as a consequence of the drastic reduction of the radiative lifetime in those areas.

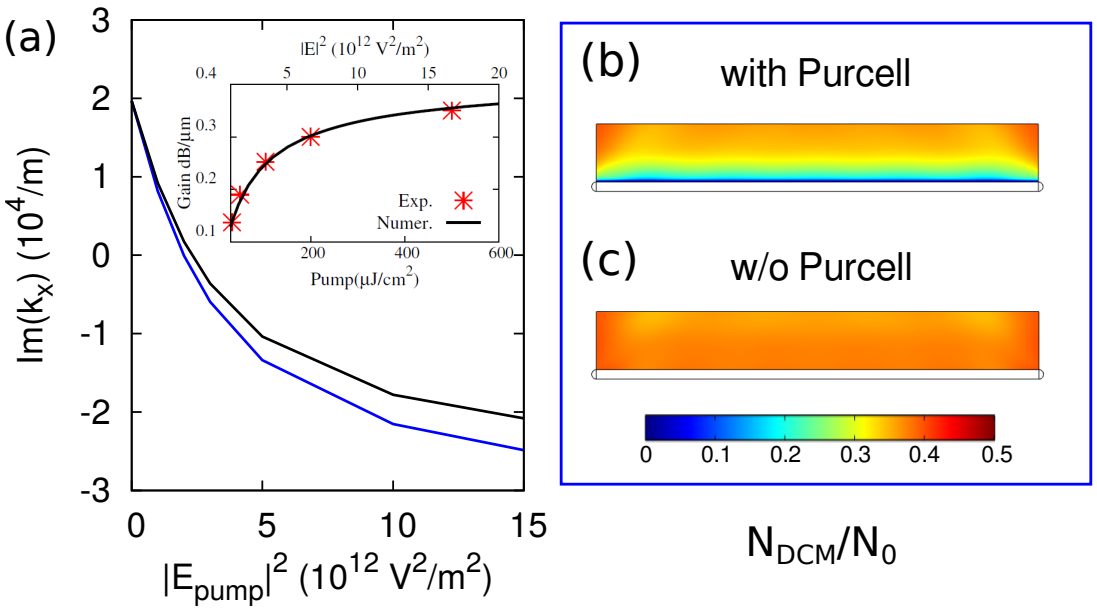

Figure 3.6: Loss compensation in LRSPP-based active waveguides. (a) Propagation properties. The solid lines show the imaginary part of the propagation constant as a function of the pump intensity for a 1 μm-wide and 21nm-high gold waveguide with a 130 nm high layer of organic molecules on top. The inset shows the agreement of the numerical results for the set of parameters used for resemblance with the experimental setup from Ref. [53]. (experimental results are taken from Fig. 3 within this reference). (b) Normalized DCM population density including the Purcell effect in the simulation, for a pump intensity of $|E_{pump}|^2 = 15 \times 10^{12}$ V^2/m^2. (c) Normalized DCM population density excluding the Purcell effect in the simulation, for the same pump value as in (b).

3.3.3. Lasing action in LRSPP-based waveguides.

We have demonstrated that the effective gain showed by LRSPP waveguides enables loss-compensation within the experimental parameters from Ref. [53]. In order to reach the lasing regime, a feedback mechanism must be implemented on the considered structure. We next explore this possibility, by adding partially reflecting boundary conditions, accounting for a reflection coefficient r (see Appendix A) at the ends of the waveguide, within a realistic 3-dimensional calculation performed by means of the time-dependent generalization of FEM (see Chapter 2, Section 2.3.5). This framework allows tracking the spatio-temporal dynamics of the corresponding plasmonic EM fields and the population dynamics, given by the set of rate equations (3.11), (3.12), and by the gain polarization field (3.14) introduced above.

Although the time-dependent 3D full calculation is very general, the experimental lengths

$l \sim 40$ μm used in Ref. [53] are computationally expensive. As a proof of principle, we will later provide a simplified two-dimensional model can be used for simulating lasing action in such class of waveguides, showing that the lasing regime is experimentally feasible. Here, we modify the system in order to allow for a higher effective gain. In particular, we introduce the following changes: First, a second layer of organic molecules is added below the waveguide, in order to take advantage of the symmetry of the LRSPP field with respect to the waveguide. Second, the height of both the top and bottom layers is increased to 300 nm, which is comparable to the decay length of the plasmon field in the vertical direction (294 nm), ensuring that 77% of the energy of the LRSPP is located within the gain layers. The density of molecules is increased by a factor of 3: $N_0 = 9 \times 10^{25}$ m^{-3}. Finally, silver instead of gold is used to model the metallic film, due to its lower inherent losses.

Figure 3.7(a) depicts the propagation properties for this new configuration. A schematic representation of the geometry can be found in the inset. By performing eigenmode calculations following the procedure above, low-loss designed waveguide leads to enhanced loss-compensation, both for the calculation in which Purcell effect is included (black line), or not (blue line). For the former case, the modifications described above make it possible to reach values of the propagation constants of $\mathrm{Im}(k_x) = -1.8 \times 10^5$ m^{-1}. Dashed lines represent the loss-compensation results found for the previous waveguide configuration, which were already shown in Fig. 3.6(a).

Spatio-temporal dynamics of lasing action.

In order to characterize the typical dynamics of the lasing action, we study the time dependence of the amplitude of the LRSPP-mode within our time-dependent FEM approach, in a 3-dimensional waveguide with $r = 0.95$ and a length of $l = 2\lambda_{SPP} = 724$ nm, where λ_{SPP} is the modal wavelength of the LRSPP. The high reflection coefficients used for the mirrors can be experimentally realized by means of Bragg mirrors [185]. Notice that the emission of the molecules and the plasmon mode are in resonance, in such a way that an optimal coupling of the plasmon to the gain medium is achieved. In these simulations, the system is optically pumped with continuous-wave light and the time-dynamics of the population densities are tracked. When a steady-state is reached in the population densities, the field component associated to the LRSPP mode is switched on. Within our formalism, this is equivalent to introduce a numerical time-domain modulation to the emission field amplitude $\mathbf{E}_e = -\partial_t \mathbf{A}_e$ as described in Section 2.3.5, at

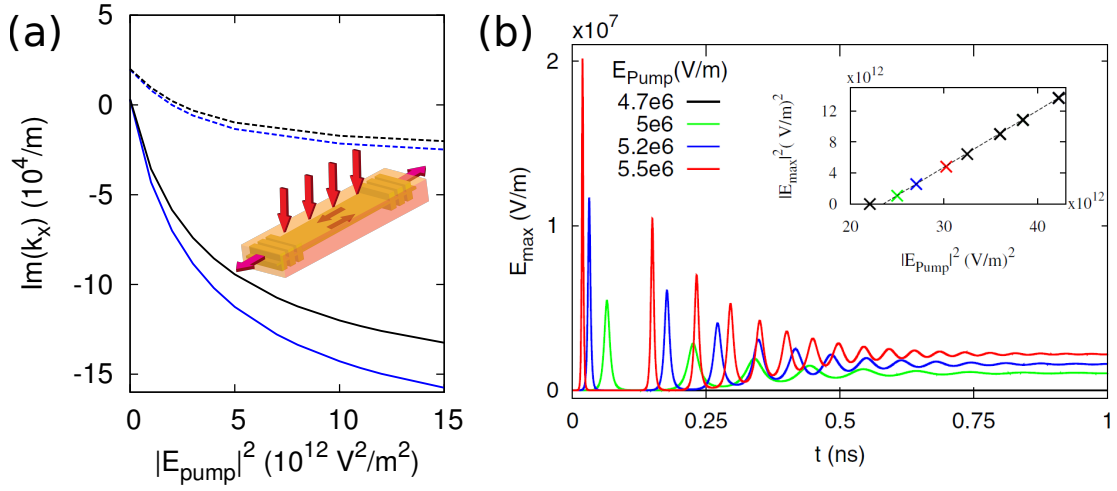

Figure 3.7: Lasing action in LRSPP-based active waveguides. (a) Propagation properties of LRSPP-waveguides composed of a silver 21 nm-thick film and sandwiched between two layers of gain material of thickness $t = 300$ nm. The DCM molecule density is $N_0 = 9 \times 10^{19}$ cm^{-3} (a schematic representation of this system is shown in the inset). Black solid line depicts the results including Purcell effect, while blue solid line accounts for the results without including it. For comparison, dashed lines represent the results for loss compensation found in Fig. 3.6(a). (b) Time-dynamics of lasing action. Main panel shows the time dependence of the amplitude of the electric field (taken at a maximum within the waveguide) for different pumps. For pump intensities above the threshold ($E_{th} \simeq 4.9 \times 10^6$ V/m) the relaxation oscillations are found. The results are shown for a waveguide length of $l = 2\lambda_{SPP} = 724$ nm and reflectivity $r = 0.95$. The inset shows the linear trend of the LRSPP intensity in the steady state (averaged over the gain layers) as a function of the pump intensity, with the presence of a threshold.

the required time. Within an experimental setup, this can be equivalent to introduce a probe field by means of a grating coupler [52, 53].

The time dependence of the LRSPP amplitude for pump intensities above the threshold ($E_{th} \simeq 4.9 \times 10^6$ V/m) shows the characteristic lasing behavior (see Fig. 3.7(b)), given by a series of spikes at early times, also called relaxation oscillations in traditional laser schemes [61, 62]. After this spiking behavior, the modal amplitude of the LRSPP reaches a steady-state. The inset shows the dependence of the intensity of the LRSPP mode in the steady state, as a function of the pump intensity. Above a lasing threshold value of the pump, a characteristic linear dependence is clearly observed. These signatures in the time-dynamics and in the steady-state behavior point out that the system is indeed lasing. We have also performed control simulations without the metallic waveguide in order to ensure that lasing action is assisted by long-range surface plasmons.

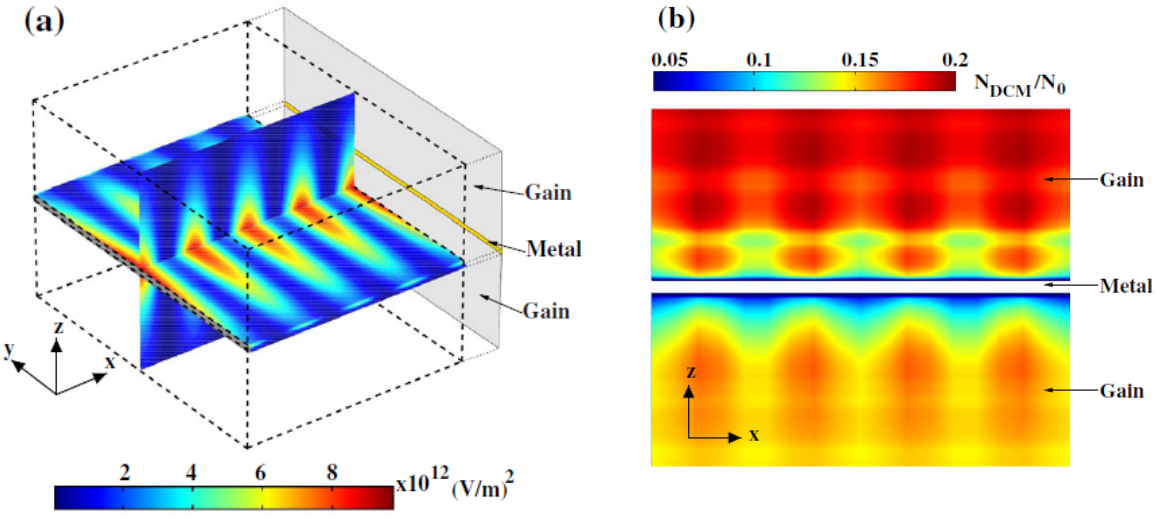

Figure 3.8: Spatial distribution of the LRSPP field intensity (a) and DCM singlet density (b) in the steady-state of the lasing regime. The results are shown for a pump of $E_{pump} = 5.5 \times 10^6$ V/m. The reflective boundaries lead to a standing wave pattern within the waveguide. Whereas the pump field is uniform along the $x-$direction of propagation, the interplay between the LRSPP-field and population densities of the gain medium conduces to a spatially non-uniform DCM density distribution.

Our numerical framework includes the full spatial and temporal dynamics of both the electromagnetic field and the population densities of the molecular states, enabling us to study the microscopic origin of the lasing action and the details of the interplay between the field distribution and the population densities. The corresponding steady-state results are shown in Fig. 3.8, for both the the spatial distribution of the electric field (panel (a)) and the population density of excited DCM molecules (panel (b)). Fig. 3.8(a) shows that the feedback introduced by the reflective boundaries leads to the formation of a standing wave with a LRSPP-field profile within the waveguide, providing subwavelength confinement in the vertical direction (the corresponding decay length is 294 nm, which is smaller than $\lambda/n_h = 370$ nm). Note that the physical mechanism responsible for this vertical confinement is of plasmonic nature, and differs from the total internal reflection mechanism that characterizes high-index dielectric (non-plasmonic) waveguides. It can be seen how the interplay between the plasmon field and the population density causes a non-uniform density of excited DCM molecules (see Fig. 3.8(b)). Remarkably, the high-field intensity areas of the electric field pattern correspond to minima in the singlet density. Furthermore, the displayed population density illustrates again how the

Purcell effect depends on the pump intensity. Given that the structure is pumped from above, the pump intensity above the waveguide is significantly higher than below. This, in turn, leads to a layer of quenched molecules below the waveguide much thicker than the one above the metal (as indicated by the blue layers below and above the waveguide in Fig. 3.8(b)). To the best of our knowledge, this study was the first to address such a dependence of the Purcell effect on the electric field intensity in the context of lasing action at subwavelength scales.

Systematic study of the lasing characteristics.

Simulations of the full spatial and temporal dynamics of the 3D system are numerically demanding and, due to the required resources, limited to waveguides with a length of around 1 μm. In order to perform a systematic study of the dependence of the lasing characteristics on different system parameters (e.g., the length of the waveguide or the reflectivity of the boundaries), it is desirable to calculate the lasing threshold from less expensive simulations. Thus, using the close similarity of the propagation and lasing properties of the considered waveguide (with a width of 1 μm) and those characterizing a waveguide of infinite width, we introduce here an approach for getting additional in-

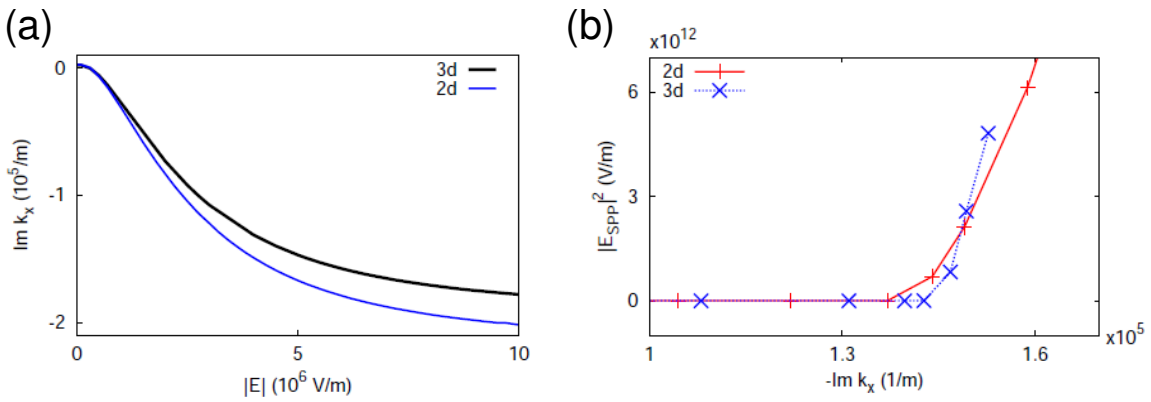

Figure 3.9: Comparison of propagation properties and lasing characteristics of a 1 μm-wide (3D) and an infinitely wide (2D) waveguide. (a) Propagation properties. Imaginary part of the propagation constant as a function of the pump amplitude for a silver waveguide with 300 nm thick layers of organic molecules above and below the waveguide. (b) Comparison of the lasing characteristics of the 3D system and the simplified 2D-version, in terms of the intensity of the LRSPP field in the steady state as a function of the propagation constant for a waveguide with a finite width (3D) and an infinitely wide slab (2D). The metallic film has a thickness of 21 nm and a length of $l = 724$ nm.

sight into lasing action, based on the simulation of the 2-dimensional counterpart of the 3D plasmonic waveguide modelled above. Indeed, the width of the waveguide is not a critical geometrical parameter, since the width of 1 μm is wide compared to the plasmon wavelength of $\lambda_{SPP} = 362$ nm. Making use of the 2D geometry enables simulating mode-propagation and lasing action in this class of active plasmonic waveguides, without the need of expensive computational resources.

A comparison of the propagation properties of either a waveguide of finite and of infinite width, is shown in Fig. 3.9(a). Both systems show the same qualitative behavior, and the absolute values are only slightly higher in the 2D case, since the overlap of the plasmon field with the gain medium is larger in this case. In order to examine the close analogy between the finite-wide waveguide and the thin film in the lasing regime, we calculate the lasing characteristics of the simplified 2D version of the waveguide with the following parameters: The height of the original waveguide is 21 nm, the width is 1 μm, and the waveguide length is $2\lambda_{SPP} = 724$ nm. The absolute value of the reflectivity of the boundaries is $r = 0.95$. The analogous 2D structure is given by a 21 nm-thick and 724 nm-long metallic slab with the same reflectivity at the boundaries. As shown in Fig. 3.9(b), the lasing characteristics of the two systems are very similar. Note that this panel shows the dependence of the intensity of the LRSPP in the steady state not as a function of the pump-intensity, but rather as a function of the propagation constant (which, in turn, depends on the pump intensity), so that the differences in the propagation properties between the 2D and 3D structures are already contemplated.

As discussed above, knowing the propagation properties of the full structure and

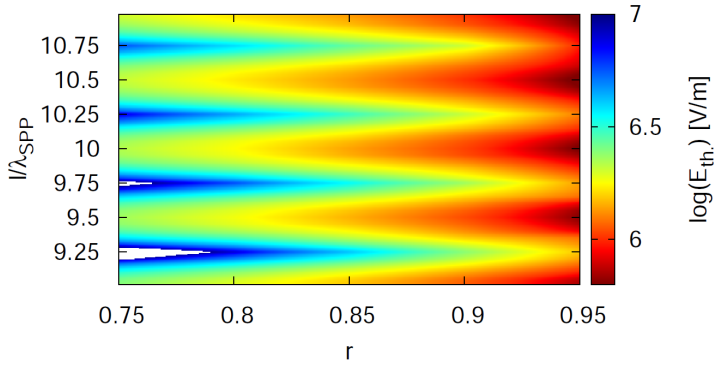

Figure 3.10: Lasing threshold E_{th} (in logarithmic scale) as a function of the waveguide length and of the reflectivity. For high values of r, and for waveguide lengths l which are a multiple of $0.5\lambda_{SPP}$, low threshold values (below 10^6 V/m) are found (the white areas account for threshold values larger than 10^7 V/m).

those corresponding to its simplified analogue enables to accurately calculate the threshold as a function of the waveguide length and of the reflectivity of the finite-width waveguide, via 2D simulations. Fig. 3.10 shows the threshold for waveguide lengths ranging from $9\lambda_{SPP} = 3.36$ μm and $11\lambda_{SPP} = 3.98$ μm, and for reflectivities between $r = 0.75$ and $r = 0.95$. As expected, the threshold decreases with an increasing value of r. Low threshold values appear for waveguide lengths which are multiples of $0.5\lambda_{SPP}$. This is due to the fact that for these lengths, a LRSPP-mode of the waveguide is in resonance with the emission frequency of the molecules. Thus, for high values of r and these values of the waveguide length, the lasing threshold is significantly low (featuring values below 10^6 V/m).

The simplified 2D model can also be used to study the lasing dynamics in similar systems to those used in recent experiments reporting a LRSPP amplifier [53]. For illustration, the time dependence of the LRSPP-field of a waveguide with length of $l = 39.9$ μm is shown in Fig. 3.11. The typical lasing dynamics given by a set of relaxation oscillations are found again. These results show that the LRSPP-based nanolasers can be realized in the current nanofabrication paradigm.

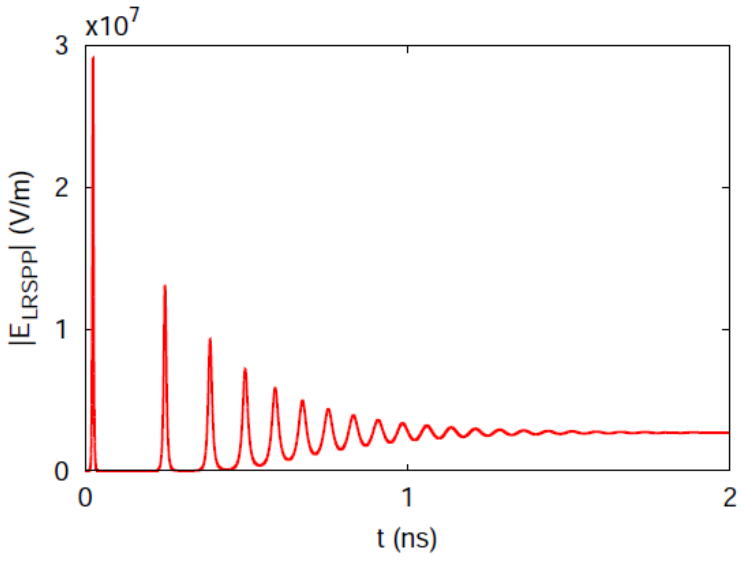

Figure 3.11: Lasing dynamics of a waveguide with a length of $l = 39.9$ μm calculated with the simplified 2D model. The values of the parameters are chosen accordingly with the setup used in Ref. [53]. The reflectivity of the boundary is $r = 0.45$ and the pump-field amplitude is $E_{pump} = 2.2 \times 10^6$ V/m.

3.4. Lasing action assisted by Channel Plasmon Polaritons.

Nanowire lasers integrated with plasmonic structures allow confining light in deep sub-wavelength volumes while preventing the high losses of purely metallic cavities [40]. Remarkably, this class of systems is a promising perpective for on-chip laser light source integration within nanophotonic circuitry. In order to achieve this technological landmark, coupling the emission of coherent light sources to the rest of the small footprint components is needed.
In the recent past, a significant number of experiments have demonstrated lasing action in this class of systems, featuring hybrid plasmonic modes in NWs assembled onto flat metallic substrates. These so-called 'NW plasmon lasers' [40, 86, 155, 162, 186] show high diffractive scattering at the nanowire facets, that difficults the efficient transfer of EM energy to the modes propagating along the metallic substrate, and its interaction with other photonic passive components. In this section we propose a substantial step towards overcoming this drawback, by means of a hybrid photonic-plasmonic device consisting of a semiconductor nanowire laser integrated with a V-groove plasmonic waveguide. We theoretically study laser light generation in this experimentally realistic, room-temperature operating configuration, focusing on the efficient coupling of the emission of the nanowire to the propagating plasmonic modes along the waveguide. In addition, we briefly explain the experimental results from a recent collaboration, which show agreement with our findings.

3.4.1. Hybrid NW/VG eigenmodes.

We investigate the lasing properties of hybrid devices accounting for a realistic experimental setup, consisting of a core-shell-cap GaAs/AlGaAs/GaAs nanowire positioned at the bottom of a gold (Au) VG waveguide (Figure 3.12), forming a NW-VG hybrid nanolaser. Upon pulsed illumination, the NW is able to partially couple its laser emission into the propagating CPP modes of the VG, which eventually couple out to free-space at the VG end mirrors. In this way, coherent light pumping excites electromagnetic modes in the nanowire whose modal shape is highly influenced by the presence of the VG. The nanowire acts as the laser medium able to provide the optical gain to overcome the inherent losses of the lasing mode. In addition, the nanowire facets act as partially reflecting surfaces that provide the feedback to confine the propagating modes and thus create a

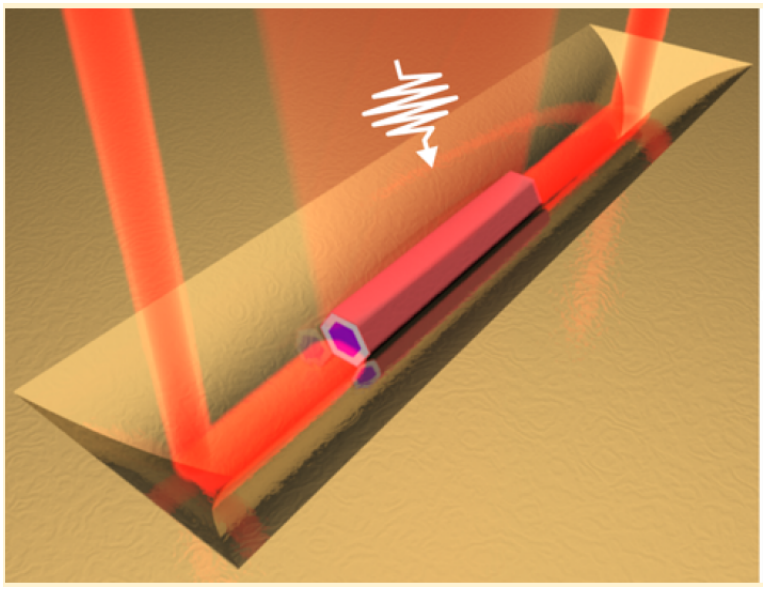

Figure 3.12: Hybrid Nanowire/V-Groove platform for an on-chip nanolaser source. Schematic illustration of a NW positioned inside a gold VG plasmonic waveguide capable of coupling its lasing emission to the propagating CPP modes upon pulsed optical excitation.

nanolaser cavity.

In order to model this experimentally feasible configuration, we consider the V-Groove geometry presented in subsection 3.2.3, sustaining channel plasmon polaritons, in which semiconducting nanowires are deterministically deposited. These nanowires have a diameter of 370 nm with a hexagonal cross section. They are situated at the VG-bottom such that two of their adjacent vertices lie at the same height on the metal surface (see Fig. 3.13(a)). The optical response of this hybrid structure is accounted for in terms of the following material properties: the Au optical response is described by a Drude-Lorentz model, fitted to available experimental data [94, 96]. The nanowire is considered uniformly made of GaAs, with a refractive index of $n_{NW} = 3.6$. Moreover, the ensemble NW/VG is embedded in air with a refractive index equal to 1. We start our analysis by examining the eigenmode solutions of the propagating modes carried by an ideally infinite VG/NW hybrid structure. The corresponding 2D simulated cross-section of this system is sketched in Fig. 3.13(a). Our numerical eigenmode FEM-based framework (see Section 2.4.2) enables us to calculate the propagating eigenmodes for the considered translationally invariant structures at the operating frequency ($\omega_e = 2\pi c/\lambda_e$ with $\lambda_e = 870$ nm, corresponding to the band-edge emission of GaAs at room temperature), and gives access to the corresponding electric field amplitude distributions. In this way,

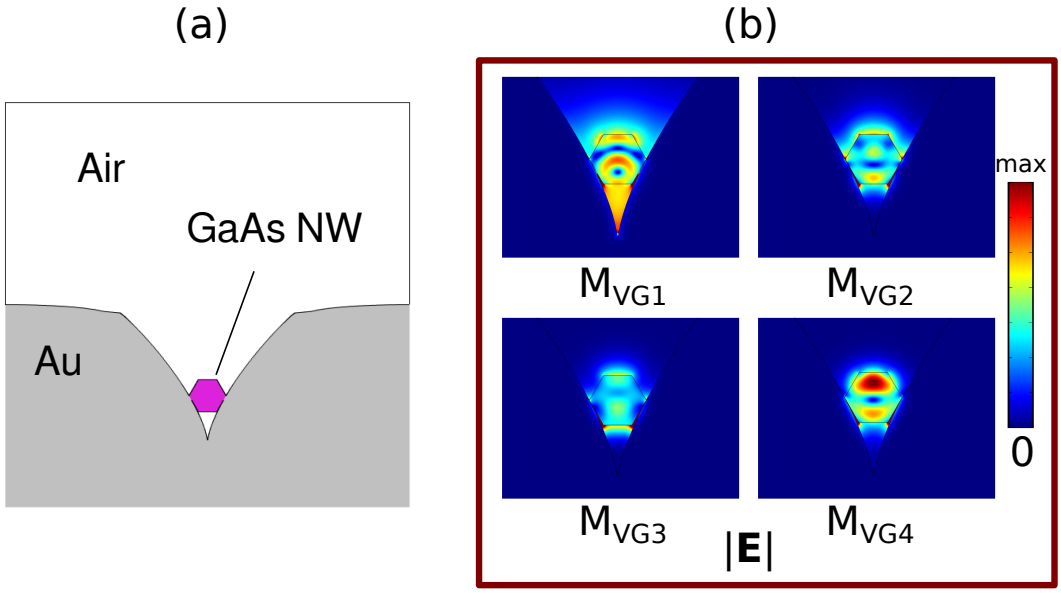

Figure 3.13: (a) Schematic representation of the hybrid V-groove/Nanowire 2D simulated structure. (b) $|\mathbf{E}|-$field distributions of M_{VG1}-M_{VG4} EM modes found for this system, by means of eigenmode FEM calculations.

we provisionally remove the effect of the pumping that would hinder the modal shape of the different modes, as well as the reflecting facets of the nanowire, that create a phase-matching condition.

The resulting modes from the 2D FEM simulations are characterized by an effective mode index n_{eff}. By inspecting up to $n_{eff} = 4$, a total number of nine modes was found. The new propagating modes are combinations between the inherent modes of the isolated waveguide (in this case, the fundamental CPP-mode, see Fig. 3.3) and the resonant modes inside the so-considered infinitely long nanowire. Interestingly, we found that one of them was mainly confined at the VG-bottom, in a way that the CPP field distribution is resembled. We denote this mode as M_{VG1} (see Fig. 3.13 (b)). The eight remaining solutions were photonic modes mainly confined inside the nanowire. The electric field intensity of each of these modes decays along the VG long-axis in an exponential fashion: $I = I_0 \exp(-z/L_p)$, where z is the transversal direction and L_p is the propagation length, given by $L_p = (2\mathrm{Im}(n_{eff}k_0))^{-1}$.

In order to provide the necessary feedback within a finite, the mode must fulfill the round-trip oscillation condition, much in the same way as occurs, for instance, in Fabry-Perot lasers [16, 140]. Therefore, we demand that the modes which may be potentially involved in the lasing performance of the structure, must meet the condition: $L_p > L_f$,

Table 3.1: Modal properties of the hybrid modes M_{VG1}-M_{VG4}

Mode	n_{eff}	L_p (μm)	R	ξ
M_{VG1}	$1.24 + i * 6.5 \times 10^{-3}$	10.6	0.46	23.8%
M_{VG2}	$1.55 + i * 1.0 \times 10^{-2}$	6.9	0.87	0.001%
M_{VG3}	$2.06 + i * 4.7 \times 10^{-3}$	14.6	0.86	0.006%
M_{VG4}	$2.52 + i * 4.0 \times 10^{-3}$	17.3	0.76	1.6%

where L_f is the length of the finite nanowire. From now on, we focus on those modes whose propagation length is higher than the considered nanowire length of 6.4 μm, yielding the four modes M_{VG1}-M_{VG4} presented in Fig. 3.13 (b). Values of the effective mode indices and of the propagation lengths of these modes can be found in the Table 3.1.
A very first analysis can already show which one of these modes can couple its emission to the modes of the CPP-waveguide, by computing the spatial overlap between the considered hybrid modes of the NW/VG system, and the bare VG waveguide [176]:

$$\eta = \langle n|m\rangle = \frac{\int dx \int dy\ \mathbf{z}\cdot(\mathbf{E}_n \times \mathbf{H}_m^*)}{\left[\int dx \int dy\ \mathbf{z}\cdot(\mathbf{E}_n \times \mathbf{H}_n^*)\right]^{1/2}\left[\int dx \int dy\ \mathbf{z}\cdot(\mathbf{E}_m \times \mathbf{H}_m^*)\right]^{1/2}} \tag{3.21}$$

where n denotes each of the hybrid modes M_{VG1}-M_{VG4}, and m stands for the CPP-mode sustained by the waveguide at the corresponding emission wavelength. The results yield 25% overlap for the 'CPP-like' M_{VG1} mode, and $< 0.2\%$ for the three remaining nanowire-like modes M_{VG2}-M_{VG4}. This result suggests that the mode M_{VG1} is more able to launch modes into the VG-waveguide. However, this simple approach does not consider the effect of back-reflections nor the free-space scattering occurring at the facets of the NW.

3.4.2. Reflection and transfer efficiency at the nanowire facets.

In order to further study the coupling of the nanowire emission to the propagating modes of the VG waveguide, we performed more realistic 3D FEM linear simulations to study the reflection of the considered propagating modes M_{VG1}-M_{VG4} from one of the NW facets and their coupling to CPP emission. In a series of separate calculations, we consider that each of the 'hybrid modes' M_{VG1}-M_{VG4} is being injected through a numerical boundary whose cross section corresponds to the 2D VG-NW profile (see Figure 3.14(a)), with the propagation length obtained from the 2D eigenmode simulations (see Table 3.1).

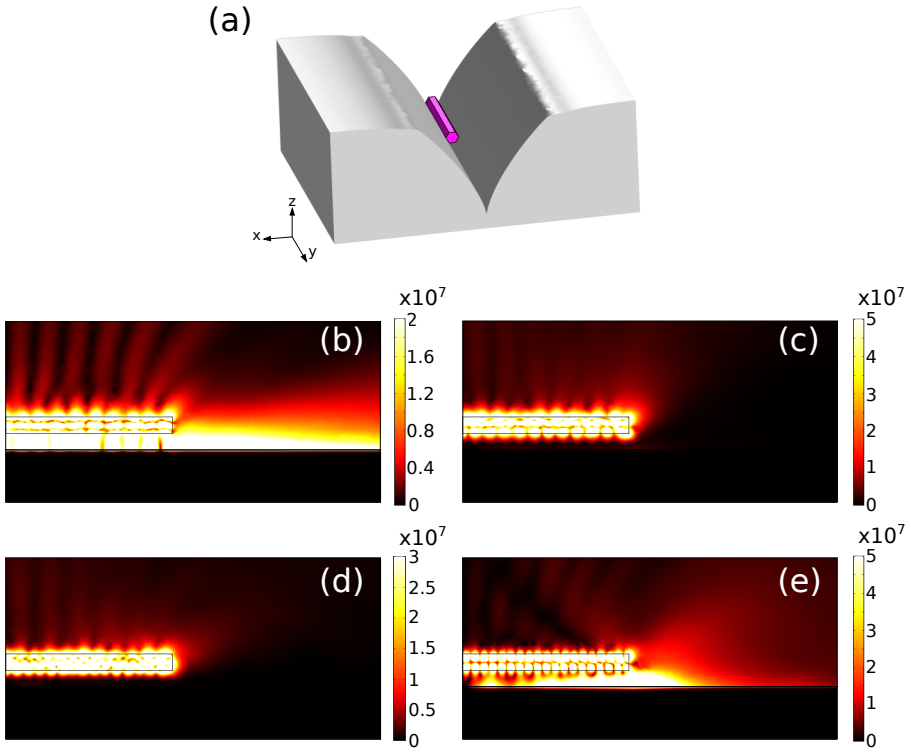

Figure 3.14: 3D FEM simulations of hybrid-mode propagation towards a NW facet. (a) Schematic representation of the simulated structure. (b)-(e), Normalized $|\mathbf{E}|$-field distribution of the modes M_{VG1}-M_{VG4}, for the $yz-$plane (cut at the VG-bottom) depicted in (a). Only the photonic-plasmonic mode M_{VG1} is able to launch CPPs beyond the NW facet.

The input electric field is normalized such that: $(1/2)\int_A \mathrm{d}^2\mathbf{r}\epsilon_0 c\epsilon(\mathbf{r})|\mathbf{E}(\mathbf{r})|^2 = 1$, at this boundary for all the modes, and absorbing conditions (perfect matched layers−see section 2.4.3) are placed at the rest of limiting boundaries of the simulation cell to avoid non-physical reflections. The considered NW-length is 3.2 μm and its diameter is 370 nm. Optical material properties mimic those used for the 2D FEM simulations. In this way, we let each mode propagate and eventually scatter and reflect at the NW facet.

Figure 3.14(b)-(e) depicts the $|\mathbf{E}|-$field distribution corresponding to the propagation and reflection of the considered hybrid modes, across a longitudinal cut at the VG-bottom. From these panels, we can see that three out-coupling channels are present: back-reflection of the propagating mode, free-space scattering at the NW facet, and coupling to the CPP mode supported by the bare VG waveguide. Mode M_{VG1} (Fig. 3.14(b)), whose field distribution is mainly confined at the VG bottom, is able to excite a CPP

at the NW facet, as it is revealed by the characteristic exponential decay of this mode propagating along the VG and beyond the NW. On the other hand, modes M_{VG2} and M_{VG3} (Figs. 3.14(c) and (d)), have a small overlap with the CPP, and the behaviour is ruled by back-reflections inside the NW. Finally, for the mode M_{VG4} (Fig. 3.14(e)), a larger field concentration is noticed at the VG-bottom when the mode reaches the NW facet, but without further propagating along the bare VG, revealing the strong presence of free-space scattering, but not launching of a CPP mode. We also note here that, in general, other guided modes with similar polarization dependence and frequency may be excited upon reflection [187].

In order to quantify the efficiency of excitation of CPPs from each hybrid mode independently, we compute the ratio of energy that is transferred to the CPP-mode compared to the total energy exiting the VG/NW ensemble. We introduce the transfer efficiency (ξ), defined as:

$$\xi = \frac{P_d \exp(d/L_p)}{P_{tot}} \tag{3.22}$$

Here, P_d stands for the optical power carried out by the CPP, calculated at a distance $d = 3.5$ μm from the NW-facet, where non-related free-space contributions are negligible. In order to isolate the CPP contribution, we integrate the optical power density over a transversal surface to the VG long-axis, with an area that extends from the bottom of the VG-structure to a height equal to the modal size of the CPP, defined as the distance where the maximum electric field intensity (found at the VG-bottom) decreases to 1/10 of its value. The obtained mode size is 538.1 nm. P_{tot} is the total power exiting the NW/VG structure, calculated as the sum of the free-space radiated power from the whole NW/VG system, and the CPP-power at a surface 100 nm away from the NW-facet. The exponential factor is introduced to compensate for the longitudinal decay of the channel plasmon, and $L_p = 19.9$ μm is the propagation length obtained numerically from 2D FEM calculations of the VG waveguide.

Values of the transfer efficiency are listed in the Table 3.1. We notice that the only significant value of the transfer efficiency is obtained for mode M_{VG1} ($\xi = 23.8\%$). These values, together with the field distributions shown in Fig. 3.14(b)-(e), enable us to conclude that M_{VG1} is the only mode able to efficiently couple to the CPP-modes sustained by the VG waveguide, and thus the CPP-launching at the NW facet is restricted to this hybrid mode. These values are also compatible with the calculated mode-overlap η of the mode M_{VG1} with the CPP mode supported by the bare VG, much higher than for

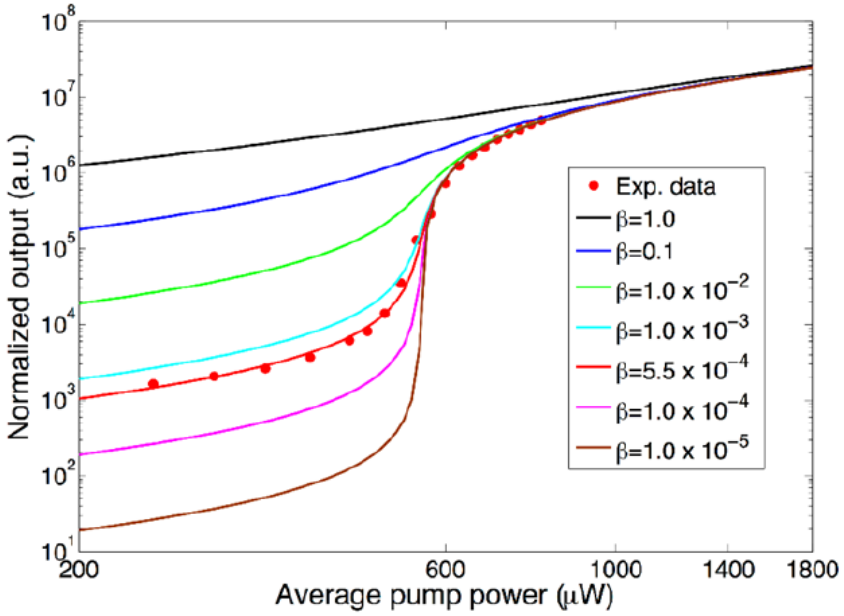

Figure 3.15: Power dependence obtained from the lasing rate equation analysis. The displayed results correspond to the CPP-like mode and several values of the spontaneous emission coupling factor (β), ranging from $\beta = 1.0$ (thresholdless laser, black line) to $\beta = 10^{-5}$ (brown line). In all cases, a reflectivity of $R = 0.44$ is assumed at the facets of the NW. For comparison, the experimental data are also shown (red dots).

the other three evaluated modes.

3.4.3. Laser rate equation analysis

In order to demonstrate that lasing action is possible in the considered hybrid VG/NW realistic system, we implement a laser rate equation analysis (see Section 2.5.2), which enables us to examine, under realistic considerations, whether the lasing threshold can be reached for a reasonable value of the pump strength, and the influence of amplified spontaneous emission (ASE) in terms of the $\beta-$factor.

Our analysis is based on a semianalytical formulation in which the population dynamics of the semiconducting nanowire are accounted for in terms of the set of rate equations (2.191) and (2.192). Furthermore, spatial averaging of the non-homogeneous profile of the electromagnetic fields, is performed. The resulting power dependence can be accounted for in terms of both the temporal and the spatial confinement, through the photon lifetime $\tau_p = Q/\omega_e$ and the confinement factor Γ defined in (2.193), respectively. Table 3.2

Table 3.2: Numerical values of the parameters used in the Laser rate-equation analysis.

Parameter	Value
η	0.01
V_a	5.7×10^{-13} cm^3
L_{NW}	6.4 μm
τ_{nr}	0.44 ns
τ_{sp}	1.0 ns
C	7×10^{-30}
g_0	715 cm^{-1}
N_{tr}	2.05×10^{18} cm^{-3}
N_s	-7.02×10^{16} cm^{-3}
$v_{g,z}$	4.92×10^7 m/s
Γ	0.88

includes the values of the parameters used in our lasing rate equation analysis, together with the values for the rest of parameters needed in this approach (all parameters describing the gain medium were obtained from Ref. [16] and references therein).

The 3D full-wave theory simulations carried out using FEM above, are purposedly designed so that a value of the reflection coefficient at the nanowire facet can be obtained. Namely, the reflection coefficient is calculated by placing a monitor transversally to the VG long-axis and close to the NW facet that integrates the total power over the whole cross section of the NW-VG system. By numerically computing the input power associated to the mode injection, and taking into account the power decay from the propagation length, it is straightforward to calculate the reflectivity (R) as a ratio between the reflected and the input power.

Values of the R for each mode are listed in Table 3.1. The M_{VG1} mode has the lowest reflectivity, and less than a half of its optical power is reflected back, since its transfer efficiency to the CPP mode of the bare VG is the highest. Also, the fact that the scattering losses at the NW-facet are high for the mode M_{VG4} (as already noticed by the presence of high field intensity at the VG-bottom) explains the lower reflectivity for this mode with respect to those of the modes M_{VG2} and M_{VG3}.

Within our laser rate-equation approach, the reflection coefficient R and the $\beta-$factor are the key parameters to determine the precise shape of the output power dependence calculated as a function of the average input power. In Fig. 3.15, the characteristic 'S-

shape' of the transition from spontaneous emission to lasing is obtained. For purposes that will be detailed below, the reflection coefficient has been chosen to be $R = 0.44$ (a value which is very close with the reflection coefficient $R = 0.46$ obtained for the mode M_{VG1}) in these results. Values of the $\beta-$factor are varied from $\beta = 1$ (black line, thresholdless laser) to $\beta = 1 \times 10^{-5}$. As expected, as β is reduced, the kink associated to the lasing threshold in the case $\beta = 0$, becomes more pronounced. From these results, we find that the lasing regime can be reached for all the cases for average pump power values of $P_{out} \gtrsim 800$ μW. As a link with the next subsection, data obtained from the experimental verification of our results is also included in Fig. 3.15.

3.4.4. Experimental results.

In this section, we describe the experimental implementation of the theoretically analyzed system above, carried by Dr. Esteban Bermúdez Ureña under the supervision of Professor Romain Quidant at ICFO, Barcelona. Dr. Gözdë Tütüncüoğlu, from EPFL in Lausanne (Switzerland) developed the nanowire growth with input from Prof. Anna Fontcuberta i Morral. Finally, Dr. Cameron L. C. Smith from the Technical University of Denmark, fabricated the V-Groove structures.

Inset of Fig. 3.16(a) shows a scanning electron microscopy (SEM) image of the nanofabricated devices. Good alignment of the NW with the VG axis, approaching to the analyzed theoretical situation, was achieved. The optical characterization was made by means of a optical microscope, incorporating a 730 nm pulsed (200 fs, 80 MHz) excitation channel for optical pumping, a EMCCD camera for imaging of the scattered EM radiation, and a fiber collection channel that allows measuring the emission spectrum. When pumped, the device is able to couple its emission to the CPP modes of the waveguide. The signature of the emission of CPP modes is given by spots in the EMCCD image collected from the transversal emission, from the mirrors at the end of the waveguide (see Fig. 3.16(c)).

In order to study if lasing action is feasible in this system, the samples were pumped with a pulsed-fs laser and the output power was measured at both ends of the VG. Panels from Figures 3.16(b) and 3.16(d) show the emission spectrum recorded at the left and at the right ends of the VG, respectively, correspondingly with the EMCCD image in (c). By increasing the pump intensity, two peaks appear and dominate the spectrum. Although linewidth narrowing of these peaks suggests that lasing action may be possible in the system, power dependence is needed to distinguish from the narrowing

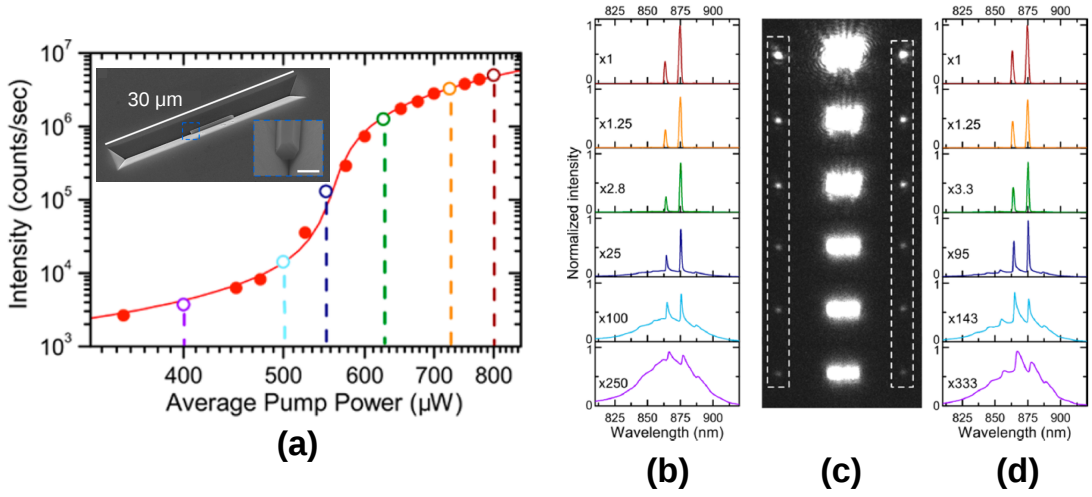

Figure 3.16: Results from experiments of lasing in hybrid V-Groove/nanowire devices. (a) Output power dependence of the measured peak intensity as a function of average pump power, for the dominating lasing peak of a NW/VG device. The signal was collected from the right VG end. The solid red line is a fit using laser rate-equations analysis, which yielded $\beta = 5.5 \times 10^{-4}$ and $R = 0.44$. (b),(d) Normalized emission spectra collected from the left and right VG ends respectively, where the spectra are color-coded accordingly to the data points in panel (a). EMCCD images of the NW-VG device at the respective pump excitation power of each colored data point. Bright spots can be appreciated at both VG ends from which the spectra were collected.

also associated to amplified spontaneous emission (ASE). Figure 3.16(a) shows the peak intensity of the dominating emission peak at $\lambda = 875$ nm, as obtained from the spectra collected from the right VG end, represented as a function of the average pump power. This Power in-Power out plot ($P_{in} - P_{out}$), represented in logarithmic scale, is characterized by three main regimes. In the first linear regime, obtained for low values of the pump power (below ~ 500 μW), spontaneous emission of the gain medium dominates the emission properties. This regime is followed by a superlinear increase of the output power, for values of the pump power ranging from ~ 500 to ~ 625 μW, which indicates that amplified spontaneous emission (ASE) governs the emission characteristics. Finally, for pump values higher than ~ 625 μW, a linear dependence is recovered, indicating that the lasing regime has been reached.

The emission spectrum measured at both ends of the VG in Figs. 3.16(b),(d), measured at each of the couloured data points in 3.16(a), together with EMCCD images, Fig. 3.16(c), enable to follow the sequence from spontaneous emission to lasing and provides further evidence of lasing action based on the temporal and spatial coherence. At

low pump powers (<450 μW, see purple line from Figs. 3.16(b),(d)), the spontaneous emission regime results in a broad emission spectrum characterized by Fabry-Perot oscillations, expected below threshold in nanowire cavities [187]. On the other hand, coupling of the spontaneous emission of the gain medium to the CPP modes of the VG waveguide results in two low-intensity spots at the VG ends in the EMCCD images (Fig. (c)). In the ASE regime, two narrow peaks emerge from the background signal (for instance, see dark-blue lines in Figs. 3.16(b),(d), for pump value of 550 μW). However, it is not until the lasing regime that linewidth narrowing is accompanied by the characteristic spatial coherence above threshold (see the corresponding spectra at 800 μW in the red lines from Fig. 3.16(c), and interference fringes in the corresponding EMCCD image at this pump intensity).

The laser rate equation approach developed above reveals that two relevant parameters allow to characterize the nature of the lasing mode: the reflectivity (R) and the $\beta-$factor. Using these parameters, we performed a fitting of the experimental results, obtaining very good agreement for the values $R = 0.46$ and $\beta = 5.5 \times 10^{-4}$ (see red line in Fig. 3.16(a)). Remarkably, the value of the reflectivity is very similar to the one obtained in the 3D simulations for the photonic-plasmonic mode M_{VG1}: $R = 0.46$ (see Table 3.1). In contrast, the fitting of the remaining photonic modes M_{VG2}-M_{VG4} yields very similar values of the $\beta-$factor, but values of R depart significantly from those expected from the 3D simulations (for instance, for the mode M_{VG4}, $\beta = 4.5 \times 10^{-4}$ and $R = 0.35$ is found, while $R = 0.73$ was found from the simulations). The very good agreement of the rate equation approach with the experimental results clearly provides evidence that a 'CPP-like' plasmonic-photonic mode is enabling lasing action in the VG/NW architecture.

Our theoretical results from the 3D simulations also demonstrated that only the hybrid mode M_{VG1} is able to couple its emission to the CPP modes of the bare VG waveguide with appreciable transfer efficiency ξ. In order to experimentally verify this fact, the contributions of the strongest lasing peak at 875 nm were collected from one VG end and quantified, comparing to the total emission decoupled from the corresponding NW facet. This gives a measure of the experimental transfer efficiency. Values of 9.3% and 7.1% were obtained, for the upper and lower halves of the device, which are less than a half of the theoretical transfer efficiency $\xi = 23.8\%$. Note, however, that the experimental measurements do not account for the fraction of energy lost from the CPP to free-space energy conversion at the VG end mirrors. This fact, together with possible experimental imperfections not included in the theoretical modeling, can explain the discrepancy pointed out above. Importantly, the experimentally obtained values of the transfer efficiency are highly competitive against previous schemes considering the

transfer of energy from a lasing device to a subwavelength EM modes [188, 189]. The compatibility of the observed emission contributions with the simulated values of the efficiency of CPP-launching, further supports the evidence that lasing action is assisted by the photonic-plasmonic mode M_{VG1}.

3.5. Conclusions.

To summarize, in this Chapter, we have analyzed lasing action in plasmonic waveguides consisting of metallic thin films incorporating organic dye molecules. These systems sustain long-range surface plasmon-polaritons (LRSPP). By performing a detailed analysis based on the spatial and temporal dynamics of the electromagnetic field and of the gain medium, we have shown that the considered active waveguides exhibit low propagation losses (manifested through a high propagation-length) that enable them to achieve full-loss compensation. Moreover, by introducing a feedback mechanism, we have shown that low-threshold lasing action is attainable in a experimentally realistic configuration. In our analysis, we have noted the relevant role played by Purcell effect, that leads to quenching of the dye molecules close to metal surfaces, and causes a reduction of the achievable effective optical gain. The structures analyzed represent promising candidates for creating novel types of coherent light sources suitable for their integration in plasmonic circuits.

In addition, we studied lasing action in a novel configuration based on a V-Groove waveguide, incorporating a nanosource consisting of a semiconducting nanowire. When pumped, the nanowire is able to couple its emission to the channel plasmon polaritons (CPPs) supported by the waveguide. We have determined the relevant eigenmodes of the hybrid VG/NW system for lasing action. Importantly, we have found a mode of plasmonic nature with considerable overlap with the CPP of the bare VG. By means of full-wave 3D simulations of mode-propagation at the nanowire facets, we were able to provide quantitative values of the efficiency of the modes to CPP emission. These values, together with the study of the reflection at the nanowire facet, enabled us to implement a laser rate equation approach that reveals that the hybrid plasmonic mode is responsible for lasing action in this system, with good coupling efficiency to the waveguide modes. Finally, we addressed results from an experimental collaboration in this line, showing good agreement with the conclusions above. This study represents a crucial step towards high-sensitivity chemical or biosensing platforms with an integrated nanolaser source.

4 | Lasing action in plasmonic crystals.

4.1. Introduction.

Patterning surfaces in nanoscale dimensions will alter dramatically their inherent optical properties. The emergence of this concept, together with the development of photolithography techniques, led to the first designs of photonic crystals. The high degree of spatial and spectral tunability of the electromagnetic modes supported by these systems allows for lasing action in two different ways: On the one hand, by introducing a defect in the perfect lattice that they conform, EM field-confinement associated to a localized cavity mode is achieved in the same way that occurs, for example, in a Fabry-Perot cavity [27]. Thus, by the integration of this system with a suitable gain material, a photonic crystal laser can be created. On the other hand, the distributed-feedback effect enabled by the slow group-velocity modes of the defect-free system may still be utilized to produce laser light over large areas [190].

Lately, the incorporation of the above ideas to plasmonic systems has allowed combining the benefits of large-area and directional laser light emission displayed by photonic crystal structures, with subwavelength confinement characteristic of plasmonic modes. Indeed, some of the already studied nanolaser cavities lack of directionality in their emission due to the mismatch of the wavevector of plasmonic modes with that of free-space light. Recently, this problem has been overcome by integrating periodic metallic nanostructures with gain materials within the same platform. Seminal works have realized plasmonic lasers in practical configurations involving periodic arrays of nanoparticles [55] or nanoholes [57]. These systems, featuring extended resonances in the plane of the array, take advantage from the absence of need of a feedback mechanism to couple external light into nanoscale volumes, that can be radiated in the form of a directional beam over large areas, allowing for a very small angular divergence.

Motivated by these experimental results, we present here a theoretical study on the lasing properties of the 2-dimensional counterparts of the systems above under an unified perspective. Such structures, here termed plasmonic crystals, have been deeply analyzed in the context of extraordinary optical transmission [191]. Moreover, their integration with organic dye molecules has been studied for strong coupling [192], or optical loss-compensation [193]. This Chapter is organized as follows: first, we study two generic configurations suitably designed to maximize the laser emission into plasmonic radiative resonances, in two different limits: a nanowire array and a nanoslit array structure. Next, we perform a systematic analysis of the lasing dynamics and steady-state characteristics of the considered structures, and investigate the role of nonradiative modes in the laser emission. Finally, we perform a fair comparison between the nanowire array and the nanoslit array, designed to optimize near-field laser light generation.

4.2. Tuning the laser emission to the passive optical response.

Fig. 4.1(a) depicts the first considered geometry of the structures analyzed in this Chapter, given by a one-dimensional periodic array (period p) of rectangular gold nanowires of width w and height h. In its active configuration, this nanowire array is embedded in a dielectric host of index $n_h = 1.62$ containing organic dye molecules, which, when optically pumped, acts as a gain medium. This active medium extends a distance t above and below the structure. Lossless dielectric regions matching the host index extend infinitely above and below the active medium. Similarly, Fig. 4.1(b) depicts a nanoslit array with period p', width w', height h' and active layer thickness t'.

The optical response of this class of systems is known to display sharp resonant spectral features accounting for radiative coupling of far-field $p-$polarized light to plasmonic modes sustained by the structure, appearing in the form of extended resonances over several unit cells, and confined in the vertical direction. This fact has motivated research along two different lines. On the one hand, the discoverment of extraordinary optical transmission [194] attracted a great deal of theoretical interest to unveil the fundamental processes that govern transmittance enhancement in subwavelength arrays of nanoslits patterned on a metallic film. There are two mechanisms that allow the efficient transfer of light from one surface to the other: either by coupling of SPP sustained by both surfaces, or through cavity modes located inside the slits (Fabry-Perot modes). The

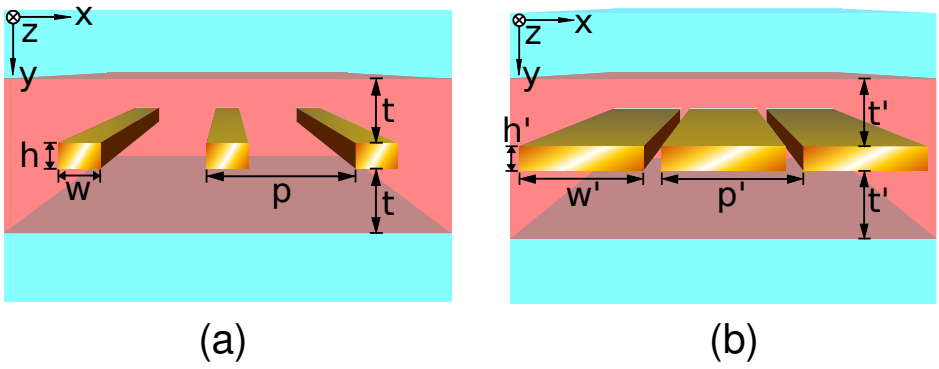

Figure 4.1: Schematic views of a perfectly periodic nanowire array (a) and a nanoslit array (b), including the definition of the reference system and the geometrical parameters.

physical nature of the resonances arising in this class of structures is generally a combination of both mechanisms, with a degree of hybridization in the modal characteristics that depends intrinsically on the geometrical parameters of the structure [191, 195, 196]. Furthermore, periodic arrays of metallic nanoparticles (of which our nanowire array is a 2-dimensional counterpart) have been reported to display sharp peaks in the extinction efficiency, due to the coupling of the localized surface plasmons supported by each of the single nanoparticles via the diffraction orders of the grating [197, 198], that lead to $Q-$factors up to 30 times higher than those featured by the individual constituents [199]. The high temporal confinement of these *lattice plasmons* enables an increase of the density of optical states and results in an improvement of light extraction [200] as well as in giant near-field enhancements [201].

Importantly, it has been noted that the radiative resonances arising for either the nanoslit array and for the nanowire array discussed above appear slightly redshifted with respect to the first Rayleigh anomaly, which is the position at which the first diffraction order becomes radiative in direction of the plane of the array. This spectral feature is related to the refractive index of the dielectric host in which the structure is embedded, the angle of incidence of the illuminating radiation, and the grating period [202, 203]. Therefore, by manipulating the geometry of the array, the resonance wavelength associated to both classes of extended plasmonic modes can be easily tuned.

In order to optimize the optical amplification of these localized resonances, spectral matching of the gain medium spectrum and the resonance wavelength λ_R is desirable. The spectral profile of gain can be described by a Lorentzian lineshape (see Eq. 2.19):

$$\mathcal{L}(\omega) \sim \frac{\Gamma_e/2}{(\omega-\omega_e)^2+(\Gamma_e/2)^2} \tag{4.1}$$

Thus, we are interested in tuning the maximum of this curve at $\lambda = \lambda_e = 2\pi c/\omega_e$ (the *emission line*) of a suitably chosen gain medium to the maximum of the passive resonance: $\lambda_e = \lambda_R$. A realistic description of the non-linear optical response of this medium is given by Eq. (2.19), together with rate equations (2.23)-(2.26), with the following selection of parameters: $\lambda_a = 680$ nm, $\lambda_e = 710$ nm, $\tau_{21} = 500$ ps, $\tau_{32} = \tau_{10} = 100$ fs, $\Gamma_a = \Gamma_e = 1/(20\text{ fs})$, $\sigma_a = 3.14 \times 10^{-16}$ cm^2, and $\sigma_e = 2.43 \times 10^{-16}$ cm^2. These values model accurately the electronic properties of Rhodamine-800 dye molecules [100] as an optically-pumped four-level gain medium. We also chose a realistic value of the total density of molecules $N_{tot} = 3 \times 10^{19}$ cm^{-3}.
As discussed above, the modification of the geometrical parameters characterizing the system enables varying the resonance to the desired location. By means of eigenmode FEM calculations, we found the following combination of parameters that yields the desired wavelength for the nanowire array: $p = 434$ nm, $w = 122$ nm, $h = 75$ nm. In addition, for the nanoslit array, we found: $p' = 436$ nm, $w' = 380$ nm, $h' = 75$ nm. In order to compare the lasing performance of both active structures, we fix the active layer thickness such that the same volume of gain material is featured for both structures, leading to the following values: $t = 187$ nm and $t' = 208$ nm. In what follows, we study the response of both the nanowire array and the nanoslit array in the optical linear regime, with the selection of parameters above.

4.2.1. Nanowire array.

In order to study the optical response of these systems in the linear regime, we first analyze the passive configuration of the considered structures, for which the concentration of dye molecules of the gain medium is negligible. By means of frequency-domain FEM simulations, we compute the absorption, transmission and reflection spectra of the structures above when probed under E_x-polarized normal incident light. Figure 4.2 shows that the nanowire array structure with the above selection of parameters presents a resonant behavior at the wavelength $\lambda = 710$ nm, characterized by a maximum in the computed absorption and a minimum in the reflection spectrum. This response is adscribed to a lattice plasmonic mode which is caused by the coupling of individual localized surface plasmons (LSPs) of each nanowire via the diffraction modes of the grating. As a consequence, the resonance arises at a wavelength close to the Rayleigh anomaly,

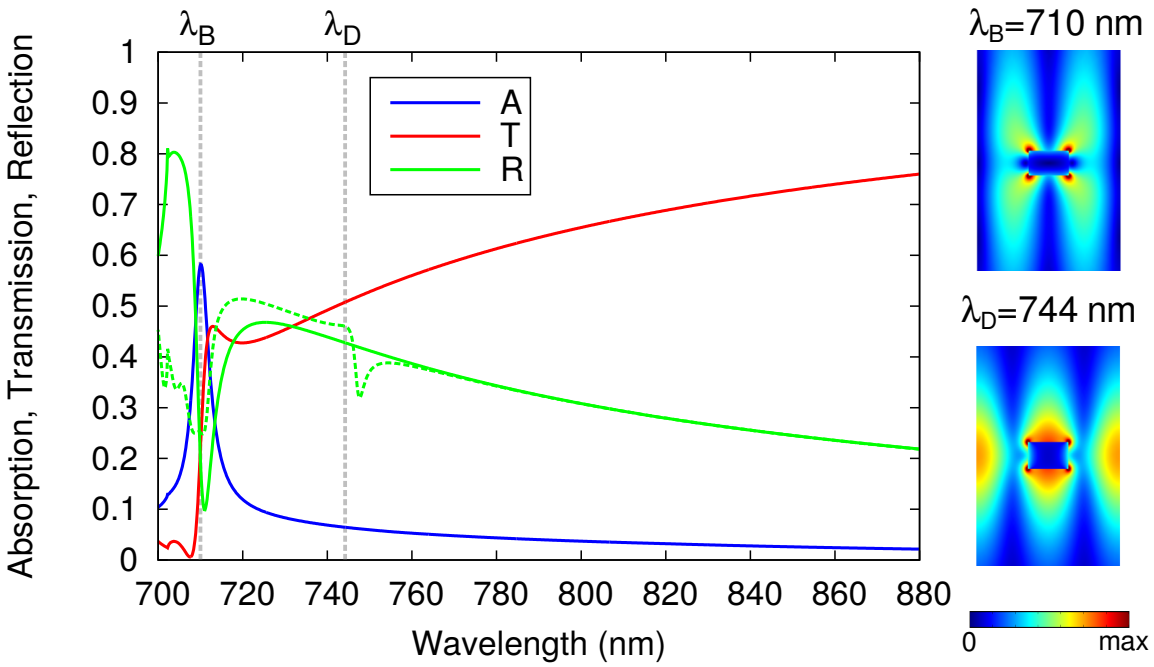

Figure 4.2: Passive response of the nanowire array in the optical linear regime, geometrically designed to tune the bright resonance wavelength to the laser emission line. Absorption (blue line) spectrum, zeroth-order transmission (red line) and reflection (green line) spectrum of the nanowire-array considered. Dashed green lines display the reflection spectrum for an incident angle of 1°. Dashed grey vertical lines mark the spectral location of the modes found by eigenmode FEM calculations. Right panels show the $E-$field distribution of the bright mode at the wavelength λ_B (upper panel), and the dark mode at λ_D (lower panel), respectively.

$\lambda_B \gtrsim \lambda_{RA} = n_h p = 703$ nm. The electric field norm distribution is depicted at the right upper panel of Fig. 4.2 for a unit cell, showing that the coupling of the impinging radiation to this radiative mode causes subwavelength confinement within the active areas with an extended distribution along the plane of the array.

Complementarily, we performed separate eigenmode FEM simulations, that reveal the presence of an additional non-radiative mode at $\lambda_D = 744$ nm. This additional *dark* mode is unable to couple to the incoming external radiation in the given situation, due to symmetry reasons, and it is thus insensitive to it. By examining the mode profile (right lower panel of Fig. 4.2), we find again a confined mode in the vertical direction and extended in the plane of the array, with high field-enhancement at the areas in which spatial $E-$field intensity is low for the *bright* mode at $\lambda_B = 710$ nm. This behavior is in agreement with previous studies on the emergence of lattice resonances in nanoparticle arrays. Indeed, the appearance of bright and dark lattice modes is also found, via the

opening of a band gap [204].
Eigenmode simulations also allow to quantify the temporal confinement of the resonances, in the absence of external stimulii. For the nanowire array under study, we calculate the $Q-$factor of the corresponding plasmonic modes, which is in close connection with their inherent losses. Namely, the dark mode is found to display higher $Q-$factor accordingly to its non-radiative nature: $Q = 286$ while for the bright mode it is obtained: $Q = 144$. It is worth discussing whether this dark mode could play a role in the active system, by polarization mixing effects that could modify the laser light polarization with respect to that of the pump or the plasmonic resonances of the system. In order to get insight in the polarization properties of this mode, we illuminated the structures with TM polarized light with an incident angle of 1° with respect to the normal. Dashed green line from Fig. 4.2 shows the reflection spectrum calculated for this situation, which reveals the presence of an additional dip at $\lambda \approx 750$ nm, accounting for coupling of far-field light to the mode D. In a similar fashion, we illuminated the structure with either normal and non-normal TE incident light, without finding remarkable spectral features. Therefore, we expect the polarization of the corresponding laser emission to be transversal-magnetic.

4.2.2. Nanoslit array.

The corresponding absorption, transmission, and reflection spectra calculated for the nanoslit array (see Fig. 4.3, left panel) under the same conditions reveals a more complex situation, with two resonant modes excited at the wavelengths $\lambda_{B1} = 710$ nm and $\lambda_{B2} = 787$ nm. As discussed above, periodic arrays of nanoapertures feature resonant modes that can display mixed character between a surface plasmonic mode (confined mainly at the surface of the metallic slabs) and a cavity Fabry-Perot mode inside the slits. Here, we find that the mode at λ_{B1} is mainly due to the coupling of two plasmonic modes at both interfaces (see right upper panels from Fig. 4.3), while the resonant pattern λ_{B2} reveals confinement within the apertures. Remarkably, this configuration also presents the emergence of dark modes as it is revealed by means of separate eigenmode calculations, at wavelengths $\lambda_{D1} = 743$ nm and $\lambda_{D2} = 757$ nm. By inspection of the $E-$field spatial distribution (right lower panels of Fig. 4.3), it is shown that plasmonic modes arise at both surfaces of the metallic slabs, coupled through the metal due to the plasmon penetration depth. These resonances display the same symmetry properties as shown in Chapter 3 (see Section 3.2.2) for the long-range and short-range surface plasmons supported by thin metallic films. Finally, as before, we calculate the $Q-$factor of the corresponding modes, showing $Q = 130$ and $Q = 61$ for the bright modes arising

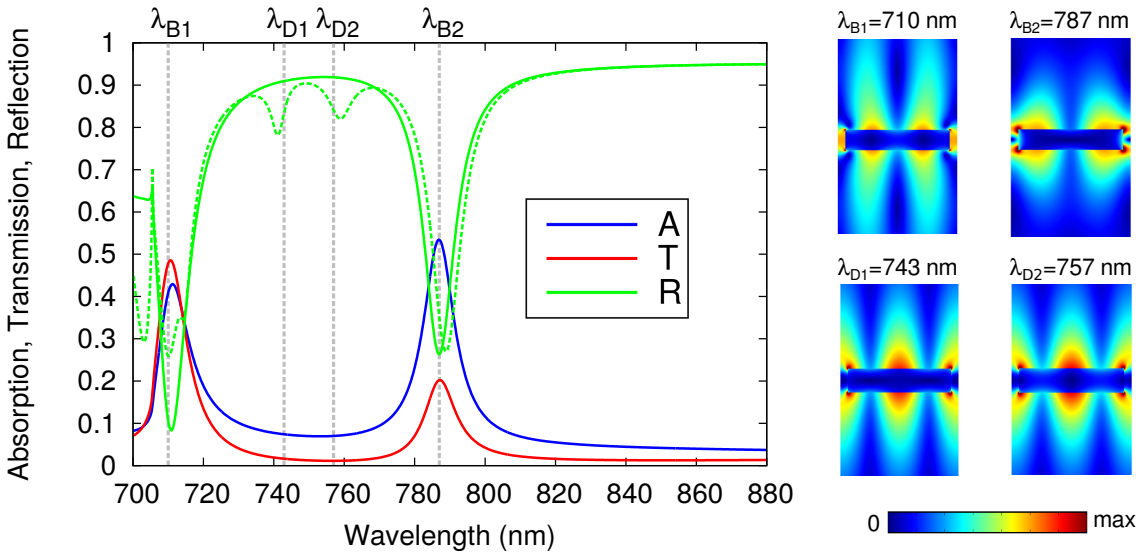

Figure 4.3: Passive response of the nanoslit array in the optical linear regime, geometrically designed to tune the dark resonance wavelength to the laser emission line. Absorption (blue line) spectrum, zeroth-order transmission (red line) and reflection (green line) spectrum of the nanowire-array considered. Dashed green lines display the reflection spectrum for an incident angle of 1°. Dashed grey vertical lines mark the spectral location of the modes found by eigenmode FEM calculations. Right panels show the $E-$field distribution of the bright modes at λ_{B1} and λ_{B2} (upper panels), and the dark mode at λ_{D1} and λ_{D2}, respectively (lower panels).

at λ_{B1} and λ_{B2}, and $Q = 215$ and $Q = 77$ for the dark modes at the wavelengths λ_{D1} and λ_{D2}, respectively.

Finally, as we did with the nanowire array, we test the polarization of the dark modes when probed with non-normal TM incident radiation. Dashed green line from Fig. 4.3 shows the presence of two additional dips in the reflection spectrum, accounting for coupling of far-field light to the modes D1 and D2. As before, no appreciable spectral features were found for TE polarization, discarding polarization-mixing effects in laser light emitted by the active configuration.

4.3. Active plasmonic crystals.

We now turn to the comparison of the lasing performance of the active counterparts of the two systems presented above. In order to analyze the complex spatio-temporal nonlinear dynamical behavior of the considered systems, we make use of the time-dependent generalization of FEM introduced in Chapter 2 (Section 2.3), for which the field equa-

tion of the vector potential is solved in the time domain around the relevant absorption and emission frequencies, through the amplitudes $\mathbf{A}_a(\mathbf{r},t)$ and $\mathbf{A}_e(\mathbf{r},t)$, respectively (see Eq. 2.81). We simulate the active counterpart of the structures above with a molecule number density of $N_0 = 3 \times 10^{-19}$ cm^{-3}, being illuminated now by a continuous-wave pump at $\lambda_p = \lambda_a$, where $\lambda_a = 2\pi c/\omega_a$ is the wavelength associated to the absorption frequency of the chosen dye molecules. This creates a boundary condition on the field amplitude $\mathbf{A}_a(\mathbf{r},t)$. Moreover, in order to account for spontaneous emission, we define a plane wave impinging on the structures at the frequency ω_e, of amplitude much smaller than the pump. We have checked numerically that this small seed excitation does not alter the physical results by varying its duration once the steady-state is reached at the lasing regime. Finally, in order to account for the nonradiative quenching of the emitters located close to the metal surfaces, a gap of 10 nm (with the same refractive index n_h as the host) in the active medium is assumed around the metallic regions of the studied systems.

Note that frequency-pulling effects are included in our formalism through an additional harmonic time dependence in the slowly varying amplitudes $\mathbf{A}_{a,e}(\mathbf{r},t)$, i.e., $\mathbf{A}_{a,e}(\mathbf{r},t) = \tilde{\mathbf{A}}_{a,e}(\mathbf{r},t)\exp(i\Delta\omega_{a,e}t)$, with $\Delta\omega_{a,e}$ being the frequency shift with respect to the corresponding carrier frequency $\omega_{a,e}$. This enable us to establish the following time-dependent definition of eigenfrequency:

$$\omega_L(t) \equiv \left\langle -\frac{\partial_t \mathbf{A}_e(\mathbf{r},t)}{i\mathbf{A}_e(\mathbf{r},t)} \right\rangle \tag{4.2}$$

where the bracket accounts for spatial averaging over the gain medium. This eigenfrequency accounts for both the emission frequency and possible frequency-pulling shifts as discussed above.

4.3.1. Optical amplification in plasmonic crystals.

We first focus on optical amplification, prior to the lasing regime, in this class of systems, for which both the nanowire array and the nanoslit array yield similar results. We pump these structures with normal incident E_x-polarized light at the absorption frequency, which creates a non-uniform $E-$field profile that determines the spatial distribution of gain of the active medium, and thus, the amount of effective optical gain that the gain medium is able to provide. Figures 4.4 (a) and (c) render the population inversion (calculated at $t = 40$ ps, prior to the lasing regime of both systems) at this frequency

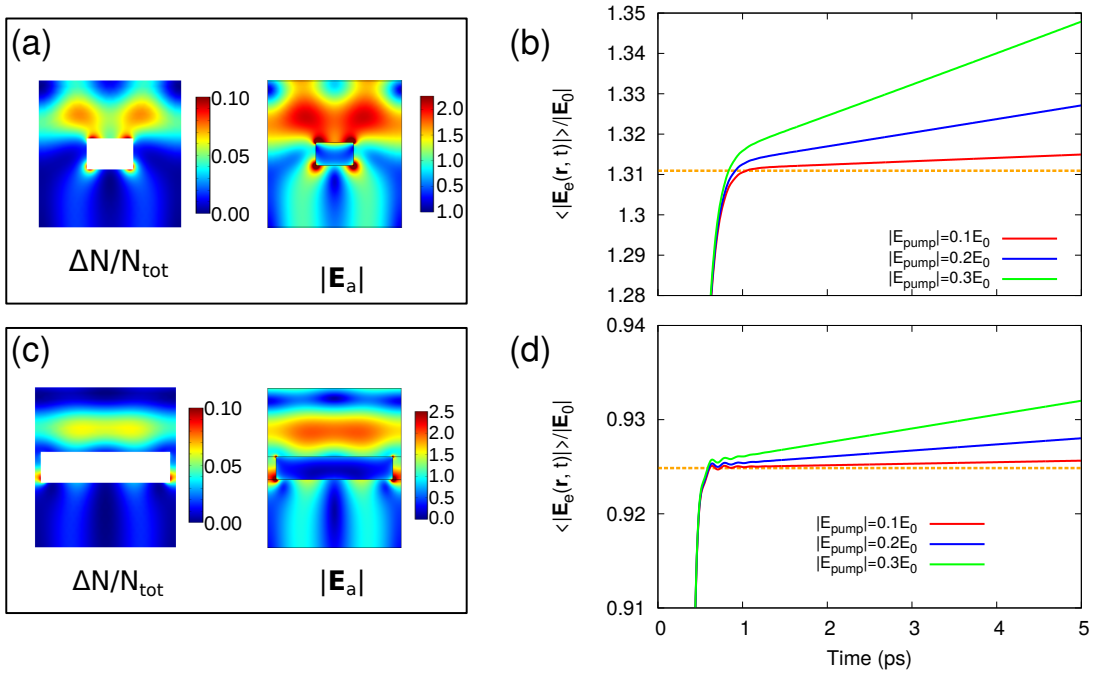

Figure 4.4: Optical amplification in plasmonic crystals. (a) Population inversion (left panel) calculated at $t = 40$ ps, and $E-$field amplitude at the absorption frequency ω_a (right panel), normalized to the incident pump amplitude, for the nanowire-array. (b) Time-evolution of the ω_e component of the calculated $E-$field (spatially averaged over the computational domain), $\langle|\mathbf{E}_e(\mathbf{r}, t_{sdst})|\rangle$, for values of the pump amplitude $|\mathbf{E}_{pump}| = 0.1E_0$ (red line), $|\mathbf{E}_{pump}| = 0.2E_0$ (blue line), and $|\mathbf{E}_{pump}| = 0.3E_0$ (green line) for the nanowire array. Orange dashed line marks the value of the average field intensity in the passive structure. (c) Population inversion (left panel) calculated at $t = 40$ ps, and $E-$field amplitude at the absorption frequency ω_a (right panel), normalized to the pump amplitude, for the nanoslit-array. (d) Time-evolution of $\langle|\mathbf{E}_e(\mathbf{r}, t)|\rangle$ for the nanoslit array, with similar considerations as noted for panel (b).

(see left panels), showing that it follows the pattern dictated by the field amplitude $\mathbf{E}_a = -\partial_t \mathbf{A}_a$ (right panels from Figs. 4.4 (a) and (c)). Under the presence of the field at the emission frequency ω_e, the inversion is forced to decay locally through stimulated-emission, giving rise to a field distribution $\mathbf{E}_e = -\partial_t \mathbf{A}_e$, with the profile of the bright modes arising at this frequency.

By tracking the near $E-$field amplitude evolution with time, the increase of optical gain in the system leads to an enhancement of the optical response at the emission frequency. We first examine the time-dynamical behavior of the nanowire array, depicted in Figure 4.4 (b). The average field amplitude, given by the computed spatial average $\langle|\mathbf{E}_e(\mathbf{r}, t)|\rangle/E_0$, is shown from $t = 0$, and the pump is initialized tens of femtoseconds

after. Here, E_0 is the *saturation electric field*, defined as $E_0 = 2\hbar\omega_a/(\epsilon_0 c n_h \tau_{21}\sigma_a)$, which is a quantity that depends only on the intrinsic electronic properties of the gain medium. In particular, the value of E_0 corresponds to the magnitude of the pump electric field ($|\mathbf{E}_{pump}|$ or E_{pump} used indistinctly in this chapter) at which the electronic population of the ground state is depleted to one half of its initial value (i.e. at which $N_0 = 0.5 \times N_{TOT}$). When pumped, $\langle|\mathbf{E}_e(\mathbf{r},t)|\rangle$ smoothly grows up from zero and stabilizes in a linear slowly growing trend around the time $t \simeq 1$ ps. By increasing the pump strength $|\mathbf{E}_{pump}|$, it is found that the system is able to evolve from an absorbing regime, in which the absorption of the dye molecules leads to a lower steady-state value of $\langle|\mathbf{E}_e(\mathbf{r},t_{sdst})|\rangle/E_0$ than expected for the passive case (marked by a dashed orange line), to a regime of optical amplification in which the average $E-$field response is amplified with respect to the passive case. Same time-dynamical behavior applies for the nanoslit-array (see Fig. 4.4(d)), although quantitative differences appear. At this point, it is already evident that the nanowire array displays higher optical response for the same value of the applied pump, due to the reduced losses of the radiative lattice plasmon mode to which the emission of the dye molecules is tuned. Pumping harder and during longer operational times (within the continuous-wave regime) will allow to reach the lasing regime in these classes of systems, which is studied next.

4.3.2. Lasing dynamics and multimode operation.

Nanowire array.

Here we analyze the conditions for lasing action in the considered active plasmonic crystals. For definiteness, we first focus on the nanowire array. Continuous-wave pumping of the structure with normal incident E_x-polarized light leads to a further increase of the optical gain provided by the gain medium, which enhances its optical response until both the radiative and dissipative losses of the passive system are overcome. Upper left panel from Figure 4.5 shows the lasing dynamics displayed when illuminating the structures with a pump strength of $E_{pump} = 0.75E_0$ and the set of electronic parameters for commonly used organic dye molecules acting as a gain medium. Noticeably, for this experimental set of parameters, the emission line is $\lambda_e = 710$ nm, and coincides with the wavelength of the bright resonance of the passive system: $\lambda_e = \lambda_B$. The time-evolution of the average lasing field amplitude $\langle|\mathbf{E}_e(\mathbf{r},t)|\rangle$ for this situation shows the canonical signatures of the lasing dynamics, characterized by sudden peaks of the signal that settle down to steady-state values for long times. This spiking behavior comes from the

non-instantaneous interaction of the population densities of the four-level system and the electric field of the lasing plasmonic resonance: When the losses are overcome, the near-field intensity is dramatically enhanced, leading to an initial exponential increase in the quantity $\langle|\mathbf{E}_e(\mathbf{r},t)|\rangle$. However, this outburst is accompanied by a destruction of the local population inversion at the areas in which the lasing field is highest, causing the available effective gain to decrease to values below the lasing threshold, and the field intensity is suddenly depleted. This process is successively followed until the steady-state is reached.

In order to get insight into the lasing dynamics, we also calculate the time-dependent eigenfrequency of the lasing field, given by expression (4.2). This allows us to track variations of the operating frequency as the system undergoes laser oscillations. Such effects can be present, for instance, due to frequency-pulling [61]. In this case (see Fig. 4.5(a)), the value of the eigenfrequency is initially given by the emission frequency, defined within our numerical formalism, and does not show any departure in time from the passive position of the bright mode (marked by the red dashed line in this panel), pointing to the fact that the single-mode lasing action of this plasmonic resonance is taking place. Inset of the Fig. 4.5(a) displays the steady-state $E-$field amplitude distribution, showing a clear correspondence with the expected profile of the bright mode (see Fig. 4.2).

Up to now, we have shown the lasing dynamics associated to the excitation of bright plasmonic resonances, for which we have purposedfully selected the geometrical parameters of the nanowire array. It is of interest to achieve full control of the lasing properties of the considered plasmonic crystals, in such a way that the efficiency and the lasing threshold are optimized. The efficiency of the gain provided by the active medium is ruled by both the temporal confinement, given by the $Q-$factor of the resonant mode, and its localization inside the active medium, given by the spatial integral of the local gain [70]:

$$g_{loc}(\omega,\mathbf{r},t)=\frac{K_e\mathcal{L}(\omega)|\mathbf{E}(\omega,\mathbf{r})|^2\Delta N_e(\mathbf{r},t)}{2\Gamma_e\int_V u\,(\omega,\mathbf{r})\,d^3\mathbf{r}} \tag{4.3}$$

where $\mathcal{L}(\omega)$ is the Lorentzian emission line (4.1), u is the electromagnetic energy density, K_e is the coupling strength to the local electric field (2.20), and ΔN_e is the population inversion.

From expression 4.3, it is clear that the gain profile plays a role on the lasing properties. Namely, varying the emission wavelength of the four-level emitters, λ_e, enables to achieve spectral alignment of the gain profile with the position of the passive resonances, which

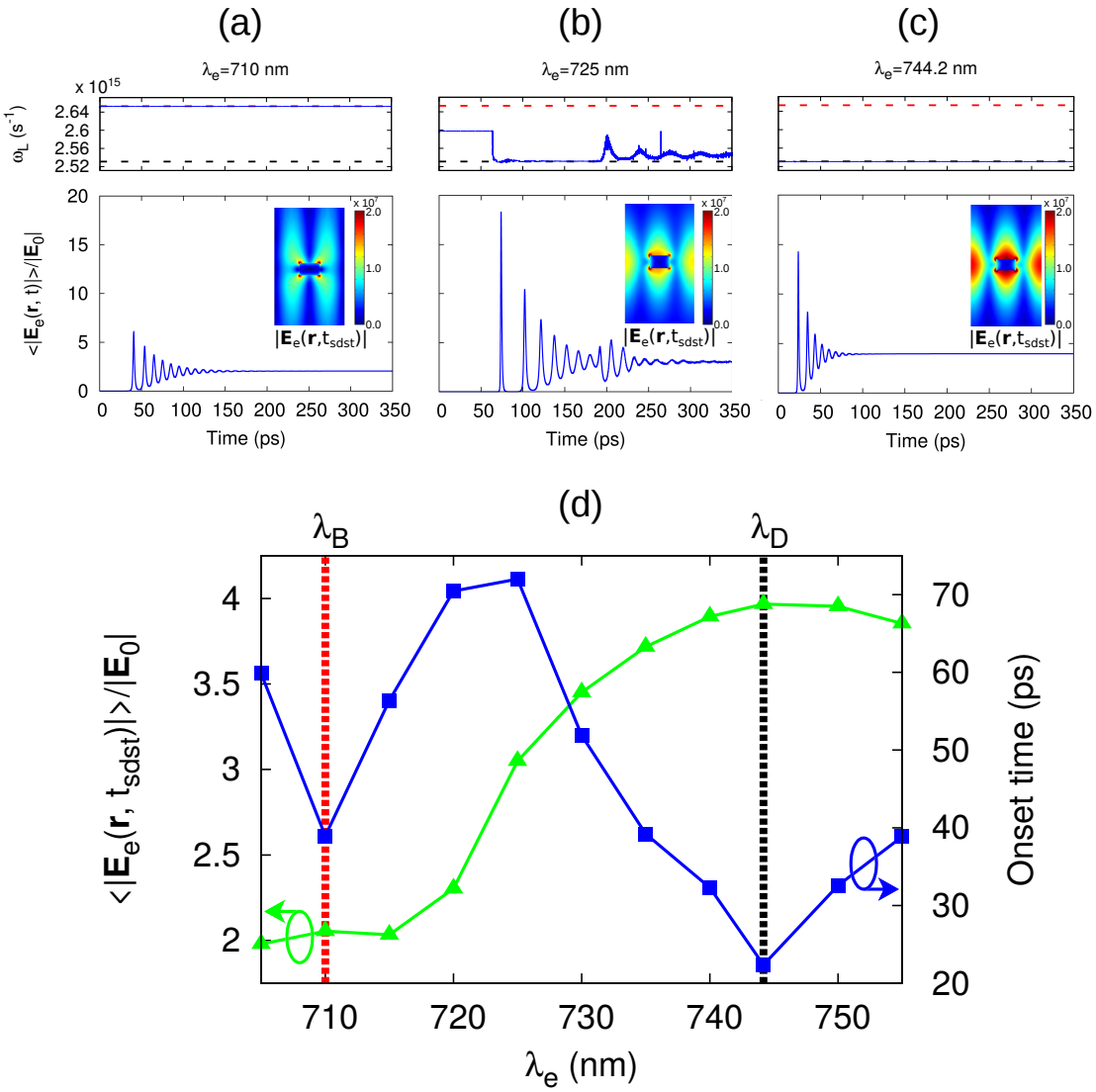

Figure 4.5: Lasing dynamics and steady-state characteristics of the nanowire array. Panels (a)-(c): Time evolution of the ω_e-component of the calculated $E-$field (spatially averaged over the computational domain), $\langle|\mathbf{E}_e(\mathbf{r},t)|\rangle$, along with the time-evolution of the corresponding eigenfrequency ω_L, for three different values of the emission wavelength: (a) $\lambda_e = 710$ nm, (b) $\lambda_e = 725$ nm, and (c) $\lambda_e = 744$ nm . Insets depict the $E-$field amplitude distribution $\mathbf{E}_e(\mathbf{r}, t_{sdst})$ at the steady-state. The wavelength and amplitude of the pump field are, respectively, $\lambda_p = 680$ nm and $E_{pump} = 0.75E_0$ (E_0 is the saturation electric field of the gain medium). The displayed results correspond to the nanowire array considered in Fig. 4.2. (d) Computed steady-state values for $\langle|\mathbf{E}_e(\mathbf{r},t)|\rangle$ (green triangles, left y axis) and lasing onset times (blue squares, right y axis) as a function of the emission wavelength λ_e, as obtained for the same system as in the panels (a)-(c). In all the panels, dashed red and black lines mark the spectral position of the passive bright and dark plasmonic resonance, respectively.

in turn allows to modify the laser emission and select the mode that undergoes laser oscillations. In order to test this possibility, we carried out a series of numerical experiments in which the emission line λ_e, is varied continuously from $\lambda_e = \lambda_B$ to $\lambda_e = \lambda_D$. The parameters accounting for the electronic properties of the gain medium, as well as the pump strength: $|\mathbf{E}_{pump}| = 0.75E_0$, remain unaltered from the case $\lambda_e = \lambda_B$ analyzed above. As expected for a large enough amplitude of the optical pump, all cases display the canonical ultrafast laser relaxation oscillations in the average lasing field amplitude $\langle|\mathbf{E}_e(\mathbf{r},t)|\rangle$, characteristic of the time-dynamical transition to the lasing regime. For all these cases, the steady state has already been reached at $t \simeq 350$ ps. In particular, the case $\lambda_e = \lambda_D$ (see Fig. 4.5(c)) presents very similar signatures than displayed for $\lambda_e = \lambda_B$. However, the eigenfrequency time-dependence reveals that lasing action is now attributed to the dark mode, characterized in this panel as a dashed black line. In addition, the inset depicts the $E-$field profile in the steady-state, corresponding to the dark mode plasmonic resonance displayed in Fig. 4.2 at λ_D. Very importantly, we note that although the dark mode is not accessible by means of coupling normal incident E_x-polarized light, it can reach the lasing regime through stimulated-emission via the gain medium.

We also depict the lasing dynamics for an intermediate wavelength between the location of the bright and the dark mode: $\lambda_e = 725$ nm. In this case, the time-dynamical signatures of lasing action are more complicated, due to the overlap of the spectral gain profile with both the bright and the dark mode, that allow both them to reach the lasing regime and compete for gain. The signatures of this class of mode competition at the subwavelength scale are manifested in time domain through a sudden change of the corresponding $E-$field amplitude oscillations (see the change of behavior in Fig. 4.5(b) at $t \simeq 200$ ps). Similar mode competition phenomena at the subwavelength scale have been reported in Ref. [70] in the case of nanoplasmonic fishnet structures. Interestingly, the eigenfrequency analysis also supports this conclusion: prior to the lasing spikes, it displays the value of the input emission line frequency, while just after the first set of relaxation oscillations, the eigenfrequency acquires the value of the dark mode passive frequency, pointing out that this mode has reached the lasing threshold. From $t \simeq 200$ ps and longer times, the eigenfrequency presents a complex fast-oscillating behavior that arises from the superposition resulting from the mode competition. The inset shows the $E-$field distribution at the steady-state, given by a mixture of both modes in space.

We have checked numerically that moving the emission line λ_e over the considered range of wavelengths enables controlling the laser emission and suppressing lasing action in either the bright or the dark mode despite their inherent losses, or even cause both of

them to surpass the lasing threshold, without varying the pump strength. This also has profound consequences in the steady-state lasing characteristics, through an unexpected nonmonotonic dependence with λ_e of both the steady-state values of the field amplitude $\langle|\mathbf{E}_e(\mathbf{r}, t_{sdst})|\rangle$ and the lasing onset time t_0 (defined as the time at which the first lasing spike occurs). This nonmonotonic dependence is more clearly visualized in Fig. 4.5(d), where the results for $\langle|\mathbf{E}_e(\mathbf{r}, t_{sdst})|\rangle$ and t_0 calculated for a larger number of values of λ_e are displayed. Due to the presence of two plasmonic modes in the system, the steady-state field amplitude (the onset time) displays two local maxima (minima) appearing when λ_e is tuned to λ_B or λ_D (see vertical dashed lines in this panel). Notably, the case $\lambda_e = \lambda_D$ displays a larger (smaller) value of $\langle|\mathbf{E}_e(\mathbf{r}, t_{sdst})|\rangle$ (t_0) than $\lambda_e = \lambda_B$. For intermediate values of λ_e, we observe how the mode competition between the bright and dark modes introduces (at $\lambda_e \simeq 722$ nm) a qualitative change of the dependence of both $\langle|\mathbf{E}_e(\mathbf{r}, t_{sdst})|\rangle$ and t_0 on the emission wavelength. The important point to realize is that a configuration in which the emission from the active medium is tuned to the main resonant feature of the spectrum (i.e., $\lambda_e = \lambda_B$) does not enable accessing the optimal lasing characteristics of this class of systems. As deduced from the above results, the optimal lasing regime is instead associated to the excitation (via the stimulated emission from the gain medium) of dark plasmonic resonances and, therefore, occurs when $\lambda_e = \lambda_D$. Much in the same way as occurs in the case of lasing action assisted by dark Fano modes in photonic crystals [149], laser photons can be emitted from the sides of the system (i.e., emitted in the plane of periodicity), or, alternatively, in the vertical direction (normal to the plane of periodicity) by perturbing the perfectly periodic lattice of the considered plasmonic crystals. Such a possibility was recently demonstrated in a plasmonic lattice, exploiting the finite size of the array, that allowed access to the sustained dark modes by means of a coherent out-coupling mechanism [205].

Nanoslit array.

The interplay of the gain medium with the nanoslit array structure presents a higher degree of complexity from the behavior of the active nanowire array above, due to the presence of four modes sustained by the passive structure (see Fig. 4.3). This leads to the appearance of four regimes of different dominating lasing modes as the emission line wavelength λ_e of the gain medium is varied across the spectral location of the corresponding passive resonances.

Fig. 4.6(a)-(c) shows the time-dynamical evolution of the average emission field amplitude $\langle|\mathbf{E}_e(\mathbf{r}, t)|\rangle$ for representative values of λ_e ranging from $\lambda_e = \lambda_{B1}$ to $\lambda = \lambda_{B2}$.

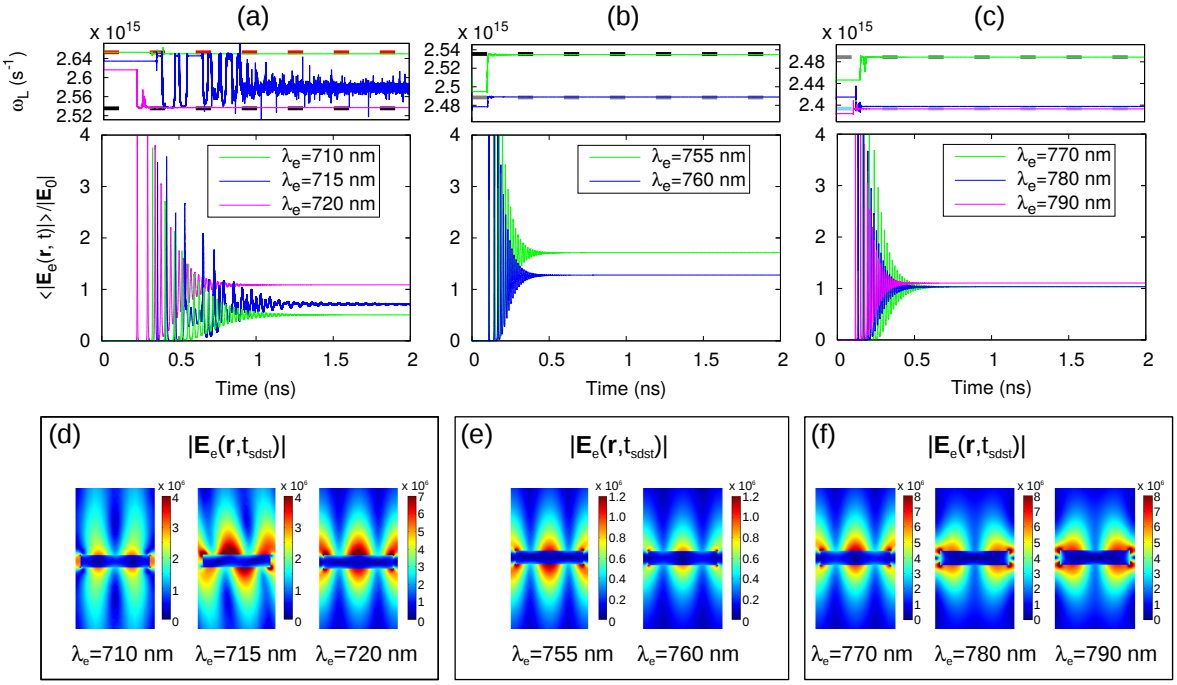

Figure 4.6: Lasing dynamics of the nanoslit array. Panels (a)-(c) Time evolution of the emission component of the calculated $E-$field (spatially averaged over the computational domain), $\langle|\mathbf{E}_e(\mathbf{r},t)|\rangle$, along with the time-evolution of the corresponding eigenfrequency ω_L, for values of the emission wavelength ranging from $\lambda_e = 710$ nm to $\lambda_e = 790$ nm. Dashed red, black, grey and light blue lines mark the eigenfrequency of the passive resonances B1, D1, D2 and B2, respectively. Panels (d)-(f) depict the $E-$field amplitude distribution $\mathbf{E}_e(\mathbf{r},t_{sdst})$ in the steady-state, at the corresponding analyzed values of λ_e. The wavelength and amplitude of the pump field are, respectively, $\lambda_p = 680$ nm and $|\mathbf{E}_{pump}| = 0.65E_0$ (E_0 is the saturation electric field of the gain medium). The displayed results correspond to the nanoslit array considered in Fig. 4.3.

We pump this nanoslit array with normal-incident continuous-wave light, with the same polarization as for the nanowire-array, and amplitude $|\mathbf{E}_{pump}| = 0.65E_0$. As we will see, this pump strength allows all the modes to reach the lasing regime when tuning the emission line to their corresponding passive spectral position, while partially preventing multimode effects that could difficult our analysis.

By numerically tuning the emission line to the bright plasmonic mode: $\lambda_e = \lambda_{B1}$, we obtain a set of spikes in the time-dependent average field amplitude $\langle|\mathbf{E}_e(\mathbf{r},t)|\rangle$ (see green line at the lower panel from Fig. 4.6(a)), that eventually settle down to reach a steady-state, generally for longer times than for the nanowire-array. We already noted that these relaxation oscillations are a signature of single-mode lasing in this class of systems. The

eigenfrequency dependence with time is sketched in at the upper panel in Fig. 4.6(a)) (green line), revealing that the characteristic frequency of laser oscillations corresponds to the frequency of the passive bright plasmonic resonance B1 (see red dashed line at the upper panel in Fig. 4.6(a)). This fact, together with the with the $E-$field intensity sketches in the steady-state (Fig. 4.6(d), left panel), which correspond to the the bright plasmonic mode at $\lambda_e = 710$ nm shown in Fig. 4.3, present clear evidence that the bright mode is lasing.

Shifting the emission line towards higher wavelengths causes other modes to come into play. Already for $\lambda_e = 715$ nm, the time-dynamics of $\langle|\mathbf{E}_e(\mathbf{r},t)|\rangle$ show the presence of mode competition phenomena, with a complex picture displaying more than one set of relaxation oscillations (see blue line at the lower panel in Fig. 4.6(a)), as well as an eigenfrequency time-dependence (see blue line in the upper panel from Fig. 4.6(a)) characterized by fast oscillations alternating between the passive spectral positions of the bright and the dark mode (dashed black line in the upper panel from Fig. 4.6(a)). This mode competition for gain emerges due to the spectral overlap of the gain profile with the dark mode at λ_{D1}. The steady-state $E-$field resulting from this case shows a mixed pattern with contributions from both competing modes (Fig. 4.6(d), central panel).

For $\lambda_e = 720$ nm, the single-mode lasing behavior is again obtained. In this case, we find that the eigenfrequency dynamics (pink line in the upper panel from Fig. 4.6(a)) lead to a shift from the emission line value to the dark mode eigenfrequency. This fact, together with the single-mode signatures in the $E-$field intensity (see Fig. 4.6(a), right panel), mark the onset of a regime in which the dark mode D1 is spectrally favoured over the rest of the modes, due to its enhanced temporal confinement. The steady-state field profile in Fig. 4.6(d) (right panel), further supports the fact that this dark mode is lasing.

Single-mode laser oscillation of the dark mode D1 continues for a wide range of values of the emission line. Figure 4.6(b) shows that this regime is maintained until a value of $\lambda_e = 760$ nm is reached. Although the typical signatures of single-mode laser oscillation remain unaltered, a clear shift of the lasing eigenfrequency, to the dark mode D2 eigenfrequency (grey dashed line in the upper panel from Fig. 4.6(b)), is found. As can be seen in Fig. 4.6(e), the field amplitude patterns of these dark modes are very similar. Nevertheless, let us recall that they follow different symmetry patterns, with respect to the plane of the array, in their E_x, E_z and H_y field components, that allow us to identify them as the counterparts of long-range and short-range surface plasmonic modes (see Chapter 3, Section 3.2.2) in this periodically structured system. Hence, eigenfrequency analysis is determining to reveal the true nature of lasing action for the set of parameters

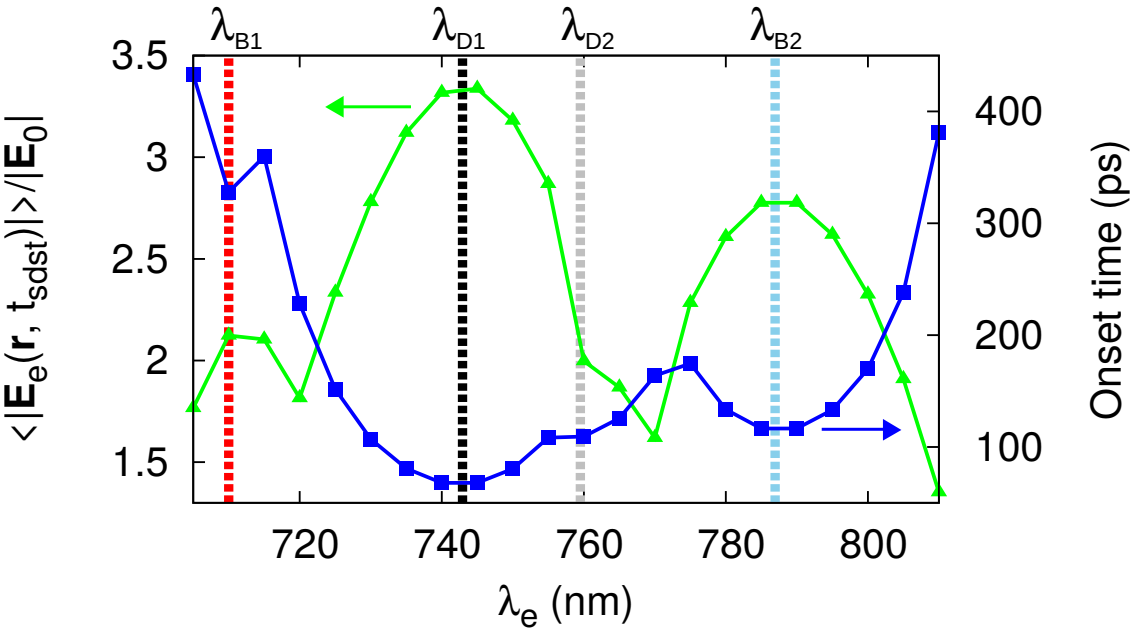

Figure 4.7: Computed steady-state values for $\langle|\mathbf{E}_e(\mathbf{r},t)|\rangle$ (green triangles, left y axis) and lasing onset times (dark blue squares, right y axis) as a function of the emission wavelength λ_e, as obtained for the same system as in Fig. 4.6. Dashed red, black, grey and light blue lines mark the spectral positions of the modes B1, D1, D2 and B2, respectively, and correspond to the eigenfrequency values depicted with the same colours in upper panels from Figs. 4.6(a)-(c).

chosen in this case. A new regime in which lasing action is dominated by the single-mode oscillation of the dark mode D2, thus starts for $\lambda_e = 760$ nm.

We conclude our analysis of the time-dynamical features of the nanoslit-array by moving the emission line towards the position of the radiative mode at $\lambda_{B2} = 788$ nm. The transition from $\lambda_e = 770$ nm to $\lambda_e = 780$ nm leads to a change in the operating eigenfrequency in the lasing regime to that of the passive resonance B2 (see light blue dashed line in the upper panel 4.6(c)), which points out to laser oscillation of this mode. Lower panel from 4.6(c) shows that in all the analyzed cases, the single-mode near-field features remain qualitatively unchanged, despite the very different nature of the oscillating modes. Indeed, note that the Fabry-Perot mode B2 is able to couple to far-field radiation, allowing laser light to be experimentally detected. Figure 4.6(f), showing the steady-state field amplitude patterns for the commented situations, supports our discussion above.

According to the complex spatio-temporal distribution of gain generated by the four modes above that leads to the emergence of distinct lasing regimes, the steady-state characteristics of the nanoslit-array displays a much richer non-mononotonic dependence on the emission line than what we found for the nanowire array in the examined range.

Figure 4.7 shows the onset time (dark blue squares) and the steady-state average field amplitude (green triangles) analogously to those depicted for the nanowire array. As it was found in Fig. 4.5(d) for the nanowire array, the spectral position of the passive resonances is linked to the appearance of maxima (minima) in the dependence of $\langle|\mathbf{E}_e(\mathbf{r}, t_{sdst})|\rangle$ (t_0) of λ_e. The higher losses featured by the mode D2 with respect to D1, together with their spectral proximity, are responsible for the lack of a maximum (minimum) associated to its single-mode lasing regime. The quantitative differences among the different maxima (minima) can be explained as a combination of the associated losses, given by the $Q-$factor, the spectral overlap of the gain profile with the corresponding passive resonances, and the spatial overlap of the plasmonic field profile with the gain medium, which is given by the integral of the local gain defined in Eq. (4.3). In the following subsection, we further provide a semianalytical approach to realize a qualitative examination of the main physical features that enable optimal lasing action.

4.3.3. Enhanced lasing performance assisted by dark plasmonic resonances.

In the last subsection, it was shown that dark plasmonic resonances feature improved lasing properties, as compared with other bright modes displayed by the considered active plasmonic crystals. In particular, we have found that both the dark mode of the nanowire array and the dark mode D1 from the two sustained by the nanoslit array, feature optimal average EM near-field intensity and lasing onset time. This is in contrast with the common belief (for example, see refs. [55, 57]) that tuning the emission line of the dye molecules to the resonant wavelength of the radiative passive resonances will allow to easily reach the lasing threshold. Instead, it turns out that the at the very least, the fact that a bright mode overlaps spectrally with other subradiant modes modifies its bare lasing characteristics.

In what follows, we take a step forward and propose an experimentally realistic situation in which the spectral alignment of the emission line of the gain medium, located at $\lambda_e = 710$ nm [100] for Rhodamine-800 dye molecules, and the eigenfrequency of the dark plasmonic resonances is attained. As discussed, the position of the plasmonic resonances can be controlled by modifying its geometry. By a separate set of additional eigenmode calculations, we found that the desired configuration is obtained for the following selection of parameters: $p = 410$ nm, $t = 200$ nm, $w = 122$ nm, $h = 75$ nm, for the nanowire

array (see Fig. 4.1 for the definition of these parameters). In addition, we found that $p' = 410$ nm, $t' = 224$ nm, $w' = 380$ nm and $h' = 75$ nm enables moving the eigenfrequency of the dark mode D1 of the nanoslit-array to the desired spectral position. As in the previous case, the amount of gain material is the same in both structures, and a layer of quenched molecules is substracted for the gain medium around the metallic surface, accounting for Purcell effect. We thus test the possibility that, by means of the gain medium, the optimal dark modes are able to undergo self-sustained laser oscillations, creating a huge near-field electromagnetic energy source of plasmons which do not couple to the external light. This configuration, which is practically limited by the finite periodicity of a realistic plasmonic lattice, ideally resembles the idea of a dark source of plasmonic modes, or *spaser* [37], which has been longely regarded due to technological applications [206].

Figure 4.8 shows the resulting spectra of absorption (blue line), transmission (red line) and reflection (green line) found for this new combination of parameters for the passive counterparts of both structures. As in the case above, the presented results are obtained for frequency-domain FEM scattering simulations under normal incident E_x-polarized light. We find very similar spectral features as for the former configuration, with resonant peaks that are blueshifted in comparison. Moreover, eigenmode analysis of this new geometry reveals that the dark modes found for the configuration above are still present. As anticipated, the position of the dark plasmonic resonances of interest is now: $\lambda_D = \lambda_{D1} = 710$ nm. For the nanoslit array configuration, a second dark mode emerges at $\lambda_{D2} \approx 733$ nm. In addition, a Fabry-Perot mode appears at $\lambda_{B2} \approx 760$ nm for this configuration. Thus, the ordering of the bright and the dark modes of both structures with wavelength, together with their associated $E-$field distribution and their physical origin, totally resemble those displayed in Figs. 4.2 and 4.3. In addition, the dark modes of both structures can be excited in the same fashion that with the previous selection of geometrical parameters, by illuminating them with non-normal incident TM-polarized light.

Next, we analyze the optical response of the active structures with the new combination of parameters. As before, the system is illuminated by a plane wave that acts as a continuous-wave optical pump illuminating the structures at $\lambda_p = \lambda_a = 680$ nm. Fig. 4.9(a) Sketches the computed average field intensity in the steady-state $\langle|\mathbf{E}_e(\mathbf{r}, t_{sdst})|\rangle$ as a function of $|\mathbf{E}_{pump}|^2$ for both the nanoslit array (red squares) and the nanowire array (blue circles). The results present a linear dependence for high enough value of the pump amplitude E_{pump}, above a lasing threshold value E^{th}_{pump}, which confirms that both systems are able to reach the lasing regime within the considered selection of parame-

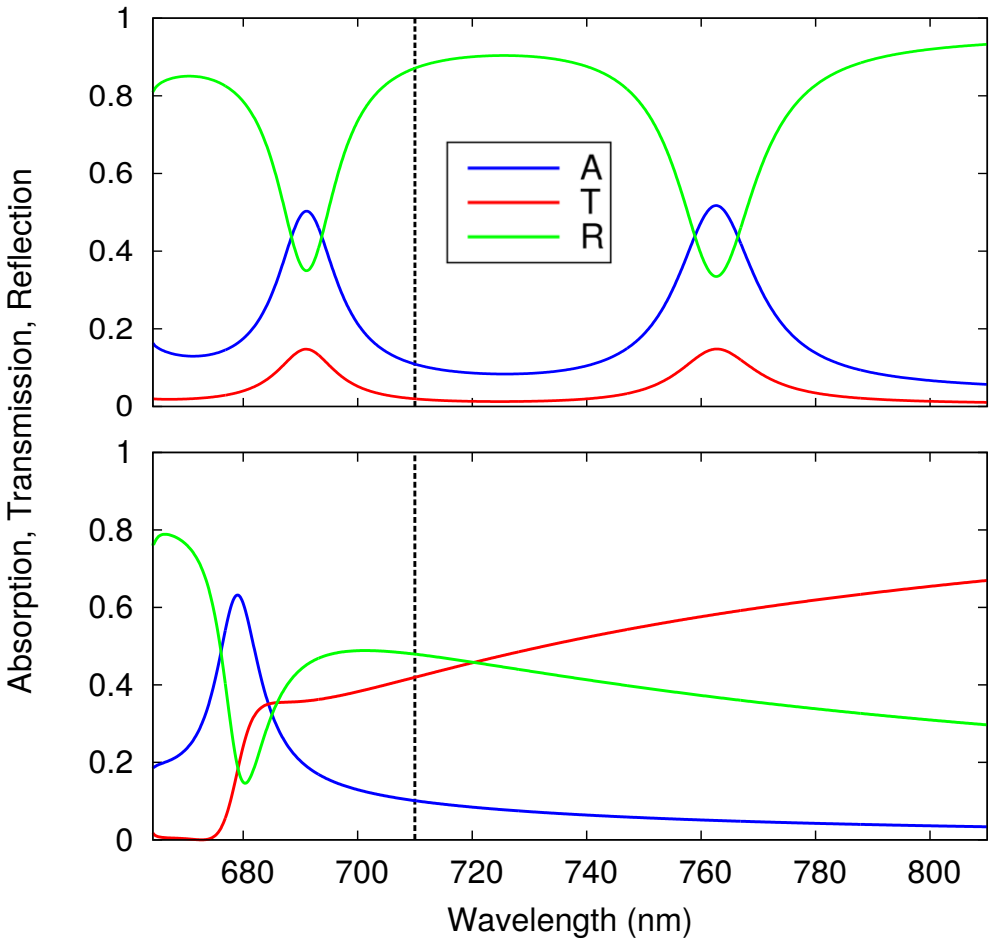

Figure 4.8: Passive response of the nanowire array and of the nanoslit array, geometrically designed to tune the dark resonance wavelength to the laser emission line at $\lambda_e = 710$ nm (see black dashed line). Upper panel: Absorption, zeroth-order transmission, and zeroth-order reflection, for a nanoslit array with the selection of geometrical parameters: $p' = 410$ nm, $t' = 224$ nm, $w' = 380$ nm and $h' = 75$. Lower panel: Absorption, zeroth-order transmission, and zeroth-order reflection, for a nanowire array with the selection of geometrical parameters: $p = 410$ nm, $t = 200$ nm, $w = 122$ nm, $h = 75$ nm (see Fig. 4.1 for the definition of the parameters).

ters. This fact is verified also in the time-dynamics depicted in the inset of Fig. 4.9(a) for the average field amplitude, $\langle|\mathbf{E}_e(\mathbf{r},t)|\rangle$, showing the signatures of single mode lasing discussed above, for both the dark mode D of the nanowire array, and the dark mode D1 displayed by the nanoslit-array. Importantly, as seen in Fig. 4.9(a), the nanowire array features a lower threshold and a significantly larger slope efficiency (by a factor larger than 2) than those obtained for the slit array. In this context, we point out that,

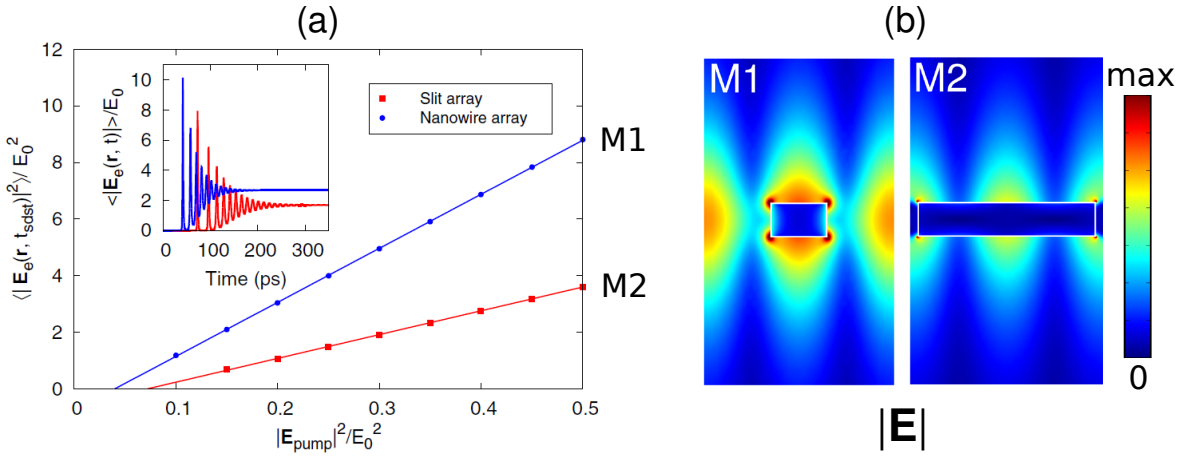

Figure 4.9: Comparison of the lasing characteristics of the nanowire array and the nanoslit array. The geometrical parameters of both structures are optimized so that the corresponding dark plasmonic resonances are tuned to the emission wavelength $\lambda_e = 710$ nm of the gain medium. (a) Computed steady-state values for $\langle|\mathbf{E}_e(\mathbf{r},t)|^2\rangle$ as a function of $|\mathbf{E}_{pump}|^2$, as obtained for the nanowire array (blue circles) and the slit array (red squares). The inset shows the time evolution of the lasing field calculated with $|\mathbf{E}_{pump}|^2 = 0.5E_0^2$. (b) $E-$field amplitude profiles of the active nanowire array (M1) and the nanoslit array (M2) calculated in the steady-state for $|\mathbf{E}_{pump}|^2 = 0.5E_0^2$.

as shown in Ref. [107], the inclusion of (amplified) spontaneous emission would result in the emergence of noise in the emitted laser signal. We do not, however, expect that those effects can change the above conclusion on the comparison of the slope efficiencies. The resulting $E-$field profile in the steady-state, is provided for both structures in Fig. 4.9(b). Its correspondence with the modes D from Fig. 4.2 and D1 from Fig. 4.3 supports the fact that lasing action is indeed enabled by dark plasmonic resonances.

Laser rate-equation analysis.

Finally, to obtain further insight into the physical origin of the above results, we apply to this problem a simple phenomenological model based on a spatially averaged formulation of the laser rate equations (see Section 2.5.2, for the case $\beta_{sp} = 0$). This model provides analytical expressions of the basic characteristics of a plasmonic laser in terms of a small set of effective parameters of the system. Specifically, within this approach, the expressions for the laser slope efficiency (G_e) and the laser pump-rate threshold (R_{th}), derived from the dependence of the photon-number on the external pump rate, can be written as $G_e = Q/\omega_e$ and $R_{th} = \omega_e S_a/(Qv_g\eta\sigma_e\tau_{21})$, respectively. Here Q stands for the

$Q-$factor of the considered modes, S_a is the total area of the active media in the system, and v_g is the group velocity of the plasmonic mode under analysis. The parameter Γ is the so-called confinement factor that quantifies the degree of overlap between the mode profile and the active regions featured by the system, whereas η provides a measure of the spatial-hole burning effects present in the lasing regime in the analyzed structures. The detailed expressions are given by (2.193) and (2.194), respectively.

For definiteness, in the following we focus on the application of this model to the numerical results shown in Fig. 4.9 (a similar analysis could be carried out for results from Figs. 4.5(d) and 4.7). To do that, we first computed the $Q-$factor of the dark mode supported by the nanowire and slit arrays considered in Fig. 4.9, and obtained $Q = 215$ and $Q = 130$, respectively. Then, using the simple expression for G_e provided above, we found that the applied model predicts slope efficiencies of $G_e = 8.1 \times 10^{-14}$ s and $G_e = 4.9 \times 10^{-14}$ s for the nanowire array and slit array lasers, respectively. For comparison, the full numerics yields $G_e = 9.2 \times 10^{-14}$ s for the nanowire array, and $G_e = 4.8 \times 10^{-14}$ s for the slit array. The good quantitative agreement between model and full numerics demonstrates that the observed larger slope efficiency of the nanowire array can be exclusively ascribed to the larger $Q-$factor of its dark mode.

Next, using the steady-state field and population inversion distributions obtained from our full laser simulations, we computed the three parameters Γ, η, and v_g, entering the analytical expression for R_{th} given above. From those values, together with the corresponding Q factors and active material parameters, we obtained $R_{th} = 2.1 \times 10^{21}$ s^{-1} m^{-1} for the nanowire array and $R_{th} = 3.0 \times 10^{21}$ s^{-1}m^{-1} for the slit array. Importantly, in both structures we numerically found similar values of v_g, Γ, and η. This suggests that the physical origin of the smaller lasing threshold displayed by the nanowire array can be also ascribed to the larger Q factor featured by the dark mode decorating that system. We note here that the model results for R_{th} show only qualitative agreement with the full numerics, which predicts $R_{th} = 1.14 \times 10^{21}$ s^{-1}m^{-1} and $R_{th} = 1.48 \times 10^{21}$ s^{-1}m^{-1} for the nanowire array and the slit array, respectively. This points to the fact that, although in this class of systems a phenomenological model can be used to unveil qualitatively the physical origin of the observed lasing behavior, a full ab-initio nonlinear approach is needed to obtain accurate predictions of all lasing characteristics.

4.4. Conclusions.

To summarize, we have examined the lasing features of active structures based on metallic periodic 2D nanostructures, so-called plasmonic crystals. First, we performed a systematic study on the optical properties of the passive counterpart of the considered structures, finding that they feature radiative plasmonic modes which are sensitive to the geometry of the array. In particular, we found that the spectral location of these resonances is controlled by the position of the Rayleigh anomaly. By modifying the geometrical parameters of the structure, we showed that it is possible to find an optimized geometry that tunes the passive resonances of the system to the emission line wavelength of a realistic gain medium (Rhodamine 800), and allows for a fair comparison between both classes of active structures.

Moreover, we found a set of nonradiative or dark eigenmodes in both classes of systems that do not couple to the external radiation. These modes, and their interplay with radiative or bright modes, are relevant for near-field lasing action. In order to analyze the role of the dark modes in the lasing properties of these structures, we numerically varied the emission line of the organic dye molecules. Our nonlinear analysis enabled us to unveil the dynamical time-domain response of the structures as well as its steady-state near-field field distribution, finding that the dark modes enable accessing the optimal lasing characteristics of this class of systems. The dark modes theoretically analyzed here may be exploited in a realistic configuration by means of perturbation of the perfect periodicity of the array.

In addition, we modified the geometrical parameters of both the nanoslit array and the nanowire array to perform a fair comparison of the lasing characteristics when the emission line of the dye molecules is tuned to the preferred dark mode. In this context, we found that nanowire arrays display superior lasing characteristics than nanoaperture arrays, with higher slope efficiency and lower lasing threshold. Due to the fact that the plasmonic modes that enable lasing action are of similar nature than those featured by the 3D experimental structures, we suggest that the results here presented may be naturally extended to the 3-dimensional counterparts studied in previous experimental configurations. These results could be of importance for further development of novel large-area light-emitting structures based on active plasmonic crystals.

5 | Lasing action in core-shell metallic nanoparticles.

5.1. Introduction.

One of the most interesting and feasible proposals to attain nanoscale lasing sources is based on the use of localized surface plasmons (LSPs) arising in subwavelength metallic particles. The main advantage of these systems is their ability to confine light below the diffraction limit, which otherwise can be shrinked down only to micrometer areas. This theoretically conceived idea [37] found its implementation in an experimental milestone based on the use of core-shell metallic nanoparticles, each one of them acting as a single plasmonic laser [39]. These spherical structures, featuring sizes of the order of tens of nanometres, represented arguably the smallest plasmonic nanolasers attained to date. Further work in this line has demonstrated that the considered nanoparticles may offer wavelength-tunable lasing, by means of the nanoparticles elongation into nanorods [69].

Providing insight into laser light generation arising in subwavelength metal particles, as well as guidance for future experimental prospects, makes it necessary to conceive an *ab-initio* theoretical framework that can account for the multilevel structure of the active molecules, the nonlocal optical response of the metallic core, Purcell effect, and saturation or retardation effects, among others [207]. This has motivated a high number of studies based on analytical approaches [208–216]. Furthermore, more detailed numerical studies have been carried out, making use of a formalism based on combining Maxwell-Bloch equations with a Green's function formalism. However, in order to reduce the computational costs, the numerically self-consistent approaches need to be implemented for simplified structures. In particular, lasing action could be simulated only for 1000 dye molecules oriented perpendicularly to the nanoparticle surface [217], which is far from the current standard experimental conditions [39]. Also worth mentioning are fully

quantum numerical calculations [218–220], deriving lasing action from first principles, in terms of quantum correlation functions. Although numerically exact, up to now only 30 quantum emitters have been included in the calculations for a spherical nanoparticle [219].

In this Chapter, we present our contribution to this research line, by introducing a semiclassical study of the lasing properties of core-shell metallic nanoparticles. Our simulations are able to track the nonlinear spatio-temporal dynamics arising from the interaction of the gain medium with the highly nonuniform field distribution of LSPs. We show how the lasing threshold as well as the slope-efficiency of the lasing considered systems can be improved by going from a spherical configuration to an elongated nanorod geometry. Finally, we account for these results using a coupled-mode theory.

5.2. Optical properties of passive core-shell metallic nanoparticles.

Surface plasmonic modes in closed metallic surfaces emerge as non-propagating excitations of the conduction electrons, which couple to incident electromagnetic radiation. Under an oscillating electromagnetic field, the weakly-bound electrons of the metal realize a restoring force, and the system behaves like a forced-damped harmonic oscillator. Hence, for certain oscillation frequencies, a resonance condition is met, leading to a dramatic increase of the optical response that results in enhanced absorption and scattering. This resonance is called the *localized* surface plasmon (LSP). Note that, in contrast to the propagating surface plasmon modes arising at open metallic surfaces (see Section 3.2), these electromagnetic modes can be excited by means of far-field light, without the need of additional coupling mechanisms.

A striking consequence of the localized plasmon resonance is subwavelength scale confinement of the electromagnetic fields at the metallic surface, accompanied of enhanced local field intensity that is the basis of multiple applications like in Raman scattering [221] or near-field imaging [222, 223]. This fact has stimulated research on 3-dimensional metallic nanoparticles supporting localized plasmons. From an experimental standpoint, these structures can be easily obtained, either from chemical synthesis [224, 225] or nanofabrication [226, 227].

In this Section, we review the main properties of LSPs arising in subwavelength metallic nanoparticles as nanospheres or nanorods. In what follows, we provide insight on the

physics of localized surface plasmons that will be of interest for their use as laser cavity modes.

5.2.1. Quasistatic approximation.

In order to illustrate the main features of localized surface plasmons in subwavelength metal particles, we analyze the scattering of a plane wave impinging on a single gold nanosphere of radius R. The action of the electric field causes charge oscillations at the metal surface, and the corresponding optical response of the nanoparticle can be described in terms of a polarization field:

$$\mathbf{P} = \epsilon_0 \alpha \mathbf{E} \tag{5.1}$$

Within the Rayleigh approximation, valid for $\lambda \gg R$, such response is accounted for in terms of the electric polarizability α, given by [228]:

$$\alpha = 4\pi R^3 \frac{\epsilon_m(\omega) - \epsilon_d}{\epsilon_m(\omega) + 2\epsilon_d} \tag{5.2}$$

where $\epsilon_m(\omega)$ is the dielectric function of gold and ϵ_d is the dielectric constant of the non-absorbing medium in which the nanosphere is embedded. The resonant behavior is found for values of the frequency that equals the denominator of (5.2) to zero. In this way, we find the resonant frequency ω_{LSP} of the localized surface plasmon resonance, given by the condition:

$$\epsilon_m(\omega_{LSP}) = -2\epsilon_d \tag{5.3}$$

The above result involves assuming that the size of the particle is small enough to consider that it is subject to an uniform electric field. We call this the *quasistatic* approximation. In this case, the response of the nanoparticle resembles a radiating electric dipole, and the absorption cross section (ACS) is given by [229]:

$$\sigma_{ext} = k\mathrm{Im}\{\alpha\} \tag{5.4}$$

where $k = 2\pi/\lambda$ is the wavevector of the plane wave. Furthermore, the scattering cross section (SCS) is given by [229]:

$$\sigma_{sc} = \frac{k^4}{6\pi}|\alpha| \tag{5.5}$$

And the extinction cross section (ECS) is simply calculated as the sum of both: $\sigma_{ext} = \sigma_{abs} + \sigma_{sc}$. This experimentally accessible magnitude is thus expected to display a strong optical response when illuminated at the resonance frequency ω_{LSP}.
From the expression of the resonance condition above (5.3) we realize that the position of the resonance only depends on the intrinsic optical properties of the metal conforming the nanosphere and the dielectric medium in which it is embedded. There is an obvious interest in designing pathways to change the resonance condition without the need of changing the size of the particle nor its composition. Such a possibility can be realized by coating the nanoparticle with a dielectric shell. In this case, the polarizability can be again calculated by using the Mie theory [230]:

$$\alpha = 4\pi R_{out}^3 \frac{(\epsilon_s - \epsilon_h)(\epsilon_1 + 2\epsilon_s) + f(\epsilon_1 - \epsilon_s)(\epsilon_h + 2\epsilon_s)}{(\epsilon_s + 2\epsilon_h)(\epsilon_1 + 2\epsilon_s) + f(2\epsilon_s - 2\epsilon_h)(\epsilon_1 - \epsilon_s)} \tag{5.6}$$

where $f = R_{out}^3/R_{in}^3$. ϵ_m is the permittivity of the inner core with radius R_{in}. ϵ_s is the permittivity of the outer shell with radius R_{out}. ϵ_h is the permittivity of the surrounding medium. Thus, by evaluating the zeros of this expression, it is apparent that the presence of the coating modifies the position of the resonance with respect to the bare nanosphere (see (5.2)), and it can be easily adjusted by controlling either the shell thickness and its composition.

5.2.2. Localized surface plasmons in core-shell metallic nanoparticles.

Theoretical studies have revealed that the spectral position and quality-factor of LSP resonance depends on shape, size, electron density, electron effective mass, and the media in which the considered nanoparticle is embedded, which characterize the dielectric response of the whole system [228, 229]. All these effects complicate the analytical approach. In fact, Mie theory is only able to treat scattering and absorption of single non-interacting spherical particles [230] in a non-absorbing medium, with accurate results. A further generalization was made by Gans [231] for spheroidal particles. Therefore, for different shapes or interacting particles, numerical approaches must be implemented. As a step towards the nonlinear analysis of core-shell metallic nanoparticles, we introduce here the

general expressions that allow to numerically characterize the linear optical response of the system.

Numerical modeling.

As exposed in Chapter 2 (Section 2.4.1), frequency-domain FEM is able to simulate scattering problems, obtaining numerically exact expressions for the absorption and scattering cross sections, as well as the $Q-$factor. These quantities are calculated as follows. The scattering cross section (SCS) is given by [129]:

$$\sigma_{sc} = \frac{1}{I_0} \int_{\partial\Omega} (\mathbf{n} \cdot \mathbf{S}_{sc}) dS \tag{5.7}$$

Here, $\mathbf{n}$ is the normal vector pointing outwards from the structure, $\mathbf{S}_{sc}$ is the intensity (Poynting) vector, and I_0 is the incident intensity. The integral is taken over a closed surface, far away from the scatterer. The absorption cross section (ACS) equals:

$$\sigma_{abs} = \frac{1}{I_0} \int_{\Omega} q dV \tag{5.8}$$

where q is the power loss density in the particle and the integral is taken over its volume. The extinction cross section (ECS) is simply the sum of the two others:

$$\sigma_{ext} = \sigma_{sc} + \sigma_{abs} \tag{5.9}$$

An important quantity throughout this Chapter is the $Q-$factor, defined as the decay rate of the total electromagnetic energy contained in the cavity, $U_{EM}(t)$, such that [232, 233]:

$$U_{EM}(t) = U_{EM}(0) \exp\left[-\frac{\omega}{Q_{tot}} t\right] \tag{5.10}$$

Here, $U_{EM}(t)$ is the sum of the modal electric-field energy, $U_E(t)$, and the magnetic-field energy, $U_M(t)$, stored in the cavity. It is convenient to separate the scattering and absorption contributions to the $Q-$factor, in terms of the radiated power P_{rad} into free space and the absorption power loss into the metal, P_{abs}, respectively. The radiative power is calculated as follows:

$$P_{rad}(t) = \int_S d^2\mathbf{r} \cdot \langle \mathbf{E}(\mathbf{r},t) \times \mathbf{H}(\mathbf{r},t) \rangle_T \tag{5.11}$$

where S is a closed surface in the far field. The absorption loss power is given by:

$$P_{abs}(t) = \int_V d^3\mathbf{r} \omega \epsilon_0 \mathrm{Im}[\epsilon_m(\omega)] \langle \mathbf{E}(\mathbf{r},t)\mathbf{E}(\mathbf{r},t) \rangle_T \tag{5.12}$$

Over the domains of the simulation cell in which $\mathrm{Im}(\epsilon_m)$ is distinct from zero. For passive structures, they are typically reduced to the metal domains. Therefore, the corresponding $Q-$factors can be calculated as follows:

$$Q_{abs} = \omega \frac{U_{EM}(t)}{P_{abs}(t)}; \qquad Q_{rad} = \omega \frac{U_{EM}(t)}{P_{rad}(t)} \tag{5.13}$$

with the total power being $P_{tot} = P_{abs}(t) + P_{rad}(t)$, and thus:

$$Q = \left(Q_{abs}^{-1} + Q_{rad}^{-1} \right)^{-1} \tag{5.14}$$

where Q is the total $Q-$factor.

From core-shell nanospheres to elongated nanorod geometries.

As a matter of illustrating the main physical features of the localized surface plasmonic mode in subwavelength spherical structures as reviewed above, we present in Fig. 5.1(a) the spectral response of a scattering simulation of a E_x-polarized plane wave impinging on a gold nanosphere of radius R_{in}, coated with a dielectric (SiO_2) shell with refractive index $n_h = 1.46$ and outer radius R_{out}. We assume that the whole structure is embedded in vacuum. Inset from Fig. 5.1(a) renders a schematic view of the considered structure. We chose $R_{in} = 7$ nm and $R_{out} = 22$ nm, so that the case $L_{rod} = 0$ corresponds to the passive counterpart of the experimentally realized spaser considered in [39]. These linear calculations have been performed with the conventional frequency-domain implementation of the finite-element method (FEM) in which a Drude-Lorentz form-fitted to available experimental data is used to model the metallic region of the system [94, 96]. In addition, we use absorbing boundary conditions (PMLs – see Section 2.4.3) placed in the far field to simulate the response of a single isolated nanoparticle.
Using the expression (5.9) and performing the corresponding integrals, the extinction

cross section of this structure (ECS) is calculated (see Fig. 5.1(a)), characterized by a broad resonant peak accounting for the first-order localized plasmon mode, or the dipolar particle plasmon. Panels from Fig. 5.1(b) display the near electric field amplitude at the planes of interest, showing local field-enhancement with an electric dipolar profile. Note that the interaction of the electron gas at the nanoparticle surface with the linearly-polarized $E-$field of the plane wave produces high-intensity lobes in the $x-$direction, in which the electric dipole oscillates. Our numerical framework enables us also to obtain the associated $Q-$factor of the plasmonic cavity. Using expression (5.13), we were able to calculate the scattering and absorption contributions to the $Q-$factor, Q_{rad} and Q_{abs}, respectively. We found a value of $Q_{rad} \simeq 770$ and $Q_{abs} \simeq 8$, obtaining a total associated $Q-$factor given by $Q \simeq 8$. From these values, it is evident that the absorption contribution to the extinction dominates over the scattering contribution, imposing a fundamental restriction given by the high dissipation losses of the metal. As we will see below, the equivalent effective gain to overcome such losses involves increasing the density of the active emitters, which can be difficult in practice: For high-concentrations of the dye molecules, realistic organic dye media may start to form aggregates, which degrades their optical properties (e.g. cross-sections). In order to implement nanolasers based on localized plasmonic modes, it is thus natural to alter the above geometry to reduce the inherent losses.

It has been demonstrated that small metallic nanorods display improved high local-field enhancement compared to spherical nanoparticles of the same size, due to the drastic reduction of the plasmon dephasing rate, because of the suppression of the decay into interband excitations [234]. Motivated by these results, we examine the optical response of isolated core-shell metallic nanorods resulting from the elongation of the spherical structure above, schematically rendered in the inset from Fig. 5.2. The metallic core can be seen as a cylindrical central body of length L_{rod} and radius R_{in}, capped by two hemispherical ends of radius equal to that of the cylindrical middle part. This core is coated by a dielectric shell (of index n_h) featuring the same external shape as the core; that is, the length L_{rod} is maintained but the hemispherical caps now have a radius $R_{out} > R_{in}$. The material properties are the same as for the spherical configuration. We fixed $R_{in} = 7$ nm and reduced continuously the value of R_{out} as L_{rod} is increased, so that the volume of the dielectric shell is the same for all considered configurations. As we show below, this is an important ingredient when analyzing the lasing characteristics of the active structures.

Main panel of Figure 5.2 displays the calculated extinction cross section (ECS) spectra for nanoparticles with different values of elongation, ranging from $L_{rod} = 0$ (i.e., the

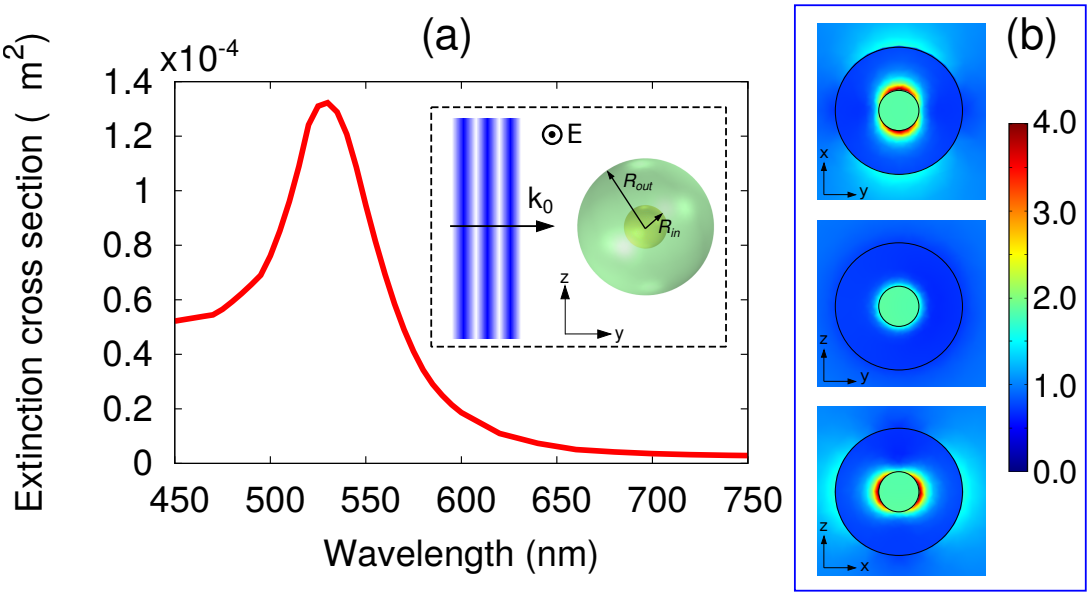

Figure 5.1: (a) Extinction cross section (ECS) spectrum obtained from the scattering simulation of a linearly E_x-polarized plane wave, impinging along the $y-$axis on a gold nanosphere with dielectric shell ($n_h = 1.46$), embedded in air (see a schematic representation in the inset). Values of the geometrical parameters are $R_{in} = 7$ nm and $R_{out} = 22$ nm. (b) $E-$field profiles show the on-resonance electric field norm (normalized to the plane-wave amplitude), characteristic of the LSP dipolar mode, at $\lambda = 528$ nm.

spherical case; see red line) to $L_{rod} = 100$ nm (elongated nanorod configuration; black line). In all cases, the system is illuminated by a plane wave, linearly polarized along the long axis of the nanoparticle and incident normally to that axis. For comparison, the inset of Figure 5.2 displays the ECS spectra for the same configurations shown in the main panel, but now the incident plane wave is polarized perpendicularly to the long axis of the nanoparticle. As observed, for the long-axis incident polarization, the ECS spectra are dominated by a broad resonant peak, whose location and maximum value increase linearly with L_{rod}. This peak corresponds again to the dipolar LSP resonance, from now on referred to as *longitudinal* LSP [228, 229, 235]. The near-field distributions calculated at resonance for three representative values of L_{rod} are shown in Figure 5.3(a) (left, center, and right panels display the cases $L_{rod} = 0$, $L_{rod} = 20$ nm, and $L_{rod} = 60$ nm, respectively). As seen, as L_{rod} grows, the local field enhancement around the caps of the nanorods increases significantly. The local field enhancement obtained by departing from the spherical geometry is accompanied by an increase of the temporal confinement of the electromagnetic (EM) fields in the system: We obtained that the $Q-$factor of the system grows from $Q \simeq 8$ for the spherical case to $Q \simeq 20$ for the larger values of L_{rod}.

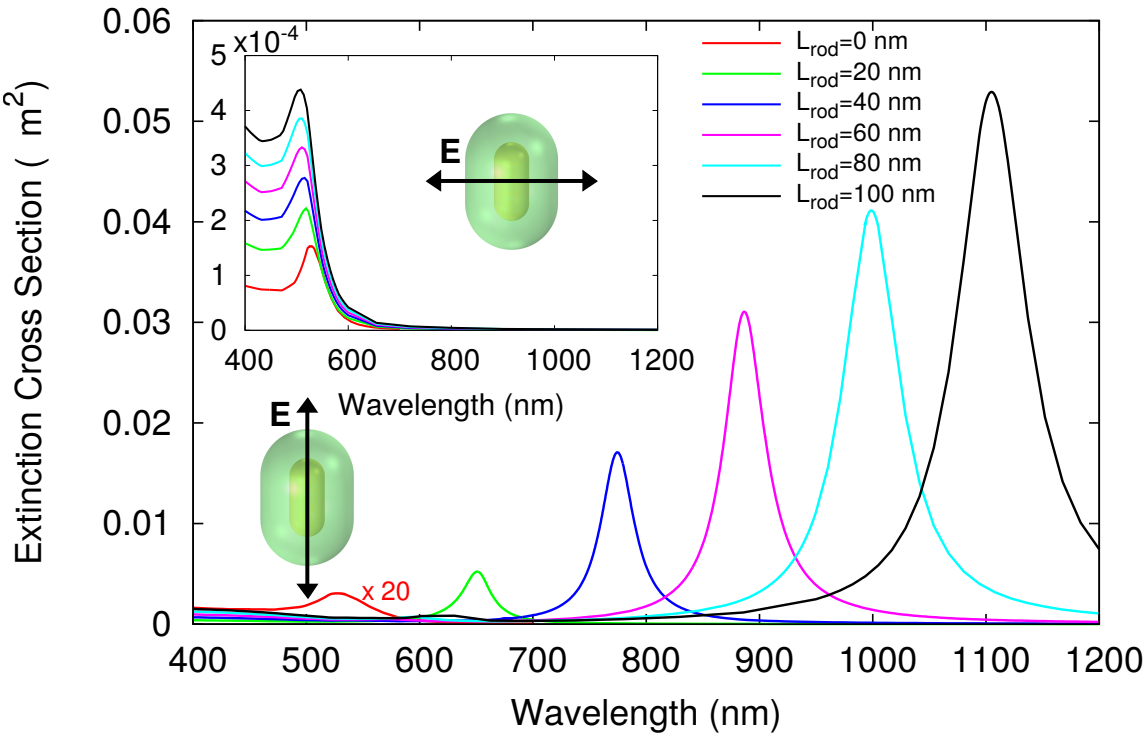

Figure 5.2: Main panel: Extinction cross section spectra calculated for nanoparticles with different values of the nanorod length L_{rod}, going from $L_{rod} = 0$ (spherical case; see red line) to $L_{rod} = 100$ nm (elongated nanorod configuration; black line). For $L_{rod} = 0$, we chose $R_{in} = 7$ nm and $R_{out} = 22$ nm. In the rest of configurations, we kept $R_{in} = 7$ nm but reduced R_{out} as L_{rod} grows, so that the volume of the dielectric shell is maintained for all cases. The system is illuminated by a plane wave linearly polarized along the long axis of the nanoparticle (see sketch in the bottom corner). Inset: Same as main panel but now the incident illumination is polarized perpendicularly to the long axis of the nanoparticle (see sketch included in the inset).

Within this range of nanoparticle sizes, $Q-$factors are dominated by absorption losses; we obtained radiative $Q-$factors of about 2 orders of magnitude larger than absorption ones. A more detailed account of the evolution of Q with L_{rod} will be given below in the context of the coupled-mode theory analysis.

In contrast, for the short-axis incident polarization we obtain much smaller peak values of ECS (see inset of Figure 5.2). These resonances correspond to the so-called dipolar *transversal* LSP resonances [32]. Note that dipolar longitudinal and transversal LSP resonances can be seen as arising from degeneracy breaking (via symmetry breaking introduced by elongation) of their counterpart modes in the spherical case. As observed in the inset of Figure 5.2, the spectral position of the transversal LSP resonant peak remains almost insensitive to L_{rod}. The near-field distributions from Fig. 5.3(b) also point

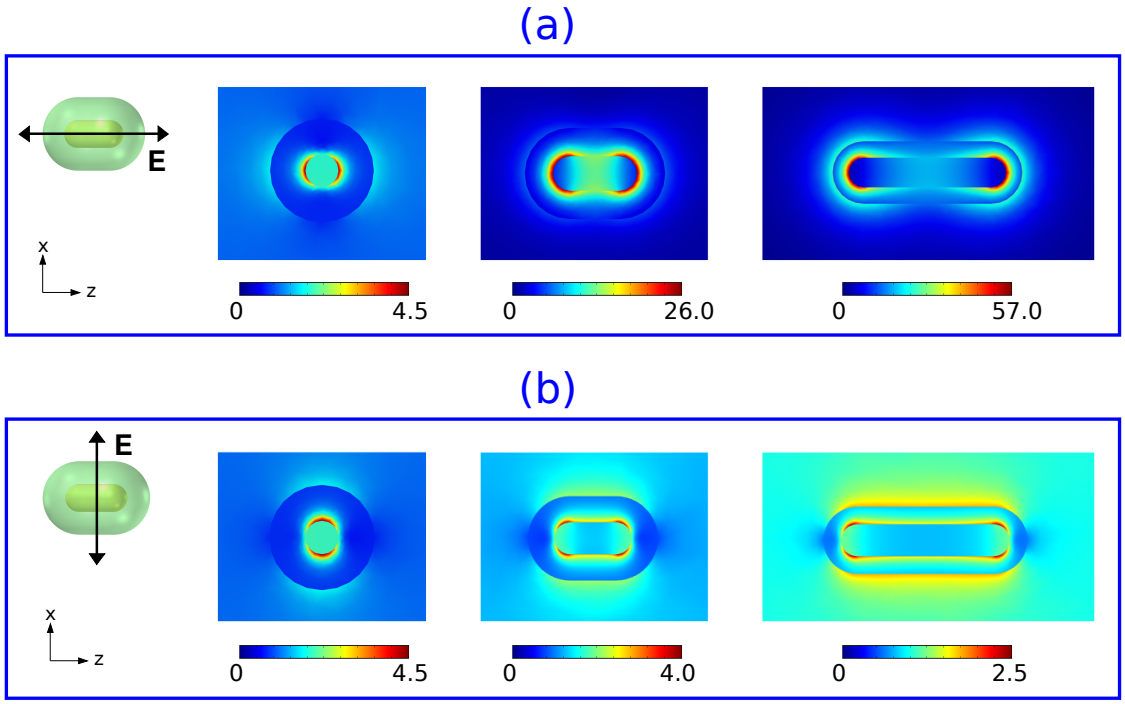

Figure 5.3: (a) Electric-field profiles ($|\mathbf{E}|$, normalized to the incident field) for the structure displayed in Figure 5.2, as computed for different values of the nanoparticle elongation, L_{rod}. Left, center, and right panels correspond to $L_{rod} = 0$, $L_{rod} = 20$ nm, and $L_{rod} = 60$ nm, respectively. The rest of the parameters defining the structure are the same as those considered in Figure 5.2. All cases have been calculated at the corresponding resonant wavelengths and assuming that the incident illumination is linearly polarized along the long axis of the nanoparticle. (b) Same as (a), but now the incident illumination is polarized along the short axis of the nanoparticle. A sketch of the incident polarization and the reference system are included in the leftmost part of both panels. The incident wave propagates along the $y-$direction (perpendicular to the page) for both polarizations.

out that elongating the nanoparticle leads, in this case, to a decrease of the field spatial-confinement and of the corresponding enhancement. In addition, our calculations show that the $Q-$factors of these resonances are also essentially independent of L_{rod} (specifically, we obtained that Q decreases monotonically from $Q \simeq 8$ to $Q \simeq 5$ when L_{rod} is increased from $L_{rod} = 0$ to $L_{rod} = 100$ nm). The described characteristics of longitudinal LSPs, together with the possibility of tuning their spectral response just by varying L_{rod}, make longitudinal resonances ideal candidates for creating nanoparticle-based laser systems. Therefore, in the rest of the work, we focus on this class of plasmonic resonances.

5.3. Active configuration.

We now turn to analyze the active counterparts of the structures above, consisting of the same configuration but now the dielectric shell is doped with 4-level optically pumped quantum emitters. In all cases, we assume that the structure is illuminated by a plane wave of wavelength $\lambda_p = 490$ nm, linearly polarized along the long axis of the nanoparticle. In addition, all laser simulations shown in this work have been obtained by tuning ω_e to the corresponding LSP dipolar resonance obtained for each L_{rod} value. The rest of the parameters modeling the emitters are the following: $\tau_{21} = 1.6$ ns, $\tau_{32} = \tau_{10} = 100$ fs, $\Gamma_a = \Gamma_e = 1/(20fs)$, and $\sigma_a = \sigma_e = 2.55 \times 10^{-16}$ cm^2 (see Eq. (2.19) of the gain polarization field coupling to the electric field, and rate equations (2.23)-(2.26) modelling the emitters, for the definitions of the parameters). These values correspond to the emitters used in Ref. [39]. Finally, the total density of molecules in the gain medium is $N_0 = 3.7 \times 10^{26}$ m^{-3}. We recall that the geometry of the considered configurations is such that the volume of the active shell surrounding the metallic core is maintained for all considered values of L_{rod}. A sketch of the considered system and the performed simulations can be seen in Fig. 5.4. As in the previous Chapters, we model this non-linear optical problem by means of the time-dependent generalization of FEM (see Chapter 2, Section 2.3), in which Maxwell equations solve for the field amplitudes at the absorption and emission frequency, $\mathbf{E}_a$ and $\mathbf{E}_e$, with $\mathbf{E}_i = -\partial_t \mathbf{A}_i$, $i = a, e$ (see Eq. 2.81); self-consistently with the corresponding polarization fields and population densities of the gain medium, and explicitly in the time domain.

Figure 5.5(a) and (b) summarize the lasing dynamics and lasing characteristics of the active counterparts of two of the structures considered in Figures 5.2 and 5.3 (Figure 5.5(a) and (b) correspond to $L_{rod} = 0$ and $L_{rod} = 60$ nm, respectively). Specifically, the main panels of Figure 5.5(a) and (b) show the time evolution of the ω_e component (the lasing component) of the $E-$field amplitude of the system, spatially averaged over the computational domain of our simulations (we denote this quantity as $\langle|\mathbf{E}_e(\mathbf{r},t)|\rangle$). For comparison, the results for several values of the pump intensity $|E_{pump}|^2$ are also included in these panels (red, green, and blue correspond respectively to $|E_{pump}|^2 = 9|E_{th}|^2$, $|E_{pump}|^2 = 16|E_{th}|^2$, and $|E_{pump}|^2 = 25|E_{th}|^2$, with $|E_{th}|^2$ being the threshold pump intensity needed to reach the lasing regime for the corresponding value of L_{rod}). The normalization constant E_0 in Figure 5.5(a) and (b) stand for the saturation electric field of the gain medium, $E_0 = 2\hbar\omega_a/(\epsilon_0 c n_h \tau_{21}\sigma_a)$, where τ_{21} and σ_a are the stimulated emission lifetime and the absorption cross section of the lasing transition, respectively; $\hbar$ is

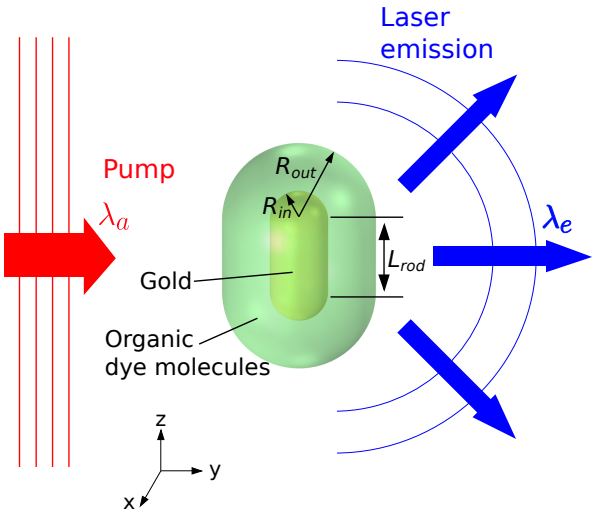

Figure 5.4: Schematic view of the optically-pumped active core-shell metallic nanoparticles under study. It consists of a gold nanorod coated by a dielectric shell (of index $n_h = 1.46$). The shell is doped with organic dye molecules, which upon optical pumping (indicated by a red arrow) can provide enough optical gain to yield laser emission (blue arrows). The geometrical parameters defining the system, as well the reference system used in this Chapter, are also included.

the reduced Planck constant, ϵ_0 is the vacuum permittivity, and c is the speed of light in a vacuum.

As observed in Figure 5.5(a) and (b) (main panels), for both $L_{rod} = 0$ and $L_{rod} = 60$ nm we obtain the canonical features of lasing dynamics, consisting of a series of sudden spikes in the laser field signal that settles down to a steady-state value for long times. As seen, the case $L_{rod} = 60$ nm displays larger steady-state values than those corresponding to the spherical case, which suggests that the elongated geometry exhibits improved lasing properties over the spherical one. This is confirmed by comparing the results of insets of Figure 5.5(a) and (b), which show the steady-state values of $\langle|\mathbf{E}_e(\mathbf{r},t)|\rangle$ as a function of $|E_{pump}|^2$ for $L_{rod} = 0$ and $L_{rod} = 60$ nm, respectively. The observed linear dependence above threshold confirms that the two considered configurations are indeed lasing. In addition, from the displayed results it can be deduced that the nanoparticle with $L_{rod} = 60$ nm features a slope efficiency factor of approximately 300 times larger than that obtained for $L_{rod} = 0$ (we obtained values for the slope efficiencies of 2.1×10^{-24} and 6.5×10^{-22} m^3 for $L_{rod} = 0$ and $L_{rod} = 60$ nm, respectively). At the same time the lasing threshold is reduced by a factor of about 24 in the elongated case with respect

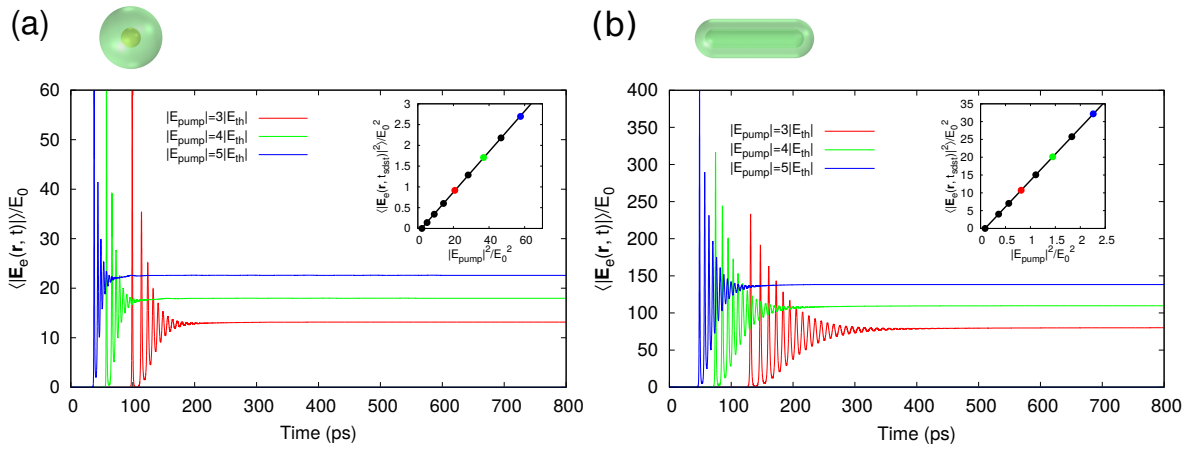

Figure 5.5: (a) Time evolution of the spatially averaged laser field amplitude $\langle|\mathbf{E}_e(\mathbf{r},t)|\rangle$ (normalized to the saturation electric field, E_0), as computed for a spherical spaser based on the active counterpart of the core-shell nanoparticle considered in the inset of Figure 5.1(a). The results for three different values of the amplitude of the pump ($|E_{pump}|$) are displayed (red, green, and blue lines correspond respectively to $|E_{pump}| = 3|E_{th}|$, $|E_{pump}| = 4|E_{th}|$, and $|E_{pump}| = 5|E_{th}|$, where $|E_{th}|$ is the corresponding pump field amplitude at the lasing threshold). In all cases the pump wavelength is $\lambda_p = 490$ nm, whereas the lasing wavelength is $\lambda_e = 530$ nm. (b) Same as panel (a) but now for an active elongated core-shell nanoparticle with $L_{rod} = 60$ nm. In this case, $\lambda_e = 890$ nm (λ_p is the same as in panel (a)). Both panels include schematic views of the corresponding core-shell nanoparticles in the top-left part. Insets of both panels display the steady-state values for the averaged field intensity $\langle|\mathbf{E}_e(\mathbf{r},t)|\rangle$ as a function of the pump intensity $|E_{pump}|^2$ (the coloured circles represent the steady-state values of the corresponding cases with the same color shown in the main panels). For $L_{rod} = 0$, $|E_{th}| = 1.5|E_0|$ is obtained, while $|E_{th}| = 0.3|E_0|$ for $L_{rod} = 60$ nm.

to the spherical one (values of 0.5×10^{12} and 11.9×10^{12} V^2/m^2 were obtained for the elongated and the spherical cases, respectively). A detailed analysis of the variation of these enhancement factors with L_{rod} is provided below.

Let us examine the very interesting comparison of our numerical results for the spherical case with those reported experimentally by Noginov *et al.* For this particular spaser, we found that a density of the molecules of at least 5 times larger than the one used in Ref. [39] is needed in the shell of the structure to reach the lasing regime at the pump intensity values of that work (the number of dye molecules per nanoparticle estimated in Ref. [39] is 2700, which, for uniformly distributed dye molecules over the silica shell, is equivalent to a concentration of $N_0 = 6.3 \times 10^{25}$ m^{-3}). For illustration, inset of Figure 5.5(a), corresponding to pump intensities similar to those considered in Ref. [39], but

a concentration of dye molecules of $N_0 = 3.7 \times 10^{26}$ m^{-3}, show the typical signatures identified as single-particle lasing action. However, for the original value of the molecule-density reported by Noginov *et al.*, we did not observe any of these signatures at those pump intensity levels. This discrepancy may be ascribed to the existence of an additional optical feedback mechanism, such as the reillumination among neighboring nanoparticles in the experimental samples. Alternatively, the experimental results might be explained for a non-uniform distribution of the active molecules over the whole silica shell, such as molecules confined in a layer of smaller volume, adjacent to the metallic core. Finally, we note that the effective reduction of the available gain close to the metallic surfaces of the system (the so-called Purcell effect) cannot explain the difference between our simulations and the experimental data, but rather would actually increase this difference. Instead, we propose below the novel strategy of tailoring the shape of the nanoparticles by elongation, which would lower the lasing threshold and thus enable single-particle laser operation for the combination of pump intensity levels and dye molecule concentration used in Ref. [39].

5.3.1. Time dynamics and spatial hole-burning.

To further characterize how the interplay of the localized plasmonic resonances and the active medium enables lasing action in the considered class of systems, we study the dynamics of the population inversion generated at the corresponding lasing transition. Considering the largest pump intensity of Fig. 5.5(b) ($|E_{pump}|^2 = 25|E_{th}|^2$), in which the nanorod with $L_{rod} = 60$ nm is analyzed, we depict the time-dynamics, between $t = 0$ and $t = 200$ ps, of the spatially averaged population inversion $\langle \Delta N(\mathbf{r}, t) \rangle$ (normalized to N_0; see red line, see left $y-$axis of Figure 5.6(a)), superimposed to the dynamics of the calculated $\langle |\mathbf{E}_e(\mathbf{r}, t)| \rangle$ (gray line, right $y-$axis of Fig. 5.6(a)). As expected for a continuous-wave pump, the average population inversion grows almost linearly prior to the lasing onset, and the active system behaves as an optical amplifier. However, at $t \simeq 50$ ps, the accumulated population inversion allows the system to generate enough optical gain to overcome both the inherent radiative and ohmic losses. Note from Fig. 5.6(a) that at this point, a first lasing spike takes place in the quantity $\langle |\mathbf{E}_e(\mathbf{r}, t)| \rangle$, leading to the local decay of population from the upper-level of the lasing transition through stimulated emission, which results in a depletion of the average population inversion, and a dramatic drop of the laser signal. However, for longer times, depleted population inversion is recovered by means of the continuous pump, and a second laser

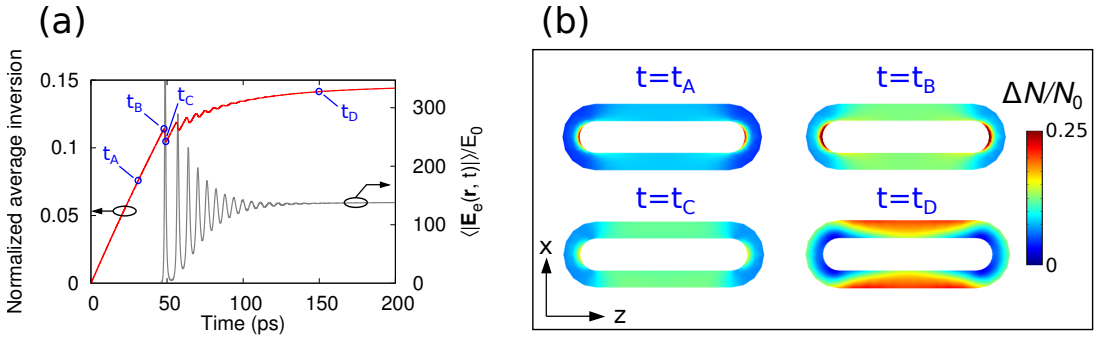

Figure 5.6: (a) Time evolution of the spatially averaged population inversion density, ΔN (normalized to the total density of dye molecules, N_0), for the spaser considered in Figure 5.5(b), as computed for $|E_{pump}| = 5|E_{th}|$ (red line, left axis). For comparison, the dynamics of the corresponding spatially averaged lasing field $\langle|\mathbf{E}_e(\mathbf{r},t)|\rangle$ (normalized to the saturation electric field, E_0) is also included (right axis, gray line). (b) Spatial distribution of the population inversion inside the active shell computed at four representative times (labeled as t_A, t_B, t_C, and t_D in both panels).

light burst emerges when the threshold population inversion is reached again. This set of spiking oscillations in the lasing signal (which are damped with time), followed by the corresponding drops (which are also smoother for longer times) in the average population inversion, are characteristic features of the time-dynamical transition to the lasing regime, and finally settle down to a steady-state in both quantities.

We next provide physical insight into the microscopic origin of the macroscopic behavior described above, by examination of the spatial distribution of the population inversion at the corresponding lasing transition, $\langle\Delta N(\mathbf{r},t)\rangle$, at four relevant values of time. Figure 5.6(b) displays cross-sectional cuts of the considered structure across the $zx-$plane, as calculated for times t_A, t_B, t_C, and t_D in Figures 4(a) and (b). Before the onset of lasing action ($t = t_A$), the population inversion follows the profile of the electric field created at the absorption frequency, ω_a. Once the losses are overcome and lasing sets in, this distribution changes drastically. In particular, after the first lasing peak, the regions with higher field-intensity experience a faster local decrease of the population inversion, due to the enhanced stimulated emission decay in those areas, while areas with lower field-intensity remain almost unaltered. As a consequence, the population inversion at the ends of the nanorod structure is selectively destroyed. This can be clearly seen in the panel of Figure 5.6(b) for the instant of time t_C, as compared with the panel for time t_B. This behavior can be seen as a novel signature at the subwavelength scale of

a macroscopically-observed phenomenon called in traditional lasing systems as *spatial hole-burning* [61, 72, 107]. The spatial distribution of population inversion for long times ($t \geq t_D$) is characterized by a complementary profile of the LSP electric field profile (see rightmost panel of Figure 5.3(a)), with maxima of the population inversion at the minima of the field, and vice versa. This highly nonuniform gain distribution at the nanoscale, and the associated LSP field pattern, characterize the steady-state response of the analyzed structure.

5.3.2. Lasing steady-state characteristics.

We next study the dependence of the steady-state laser characteristics on the elongation of the active nanorods, L_{rod}. Figure 5.7 displays the results of the time-domain simulations above, from which we have obtained the lasing threshold (blue squares; left $y-$axis) and the slope efficiency (red squares; right $y-$axis) as a function of L_{rod} (the emission wavelength is varied accordingly to ensure spectral matching with the passive location of the longitudinal LSP, and the rest of the geometrical and gain medium parameters are the same as those used in Figure 5.5). Both magnitudes have been normalized to the corresponding values for the spherical configuration, and display a non-monotonic dependence with L_{rod}. As the particle is elongated, the lasing threshold decreases for low values of L_{rod}, reaching value for $L_{rod} = 20$ nm which is 0.06 times lower than the threshold for $L_{rod} = 0$. If the particle is further elongated, the threshold becomes roughly insensitive to an increase of L_{rod}. A careful inspection (see inset of Figure 5.7) enables to identify an optimum value of the elongation: $L_{rod} \simeq 50$ nm, for which the optimal lasing threshold is found. On the other hand, the slope efficiency also changes dramatically for increasing values of L_{rod}, reaching a maximum for $L_{rod} = 70$, and a plateau for higher elongation values. Although this high-performance regime occurs at higher values than the one found for the lasing threshold dependence, the presence of a broad interval in which the slope-efficiency and the threshold optimal values coexist, is clearly identified for 60 nm $< L_{rod} <$ 80 nm. In this range, both magnitudes are improved by a factor close to 300 and to 24, with respect to the spherical spaser values, respectively. This result will allow for further engineering and practical implementation of optimized lasers based on subwavelength metallic particles.

Coupled-mode theory analysis.

The traditional schemes used to achieve fundamental understanding on macroscopic laser architectures can be extended to qualitatively explain the overall trend of the numerical

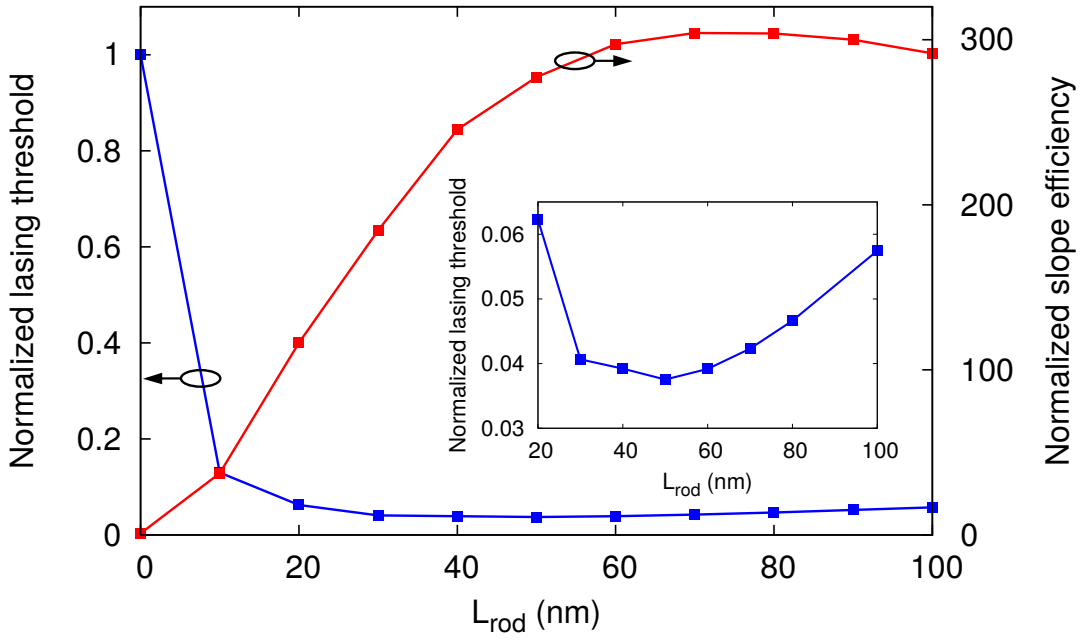

Figure 5.7: Simulation results for the steady-state values of the lasing threshold (blue squares, left axis) and the slope efficiency (red squares, right axis) as a function of the nanoparticle elongation L_{rod}. The same volume of the active shell is assumed for all L_{rod} values. The rest of geometrical and gain medium parameters are the same as in Figure 5.5. Both the lasing threshold and the slope efficiency are normalized to the corresponding values obtained for the spherical configuration ($L_{rod} = 0$). The inset shows an enlarged view of the normalized lasing threshold between $L_{rod} = 20$ nm and $L_{rod} = 100$ nm.

steady-state lasing results above. As discussed, this analysis relies on analyzing the temporal and spatial light field confinement properties of the core-shell passive nanorods, through the quality factor ($Q-$factor) of the longitudinal LSP modes, and the fraction of electromagnetic energy stored in the gain medium (or confinement factor), respectively. With this motivation, we implement here a coupled-mode theory (CMT) analysis based on the analytical expressions (2.187) and (2.188) from Chapter 2 (Section 2.5.1) for the values of the the lasing threshold (R_{th}) and slope efficiency (S), respectively. As stated, our analyis relies on three ingredients: the fraction of the field that resides in the active region of the structure (the confinement factor, ξ_1), the $Q-$factor of the plasmonic mode, and the quantity ξ_2 coming from the spatial averaging of the population inversion distribution, so called spatial hole-burning factor.

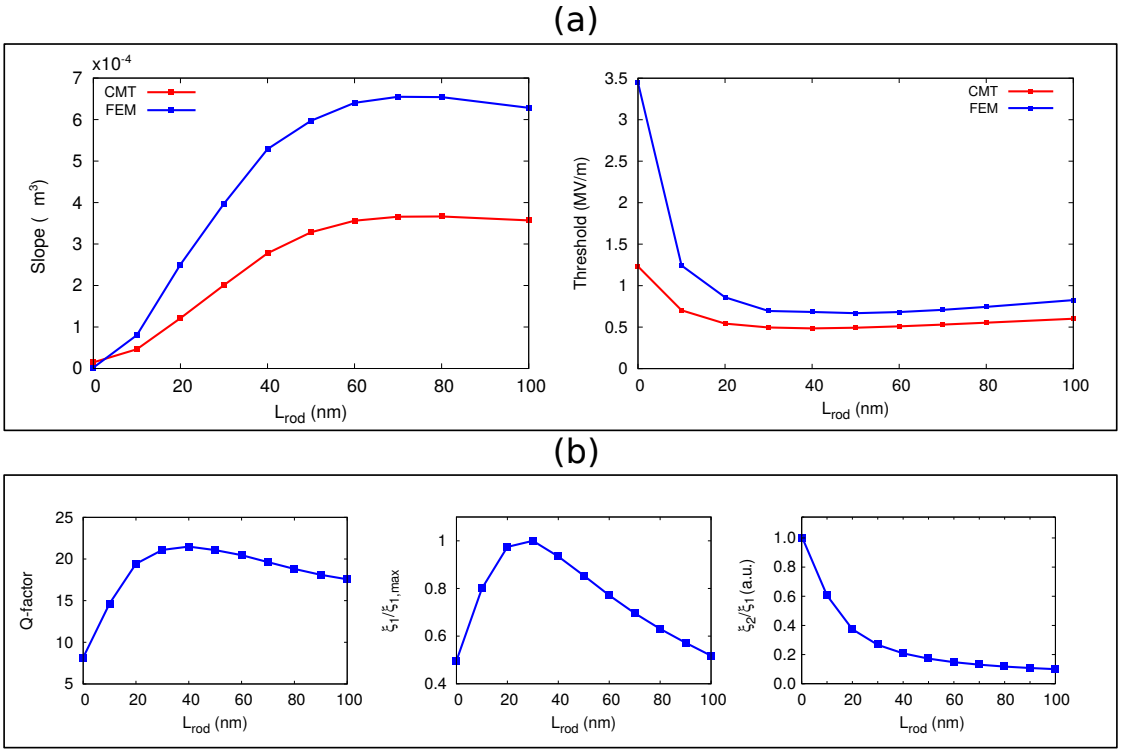

Figure 5.8: Coupled-mode theory vs time-dependent FEM steady-state results. (a) Numerical comparison of the values obtained both for the slope efficiency (left panel) and for the lasing threshold (right panel) as a function of the nanorod elongation. Qualitative agreement is found. (b) $Q-$factor (left panel), normalized confinement factor ξ_1 (central panel), and the ratio ξ_2/ξ_1 (right panel), calculated as a function of L_{rod} from frequency-domain passive simulations.

Figure 5.8(a) (red squares) renders the CMT results for the slope efficiency and the lasing threshold as functions of L_{rod}. For comparison, previous results obtained by full time-domain FEM semiclassical simulations (blue squares) are also shown. Although the numerical values of the full simulations could not be retrieved, the CMT clearly captures the general trend of the lasing characteristics. Importantly, this approach allows to predict the values of L_{rod} for which optimal lasing threshold and slope-efficiency are obtained. Figure 5.8(b) displays the results of the relevant parameters of the CMT as functions of L_{rod}, which allow to give physical insight into the lasing characteristics. We have found numerically that, unlike the ratio ξ_2/ξ_1 (right panel in Fig. 5.8(b)), the $Q-$factor and the confinement factor ξ_1 (left and central panels in Fig. 5.8(b)), are non-monotonic functions of L_{rod}. Hence, in view of the expression (2.188) of the slope efficiency S, we deduce that the dependence of this quantity on the nanorod elongation is given exclusively by the $Q-$factor, which is in agreement with the trend in the left

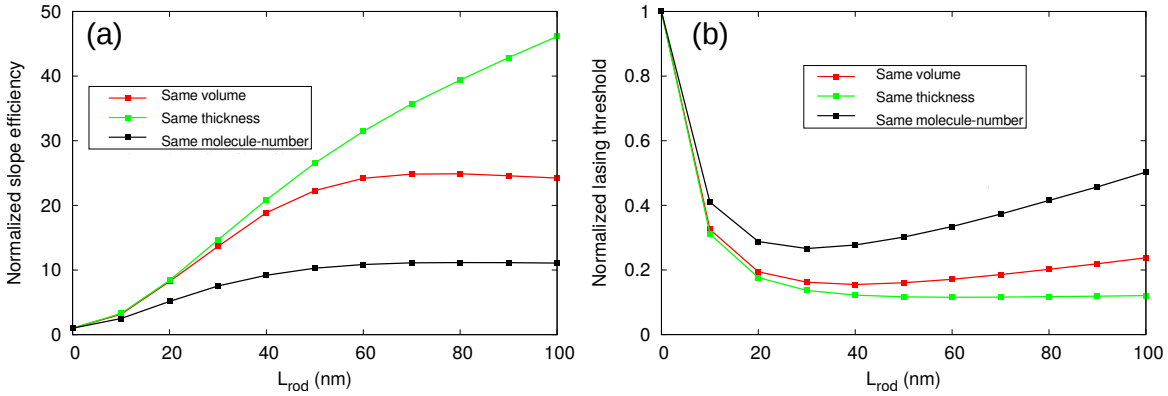

Figure 5.9: Coupled-mode theory results. (a) Normalized slope efficiency calculated for the same configurations as in Figure 5.3(a) (red squares). The panel also includes the results for two alternative conditions to the same-volume condition applied to the shell: green squares correspond to assuming the same shell thickness for all L_{rod} values, whereas black squares correspond to imposing the same molecule number for all elongations. (b) Same as (a) but now for the normalized lasing threshold.

panel of Fig. 5.8(b).

Under examination of the expression (2.187) for the lasing threshold, we find that both temporal and spatial EM field confinement are responsible for the displayed dependence of R_{th} on L_{rod}, since it is inversely proportional to the product $\xi_1 Q$. The central panel of Fig. 5.8(b) shows the computed dependence of ξ_1 on L_{rod}. By inspection of the trends of this magnitude and of Q, it can be seen that the reduction of the lasing threshold for small elongation values is given by the growth of both magnitudes. Moreover, the behavior for larger L_{rod} values is the result of the combined non-monotonic behavior of both Q and ξ_1, giving rise to the aforementioned optimal minimum value of the lasing threshold. In particular, our analysis reveals that the dependence of R_{th} on the nanorod elongation L_{rod} is given by the product $Q\xi_1/\omega_e$, while the rest of the parameters are not functions of L_{rod}. Therefore, the dependence of the lasing threshold for large values of L_{rod} is the result of the combination of both the temporal light confinement properties (given by the $Q-$factor), the spatial field confinement (through the quantity ξ_1), together with the frequency ω_e redshift of the respective lasing LSP modes. We also note that our CMT is a generalization of the conventional approaches followed to characterize macroscopical laser sources, and generalizes previous analytical approaches based on quasi-static descriptions of lasing action [236].

In order to investigate the generality of our findings from a experimental viewpoint, and taking advantage of the fact that CMT can yield qualitative results in a timely

manner, we have applied this approach to two cases that could be of relevance for the practical implementation of single-particle based nanolasers. Namely, we have removed the constraint of setting the volume of the active shell to a constant value for all the considered L_{rod}. Instead, we have considered that the thickness of the active shell (rather than the volume) is fixed for all the values of L_{rod} to $R_{out} = 22$ nm. Green squares in Fig. 5.9(a) and (b) show the corresponding results of the slope-efficiency and the lasing threshold, respectively. In addition, black squares in the same panels are calculated assuming that the density of the organic dye molecules is varied with increasing L_{rod}, so that the number of active emitters is the same for all the elongation values. Despite the differences in the gain medium volume among the different configurations, which in turn lead to relative variations in the magnitude of the slope efficiency and the lasing threshold, our analysis reveals a general trend that is maintained under the analyzed conditions, which ensures the robustness of our numerical results.

5.4. Conclusions.

To summarize, we studied lasing action in isolated core-shell metallic nanoparticles, putting our focus on how the lasing characteristics of this class of structures are influenced by the nanoparticle shape. These structures take advantage of the dipolar resonance displayed by subwavelength particles to provide the feedback for lasing action within a single particle. By fitting the optical and geometrical parameters to those from a recent reference [39], we found that single-particle lasing is not attainable for an uniform distribution of the molecules and the used experimental molecule concentration. We suggest that the observed lasing action may be the result of a non-homogeneous distribution of the dye molecules or by random lasing enabled by multiple-scattering effects of the collection of nanoparticles within the sample. Remarkably, quenching effects coming from Purcell effect cannot alter these conclusions, since the depletion due to the hot spots displayed by plasmonic resonances leads to a lower effective gain than considered here.

The increase of the molecule density up to six times the value from Ref. [39] allows to achieve the necessary effective gain to reach the lasing regime for all the values of the elongation considered for the nanorods. We have analyzed the spatio-temporal dynamics of lasing action in spasers based on core-shell metallic nanoparticles. We have found that both the lasing threshold and the slope efficiency of conventional spherical spasers can be significantly improved simply by elongating the nanoparticle. In this context, we have also found that the enhancement of the laser characteristics is maintained across a broad range of elongation values. Finally, we accounted for these results by implementing a semianalytical coupled-mode theory, based on the spatial averaging of the electromagnetic fields and the population inversion. This analysis enables us to conclude that the origin of the nonmonotonic dependence of the slope-efficiency on the nanorod elongation can be explained in terms of the temporal confinement shown by these structures, while the lasing threshold trend is resulting from a combination of both the temporal and the spatial confinement of the electromagnetic fields within the gain medium. This work could be relevant across a broad spectrum of different research areas, including emerging quantum technologies, photovoltaics, nanoscale microscopy, and molecular sensing.

6 | General conclusions.

6.1. English.

In this thesis, we have studied lasing action emerging in plasmonic nanostructures. We have developed a theoretical formalism based on a time-domain generalization of the Finite Element Method (FEM) that enables us to track the spatio-temporal nonlinear interaction of the electromagnetic field of plasmonic modes and the active medium. Additionally in some cases, we have accounted for these results by introducing different semianalytical formalisms based on a linear treatment of the considered systems, through a spatially-averaged formulation of the Maxwell equations and of the rate equations describing the population dynamics of the gain medium.

As a first step, we have considered active schemes for lasing action based on plasmonic waveguides integrated with a gain medium and enclosed within a feedback mechanism. Two systems are studied, following two breaking research lines in this topic. The first one is a plasmonic waveguide supporting long-range surface plasmon polariton modes, consisting of a thin metallic slab, embedded in a gain medium. For experimentally realistic conditions, we have demonstrated that the considered active structure is able to accumulate the necessary effective gain to achieve optical amplification and loss compensation. Moreover, by delimiting the structure above with a feedback mechanism based on partially reflecting conditions (Bragg mirrors), we found that the system is able to undergo laser oscillations, and presents the steady-state signatures of lasing. In the analysis above, we examined explicitly the influence of Purcell effect, finding that it leads to a reduction of the effective gain for loss-compensation and for lasing action.

The second active plasmonic waveguide studied is a V-Groove channel carved on a metallic surface supporting plasmon polaritons propagating at its bottom, incorporating a semiconducting nanowire that acts both as the active medium, and as the feedback mechanism at its high-refractive index facets. In this case, we showed that the nanowire is able to efficiently couple its laser emission to the modes propagating through the

waveguide, by means of a hybrid V-Groove/Nanowire mode of plasmonic nature. This result was tested in the context of a collaboration with an experimental group, finding good agreement between theory and experiment.

We also studied lasing action in two-dimensional periodic metallic nanostructures, so-called plasmonic crystals. Under an unified perspective, two different limits are studied: nanowire array and nanoslit array. These two systems display radiative plasmonic resonances that can be easily controllable by modifying the period of the array. In addition, they are found to display subradiant, or dark modes, unable to be excited by far-field radiation. We have investigated the active counterparts of these systems, by analyzing their optical properties when they are embedded in a optically-pumped four level gain medium. We have examined the popular belief that tuning the laser emission to the radiative passive resonances will lead to the optimal lasing characteristics. In contrast, we found that dark plasmonic resonances enable accessing an optimal lasing regime, with improved near-field lasing intensity and onset time. Next, in order to perform a fair comparison of the optimal lasing features of both structures, we manipulated their geometrical parameters to tune the laser emission of the active medium to the dark modes, showing that the nanowire array displays larger slope-efficiency and lower lasing threshold.

Finally, we analyzed laser light generation in core-shell metallic nanoparticles, exploiting localized surface plasmon modes, which display a dipolar response, as a feedback mechanism. We have focused on how the lasing characteristics of this class of structures are influenced by the nanoparticle shape, finding that both the lasing threshold and the slope efficiency of spherical nanoparticles can be significantly improved simply by elongating the nanoparticle. The enhancement of the laser characteristics is maintained across a broad range of elongation values. Remarkably, within the current experimental standpoint, single-particle lasing is not expected for core-shell metallic nanospheres. To conclude, we have used an analytical coupled-mode theory to explain these findings in terms of the spatial and temporal light confinement properties of the localized surface plasmon modes supported by the nanoparticles.

6.2. Castellano.

En esta tesis, se ha estudiado la acción láser creada en nanoestructuras plasmónicas. Con ese fin, hemos desarrollado un formalismo teórico, basado en una generalización en dominio de tiempos del método de elementos finitos (MEF) que permite calcular la interacción no lineal, dependiente en el espacio y en el tiempo, de los campos electromagnéticos asociados a modos plasmónicos con el medio activo. Adicionalmente, en algunos casos se ha efectuado un análisis de los resultados según formalismos alternativos, consistentes en un tratamiento en el régimen óptico lineal de los sistemas en cuestión, implementando para ello una formulación basada en promedios espaciales sobre las ecuaciones de Maxwell y sobre las ecuaciones que describen la dinámica de poblaciones del medio activo.

Para comenzar, hemos considerado estructuras activas capaces de desarrollar acción láser, basadas en guías de onda plasmónicas integradas con medios activos, a las que se incorpora un mecanismo de retroalimentación. Se han estudiado dos sistemas, de acuerdo con dos líneas de investigación de vanguardia. La primera es una guía de ondas consistente en una fina lámina metálica, que transporta plasmones de superficie de largo alcance, sumergida en un medio activo. En condiciones experimentalmente realistas, se ha encontrado que la estructura activa considerada puede acumular la ganancia efectiva necesaria para conseguir amplificación óptica y compensación de pérdidas en este sistema. Además, delimitando dicha estructura con un mecanismo de retroalimentación, basado en condiciones de frontera parcialmente reflectantes (espejos tipo Bragg), se ha encontrado que el sistema exhibe oscilaciones láser, y presenta las características típicas de sistemas láser al alcanzar el estado estacionario. Durante dicho análisis, se ha examinado explícitamente la influencia del Efecto Purcell, encontrándose que da lugar a una reducción de la ganancia efectiva tanto en los resultados de compensación de pérdidas como en los calculados en el régimen láser.

La segunda guía plasmónica activa que se ha estudiado es un canal con sección eficaz en forma de V, perforado sobre una superficie metálica, por cuyo vértice se propagan modos plasmónicos. Se incorpora además un nanohilo semiconductor que realiza el papel tanto de medio activo, como de mecanismo de retroalimentación, debido a sus caras delimitantes con alto índice de refracción. En este caso, se muestra que el nanohilo puede acoplar eficientemente su emisión láser a los modos propagantes de la guía de ondas, a través de un modo híbrido de naturaleza plasmónica. Este resultado ha sido contrastado en el contexto de una colaboración con un grupo experimental, encontrándose buen

acuerdo entre teoría y experimento.
A continuación, se ha estudiado la acción láser en estructuras metálicas periódicas bidimensionales, denominadas cristales plasmónicos. Se estudian dos límites bajo un mismo marco: cristal de nano-rendijas y cristal de nanohilos. Estos dos sistemas exhiben resonancias plasmónicas radiativas, que pueden ser fácilmente controladas a través del periodo del cristal. Por otro lado, se encuentra que también exhiben modos no radiantes, u oscuros, incapaces de ser excitados por radiación de campo lejano. Se han investigado las estructuras activas equivalentes a dichos cristales, analizando sus propiedades ópticas cuando se encuentran sumergidas en un medio activo con bombeo óptico, representado por un sistema de cuatro niveles cuánticos. Se ha examinado la creencia común de que sintonizar la emisión láser a la posición de resonancias plasmónicas radiativas de las estructuras pasivas dará lugar a características láser óptimas. En su lugar, se ha encontrado que los modos plasmónicos de tipo oscuro permiten acceder a un régimen láser óptimo, en lo que se refiere a una mayor intensidad de campo electromagnético cercano, y a un tiempo necesario para alcanzar el régimen láser menor. A continuación, para realizar una comparación de las características óptimas láser asociadas a cada sistema, se han manipulado los parámetros geométricos para sintonizar la emisión láser del medio activo a los modos oscuros, llegando a la conclusión de que el cristal de nanohilos ofrece mayor eficiencia y menor umbral láser que el cristal de nano-rendijas.
Finalmente, se ha analizado la generación de luz láser en nanopartículas metálicas con recubrimiento dieléctrico dopado con moléculas orgánicas. Estas estructuras aprovechan los modos plasmónicos localizados, con perfil de tipo dipolar eléctrico, como mecanismo de retroalimentación. Considerando la elongación de las partículas desde un caso esférico hacia una configuración tipo nanovarilla, se ha realizado un análisis de la variación de las características láser de estos sistemas como función de la elongación de la nanopartícula, encontrándose que tanto la eficiencia como el umbral láser mejoran significativamente con la elongación. Dicha mejora se mantiene para un amplio rango de longitudes. Notablemente, en las condiciones experimentales estándar analizadas en la literatura, la acción láser basada en una partícula individual no es esperable para el caso esférico. Para concluir, se ha utilizado una teoría de modos acoplados para explicar estos resultados en términos del confinamiento espacial y temporal de los modos plasmónicos localizados característicos de las nanopartículas.

A | Weak formulation of boundary conditions for a partially reflecting plasmonic cavity.

Here, we discuss the implementation of partially-reflecting boundary conditions at the ends of the waveguide between which LRSPP-propagation takes place. This Appendix connects with Section 2.3.5, in which the weak formulation of boundary conditions is explained in detail, and with Section 3.3.3, that makes use of the resulting weak form expression to recreate optical feedback in a plasmonic waveguide incorporating Bragg mirrors, enabling lasing action.
We recall that the magnetic field $\mathbf{H}$ can be calculated via $\mathbf{A}$ by:

$$\mu_0 \mathbf{H} = \nabla \times \mathbf{A} \tag{A.1}$$

Thus, the boundary term is given by:

$$-\int_{\partial\Omega} d^2 r \tilde{\mathbf{A}} \cdot [\mathbf{H} \times \mathbf{n}] \tag{A.2}$$

For the formulation of the boundary conditions we will assume that the considered plasmon is propagating along the $x-$direction. As an example of how to obtain the correct boundary conditions, we derive the expression for the boundary with an normal vector in $x-$direction. The magnetic field at the boundary is split in three parts:

$$\mathbf{H} = \mathbf{H}^{inc} + \mathbf{H}^{(-)} + \mathbf{H}^{r}, \tag{A.3}$$

where $\mathbf{H}_{inc}$ is an incident field, which can be used to excite the LRSPP. $\mathbf{H}^{(-)}$ is the contribution of the magnetic field at the boundary, which propagates in $x-$direction. $\mathbf{H}_r$ is the reflected part of the field. This reflected field is related to $\mathbf{H}^{(-)}$ via the reflection coefficient r:

$$\mathbf{H}_r = r\mathbf{H}^{(-)} \tag{A.4}$$

Next, we assume that the propagation constant of the plasmon k_x is known. In our numerical simulations, we calculate k_x with the help of eigenmode calculations of the passive system.
If the propagation constant k_x is known, the spatial derivatives of the different contribution of $\mathbf{H}$ can be written as:

$$\nabla \times \mathbf{H}^{inc} = \begin{pmatrix} ik_x \\ \partial_y \\ \partial_z \end{pmatrix} \times \mathbf{H}^{inc};\ \nabla \times \mathbf{H}^{(-)} = \begin{pmatrix} -ik_x \\ \partial_y \\ \partial_z \end{pmatrix} \times \mathbf{H}^{(-)};\ \nabla \times \mathbf{H}^{r} = \begin{pmatrix} ik_x \\ \partial_y \\ \partial_z \end{pmatrix} \times \mathbf{H}^{r} \tag{A.5}$$

Assuming an harmonic time-dependence, we obtain:

$$\mathbf{H}^{(-)} = \frac{1}{i\omega\mu_0}\nabla^{(-)} \times \mathbf{E}^{(-)} \tag{A.6}$$

$$\mathbf{H} - \mathbf{H}^{inc} - \mathbf{H}^{r} = \frac{1}{i\omega\mu_0}\nabla^{(-)} \times \left[\mathbf{E} - \mathbf{E}^{inc} - \mathbf{E}^{r}\right] \tag{A.7}$$

where the contribution of the electric field are defined in the same way as to the ones of the magnetic field. Using:

$$\nabla^{inc} - \nabla^{(-)} = \nabla^{r} - \nabla^{(-)} = 2ik_x\mathbf{x} \tag{A.8}$$

and:

$$\mathbf{E}^{r} = \frac{r}{1+r}\left(\mathbf{E} - \mathbf{E}^{inc}\right) \tag{A.9}$$

we end up with:

$$\begin{aligned}\mathbf{H} &= \frac{1}{i\omega\mu_0}\Big[\nabla^{(-)}\times\mathbf{E} - \nabla^{(-)}\times\mathbf{E}^{inc} - \nabla^{(-)}\times\mathbf{E}^{r} \\ &\qquad + \nabla^{inc}\times\mathbf{E}^{inc} + \nabla^{r}\times\mathbf{E}^{r}\Big] \\ &= \frac{1}{i\omega\mu_0}\left[\nabla^{(-)}\times\mathbf{E} + 2ik_x\mathbf{x}\times\left(\mathbf{E}^{inc} + \frac{r}{1+r}\left(\mathbf{E}-\mathbf{E}^{inc}\right)\right)\right] \end{aligned} \tag{A.10}$$

In the boundary term $\mathbf{H}\times\mathbf{n}$ appears, and, therefore, the first term in Eq. (A.10) is given by $\mathbf{n} = -\mathbf{x}$:

$$\left(\nabla^{(-)}\times\mathbf{E}\right)\times(-\mathbf{x}) = \begin{pmatrix} 0 \\ \partial_y E_x + ik_x E_y \\ \partial_z E_x + ik_x E_z \end{pmatrix} \tag{A.11}$$

Now using again the assumption that the spatial field profile is given by the field profile of a propagating LRSPP, we can express the derivatives by using spatial-dependent functions:

$$\partial_y E_x(x_b, y, z) = f_y(y,z)E_x(x_b,y,z),\ \ \partial_z E_x(x_b,y,z) = f_z(y,z)E_x(x_b,y,z), \tag{A.12}$$

where the boundary is parametrized by $x = x_b$. The functions $f_y(y,z)$ and $f_z(y,z)$ are calculated via eigenmode calculations. Combining now Eqs. (A.10) and (A.12), $\mathbf{H}$ at the boundary can be expressed via known quantities (k_x, f_y, f_z) and the temporal derivative of $\mathbf{A}$ (by applying $\mathbf{E} = -\partial_t\mathbf{A}$). Thus, this formulation of the boundary conditions can be used in finite-elements simulations. In an analogous manner, the boundary conditions for the boundary with an normal vector in positive $x-$direction can be calculated.
For the boundaries with normal vectors in $y-$ and $z-$directions, boundary conditions are used. This boundary conditions are designed to absorb plane waves propagating normal to the boundary. However, given that for sufficient large computational cells these boundaries are reasonable far away from the waveguide (and therefore from the region of high field intensities), the obtained solution is not so sensitive to these boundary conditions.

Bibliography

[1] A. Einstein. The quantum theory of radiation. Physikalische Zeitschrift **18**, 121 (1917). (cited on p. 1)

[2] A. L. Schawlow and C. H. Townes. Infrared and Optical Masers. Phys. Rev. **112**, 1940 (1958). (cited on p. 1)

[3] M.Smit, J. van der Tol, and M. Hill. Moore's law in photonics. Laser. Phot. Rev. **6**, 1-13 (2012). (cited on p. 1)

[4] J. Leuthold, C. Hoessbacher, S. Muehlbrandt, A. Melikyan, M. Kohl, C. Koos, W. Freude, V. Dolores-Calzadilla, M. Smit, I. Suarez, J. Martínez-Pastor, E.P. Fitrakis, and I. Tomkos. Plasmonic communications: light on a wire. Optics and Photonics News **24**, 28 (2013). (cited on p. 1)

[5] M. C. Gather and S. H. Yun. Single-cell biological lasers. Nature Photonics, **5**, 406 (2011). (cited on p. 1)

[6] P.-A. Blanche, A. Bablumian, R. Voorakaranam, C. Christenson, W. Lin, T. Gu, D. Flores, P. Wang, W.-Y. Hsieh, M. Kathaperumal, B. Rachwal, O. Siddiqui, J. Thomas, R. A. Norwood, M. Yamamoto, and N. Peyghambarian. Holographic three-dimensional telepresence using large-area photorefractive polymer. Nature **468**, 80 (2010). (cited on p. 1)

[7] M. T. Hill and M. C. Gather. Advances in small lasers. Nat. Photonics **8**, 908 (2014). (cited on pages 2, 4, 5, and 15)

[8] A. Yang, D. Wang, W. Wang and T. W. Odom. Coherent light sources at the nanoscale. Annu. Rev. Phys. Chem. **68**, 83-99 (2017). (cited on p. 3)

[9] K. Iga. Surface-emitting laser − its birth and generation of new optoelectronics field. IEEE J. Sel. Top. Quant. Electron. **6**, 1201 (2000). (cited on p. 4)

[10] Y. H. Lee, J. L. Jewell, A. Scherer, S. L. McCall, J. P. Harbison, and L. T. Florez. Room-temperature continuous-wave vertical-cavity single-quantum-well microlaser diodes. Electron. Lett. **25**, 1377 (1989). (cited on p. 4)

[11] K. Tai, R. J. Fischer, C. W. Seabury, N. A. Olsson, T.-C. D. Huo, Y. Ota, and A. Y. Cho. Room-temperature continuous-wave vertical-cavity surface-emitting GaAs injection lasers. Appl. Phys. Lett. **55**, 2473 (1989). (cited on p. 4)

[12] M. S. Lebby, C. A. Gaw, W. Jiang, P. A. Kiely, C. L. Shieh, P. R. Claisse, J. Ramdani, D. H. Hartman, D. B. Schwartz, and J. Grula. Characteristics of VCSEL arrays for optical parallel interconnects. Proc. SPIE Fabrication, Testing, and Reliability of Semiconductor Lasers **2683**, 81 (1996). (cited on p. 4)

[13] X. Duan, Y. Huang, R. Agarwal, and C. M. Lieber. Single-nanowire electrically driven lasers. Nature **421**, 241 (2003). (cited on p. 4)

[14] C. Z. Ning. Semiconductor nanolasers. Phys. Status Solidi B **247**, 774 (2010). (cited on p. 4)

[15] R. Chen, T.-T. D. Tran, K. W. Ng, W. S. Ko, L. C. Chuang, F. G. Sedgwick, and C. Chang-Hasnain. Nanolasers grown on silicon. Nature Photonics **5** (2011). (cited on p. 4)

[16] D. Saxena, S. Mokkapati, P. Parkinson, N. Jiang, Q. Gao, H. H. Tan, and C. Jagadish. Optically pumped room-temperature GaAs nanowire lasers. Nat. Phot. **7**, 963–968 (2013). (cited on pages 4, 82, 85, 112, and 117)

[17] D. O'Carroll, I. Lieberwirth, and G. Redmond. Microcavity effects and optically pumped lasing in single conjugated polymer nanowires. Nature Nanotechnology **2**, 180-184 (2007). (cited on p. 4)

[18] A. Polman, B. Min, J. Kalkman, T. J. Kippenberg, and K. J. Vahala. Ultralow-threshold erbium-implanted toroidal microlaser on silicon. Appl. Phys. Lett. **84**, 1037-1039 (2004). (cited on p. 4)

[19] M. Fujita, R. Ushigome, and T. Baba. Continuous wave lasing in GaInAsP microdisk injection laser with threshold current of 40 μA. Electron. Lett. **36**, 790-791 (2000). (cited on p. 4)

[20] A. F. J. Levi, R. E. Slusher, S. L. McCall,T. Tanbun-Ek, D. L. Coblentz, S. J. Pearton. Room temperature operation of microdisc lasers with submilliampere threshold current. Electron. Lett. **28**, 1010-1012 (1992). (cited on p. 4)

[21] C.-Y. Lu, S.-W. Chang and S. L. Chuang. Low-footprint optical interconnect on a SOI chip through heterogeneous integration of InP-based microdisk lasers and microdetectors. IEEE. Photon. Technol. Lett. **21**, 522-524 (2009). (cited on p. 4)

[22] Q. Zhang, S. T. Ha, X. Liu, T. C. Sum, and Q. Xiong. Room-temperature near-infrared high-Q perovskite whispering-gallery planar nanolasers. Nano Lett. **14**(10), 5995-6001 (2014). (cited on p. 4)

[23] J. D. Joannopoulos, S. G. Johnson, R. D. Meade, and J. N. Winn. *Photonic Crystals: Molding the Flow of Light* (Princeton Univ. Press, 2008). (cited on pages 5 and 76)

[24] H. Altug, D. Englund, and J. Vuckovic. Ultrafast photonic crystal nanocavity laser. Nat. Phys. **2**, 484 (2006). (cited on p. 5)

[25] B. Ellis, M. A. Mayer, G. Shambat, T. Sarmiento, J. Harris, E. E. Haller, and J. Vuckovic. Nature Photonics **5**, 297 (2011). (cited on p. 5)

[26] S. Wu, S. Buckley, J. R. Schaibley, L. Feng, J. Yan, D. G. Mandrus, F. Hatami, W. Yao, J. Vuckovic, A. Majumdar, and X. Xu. Monolayer semiconductor cavity lasers with ultralow thresholds. Nature **520**, 69 (2015). (cited on p. 5)

[27] O. Painter, R. K. Lee, A. Scherer, A. Yariv, J. D. O'Brien, P. D. Dapkus, and I. I. Kim. Two-dimensional photonic band-Gap defect mode laser. Science **284**, 1819-1821 (2010). (cited on pages 5 and 123)

[28] H.-G. Park, S.-H. Kim, S.-H. Kwon, Y.-G. Ju, J.-K. Yang, J.-H. Baek, S.-B. Kim, Y.-H. Lee. Electrically Driven Single-Cell Photonic Crystal Laser. Science **305**, 1444-1447 (2004). (cited on p. 5)

[29] A. Tandaechanurat, S. Ishida, D. Guimard, M. Nomura, S. Iwamoto and Y. Arakawa. Lasing oscillation in a three-dimensional photonic crystal nanocavity with a complete bandgap. Nature Photonics **5**, 91-94 (2011). (cited on p. 5)

[30] C.-Y. Lu, S.-W. Chang and S. L. Chuang. Low Thermal Impedance of Substrate-Free Metal Cavity Surface-Emitting Microlasers. IEEE. Photon. Technol. Lett. **23**, 1031-1033 (2011). (cited on p. 6)

[31] M. T. Hill, Y.-S. Oei, B. Smalbrugge, Y. Zhu, T. de Vries, P. J. van Veldhoven, F. W. M. van Otten, T. J. Eijkemans, J. P. Turkiewicz, H. de Waardt, E. J. Geluk, S.-H. Kwon, Y.-H. Lee, R. Nötzel and M. K. Smit. Lasing in metallic-coated nanocavities. Nat. Photonics **1**, 589-94 (2007). (cited on pages 6 and 17)

[32] S. A. Maier. *Plasmonics: Fundamentals and Applications.* (Springer, New York, 2007). (cited on pages 6, 20, 22, 90, 92, and 155)

[33] W. L. Barnes, A. Dereux, and T. W. Ebbesen. Surface plasmon subwavelength optics. Nature **424**, 824-830 (2003). (cited on p. 6)

[34] D. K. Gramotnev, and S. I. Bozhevolnyi. Plasmonics beyond the diffraction limit. Nature Photon. **4**, 83-91 (2010). (cited on p. 6)

[35] S. Kawata, Y. Inouye, and P. Verma. Plasmonics for near-field nano-imaging and superlensing. Nature Photon. **3**, 388-394 (2009). (cited on p. 6)

[36] J. Homola. Surface plasmon resonance sensors for detection of chemical and biological species. Chem. Rev. **108**, 462-493 (2008). (cited on p. 6)

[37] D. J. Bergman and M. I. Stockman. Surface Plasmon Amplification by Stimulated Emission of Radiation: Quantum Generation of Coherent Surface Plasmons in Nanosystems. Phys. Rev. Lett. **90**, 027402 (2003). (cited on pages 6, 141, and 147)

[38] N. I. Zheludev, S. L. Prosvirnin, N. Papasimakis and V. A. Fedotov. Lasing spaser. Nature Photonics 2, 351-354 (2008). (cited on pages 6 and 10)

[39] M. Noginov, G. Zhu, A. M. Belgrave, R. Bakker, V. M. Shalaev, E. E. Narimanov, S. Stout, E. Herz, T. Suteewong, and U. Wiesner. Demonstration of a spaser-based nanolaser. Nature (London) **460**, 1110 (2009).
(cited on pages 7, 13, 17, 147, 152, 157, 159, 160, and 167)

[40] R. F. Oulton, V. J. Sorger, T. Zentgraf, R.-M. Ma, C. Gladden, L. Dai, G. Bartal, and X. Zhang. Plasmon lasers at deep subwavelength scale. Nature (London) **461**, 629 (2009).
(cited on pages 7, 8, 17, 82, 87, and 110)

[41] G. A. Plotz, H. J. Simon, and J. M. Tucciarone. Enhanced total reflection with surface plasmons. J. Opt. Soc. Am. **69**, 419-22 (1979). (cited on pages 8 and 87)

[42] A. N. Sudarkin and P. A. Demkovich. Excitation of surface electromagnetic waves on the boundary of a metal with an amplifying medium. Sov. Phys. Tech. Phys. **34**, 764-766 (1988). (cited on pages 8 and 92)

[43] C. Sirtori, C. Gmachl, F. Capasso, J. Faist, D. L. Sivco, A. L. Hutchinson, and A. Y. Cho. Long-wavelength ($\lambda \simeq 11.5$ μm) semiconductor lasers with waveguides based on surface plasmons. Opt. Lett. **23**, 1366-1368 (1998). (cited on p. 8)

[44] A. Tredicucci, C. Gmachl, F. Capasso, A. L. Hutchinson, D. L. Sivco, and A. Y. Cho. Single-mode surface-plasmon laser. App. Phys. Lett. 76, 2164-2166 (2000). (cited on p. 8)

[45] J. Seidel, S. Grafström, and L. Eng. Stimulated Emission of Surface Plasmons at the Interface between a Silver Film and an Optically Pumped Dye Solution. Phys. Rev. Lett. **94**, 177401 (2005). (cited on pages 8, 17, and 92)

[46] M. A. Noginov, V. A. Podolskiy, G. Zhu, M. Mayy, M. Bahoura, J. A. Adegoke, B. A. Ritzo, and K. Reynolds. Compensation of loss in propagating surface plasmon polariton by gain in adjacent dielectric medium. Optics Express **16**, 1385-1392 (2008). (cited on p. 8)

[47] M. A. Noginov, G. Zhu, M. Mayy, B. A. Ritzo, N. Noginova, and V. A. Podolskiy. Stimulated Emission of Surface Plasmon Polaritons. Phys. Rev. Lett. **101**, 226806 (2008). (cited on pages 8 and 17)

[48] P. Berini. Long-range surface plasmon polaritons. Advances in Optics and Photonics **1**, 484-588 (2009). (cited on p. 8)

[49] A. Boltasseva, T. Nikolajsen, K. Leosson, K. Kjaer, M.S. Larsen, and S.I. Bozhevolnyi. Integrated optical components utilizing long-range surface plasmon polaritons. J. Lightwave Technol. **23**, 413–422 (2005). (cited on pages 9 and 97)

[50] R. Charbonneau, C. Scales and I. Breukelaar. Passive integrated optics elements based on long-range surface plasmon polaritons. J. Lightwave Technol. **24**, 477-494 (2006). (cited on pages 9 and 97)

[51] M. Ambati, S. H. Nam, E. Ulin-Avila, D. A. Genov, G. Bartal, and X. Zhang. Observation of stimulated emission of surface plasmon polaritons. Nano Lett. **8**, 3998-4001 (2008). (cited on p. 9)

[52] I. De Leon and P. Berini. Amplification of long-range surface plasmons by a dipolar gain medium. Nat. Photon. **4**, 382 (2010). (cited on pages 8, 9, 13, 17, 87, 94, 97, and 105)

[53] S. Kéna-Cohen, P. N. Stavrinou, D. D. C. Bradley, and S. A. Maier. Confined Surface Plasmon-Polariton Amplifiers Nano Lett. **13**, 1323-1329 (2013). (cited on pages 9, 10, 53, 87, 94, 97, 98, 99, 101, 103, 104, 105, and 109)

[54] J. Y. Suh, C. H. Kim, W. Zhou, M. D. Huntington, D. T. Co, M. R. Wasielewski, and T. W. Odom. Plasmonic Bowtie Nanolaser Arrays. Nano Lett. **12** (11), 5769-5774 (2012). (cited on p. 10)

[55] W. Zhou, M. Dridi, J. Y. Suh, C. H. Kim, D. T. Co, M. R. Wasielewski, G. C. Schatz, and T.W. Odom. Lasing action in strongly coupled plasmonic nanocavity arrays. Nat. Nanotechnol. **8**, 506 (2013). (cited on pages 10, 11, 17, 123, and 140)

[56] A. Yang, T. B. Hoang, M. Dridi, C. Deeb, M. H. Mikkelsen, G. C. Schatz, and T. W. Odom. Real-time tunable lasing from plasmonic nanocavity arrays. Nature Communications **6**, 6939 (2015). (cited on p. 10)

[57] F. van Beijnum, P. J. van Veldhoven, E. J. Geluk, M. J. A. de Dood, G.W. 't Hooft, and M. P. van Exter, Surface Plasmon Lasing Observed in Metal Hole Arrays. Phys. Rev. Lett. 110, 206802 (2013). (cited on pages 10, 11, 17, 123, and 140)

[58] X. Meng, J. Liu, A. V. Kildishev, and V. M. Shalaev. Highly Directional Spaser Array for the Red Wavelength Region. Laser. Phot. Rev. **8**, 896 (2014). (cited on p. 10)

[59] Nature Publishing Group. Scrutinizing lasers (Editorial). Nature Photonics **11**, 139 (2017). (cited on p. 12)

[60] I. D. W. Samuel, E. B. Namdas, and G. A. Turnbull. How to recognize lasing. Nat. Photon. **3**, 546-549 (2009). (cited on p. 12)

[61] A. E. Siegman. *Lasers* (University Science Books, 1986). (cited on pages 12, 13, 24, 26, 79, 105, 133, and 162)

[62] O. Svelto. *Principles of lasers*. Springer, 2010. (cited on pages 12, 13, 24, and 105)

[63] P. Blood. *Quantum Confined Laser Devices: Optical gain and Recombination in Semiconductors*. (Oxford Univ. Press, 2015). (cited on p. 12)

[64] V. G. Kozlov, V. Bulović, P. E. Burrows, and S. R. Forrest. Laser action in organic semiconductor waveguide and double-heterostructure devices. Nature **389**, 362-364 (1997). (cited on p. 12)

[65] M. D. McGehee and A. J. Heeger. Semiconducting (Conjugated) Polymers as Materials for Solid-State Lasers. Adv. Mater. **12**, 1655-1668 (2000). (cited on p. 12)

[66] D. Yokoyama, M. Moriwake and C. Adachi. Spectrally narrow emissions at cutoff wavelength from edges of optically and electrically pumped organic anisotropic films. J. Appl. Phys. **103**, 123104 (2008). (cited on p. 12)

[67] Y. Tian, Z. Gan, Z. Zhou, D. W. Lynch, and J. Shinara. Spectrally narrowed edge emission from organic light-emitting diodes. Appl. Phys. Lett. **91**, 143504 (2007).

(cited on p. 12)

[68] M. C. Gather. A rocky road to plasmonic lasers. Nat. Photonics **6**, 708 (2012). (cited on p. 13)

[69] X. Meng, A. V. Kildishev, K. Fujita, K. Tanaka, and V. M. Shalaev. Wavelength-Tunable Spasing in the Visible. Nano Lett. **13** (9), 4106-4112 (2013). (cited on pages 13 and 147)

[70] S. Wuestner, J. M. Hamm, A. Pusch, F. Renn, K. L. Tsakmakidis, and O. Hess. Control and dynamic competition of bright and dark lasing states in active nanoplasmonic metamaterials. Phys. Rev. B **85**, 201406(R) (2012). (cited on pages 14, 133, and 135)

[71] R. Röder, T. P. H. Sidiropoulos, R. Buschlinger, M. Riediger, U. Peschel, R. F. Oulton, and C. Ronning. Mode Switching and Filtering in Nanowire Lasers. Nano Lett. **16**, 2878-2884 (2016). (cited on p. 14)

[72] L. Ge, O. Malik, and H. E. Türeci. Enhancement of laser power-efficiency by control of spatial hole burning interactions. Nat. Photon. **8**, 871–875 (2014). (cited on pages 14 and 162)

[73] O. Hess and T. Kuhn. Maxwell-Bloch equations for spatially inhomogeneous semiconductor lasers. II. Spatiotemporal dynamics. Phys.Rev.A **54**, 3360 (1996). (cited on p. 14)

[74] K. Böhringer and O. Hess. A full-time-domain approach to spatio-temporal dynamics of semiconductor lasers. I. Theoretical formulation. Prog. Quantum Electron. **32**, 159 (2008). (cited on pages 14 and 19)

[75] K. Böhringer and O. Hess. A full time-domain approach to spatio-temporal dynamics of semiconductor lasers. II. Spatio-temporal dynamics. Prog. Quantum Electron. **32**, 247 (2008). (cited on pages 14 and 19)

[76] D. Li and M. I. Stockman. Electric spaser in the extreme quantum limit. Phys. Rev. Lett. **110**, 106803 (2013). (cited on p. 14)

[77] R.-M. Ma, R. F. Oulton, V. J. Sorger, and X. Zhang. Plasmon lasers: coherent light source at molecular scales. Laser Photonics Rev. **7**, 1-21 (2013). (cited on p. 14)

[78] E. I. Galanzha, R. Weingold, D. A. Nedosekin, M. Sarimollaoglu, J. Nolan, W. Harrington, A. S. Kuchyanov, R. G. Parkhomenko, F. Watanabe, Z. Nima, A. S. Biris, A. I. Plekhanov, M. I. Stockman, and Vladimir P. Zharov. Spaser as a biological probe. Nat. Commun. 8, 15528 (2017). (cited on p. 15)

[79] S.-W. Chang, T.-R. Lin, and S. L. Chuang. Theory of plasmonic Fabry-Perot nanolasers. Optics Express **18**, 15039-15053 (2010). (cited on p. 15)

[80] C.-Y. A. Ni and S. L. Chuang. Theory of high-speed nanolasers and nanoLEDs. Optics Express **20** 16450-16470 (2012). (cited on p. 15)

[81] P. Molina, E. Yraola, M. O. Ramírez, C. Tserkezis, J. L. Plaza, J. Aizpurua, J. Bravo-Abad and L. E. Bausá. Plasmon-assisted Nd3+-based solid-state nanolaser. Nano Letters **16**, 895 (2016). (cited on p. 15)

[82] P. Zhang, Y. Song, J. Tian, X. Zhang, and Z. Zhang Gain characteristics of the InGaAs strained quantum wells with GaAs, AlGaAs, and GaAsP barriers in vertical-external-cavity surface-emitting lasers. Journal of Applied Physics **105**, 053103 (2009). (cited on p. 15)

[83] S. Xiao, V. P. Drachev, A. V. Kildishev, X. Ni, U. K. Chettiar, H.-K. Yuan, and V. M. Shalaev. Loss-free and active optical negative-index metamaterials. Nature (London) **466**, 735 (2010). (cited on p. 17)

[84] M. Ambati, S. H. Nam, E. Ulin-Avila, D. A. Genov, G. Bartal, and X. Zhang, Observation of Stimulated Emission of Surface Plasmon Polaritons. Nano Lett. **8**, 3998 (2008). (cited on p. 17)

[85] R.-M. Ma, R. F. Oulton, V. J. Sorger, G. Bartal, and X. Zhang. Room-temperature sub-diffraction-limited plasmon laser by total internal reflection. Nat. Mater. **10**, 110 (2011). (cited on p. 17)

[86] Y.-J. Lu, J. Kim, H.-Y. Chen, C.Wu, N. Dabidian, C. E. Sanders, C.-Y. Wang, M.-Y. Lu, B.-H. Li, X. Qiu, W.-H. Chang, L.-J. Chen, G. Shvets, C.-K. Shih, and S. Gwo. Plasmonic nanolaser using epitaxially grown silver film. Science **337**, 450 (2012). (cited on pages 17, 87, and 110)

[87] R.-M. Ma, R. F. Oulton, V. J. Sorger, and X. Zhang. Plasmon lasers: coherent light source at molecular scales. Laser Photon. Rev. **7**, 1 (2012). (cited on p. 17)

[88] K. E. Dorfman, P. K. Jha, D. V. Voronine, P. Genevet, F. Capasso, and M. O. Scully. Quantum-Coherence-Enhanced Surface Plasmon Amplification by Stimulated Emission of Radiation. Phys. Rev. Lett. **111**, 043601 (2013) (cited on p. 19)

[89] H. T. Dung, L. Knöll, and D.-G. Welsch. Spontaneous decay in the presence of dispersing and absorbing bodies: General theory and application to a spherical cavity.

Phys. Rev. A **62**, 053804 (2000). (cited on p. 19)

[90] A. Delga, J. Feist, J. Bravo-Abad, and F. J. García-Vidal. Quantum Emitters Near a Metal Nanoparticle: Strong Coupling and Quenching. Phys. Rev. Lett. **112**, 253601 (2014). (cited on p. 19)

[91] J. D. Jackson. *Classical Electrodynamics, Third Edition* (Wiley, 1998). (cited on p. 19)

[92] L. Novotny and B. Hecht, *Principles of Nano-optics* (Cambridge University Press, 2006). (cited on pages 20 and 90)

[93] N. W. Ashcroft and N. D. Mermin, *Solid State Physics*. (Saunders College Publishing, Orlando, FL, 1976). (cited on pages 22 and 23)

[94] S. G. Rodrigo, F. J. García-Vidal, and L. Martín-Moreno. Influence of material properties on extraordinary optical transmission through hole arrays. Phys. Rev. B **77**, 075401 (2008). (cited on pages 22, 111, and 152)

[95] A. Vial, A.-S. Grimault, D. Macías, D. Barchiesi, and M. L. de la Chapelle. Improved analytical fit of gold dispersion: Application to the modeling of extinction spectra with a finite-difference time-domain method. Phys. Rev. B **71**, 085416 (2005). (cited on p. 23)

[96] P. B. Johnson and R. W. Christy. Optical Constants of the Noble Metals. Phys. Rev. B **6**, 4370 (1972). (cited on pages 23, 111, and 152)

[97] M. Born and E. Wolf. *Principles of Optics*. 4th. edition. Pergamon Press, 1970. (cited on p. 23)

[98] P. de Vries and A. Lagendijk, Resonant Scattering and Spontaneous Emission in Dielectrics: Microscopic Derivation of Local-Field Effects. Phys. Rev. Lett. **81**, 1381 (1998). (cited on p. 25)

[99] S. Wuestner, A. Pusch, K. L. Tsakmakidis, J. M. Hamm, and O. Hess, Overcoming Losses with Gain in a Negative Refractive Index Metamaterial. Phys. Rev. Lett. **105**, 127401 (2010). (cited on p. 25)

[100] P. Sperber, W. Spangler, B. Meier, and A. Penzkofer. Experimental and theoretical investigation of tunable picosecond pulse generation in longitudinally pumped dye laser generators and amplifiers. Opt. Quantum Electron. **20**, 395 (1988). (cited on pages 26, 79, 126, and 140)

[101] F. Bloch. Nuclear induction. Phys. Rev. **70**, 460–474 (1946). (cited on p. 27)

[102] S. Wuestner, A. Pusch, K. L. Tsakmakidis, J. M. Hamm, and O. Hess. Gain and plasmon dynamics in active negative-index metamaterials. Phil. Trans. R. Soc. A **369**, 3525-3550 (2011). (cited on pages 27 and 28)

[103] L. Allen and G. I. Peters. Amplified Spontaneous Emission and External Signal Amplification in an Inverted Medium. Phys. Rev. A **8**, 2031 (1975). (cited on p. 27)

[104] P. D. Drummond and M. G. Raymer. Quantum theory of propagation of nonclassical radiation in a near-resonant medium. Phys. Rev. A **44**, 2072 (1991). (cited on p. 27)

[105] C. W. Gardiner. *Quantum noise.* (Springer-Verlag: Berlin, 1991). (cited on p. 27)

[106] J. Andreasen, and H. Cao. Numerical study of amplified spontaneous emission and lasing in random media. Phys. Rev. A **82**, 063835 (2010). (cited on p. 28)

[107] A. Pusch, S. Wuestner, J. M. Hamm, K. L. Tsakmakidis, and O. Hess. Coherent Amplification and Noise in Gain-Enhanced Nanoplasmonic Metamaterials: A Maxwell-Bloch Langevin Approach. ACS Nano **6**, 2420 (2012). (cited on pages 28, 143, and 162)

[108] X. Jiang and C. M. Soukoulis. Time Dependent Theory for Random Lasers. Phys. Rev. Lett. **85**, 70 (2000). (cited on p. 28)

[109] E. Purcell. Resonance Absorption by Nuclear Magnetic Moments in a Solid. Phys. Rev. **69** 681 (1946). (cited on p. 28)

[110] G. Colas des Francs, J. Barthes, A. Bouhelier, J. C. Weeber, A. Dereux, A. Cuche and C. Girard, Plasmonic Purcell factor and coupling efficiency to surface plasmons. Implications for addressing and controlling optical nanosources. Journal of Optics **18**, 094005 (2016). (cited on p. 29)

[111] H. Yokoyama. Physics and device applications of optical microcavities. Science **256**, 66-70 (1992). (cited on p. 30)

[112] H. Yokoyama and S. D. Brorson, Rate equation analysis of microcavity lasers. J. Appl. Phys. **66**, 4801 (1989). (cited on p. 30)

[113] A. Taflove and S. C. Hagness, *Computational electrodynamics. The finite-difference time-domain method.* 3rd Edition. (Artech House, 2005). (cited on p. 32)

[114] J. B. Keller. Geometrical theory of diffraction J. Optical Society of America, **52**, 116-130 (1962). (cited on p. 32)

[115] R. F. Harrington, *Field computation by moment methods*, New York, MacMillan, 1968. (cited on p. 32)

[116] K. S. Yee. Numerical solution of initial boundary value problems involving Maxwell's equations in isotropic media. IEEE Trans. Antennas Propagat., **14**, 302-307 (1966). (cited on p. 32)

[117] A. Taflove, Application of the finite-difference time-domain method to sinusoidal steady-state electromagnetic penetration problems. IEEE Trans. Electromagn. Compat., **22**, 191-202 (1980). (cited on p. 32)

[118] G. Mur, Absorbing boundary conditioDs for the finite-difference approximation of the time-domain electromagnetic field equations. IEEE Trans. Electromagn. Campat., **23**, 317-382 (1981). (cited on p. 32)

[119] D. H. Choi, and W. J. Hoefer. The finite-difference time-domain method and its application to eigenvalue problems. IEEE Trans. Microwave Theory Tech. **34**, 1464-1470 (1986). (cited on p. 32)

[120] K. R. Umashankar, A. Taflove, and B. Beker. Calculation and experimental validation of induced currents on coupled wires in an arbitrary shaped cavity. IEEE Trans, Antennas Propagal. **35**, 1248-1257 (1987). (cited on p. 32)

[121] X. Zhang, J. Fang, K. K. Mei, and Y. Liu. Calculation of the dispersive characteristics of microstrips by the time-domain finite-difference method. IEEE Trans. Microwave Theory Tech. **36**, 263-267 (1988). (cited on p. 32)

[122] T. Kashiwa and I. Fukai. A treatment by FDTD method of dispersive characteristics associated with electronic polarization.Microwave Optics Tech. Lett. **3**, 203-205 (1990). (cited on p. 32)

[123] R. Luebbers, F. Hunsberger, K. Kunz, R. Standler, and M. Schneider. A frequency-dependent finite-difference time-domain formulation for dispersive materials. IEEE Trans. Electromagn. Compat. **32**, 222-229 (1990). (cited on p. 32)

[124] P. M. Goorjian, and A. Taflove. Direct time integration of Maxwell's equations in nonlinear dispersive media for propagation and scattering of femtosecond electromagnetic solitons. Optics Lett. **17**, 180-182 (1992). (cited on p. 32)

[125] Y. Huang. *Simulation of Semiconductor Materials Using FDTD Method.* M.S. Thesis, Northwestern University, Evanston, IL (2002). (cited on p. 32)

[126] S.-H. Chang and A. Taflove. Finite-difference time-domain model of lasing action in a four-level two-electron atomic system. Optics Express, **12**, 3827-3833 (2004). (cited on p. 32)

[127] A. Taflove, A. Oskooi, and S. G. Johnson. *Advances in FDTD Computational Electrodynamics: Photonics and Nanotechnology* (Artech House, 2013). (cited on p. 33)

[128] A. Z. Elsherbeni and V. Demir. *The Finite-Difference Time-Domain Method for Electromagnetics with MATLAB Simulations*. 2nd Edition. The ACES Series on Computational Electromagnetics and Engineering (CEME) (2015). (cited on p. 33)

[129] Comsol Multiphysics, User's guide (version 4.3) (cited on pages 18, 34, 38, 40, 45, and 151)

[130] J. Jin, *The finite element method in electromagnetics*. (Wiley, 2002). (cited on pages 34, 44, 45, and 75)

[131] C. Fietz and C. M. Soukoulis, Finite element simulation of microphotonic lasing system. Opt. Express **20**, 11548-11560 (2012). (cited on pages 34, 45, and 52)

[132] Z.-L. Deng and J.-W. Dong, "Lasing in plasmon-induced transparency nanocavity", Opt. Express **21**, 20291-20302 (2013). (cited on p. 34)

[133] J. N. Reddy. *An introduction to the finite element method*. McGraw-Hill, New York, 2005. (cited on pages 40 and 45)

[134] B. A. Finlayson. *The Method of Weighted Residuals and Variational Principles*. (Academic Press, 1972). (cited on pages 45 and 46)

[135] W. B. J. Zimmerman. *Process Modelling and Simulation with Finite Element Methods*. (World scientific, 2004). (cited on p. 45)

[136] K. E. Jansen, C. H. Whiting, and G. M. Hulbert. A Generalized$-\alpha$ Method for Integrating the Filtered Navier-Stokes Equations with a Stabilized Finite Element Method Comput. Methods Appl. Mech. Engrg. **190**, 305–319 (2000). (cited on p. 62)

[137] J. Chung, G.M. Hulbert. A Time Integration Algorithm for Structural Dynamics with Improved Numerical Dissipation: The Generalized$-\alpha$ Method. J. Appl. Mech. **60**, 371–375 (1993). (cited on p. 63)

[138] The ARPACK Arnoldi package, www.caam.rice.edu/software/ARPACK. (cited on p. 70)

[139] J. P. Berenger. A perfectly matched layer for the absorption of electromagnetic waves. J. Comp. Phy. **114**, 185-200 (1994). (cited on p. 74)

[140] L. A. Coldren, S. W. Corzine, M. L. Masanovic. *Diode Lasers and Photonic Integrated Circuits*. Wiley, 1995. (cited on pages 76, 83, 85, and 112)

[141] H. A. Haus. *Waves and Fields in Optoelectronics*. Prentice-Hall, 1984. (cited on p. 77)

[142] W. Suh, Z. Wang, and S. Fan. Temporal coupled-mode theory and the presence of non-orthogonal modes in lossless multimode cavities. IEEE Journal of Quantum Electronics **40**, 1511-1518 (2004). (cited on p. 76)

[143] J. R. Pierce. Coupling of modes of propagation. J. Appl. Phys. **25**, 179-183 (1954). (cited on p. 76)

[144] H. A. Haus, and W. Huang. Coupled-mode theory. Proc. IEEE **79** 1505-1518 (1991). (cited on p. 76)

[145] W. H. Louisell. *Coupled mode and parametric electronics*. New York Wiley, 1960. (cited on p. 76)

[146] L. D. Landau, and E. M. Lifshitz *Quantum mechanics*, 3rd ed. Oxford: Butterworth-Heinemann, 1977. (cited on p. 76)

[147] S. G. Johnson, P. Bienstman, M. Skorobogatiy, M. Ibanescu, E. Lidorikis, and J. D. Joannopoulos. Adiabatic theorem and continuous coupled-mode theory for efficient taper transitions in photonic crystals. Phys. Rev. E **66**, 066608 (2002). (cited on p. 76)

[148] M. L. Povinelli, S. G. Johnson, S. Fan, and J. D. Joannopoulos. Emulation of two-dimensional photonic crystal defect modes in a photonic crystal with a three-dimensional photonic band gap. Phys. Rev. B **64**, 075313 (2001). (cited on p. 76)

[149] S.-L. Chua, Y. Chong, A. D. Stone, A. Douglas, M. Soljacic, and J. Bravo-Abad. Low-threshold lasing action in photonic crystal slabs enabled by Fano resonances. Optics Express **19**, 1539 (2011). (cited on pages 76 and 136)

[150] M. Soljacic, M. Ibanescu, S. G. Johnson, Y. Fink, and J. D. Joannopoulos. Optimal bistable switching in nonlinear photonic crystals. Phys. Rev. E **66**, 055601 (2002). (cited on p. 76)

[151] J. Bravo-Abad, A. Rodriguez, P. Bermel, S. G. Johnson, J. D. Joannopoulos, and M. Soljacic. Enhanced nonlinear optics in photonic-crystal microcavities. Opt. Express **15**,

16161–16176 (2007). (cited on p. 76)

[152] R. E. Hamam, M. Ibanescu, E. J. Reed, P. Bermel, S. G. Johnson, E. Ippen, J. D. Joannopoulos, and M. Soljacic. Purcell effect in nonlinear photonic structures: A coupled mode theory analysis. Opt. Express **16**, 12523-12537 (2008). (cited on p. 76)

[153] J. Bravo-Abad, E. P. Ippen and M. Soljacic. Ultrafast photodetection in an all-silicon chip enabled by two-photon absorption. Appl. Phys. Lett. **94**, 241103 (2009). (cited on p. 76)

[154] H. Hashemi, A. W. Rodriguez, J. D. Joannopoulos, M. Soljacic, and S. G. Johnson. Nonlinear harmonic generation and devices in doubly-resonant Kerr cavities. Phys. Rev. A **79**, 013812 (2009). (cited on p. 76)

[155] Y.-J. Lu, C.-Y. Wang, J. Kim, H.-Y. Chen, M.-Y. Lu, Y.-C. Chen, W.-H. Chang, L.-J. Chen, M. I. Stockman, C.-K- Shih, and S. Gwo. All-Color Plasmonic Nanolasers with Ultralow Thresholds: Autotuning Mechanism for Single-Mode Lasing. Nano Lett., **14**, 4381–4388 (2014). (cited on pages 82 and 110)

[156] J. M. Hamm, S. Wuestner, K. L. Tsakmakidis, and O. Hess. Theory of Light Amplification in Active Fishnet Metamaterials Phys. Rev. Lett **107**, 167 (2011). (cited on p. 82)

[157] S.-W. Chang, and S. L. Chuang. Fundamental Formulation for Plasmonic Nanolasers. IEEE J. Quant. Electron. **45**, 1014–1023 (2009). (cited on p. 83)

[158] T. Pickering, J. M. Hamm, A. F. Page, S. Wuestner and O. Hess. Cavity-free plasmonic nanolasing enabled by dispersionless stopped light. Nat. Comm. **5**, 4972 (2014). (cited on p. 84)

[159] P. Berini and I. De Leon. Surface plasmon–polariton amplifiers and lasers. Nat. Photonics **6**, 16-24 (2012). (cited on p. 87)

[160] M. C. Gather, K. Meerholz, N. Danz, and K. Leosson. Net optical gain in a plasmonic waveguide embedded in a fluorescent polymer. Nat. Photonics **4**, 457-461 (2010). (cited on p. 87)

[161] J. Grandidier, G. Colas des Francs, S. Massenot, A. Bouhelier, L. Markey, J.-C. Weeber, C. Finot and A. Dereux. Gain-Assisted Propagation in a Plasmonic Waveguide at Telecom Wavelength. Nano Lett. **9**(8), 2935-2939 (2009). (cited on p. 87)

[162] T. P. H. Sidiropoulos, R. Röder, S. Geburt, O. Hess, S. A. Maier, C. Ronning and R. F.

Oulton. Ultrafast plasmonic nanowire lasers near the surface plasmon frequency. Nature Physics **10**, 870-876 (2014). (cited on pages 87 and 110)

[163] Israel De Leon and Pierre Berini. Theory of surface plasmon-polariton amplification in planar structures incorporating dipolar gain media. Phys. Rev. B **78**, 161401(R) (2008). (cited on p. 87)

[164] Israel De Leon and Pierre Berini. Spontaneous emission in long-range surface plasmon-polariton amplifiers. Phys. Rev. B **83**, 081414(R) (2011). (cited on pages 87 and 96)

[165] Israel De Leon and Pierre Berini. Theory of noise in high-gain surface plasmon-polariton amplifiers incorporating dipolar gain media. Optics Express **19**, 20506 (2011). (cited on p. 87)

[166] S. E. Bozhevolnyi. *Plasmonic nanoguides and circuits* (Singapore: Pan Stanford, 2009). (cited on p. 89)

[167] G. Goubau. Surface waves and their application to transmission lines. J. Appl. Phys. **21**, 1119-1128 (1950). (cited on p. 91)

[168] A. Otto. Excitation of nonradiative surface plasma waves in silver by the method of frustrated total reflection. Zeits. Phys. **216**, 398 (1968). (cited on p. 91)

[169] E. Kretschmann and H. Raether. Radiative decay of non radiative surface plasmons excited by light. Z. Naturforschung, A **23**, 2135 (1968). (cited on p. 91)

[170] Lei Dai and Chun Jiang. Anomalous near-perfect extraordinary optical absorption on subwavelength thin metal film grating. Optics Express **17**, 20502-20514 (2009). (cited on p. 93)

[171] E. Moreno, F. J. García-Vidal, S. G. Rodrigo, L. Martín-Moreno and S. I. Bozhevolnyi. Channel plasmon-polaritons: modal shape, dispersion, and losses. Optics Letters **31**, 23 (2006). (cited on p. 95)

[172] I. V. Novikov and A. A. Maradudin. Channel polaritons. Phys. Rev. B **66**, 035403 (2002). (cited on p. 95)

[173] S. I. Bozhevolnyi, V. S. Volkov, E. Devaux, J.-Y. Laluet and T. W. Ebbesen. Channel plasmon subwavelength waveguide components including interferometers and ring resonators. Nature **440**, 508-511 (2006). (cited on p. 95)

[174] S. I. Bozhevolnyi, V. S. Volkov, E. Devaux, and T. W. Ebbesen. Channel Plasmon-Polariton Guiding by Subwavelength Metal Grooves. Phys. Rev. Lett. **95**, 046802 (2005). (cited on p. 95)

[175] C. L. C. Smith, A. H. Thilsted, C. E. Garcia-Ortiz, I. P. Radko, R. Marie, C. Jeppesen, C. Vannahme, S. I. Bozhevolnyi, and A. Kristensen. Efficient Excitation of Channel Plasmons in Tailored, UV-Lithography-Defined V-Grooves. Nano Lett. **14**(3), 1659-1664 (2014). (cited on p. 95)

[176] E. Moreno, S. G. Rodrigo, S. I. Bozhevolnyi, L. Martín-Moreno, and F. J. García-Vidal. Guiding and Focusing of Electromagnetic Fields with Wedge Plasmon Polaritons. Physical Review Letters, **100**, 023901 (2008). (cited on pages 95 and 113)

[177] P. Berini. Bulk and surface sensitivities of surface plasmon waveguides. New J. Phys. **10**, 105010 (2008). (cited on p. 97)

[178] M. Berggren, A. Dodabalapur, and R. E. Slusher. Stimulated emission and lasing in dye-doped organic thin films with Forster transfer. Appl. Phys. Lett. **71**, 2230 (1997). (cited on p. 97)

[179] V. V. Bulović, V. G. Kozlov, V. B. Khalfin, and S. R. Forrest. Transform-limited, narrow-linewidth lasing action in organic semiconductor microcavities. Science **279** (5350), 553-555 (1998). (cited on p. 97)

[180] V. G. Kozlov, V. Bulovic, P. E. Burrows, M. Baldo, V. B. Khalfin, G. Parthasarathy, S. R. Forrest, Y. You, and M. E. Thompson. Study of lasing action based on Förster energy transfer in optically pumped organic semiconductor thin films. J. Appl. Phys. **84** (8), 4096-4108. (cited on p. 97)

[181] S. Kéna-Cohen, P. N. Stavrinou, D. D. C. Bradley, and S. A. Maier. Random lasing in low molecular weight organic thin films. Appl. Phys. Lett. **99** (4), 041114 (2011). (cited on p. 97)

[182] G. W. Ford and W. H. Weber. Electromagnetic interactions of molecules with metal surfaces. Phys. Rep. **113**, 195 (1984). (cited on pages 99 and 102)

[183] Y. Zhang and S.R. Forrest. Existence of continuous-wave threshold for organic semiconductor lasers. Phys. Rev. B **84**, 241301 (2011). (cited on p. 100)

[184] S. Kéna-Cohen, A. Wiener, Y. Sivan, P. N. Stavrinou, D. D. C. Bradley, A. Horsfield, and S.A. Maier. Plasmonic Sinks for the Selective Removal of Long-Lived States. ACS

Nano **5** (12), 9958-9965 (2011). (cited on p. 100)

[185] A. Boltasseva, S. I. Bozhevolnyi, T. Nikolajsen, and K. Leosson. Compact Bragg Gratings for Long-Range Surface Plasmon Polaritons. J. Lightwave Technol. **24**, 912 (2006). (cited on p. 104)

[186] Q. Zhang, G. Li, X. Liu, F. Qian, Y. Li, T. C. Sum, C. M. Lieber, and Q. Xiong. A room temperature low-threshold ultraviolet plasmonic nanolaser. Nature Communications **5**, 4953 (2014). (cited on p. 110)

[187] M. A. Zimmler, F. Capasso, S. Müller, and C. Ronning. Optically pumped nanowire lasers: invited review. Semicond. Sci. Technol. **25** (2000), 024001 (2010). (cited on pages 115 and 120)

[188] C. P. T. McPolin, J.-S. Bouillard, S. Vilain, A. V. Krasavin, W. Dickson, D. 0'Connor, G. A. Wurtz, J. Justice, B. Corbett, and A. V. Zayats. Integrated plasmonic circuitry on a vertical-cavity surface-emitting semiconductor laser platform. Nat. Commun. **7**, 12409 (2016). (cited on p. 121)

[189] X. Wu, Y. Xiao, C. Meng, X. Zhang, S. Yu, Y. Wang, C. Yang, X. Guo, C. Z. Ning, and L. Tong. Hybrid Photon-Plasmon Nanowire Lasers. Nano Lett. **13**, 5654 (2013). (cited on p. 121)

[190] S. Noda, M. Yokoyama, M. Imada A. Chutinan, and M. Mochizuki. Polarization Mode Control of Two-Dimensional Photonic Crystal Laser by Unit Cell Structure Design. Science **293**, 1123-1125 (2001). (cited on p. 123)

[191] Light passing through subwavelength apertures. F. J. García-Vidal, L. Martín-Moreno, T. W. Ebbesen, and L. Kuipers. Rev. Mod. Phys. **82**, 729 (2010). (cited on pages 124 and 125)

[192] A. Salomon, R. J. Gordon, Y. Prior, T. Seideman, and M. Sukharev. Strong Coupling between Molecular Excited States and Surface Plasmon Modes of a Slit Array in a Thin Metal Film. Physical Review Letters **109**(7), 073002 (2012). (cited on p. 124)

[193] R. Marani, A. D'Orazio, V. Petruzzelli, S. G. Rodrigo, L. Martín-Moreno, F. J. García-Vidal, and J Bravo-Abad. Gain-assisted extraordinary optical transmission through periodic arrays of subwavelength apertures. New Journal of Physics **14**, 013020 (2012). (cited on p. 124)

[194] T. W. Ebbesen, H. J. Lezec, H. F. Ghaemi, T. Thio and P. A. Wolff. Extraordinary

optical transmission through sub-wavelength hole arrays. Nature **391**, 667 (1998). (cited on p. 124)

[195] J. A. Porto, F. J. García-Vidal, and J. B. Pendry. Transmission Resonances on Metallic Gratings with Very Narrow Slits. Phys. Rev. Lett. **83**, 2845 (1999). (cited on p. 125)

[196] F. J. García-Vidal and L. Martín-Moreno. Transmission and focusing of light in one-dimensional periodically nanostructured metals. Phys. Rev. B **66**, 155412 (2002). (cited on p. 125)

[197] S. Zou, N. Janel, and G. C. Schatz. Silver nanoparticle array structures that produce remarkably narrow plasmon lineshapes. The Journal of Chemical Physics **120**, 10871 (2004). (cited on p. 125)

[198] B. Auguié and W. L. Barnes. Collective Resonances in Gold Nanoparticle Arrays. Phys. Rev. Lett. **101**, 143902 (2008). (cited on p. 125)

[199] G. Vecchi, V. Giannini, and J. Gómez Rivas. Surface modes in plasmonic crystals induced by diffractive coupling of nanoantennas. Phys. Rev. B **80**, 201401 (2009). (cited on p. 125)

[200] G. Vecchi, V. Giannini, and J. Gómez-Rivas. Shaping the fluorescent emission by lattice resonances in plasmonic crystals of nanoantennas. Phys. Rev. Lett. **102**, 146807 (2009). (cited on p. 125)

[201] S. I. Zou and G. C. Schatz. Silver Nanoparticle Array Structures that Produce Giant Enhancements in Electromagnetic Fields. Chem. Phys. Lett. **403**, 62 (2005). (cited on p. 125)

[202] F. J. García de Abajo. Light scattering by particle and hole arrays. Rev. Mod. Phys. **79**, 1267 (2007). (cited on p. 125)

[203] V. G. Kravets, F. Schedin, and A. N. Grigorenko. Extremely narrow plasmon resonances based on diffraction coupling of localized plasmons in arrays of metallic nanoparticles. Phys. Rev. Lett. **101**, 087403 (2008). (cited on p. 125)

[204] S. R. K. Rodriguez, A. Abass, B. Maes, O. T. A. Janssen, G. Vecchi, and J. Gómez-Rivas. Coupling Bright and Dark Plasmonic Lattice Resonances. Phys. Rev. X **1**, 021019 (2011). (cited on p. 128)

[205] T. K. Hakala, H. T. Rekola, A. I. Väkeväinen, J.-P. Martikainen, M. Nečada, A. J. Moilanen, and P. Törmä. Lasing in dark and bright modes of a finite-sized plasmonic

lattice. Nature Communications **8**, 13687 (2017). (cited on p. 136)

[206] M. I. Stockman. Spasers explained. Nature Photonics **2**, 327-329 (2008). (cited on p. 141)

[207] V. G. Bordo. Cooperative effects in spherical spasers: *Ab-initio* analytical model. Phys. Rev. B **95**, 235412 (2017). (cited on p. 147)

[208] X. F. Li and S. F. Yu. Design of low-threshold compact Au-nanoparticle lasers. Opt. Lett. **35**, 2535 (2010). (cited on p. 147)

[209] A. De Luca, M. Ferrie, S. Ravaine, M. La Deda, M. Infusino, A. R. Rashed, A. Veltri, A. Aradian, N. Scaramuzza, and G. Strangi. Gain functionalized core–shell nanoparticles: the way to selectively compensate absorptive losses. J. Mater. Chem. **22**, 8846 (2012). (cited on p. 147)

[210] N. Calander, D. Jin, and E. M. Goldys. Taking Plasmonic Core-Shell Nanoparticles Toward Laser Threshold. J. Phys. Chem. C **116**, 7546 (2012). (cited on p. 147)

[211] A. Veltri and A. Aradian. Optical response of a metallic nanoparticle immersed in a medium with optical gain. Phys. Rev. B **85**, 115429 (2012). (cited on p. 147)

[212] H. Zhang, J. Zhou, W. Zou, and M. He. Surface plasmon amplification characteristics of an active three-layer nanoshell-based spaser. J. Appl. Phys. **112**, 074309 (2012). (cited on p. 147)

[213] X.-L. Zhong and Z.-Y. Li. All-analytical semiclassical theory of spaser performance in a plasmonic nanocavity. Phys. Rev. B **88**, 085101 (2013). (cited on p. 147)

[214] Y. Huang, X. Bian, Y. X. Ni, A. E. Miroshnichenko, and L. Gao. Nonlocal surface plasmon amplification by stimulated emission of radiation. Phys. Rev. A **89**, 053824 (2014). (cited on p. 147)

[215] Y. Huang, J. J. Xiao, and L. Gao. Antiboding and bonding lasing modes with low gain threshold in nonlocal metallic nanoshell. Opt. Express **23**, 8818 (2015). (cited on p. 147)

[216] N. Arnold, K. Piglmayer, A. Kildishev, and T. A. Klar. Spasers with retardation and gain saturation: electrodynamic description of fields and optical cross-sections. Opt. Mater. Express **5**, 2546 (2015). (cited on p. 147)

[217] V. N. Pustovit, A. M. Urbas, A. V. Chipouline, and T. V. Shahbazyan. Coulomb and quenching effects in small nanoparticle-based spasers. Phys. Rev. B **93**, 165432 (2016).

(cited on p. 147)

[218] V. M. Parfenyev and S. S. Vergeles. Quantum theory of a spaser-based nanolaser. Opt. Express **22**, 13671 (2014). (cited on p. 148)

[219] M. Richter, M. Gegg, T. S. Theuerholz, and A. Knorr. Numerically exact solution of the many emitter–cavity laser problem: Application to the fully quantized spaser emission. Phys. Rev. B 91, 035306 (2015). (cited on p. 148)

[220] Y. Zhang and V. May, J. Chem. Phys. **142**, 224702 (2015). Theory of molecule metal nano-particle interaction: Quantum description of plasmonic lasing. The Journal of Chemical Physics **142**, 224702 (2015). (cited on p. 148)

[221] S. M. Nie and S. R. Emory. Probing Single Molecules and Single Nanoparticles by Surface-Enhanced Raman Scattering. Science **275**, 1102 (1997). (cited on p. 148)

[222] J. B. Pendry. Negative Refraction Makes a Perfect Lens. Phys. Rev. Lett. **85**, 3966 (2000). (cited on p. 148)

[223] P. Anger, P. Bharadwaj, and L. Novotny. Enhancement and quenching of single-molecule fluorescence. Phys. Rev. Lett. **96**, 113002 (2006). (cited on p. 148)

[224] Y. G. Sun and Y. N. Xia. Shape-controlled synthesis of gold and silver nanoparticles. Science **298**, 2176 (2002). (cited on p. 148)

[225] R. Jin, Y. C. Cao, E. Hao, G. S. Métraux, G. C. Schatz, and C. A. Mirkin. Controlling anisotropic nanoparticle growth through plasmon excitation Nature (London) **425**, 487 (2003). (cited on p. 148)

[226] T. Ito and S. Okazaki. Pushing the limits of lithography. Nature (London) **406**, 1027 (2000). (cited on p. 148)

[227] P. Mühlschlegel, H. J. Eisler, O. J. Martin, B. Hecht, and D. W. Pohl. Resonant optical antennas. Science **308**, 1607 (2005). (cited on p. 148)

[228] C. F. Bohren and D. R. Huffman. *Absorption and Scattering of Light by Small Particles.* (Wiley, 1983). (cited on pages 149, 150, and 154)

[229] U. Kreibig and M. Vollmer. *Optical Properties of Metal Clusters.* (Springer-Verlag, 1995). (cited on pages 149, 150, and 154)

[230] Gustav Mie. Beiträge zur optik trüber medien, speziell kolloidaler metallösungen

(contributions to the optics of diffusing media). Annalen der Physik **330**, 377 (1908). (cited on p. 150)

[231] R Gans. Fortpanzung des lichts durch ein inhomogenes medium (propagation of light through a inhomogeneous medium). Annalen der Physik **352**, 709 (1915). (cited on p. 150)

[232] S.-H. Kim, J. Huang, and A. Scherer. From vertical-cavities to hybrid metal/photonic-crystal nanocavities: towards high-efficiency nanolasers. J. Opt. Soc. Am. B **29**, 577-588 (2012). (cited on p. 151)

[233] F. Wang and Y. R. Shen. General properties of local plasmons in metal nanostructures. Phys. Rev. Lett. **97**, 206806 (2006). (cited on p. 151)

[234] C. Sönnichsen, T. Franzl, T. Wilk, G. von Plessen, J. Feldmann, O. Wilson, and P. Mulvaney. Drastic Reduction of Plasmon Damping in Gold Nanorods. Phys. Rev. Lett. **88**, 077402 (2002). (cited on p. 153)

[235] M. Pelton, J. Aizpurua, and G. Bryant. Metal-nanoparticle plasmonics. Laser Photonics Rev. **2**, 136-159 (2008). (cited on p. 154)

[236] M. I. Stockman. Nanoplasmonics: past, present, and glimpse into future. Opt. Express **19**, 22029 (2011). (cited on p. 165)

List of Figures

List of Tables

List of publications

Publications related to the content of this Thesis:

- *Plasmonic waveguide-integrated nanowire laser.*
  E. Bermúdez-Ureña, G. Tütüncüoğlu*, **J. Cuerda***, C. L. C. Smith, J. Bravo-Abad, S. Bozhevolnyi, A. Fontcuberta i Morral, F. J. García-Vidal, and R. Quidant.
  Nano Letters, 17(2), 747-754 (2017).

- *Spatio-temporal modeling of lasing action in core-shell metallic nanoparticles.*
  J. Cuerda, F.J. García-Vidal, and J. Bravo-Abad.
  ACS photonics 3 (10), 1952-1960 (2016).
  Highlighted as ACS Editor's choice.

- *Theory of lasing action in plasmonic crystals.*
  J. Cuerda, F. Rüting, F.J. García-Vidal, and J. Bravo-Abad.
  Physical Review B 91 (4), 041118 (2015).
  Highlighted as an Editor's suggestion.

- *Lasing action assisted by long-range surface plasmons.*
  F. Rüting, **J. Cuerda**, J. Bravo-Abad, and F.J. García-Vidal.
  Laser & Photonics Reviews 8 (5), L65-L70 (2014).

Other publications:

- *Magnetic localized surface plasmons.*
  P. A. Huidobro, X. Shen, **J. Cuerda**, E. Moreno, L. Martín-Moreno, F. J. García-Vidal, T. J. Cui, and J. B. Pendry.
  Physical Review X 4, 021003 (2014).

*Equal contribution.